

ILC HIGGS WHITE PAPER

arXiv:1310.0763v2 [hep-ph] 23 Oct 2013

AUTHORS

D.M. Asner¹, T. Barklow², C. Calancha³, K. Fujii³, N. Graf², H. E. Haber⁴, A. Ishikawa⁵,
S. Kanemura⁶, S. Kawada⁷, M. Kurata⁸, A. Miyamoto³, H. Neal², H. Ono⁹, C. Potter¹⁰, J. Strube¹¹,
T. Suehara⁵, T. Tanabe⁸, J. Tian³, K. Tsumura¹², S. Watanuki⁵, G. Weiglein¹³, K. Yagyu¹⁴,
H. Yokoya⁶

¹*Pacific Northwest National Laboratory, Richland, USA*

²*SLAC National Accelerator Laboratory, Menlo Park, USA*

³*KEK, Tsukuba, Japan*

⁴*University of California, Santa Cruz, USA*

⁵*Tohoku University, Sendai, Japan*

⁶*University of Toyama, Toyama, Japan*

⁷*Hiroshima University, Hiroshima, Japan*

⁸*University of Tokyo, Tokyo, Japan*

⁹*Nippon Dental University, Niigata, Japan*

¹⁰*University of Oregon, Eugene, USA*

¹¹*CERN, Geneva, Switzerland*

¹²*University of Nagoya, Nagoya, Japan*

¹³*DESY, Hamburg, Germany*

¹⁴*National Central University, Zhongli, Taiwan*

Contents

Table of Contents	5
Introduction	9
1 Higgs Theory	11
1.1 Introduction: the Higgs mechanism	11
1.1.1 Vector boson mass generation and the unitarity of $VV \rightarrow VV$ scattering ($V = W$ or Z)	12
1.1.2 Chiral fermion mass generation and the unitarity of $VV \rightarrow f\bar{f}$ scattering	13
1.2 Theoretical structure of the Standard Model Higgs boson	14
1.2.1 Tree level Higgs boson couplings	14
1.2.2 Higgs couplings at one-loop	17
1.2.3 Higgs decays	18
1.2.4 Higgs production at the ILC	19
1.2.5 Vacuum Stability	21
1.3 The two-Higgs-doublet model (2HDM)	22
1.3.1 Model-independent treatment	22
1.3.2 Constraints on 2HDM scalar potential parameters	24
1.3.3 Tree-level Higgs boson couplings—the general case	26
1.3.4 Tree-level Higgs boson couplings—the CP-conserving case	28
1.3.5 The decoupling/alignment limit of the 2HDM	29
1.3.6 Higgs production at the ILC	32
1.3.7 Special forms for the Higgs-fermion Yukawa interactions	33
1.3.8 Constraints due to flavor physics	38
1.3.9 The inert 2HDM	42
1.3.10 The MSSM Higgs sector	44
1.4 Other extended Higgs sectors	50
1.4.1 Constraints from the tree-level rho parameter	50
1.4.2 An upper bound for the Higgs coupling to vector boson pairs	51
1.4.3 Adding Higgs singlets	52
1.4.4 Adding Higgs triplets	53
1.4.5 The NMSSM Higgs sector	55
1.5 Model-independent treatments of Higgs properties	57
1.5.1 Effective Lagrangian treatments	58
1.5.2 Simplified approach for the analysis of Higgs couplings	58
1.6 Alternative approaches to electroweak symmetry breaking dynamics	60
1.6.1 The Higgs boson as a pseudo-Goldstone boson	61
1.6.2 The Higgs boson as a dilaton	62

1.7	Probing the properties of the signal at 126 GeV	62
1.7.1	Present status and prospects for the upcoming LHC runs	62
1.7.2	Experimental precision required to discriminate between different possible interpretations	64
1.7.3	Examples of analyses in different models	65
1.7.4	The hhh coupling and electroweak baryogenesis	69
1.7.5	Value added by the ILC Higgs program post-LHC	70
2	ILC Accelerator Parameters and Detector Concepts	73
2.1	ILC Accelerator Parameters	73
2.1.1	TDR Baseline ILC 250 - 500 GeV	73
2.1.2	Luminosity and Energy Upgrade Options	76
2.1.3	Gamma-Gamma Option	77
2.1.4	Energy/Luminosity Running Scenarios	78
2.2	Detector Concepts	79
2.2.1	ILD	79
2.2.2	SiD	80
2.3	Systematic Errors	83
2.3.1	Flavor Tagging	83
2.3.2	Luminosity	85
2.3.3	Polarization	86
2.3.4	Systematic Error Summary	86
3	Higgs Mass, ZH Cross Section, Spin and CP	87
3.1	Higgs Mass and $\sigma(ZH)$ Measurements	87
3.1.1	l^+l^-h at $\sqrt{s} = 250$ GeV	87
3.1.2	l^+l^-h at $\sqrt{s} = 500$ GeV	87
3.1.3	$q\bar{q}h$ at $\sqrt{s} = 500$ GeV	89
3.2	Higgs Spin Measurement	90
3.3	Higgs Sector CP Measurements	91
3.3.1	Introduction	91
3.3.2	$e^+e^- \rightarrow ZH$	91
3.3.3	$H \rightarrow \tau^+\tau^-$	92
3.3.4	$e^+e^- \rightarrow t\bar{t}H$	92
4	Cross Section Times Branching Ratio Measurements I	95
4.1	$h \rightarrow b\bar{b}, c\bar{c}, gg$	95
4.1.1	250 GeV and 350 GeV	95
4.1.2	500 GeV	96
4.1.3	1 TeV	97
4.2	$h \rightarrow WW^*$	98
4.2.1	500 GeV	98
4.2.2	1 TeV	99
4.3	$h \rightarrow \tau^+\tau^-$	100
4.3.1	250 GeV	100
4.3.2	500 GeV	100

5	Cross Section Times Branching Ratio Measurements II	103
5.1	$h \rightarrow ZZ^*$	103
5.1.1	Event reconstruction for $h \rightarrow ZZ^*$	103
5.1.2	Multi-Variate Analysis	104
5.1.3	Results for $f^+ f^- h \rightarrow ZZ^*$	106
5.2	$h \rightarrow \gamma\gamma$	106
5.3	$h \rightarrow \mu^+ \mu^-$	107
5.4	Invisible Higgs Decays	107
5.5	Top Yukawa Coupling Measurement	108
5.6	Higgs Self Coupling Measurement	109
5.7	Cross Section Times Branching Ratio Summary	110
6	Higgs Couplings, Total Width and Branching Ratios	111
6.1	Model Independent Determination of Higgs Couplings	111
6.2	Model Independent Determination of Higgs Cross Sections and Higgs Branching Ratios	113
6.3	Model-Dependent Coupling Parameterizations	113
6.3.1	Benchmark Parameterizations of the LHC HXSWG	113
6.3.2	Higgs Couplings to W and Z Bounded by SM Couplings	115
6.4	Effective Higgs Operators	115
7	Non-Minimal Higgs Models	119
7.1	Direct Production of Non-Minimal Higgs Bosons	119
7.1.1	Neutral Higgs pair production at ILC	119
7.1.2	Charged Higgs boson production	120
7.2	Measurements of $\tan\beta$ at the ILC	122
8	Gamma-Gamma and e-Gamma Option	125
8.1	Production Cross Sections and Luminosity Spectra	126
8.2	Higgs Studies	126
8.2.1	h_{SM} Mass Measurement	128
8.2.2	Branching Fractions	129
8.2.3	Determining CP Nature of a Higgs Boson	131
8.3	Understanding gamma-gamma backgrounds at the ILC	134
8.4	Summary	134
9	Summary	135
	Bibliography	139

Introduction

Following an intense and successful R&D phase, the ILC has now achieved a state of maturity and readiness, culminating recently with the publication of the Technical Design Report [1, 2, 3, 4, 5]. Several important physics goals at the TeV energy scale have motivated this effort. These include a detailed study of the properties of the recently discovered Standard Model-like Higgs boson, including precision measurements of its couplings to fermions and bosons, and an improved knowledge of the top quark and W, Z boson interactions to a high level of precision. In all of these, the ILC will yield substantial improvements over LHC measurements and will have a qualitative advantage on signatures that have high backgrounds at LHC or are difficult to trigger on. Moreover, the ILC provides a unique sensitivity in the search for signals of new physics beyond the Standard Model arising from the electroweak production of new particles (assuming these are kinematically accessible), as well as extending the probe of new interactions to higher mass scales via the precision measurements of W, Z and two-fermion processes. In this way, the ILC experiments will be sensitive to new phenomena such as supersymmetric partners of known particles, new heavy gauge bosons, extra spatial dimensions, and particles connected with alternative theories of electroweak symmetry breaking [2]. Indeed, the ILC experiments will bring qualitatively new capabilities; detailed simulations with realistic detector designs show that the ILC can reach the precision goals needed [5].

The requirements of the ILC [6] include tunability between center-of-mass energies of 200 and 500 GeV, with rapid changes in energy over a limited range for threshold scans. The luminosity, which must exceed $10^{34} \text{ cm}^{-2}\text{s}^{-1}$ at 500 GeV, roughly scales proportionally with center-of-mass collision energy. Highly polarized electrons ($> 80\%$) are specified, with polarized positrons desirable. The TDR design [3, 4] has met these specifications. R&D has achieved the accelerating gradient goal of 35 MV/m in test stands and 31.5 MV/m in installed cryomodules with beam loading. Cavity fabrication to these specifications has been industrialized. The effects of the electron cloud in the positron damping ring have been studied experimentally, leading to proven techniques for its mitigation. Fast kickers needed for damping ring beam injection and ejection have been developed. The required small final focus spot size is being demonstrated in a test facility. The final focus and interaction region, including the detector push-pull system, has been designed. Two detailed detector designs have been developed [5], with R&D supporting these designs. Beam tests with highly granular calorimeters have demonstrated the calorimetry performance needed by using the particle flow technique. Similarly, tracking R&D has advanced for vertex detection based on thin CMOS monolithic pixel sensors, outer tracking with low-mass supported silicon microstrips, and advanced TPC technologies employing micropattern gas detectors or silicon sensors for readout.

Recently, the Japanese government has expressed a desire to host the ILC, and international negotiations are underway. In a staged approach, beginning at a center-of-mass energy of 250 GeV, a physics program would start with precision measurements of the Higgs branching ratios and properties. Raising the energy to 500 GeV would move to precision measurements of top quark properties well beyond those possible at the LHC. Measurements of the top coupling to the Higgs and the Higgs self coupling would begin at 500 GeV. Should there be accessible new particles such as supersymmetric

partners of gauge bosons, Higgs bosons and leptons, the ILC with the power of polarized beams is the only place where they can be studied in full detail. If there are additional Higgs boson states (which are often difficult to observe at the LHC even if not too heavy), the ILC would be needed to measure their masses, quantum numbers, and couplings to Standard Model particles. Extension of the ILC to 1 TeV is straightforward, with lengthened linac tunnels and additional cryomodules, building on the original ILC sources, damping rings, final focus and interaction regions, and beam dumps.

Chapter 1

Higgs Theory

1.1 Introduction: the Higgs mechanism

Quantum field theory has been enormously successful in describing the behavior of fundamental point particles and their interactions in a framework that is consistent with the principles of relativity and quantum mechanics. Indeed, once these principles are invoked, quantum field theory appears to be the only consistent framework for incorporating interacting fundamental point particles. If such a framework is to be predictive (i.e., dependent only on a finite number of input parameters that are provided by experimental measurements), then the properties of such fundamental particles are highly constrained—only spin 0, spin 1/2 and spin 1 are allowed [7, 8]. Moreover, if the spin 1 particles are self-interacting, they must be described by a gauge theory. It is remarkable that this is precisely the spectrum of fundamental particles that have been observed in nature.

A gauge theory of fundamental self-interacting spin-1 gauge bosons naively appears to require that gauge bosons should be massless, since an explicit mass term for the gauge boson in the Lagrangian manifestly violates the gauge symmetry. However, due to the seminal work of Brout, Englert [9] and Higgs [10, 11] and subsequent work by Guralnik, Hagen and Kibble [12, 13, 14], a mass-generation mechanism for gauge bosons that is consistent with the gauge symmetry was developed. The simplest realization of this mechanism was subsequently employed by Weinberg, when he incorporated a self-interacting complex scalar doublet into a gauge theory of electroweak interactions [15]. The neutral scalar of the doublet acquires a vacuum expectation value (vev), which spontaneously breaks the gauge symmetry and generates mass for the W^\pm and Z bosons of electroweak theory while leaving the photon massless. Moreover, by coupling the complex scalar doublet to the chiral fermions of the Standard Model (where no gauge-invariant mass terms for the fermions are allowed prior to symmetry breaking), one can also generate masses for all quarks and charged leptons. In the Glashow-Weinberg-Salam theory of the electroweak interactions [15, 16, 17], the gauge bosons acquire mass via the Higgs mechanism by absorbing three of the four degrees of freedom of the complex scalar doublet, which provide for the longitudinal degrees of freedom of the W^\pm and Z bosons. One physical scalar degree of freedom is left over—the Higgs boson of the Standard Model.

There are other possible dynamics that can be used for achieving a spontaneously broken gauge theory of the electroweak interactions (via the Higgs mechanism) in which elementary scalar bosons are not employed. For example, it is possible to spontaneously break a gauge theory by introducing a strongly interacting fermion pair that condenses in the vacuum, in analogy with Cooper pairs of superconductivity (for a nice review, see Ref. [18]). However, in the summer of 2012 a new scalar boson was discovered at the LHC by the ATLAS and CMS Collaborations [19, 20], whose properties appear to be consistent (within the experimental error) with those expected of the Standard Model Higgs boson [21, 22, 23, 24]. Consequently, it appears that nature has chosen to realize the Higgs mechanism via scalar fields that are either elementary or appear elementary at the electroweak scale.

Although the scalar sector need not be a minimal one, the data seems to favor the existence of one state of the scalar sector whose properties resemble those of the Standard Model Higgs bosons; any deviations from Standard Model behavior, if they exist, are likely to be small. Clearly, precision measurements of the newly discovered scalar state will be critical for establishing and testing the theory that governs the dynamics of electroweak symmetry breaking.

1.1.1 Vector boson mass generation and the unitarity of $VV \rightarrow VV$ scattering ($V = W$ or Z)

Consider the theory of electroweak interactions without the attendant scalar sector. If one attempts to simply add an explicit mass term to the W^\pm and Z bosons, then the resulting theory would be mathematically inconsistent. One signal of this inconsistency would be revealed by using the theory to compute the cross section for the scattering of longitudinally polarized gauge bosons, $VV \rightarrow VV$ (where $V = W$ or Z) at tree-level. Such a calculation would yield a scattering amplitude whose energy dependence grows with the square of the center of mass energy, a result that grossly violates unitarity. Such a result would be in violation of one of the sacred principles of quantum mechanics (which requires that the sum of probabilities can never exceed unity).

It is remarkable that this tree-level unitarity violation can be mitigated by postulating the existence of an elementary scalar particle that couples to W^+W^- and ZZ with coupling strength gm_V^2/m_W (where $V = W$ or Z). This new interaction introduces an additional contribution to $VV \rightarrow VV$, which exactly cancels the bad high energy behavior of the scattering amplitude, and leaves a result that approaches a constant at infinite energy. Thus, one can reconstruct the Standard Model by imposing tree-level unitarity on all scattering amplitudes of the theory [25, 26, 27]. Thus, if the newly discovered scalar h is to be interpreted as the Higgs boson of the Standard Model, one should confirm that

$$g_{hVV} = \frac{\sqrt{2}m_V^2}{v}, \quad g_{hhVV} = \frac{\sqrt{2}m_V^2}{v^2}, \quad (1.1)$$

where the Higgs vev, $v = 174$ GeV, is related to the W mass via $m_W = gv/\sqrt{2}$.

Suppose deviations from eq. (1.1) were uncovered by experimental Higgs studies. Then, one would surmise that the scalar Higgs sector is not minimal, and other scalar states play a role in achieving tree-level unitarity [28]. Indeed, one can examine the case of an arbitrary scalar sector and derive unitarity sum rules that replace eq. (1.1) in the more general Higgs model. We shall impose one constraint on all extended Higgs sectors under consideration—the scalar multiplets and vevs employed should satisfy the tree-level constraint that

$$\rho \equiv \frac{m_W^2}{m_Z^2 \cos^2 \theta_W} = 1, \quad (1.2)$$

a result that is strongly suggested by precision electroweak measurements [29, 30]. For example, consider a CP-conserving extended Higgs sector that has the property that $\rho = 1$ and no tree-level $ZW^\pm\phi^\mp$ couplings (where ϕ^\pm are physical charged scalars that might appear in the scalar spectrum), then it follows that [28]

$$\sum_i g_{h_i VV}^2 = \frac{2m_V^4}{v^2}, \quad (1.3)$$

$$m_W^2 g_{h_i ZZ} = m_Z^2 g_{h_i WW}, \quad (1.4)$$

where the sum in eq. (1.3) is taken over all neutral CP-even scalars h_i . In this case, it follows that $g_{h_i VV} \leq g_{hVV}$ for all i (where h is the Standard Model Higgs boson). Models that contain only scalar singlets and doublets satisfy the requirements stated above and hence respect the sum rule given in eq. (1.3) and the coupling relation given in eq. (1.4). However, it is possible to violate

$g_{h_i VV} \leq g_{h VV}$ and $m_W^2 g_{h_i ZZ} = m_Z^2 g_{h_i WW}$ if tree-level $ZW^\pm \phi^\mp$ couplings are present. Indeed, in this case, one can show that doubly charged Higgs bosons must also occur in the model [28].

1.1.2 Chiral fermion mass generation and the unitarity of $VV \rightarrow f\bar{f}$ scattering

In the Standard Model, left-handed fermions are electroweak doublets and right-handed fermions are electroweak singlets. A fermion mass term would combine a left-handed and right-handed fermion field, so that gauge invariance does not allow for explicit fermion mass terms. However, in the Standard Model, it is possible to couple a left-handed and right-handed fermion field to the scalar doublets. Such interactions comprise the Yukawa couplings of the Standard Model. When the scalar field acquires a vev, mass terms for the quarks and charged leptons are generated.

One can repeat the previous analysis by again considering the theory of electroweak interactions without the attendant scalar sector. If one attempts to simply add explicit mass terms to the quarks and charged leptons and the W^\pm and Z bosons, then the resulting theory would again be mathematically inconsistent. One signal of this inconsistency would be revealed by using the theory to compute the cross section for the scattering of longitudinally polarized gauge bosons into a pair of top quarks, $VV \rightarrow t\bar{t}$ at tree-level. Such a calculation would yield a scattering amplitude whose energy dependence grows with the the center of mass energy, which violates tree-level unitarity.

Once again, the addition of an elementary particle that couples to W^+W^- and ZZ with coupling strength gm_V^2/m_W and couples to $t\bar{t}$ with coupling strength $gm_t/(2m_W)$ is sufficient to cure the bad high energy behavior. Thus, if the newly discovered scalar h is to be interpreted as the Higgs boson of the Standard Model, one should confirm that

$$g_{hVV}g_{hff} = \frac{m_V^2 m_f}{v^2}, \quad (1.5)$$

for all quarks and charged leptons f (in practice, $f = t, b, c$ and τ are the most relevant). In models of extended Higgs sectors, eq. (1.5) would be replaced by a unitarity sum rule in which the right-hand side of eq. (1.5) would be the result of summing over multiple Higgs states in the model [28].

1.2 Theoretical structure of the Standard Model Higgs boson

1.2.1 Tree level Higgs boson couplings

The Higgs sector of the Standard Model (SM), which takes the minimal form, consists of one isospin doublet scalar field Φ with the hypercharge $Y = 1$ [31]. The most general $SU(2) \times U(1)$ -invariant renormalizable Higgs potential is give by

$$V(\Phi) = \mu^2 |\Phi|^2 + \frac{1}{2} \lambda |\Phi|^4. \quad (1.6)$$

The Higgs doublet field is parameterized as

$$\Phi = \begin{pmatrix} \omega^+ \\ v + (h + iz)/\sqrt{2} \end{pmatrix}, \quad (1.7)$$

where ω^\pm and z represent the Nambu-Goldstone boson, h is a physical state, the Higgs boson, and $v = 174$ GeV is the vacuum expectation value (vev) of the Higgs field. The self-coupling constant λ is positive to guarantee the stability of vacuum. Assuming that $\mu^2 < 0$, the shape of the potential resembles the Mexican hat, and the minimum of the scalar potential occurs at $\langle \Phi \rangle = v$, where $\mu^2 = -\lambda v^2$. The $SU(2) \times U(1)$ electroweak symmetry is then broken down to $U(1)_{EM}$. Expanding the scalar field around its vacuum expectation value, the scalar potential immediately yields the mass and the self-couplings of the Higgs boson h ,

$$m_h^2 = 2\lambda v^2, \quad \lambda_{hhh} = 3\sqrt{2}\lambda v, \quad \lambda_{hhhh} = 3\lambda. \quad (1.8)$$

Hence, the Higgs mass and self-couplings are related by

$$\lambda_{hhh} = \frac{3m_h^2}{v\sqrt{2}}, \quad \lambda_{hhhh} = \frac{3m_h^2}{2v^2}. \quad (1.9)$$

That is, the Higgs mass is directly related to the dynamics of the Higgs sector. In particular, the heavier the Higgs mass the stronger the strength of the Higgs self-couplings. Indeed, the observed Higgs mass of 126 GeV implies that $\lambda_{hhhh} \simeq 0.787$, which implies that the Higgs dynamics is weakly coupled.

The Higgs field couples to the weak gauge bosons (W and Z) via the covariant derivative [32], $|\mathcal{D}_\mu \Phi|^2$, where $\mathcal{D}_\mu = \partial_\mu + \frac{1}{2}igA_\mu^a\tau^a + \frac{1}{2}ig'B_\mu Y$. Here, the τ^a are the usual Pauli matrices, the electric charge operator is $Q = \frac{1}{2}(\tau^3 + Y)$, and g and g' are gauge coupling constants for $SU(2)_T$ and $U(1)_Y$, respectively. The masses of the gauge bosons, which are generated by electroweak symmetry breaking via the Higgs mechanism, are proportional to the neutral scalar field vev,

$$m_W^2 = \frac{1}{2}g^2v^2, \quad m_Z^2 = \frac{1}{2}(g^2 + g'^2)v^2. \quad (1.10)$$

Electroweak symmetry breaking also generates the hWW and hZZ couplings,

$$g(hWW) = \frac{1}{\sqrt{2}}g^2v, \quad g(hZZ) = \frac{1}{\sqrt{2}}(g^2 + g'^2)v. \quad (1.11)$$

Therefore, the gauge boson masses and the couplings to the Higgs boson are related as noted previously in eq. (1.1).

The Higgs field also couples to quarks and leptons via Yukawa interactions. For example, the

coupling of the Higgs fields to the three generations of quarks is given by

$$-\mathcal{L}_{\text{Yukawa}} = Y_U^{0ij} (\bar{U}_L^{0i} U_R^{0j} \Phi^{0*} - \bar{D}_L^{0i} U_R^{0j} \Phi^-) + Y_D^{0ij} (\bar{D}_L^{0i} D_R^{0j} \Phi^0 + \bar{U}_L^{0i} D_R^{0j} \Phi^+) + \text{h.c.}, \quad (1.12)$$

where i, j are generation labels, $U^0 = (u^0, c^0, t^0)$ and $D^0 = (d^0, s^0, b^0)$ are the interaction-eigenstate quark fields, and Y_U^0 and Y_D^0 are arbitrary complex 3×3 matrices (the sum over repeated indices is implied). In eq. (1.12) we have introduced left and right-handed quark fields via $Q_L^0 \equiv P_L Q^0$ and $Q_R^0 \equiv P_R Q^0$ where $P_{R,L} \equiv \frac{1}{2}(1 \pm \gamma_5)$. Setting the Goldstone boson fields to zero and writing $\Phi^0 = v + h^0/\sqrt{2}$, we identify the quark mass matrices,

$$M_U^0 \equiv v Y_U^0, \quad M_D^0 \equiv v Y_D^0. \quad (1.13)$$

We now determine the quark mass eigenstate fields, $U = (u, c, t)$ and $D = (d, s, b)$ by introducing the following unitary transformations,

$$U_L = V_L^U U_L^0, \quad U_R = V_R^U U_R^0, \quad D_L = V_L^D D_L^0, \quad D_R = V_R^D D_R^0, \quad (1.14)$$

where V_L^U, V_R^U, V_L^D , and V_R^D are unitary matrices chosen such that

$$M_U \equiv V_L^U M_U^0 V_R^{U\dagger} = \text{diag}(m_u, m_c, m_t), \quad M_D \equiv V_L^D M_D^0 V_R^{D\dagger} = \text{diag}(m_d, m_s, m_b), \quad (1.15)$$

such that the m_i are the positive quark masses (this is the *singular value decomposition* of linear algebra).

Having diagonalized the quark mass matrices, the neutral Higgs Yukawa couplings are automatically flavor-diagonal. That is, if we define

$$Y_U \equiv V_L^U Y_U^0 V_R^{U\dagger} = M_U/v, \quad Y_D \equiv V_L^D Y_D^0 V_R^{D\dagger} = M_D/v, \quad (1.16)$$

then eq. (1.12) can be rewritten in terms of quark mass eigenstates as:

$$-\mathcal{L}_{\text{Yukawa}} = \bar{U}_L Y_U U_R \Phi^{0*} - \bar{D}_L K^\dagger Y_U U_R \Phi^- + \bar{U}_L K Y_D D_R \Phi^+ + \bar{D}_L Y_D D_R \Phi^0 + \text{h.c.}, \quad (1.17)$$

where

$$K \equiv V_L^U V_L^{D\dagger}, \quad (1.18)$$

is the Cabibbo-Kobayashi-Maskawa (CKM) matrix. Hence the SM possesses no flavor-changing neutral currents (FCNCs) mediated by neutral Higgs boson exchange at tree-level. Note that independently of the Higgs sector, the quark couplings to Z and γ are automatically flavor diagonal. Flavor dependence only enters the quark couplings to the W^\pm via the CKM matrix.

The Yukawa coupling of the Higgs doublets to the leptons can be similarly treated by replacing $U \rightarrow N$, $D \rightarrow E$, $M_U \rightarrow 0$, $M_D \rightarrow M_E$ and $K \rightarrow \mathbb{1}$, where $N = (\nu_e, \nu_\mu, \nu_\tau)$, $E = (e, \mu, \tau)$ and M_E is the diagonal charged lepton mass matrix. In the present treatment, the right-handed neutrino fields are absent, in which case the neutrinos are exactly masses. One can accommodate the very small neutrino masses by including the right-handed neutrino fields and adding a $\text{SU}(2) \times \text{U}(1)$ -invariant mass term $\bar{N}_L M_N N_R + \text{h.c.}$ to eq. (1.17). Assuming that the eigenvalues of M_N are much larger than the scale of electroweak symmetry breaking, one obtains three very light Majorana neutrino mass eigenstates due to the seesaw mechanism [33, 34, 35, 36, 37]. The very small neutrino masses have almost no impact on Higgs physics. Consequently, we shall simply treat the neutrinos as massless in this chapter.

In the SM, there is an universal relation between the masses of the fundamental particles and

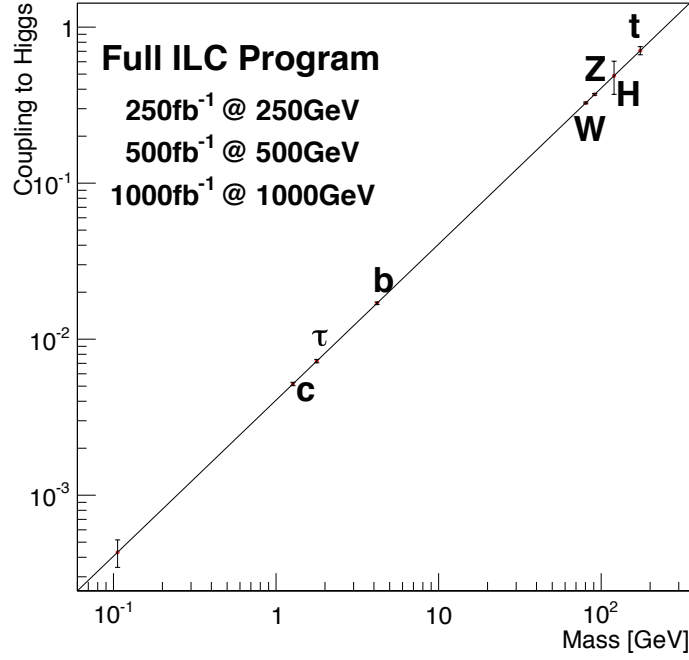


Figure 1.1. The Standard Model prediction that the Higgs coupling to each particle is proportional to its mass. Expected precision from the full ILC program for the coupling determination is also shown.

their couplings to the Higgs boson,

$$\frac{g(hWW)}{\sqrt{2}m_W^2} = \frac{g(hZZ)}{\sqrt{2}m_Z^2} = \frac{y_c}{m_c} = \frac{y_\tau}{m_\tau} = \frac{y_b}{m_b} = \frac{y_t}{m_t} = \frac{\sqrt{2}\lambda(hhh)}{3m_h^2} = \dots = \frac{1}{v}. \quad (1.19)$$

This is a unique feature of the SM with one Higgs doublet field. By accurately measuring the mass and coupling to the Higgs boson independently for each particle, one can test the mass generation mechanism of the SM by using this relation. In Fig. 1.1, the Standard Model relation is shown along with expected precision from the full ILC program for the coupling determinations. If the Higgs sector takes a non-minimal form, deviations from this universal relation are expected. Each non-minimal Higgs sector possesses a specific pattern of deviations. Thus, if the Higgs couplings can be measured with sufficient precision, these measurements would provide a way to distinguish among different models of extended Higgs sectors.

1.2.2 Higgs couplings at one-loop

The Higgs boson h is a charge and color neutral state; hence, it does not couple to photons and gluons at the tree level. However, beyond the tree level, the coupling hgg , $h\gamma\gamma$ and $h\gamma Z$ appear via the dimension-6 operators,

$$\frac{1}{\Lambda^2} |\Phi|^2 F_{\mu\nu} F^{\mu\nu}, \quad \frac{1}{\Lambda^2} |\Phi|^2 G_{\mu\nu} G^{\mu\nu}. \quad (1.20)$$

In the SM, the effective hgg coupling is induced at the one-loop level via quark-loop diagrams, with the dominant contribution arising from the top quark loop. In contrast, the $h\gamma\gamma$ and $h\gamma Z$ couplings are induced via the top loop diagram and the W -loop diagram in the SM. The leading contribution to the coupling of $h\gamma\gamma$ is the W^\pm boson loop, which is roughly 4.5 times larger in amplitude than the contribution of the top quark loop. Analytic expressions for the $h \rightarrow gg$ decay width and the diphoton partial width are given by [38, 39]

$$\Gamma(h \rightarrow gg) = \frac{G_F \alpha_s^2 m_h^3}{512 \sqrt{2} \pi^3} |N_c Q_t^2 A_{1/2}(\tau_t)|^2, \quad (1.21)$$

$$\Gamma(h \rightarrow \gamma\gamma) = \frac{G_F \alpha^2 m_h^3}{128 \sqrt{2} \pi^3} |A_1(\tau_W) + N_c Q_t^2 A_{1/2}(\tau_t)|^2, \quad (1.22)$$

where G_F is the Fermi constant, $N_c = 3$ is the number of color, $Q_t = +2/3$ is the top quark electric charge in units of e , and $\tau_i \equiv 4m_i^2/m_h^2$ (for $i = t, W$). Below the WW threshold, the loop functions for spin-1 (W boson) and spin-1/2 (top quark) particles are given in the Appendix in Ref. [40].

In the limit that the particle running in the loop has a mass much heavier than the Higgs, we have

$$A_1 \rightarrow -7, \quad N_c Q_t^2 A_{1/2} \rightarrow \frac{4}{3} N_c Q_t^2. \quad (1.23)$$

For a Higgs mass below the WW threshold, the W boson contribution is always dominant and monotonically decreasing from $A_1 = -7$ for very small Higgs masses to $A_1 \approx -12.4$ at the threshold, while the top quark contribution is well-approximated by the asymptotic value of $(4/3)^2 \approx 1.78$. If we consider a Higgs mass at 126 GeV, the W and top contributions are

$$m_h = 126 \text{ GeV} : A_1 = -8.32, \quad N_c Q_t^2 A_{1/2} = 1.84. \quad (1.24)$$

There have been many studies on the new physics loop contributions to the hgg as well as $h\gamma\gamma$ couplings. Recently, Carena, Low and Wagner have performed a comprehensive study for the effects on the diphoton width from adding new colorless charged particles of spin-0, spin-1/2, and spin-1, which would interfere with the SM contributions [40].

In general, contributions of particles in loop diagrams can decouple in their large mass limit by the negative power of the mass. This is the consequence of the decoupling theorem by Appelquist and Carazzone [41]. However, in cases where the origin of the mass of the particle is due to electroweak symmetry breaking, then the squared-mass of the boson or the mass of the fermion is proportional to the vacuum expectation value as indicated in eq. (1.19) and the constant of proportionality is the corresponding Higgs coupling. Thus in this case, one can only take the limit of large mass by taking the corresponding Higgs coupling to be large. As a result, the corresponding contribution of such particles in loop diagrams do *not* decouple. For example, the loop contributions of weak gauge bosons (W and Z) and chiral fermions such as the top quark to $h \rightarrow gg$ and $h \rightarrow \gamma\gamma$ are examples where the corresponding one-loop contributions to the decay amplitudes approach a constant in the large mass limit. Non-decoupling effects can also appear in radiative corrections to various observables. As a dramatic example, the one loop correction to the triple Higgs boson coupling hhh is large because

it receives a non-decoupling effect proportional to the quartic power of the top quark mass after renormalization [42, 43],

$$\lambda_{hhh}^{\text{ren}} \simeq \frac{3m_h^2}{\sqrt{2}v} \left(1 - \frac{N_c m_t^4}{16\pi^2} \right). \quad (1.25)$$

These one-loop effects can also appear in the loop contributions of new particles in models beyond the Standard Model. Note that the bosonic loop contributions give positive corrections and fermionic loop diagrams give negative contributions to the hhh coupling. The loop induced couplings hgg , $h\gamma\gamma$, $hZ\gamma$ and the hhh are therefore sensitive to new particles especially when masses of new particles come mainly from the vacuum expectation values. Notice that these loop effect deviates coupling constant even when there is no mixing between the SM-like Higgs h and new particles.

The non-decoupling contribution of new particles can affect the effective potential at finite temperatures. If it is the bosonic loop effect, it can make the electroweak phase transition to be strongly first order as required for a successful scenario of electroweak baryogenesis [44, 45]. Such a non-decoupling effect results in a large deviation in the hhh coupling, so that one can test the scenario by measuring the hhh coupling accurately. In Ref. [46], the correlation between the condition of first order phase transition and the deviation in the hhh coupling is studied, and to test the scenario of electroweak baryogenesis via the determination of the hhh coupling, one needs to measure it by the 10-20 % accuracy. Such a precision measurement of the hhh coupling can only be attained at the ILC.

1.2.3 Higgs decays

The Higgs boson couples to all the particles of the SM. Therefore, there are many decay modes. In particular, with the mass of about 126 GeV the Higgs boson decays into $b\bar{b}$, WW^* , $\tau^+\tau^-$, gg , $c\bar{c}$, ZZ^* , $\gamma\gamma$ and γZ , $\mu\mu$, where $\gamma\gamma$ and γZ are one-loop induced decay processes.

In Fig. 1.2, branching ratios for various decay modes are shown as a function of the mass of the Higgs boson. The decay branching ratios strongly depend on the mass of the Higgs boson m_h . In Tables 1.1 and 1.2, the predicted values of decay branching ratios of the Standard Model Higgs boson are listed for $m_h = 125.0, 125.3, 125.6, 125.9, 126.2$ and 126.5 GeV [47]. In Table 1.2 the predicted values of the total decay width of the Higgs boson are also listed. It is quite interesting that with a Higgs mass of 126 GeV, a large number of decay modes have similar sizes and are accessible to experiments. Indeed, the universal relation between the mass and the coupling to the Higgs boson for

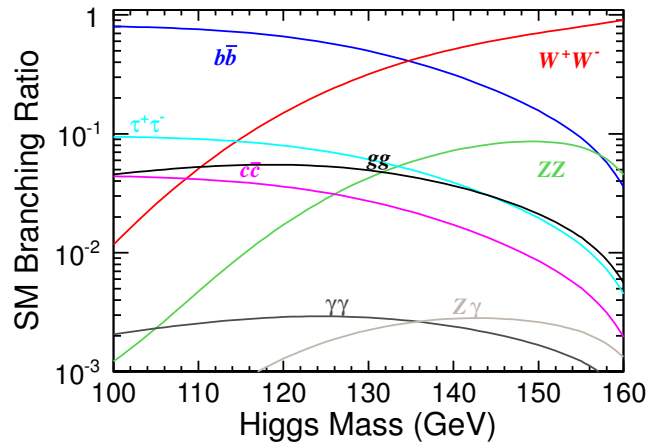


Figure 1.2. Branching ratio of the Higgs boson in the SM as a function of the mass.

Table 1.1. The Standard Model values of branching ratios of fermionic decays of the Higgs boson for each value of the Higgs boson mass m_h .

m_h (GeV)	$b\bar{b}$	$\tau^+\tau^-$	$\mu^+\mu^-$	$c\bar{c}$	$s\bar{s}$
125.0	57.7 %	6.32 %	0.0219 %	2.91 %	0.0246 %
125.3	57.2 %	6.27 %	0.0218 %	2.89 %	0.0244 %
125.6	56.7 %	6.22 %	0.0216 %	2.86 %	0.0242 %
125.9	56.3 %	6.17 %	0.0214 %	2.84 %	0.0240 %
126.2	55.8 %	6.12 %	0.0212 %	2.81 %	0.0238 %
126.5	55.3 %	6.07 %	0.0211 %	2.79 %	0.0236 %

Table 1.2. The Standard Model values of branching ratios of bosonic decays of the Higgs boson for each value of the Higgs boson mass m_h . The predicted value of the total decay width of the Higgs boson is also listed for each value of m_h .

m_h (GeV)	gg	$\gamma\gamma$	$Z\gamma$	W^+W^-	ZZ	Γ_H (MeV)
125.0	8.57 %	0.228 %	0.154 %	21.5 %	2.64 %	4.07
125.3	8.54 %	0.228 %	0.156 %	21.9 %	2.72 %	4.11
125.6	8.52 %	0.228 %	0.158 %	22.4 %	2.79 %	4.15
125.9	8.49 %	0.228 %	0.162 %	22.9 %	2.87 %	4.20
126.2	8.46 %	0.228 %	0.164 %	23.5 %	2.94 %	4.24
126.5	8.42 %	0.228 %	0.167 %	24.0 %	3.02 %	4.29

each particle shown in Fig. 1.1 can be well tested by measuring these branching ratios as well as the total decay width accurately at the ILC. For example, the top Yukawa coupling and the triple Higgs boson coupling are determined respectively by measuring the production cross sections of top pair associated Higgs boson production and double Higgs boson production mechanisms.

1.2.4 Higgs production at the ILC

At the ILC, the SM Higgs boson h is produced mainly via production mechanisms such as the Higgsstrahlung process $e^+e^- \rightarrow Z^* \rightarrow Zh$ (Fig. 1.3 Left) and the the weak boson fusion processes $e^+e^- \rightarrow W^{+*}W^{-*}\nu\bar{\nu} \rightarrow h\nu\bar{\nu}$ (Fig. 1.3 (Middle)) and $e^+e^- \rightarrow Z^*Z^*e^+e^- \rightarrow he^+e^-$. The Higgsstrahlung process is an s -channel process so that it is maximal just above the threshold of the process, whereas vector boson fusion is a t -channel process which yields a cross section that grows logarithmically with the center-of-mass energy. The Higgs boson is also produced in association with a fermion pair. The most important process of this type is Higgs production in association with a top quark pair, whose typical diagram is shown in Fig. 1.3 (Right). The corresponding production cross sections at the ILC are shown in Figs. 1.4 (Left) and (Right) as a function of the collision energy by assuming the initial electron (positron) beam polarization to be -0.8 ($+0.2$).

The ILC operation will start with the e^+e^- collision energy of 250 GeV (just above threshold for hZ production), where the Higgsstrahlung process is dominant and the contributions of the fusion processes are small, as shown in Fig. 1.4 (Left). As the center-of-mass energy, \sqrt{s} increases, the Higgsstrahlung cross-section falls off as $1/s$. Consequently, the W -boson fusion mechanism is more significant at higher energies, and its production cross section grows logarithmically and becomes larger than that of the Higgsstrahlung cross section for $\sqrt{s} > 450$ GeV. At $\sqrt{s} = 500$ GeV, both the Higgsstrahlung process and the W -boson fusion process are important, and at $\sqrt{s} = 1$ TeV the W -boson fusion is dominant. The cross section of $e^+e^- \rightarrow t\bar{t}h$ is shown in Fig. 1.4 (Right). The threshold of the production process is roughly 480 GeV, so that the $t\bar{t}h$ cross section can be measured at the ILC with the energy of 1 TeV.

Finally, the triple Higgs boson coupling can be determined from measuring the double Higgs production mechanisms $e^+e^- \rightarrow Zh\bar{h}$ and $e^+e^- \rightarrow \nu\bar{\nu}h\bar{h}$ by extracting the contribution of the Feynman diagram shown in Fig. 1.5. The production cross section for the $Zh\bar{h}$ process is typically of the order of 0.1 fb at the collision energy just above the threshold at about 400 GeV as shown in Fig. 1.4(Right). At the ILC with a center-of-mass energy of 500 GeV, the triple Higgs boson coupling can be measured via this process. On the other hand, at higher energies the cross section of the

x

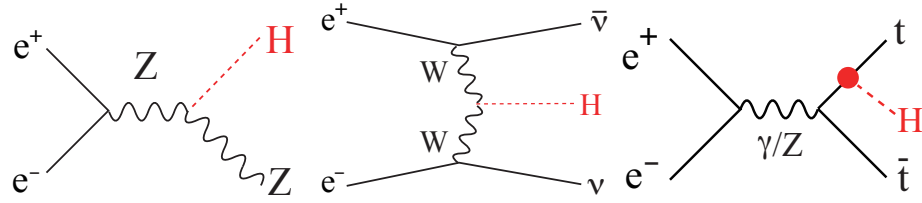


Figure 1.3. Two important Higgs boson production processes at the ILC. The Higgsstrahlung process (Left), the W-boson fusion process (Middle) and the top-quark association (Right).

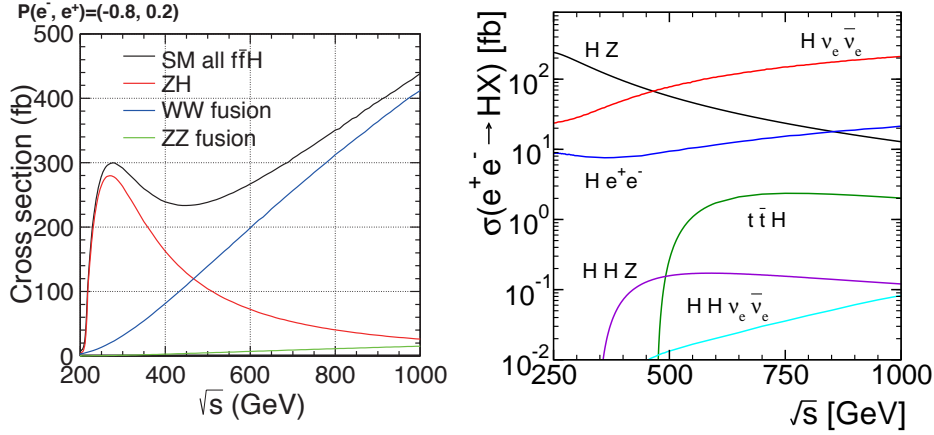


Figure 1.4. (Left) The production cross sections of the Higgs boson with the mass of 125 GeV at the ILC as a function of the collision energy \sqrt{s} . Polarization of the electron beam (80%) and the positron beam (20%) is assumed. (Right) The cross sections of the production processes $e^+e^- \rightarrow hZ$, $e^+e^- \rightarrow H\nu_e\bar{\nu}_e$, $e^+e^- \rightarrow He^+e^-$, $e^+e^- \rightarrow t\bar{t}H$, $e^+e^- \rightarrow HHZ$ and $e^+e^- \rightarrow HH\nu_e\bar{\nu}_e$ as a function of the collision energy for the mass of 125 GeV. No polarization is assumed for the initial electron and positron beams.

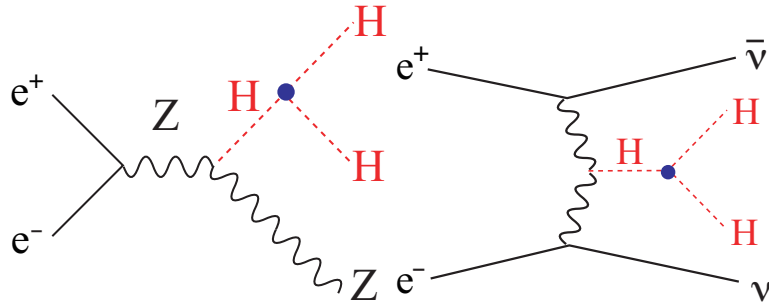


Figure 1.5. Typical diagrams for double Higgs boson production via off-shell Higgsstrahlung (Left) and W-boson fusion (Right) processes.

fusion process $e^+e^- \rightarrow \nu\bar{\nu}hh$ becomes larger. This process becomes relevant for the measurement of the triple Higgs boson coupling at the energies around 1 TeV.

1.2.5 Vacuum Stability

The mass of the Higgs boson is proportional to the strength of the Higgs self-coupling λ via $m_h^2 = 2\lambda v^2$. The magnitude of λ at high energies can be predicted from the size of λ at the electroweak scale by using the renormalization group equation (RGE). The RGE for the coupling constant λ is given by [48]

$$16\pi^2 \mu \frac{d}{d\mu} \lambda = 12(\lambda^2 + \lambda y_t^2 - y_t^4) - 3\lambda(3g^2 + g'^2) + \frac{3}{4}[2g^4 + (g^2 + g'^2)^2] + \dots, \quad (1.26)$$

where the \dots indicates terms proportional to the Yukawa couplings of the five light quarks and the charged leptons, which can be neglected in first approximation. If the mass is large, λ is large and the β -function is positive. Then, λ is larger for higher energies and blows up at some high energy point (the Landau pole), which can be below the Planck scale. In contrast, when the mass is small and the β -function is negative due to the term proportional to the fourth power of the top-quark Yukawa coupling. In this case, the coupling λ decreases as the energy scale increases and finally becomes negative. If λ is driven negative below the Planck scale (at which point quantum gravitational effects would have to be taken into account), then we could conclude that electroweak vacuum is not the global minimum, since either a deeper scalar potential minimum exists or the scalar potential is unbounded from below. In either case, the electroweak minimum would no longer be stable. By assuming that the electroweak minimum is stable up to a given high energy scale Λ , below which the coupling λ does not blow up nor is driven negative, one can derive upper and the lower Higgs mass bounds as a function of Λ .

Given that the mass of the Higgs boson is now known to be around 126 GeV, which corresponds to $\lambda \sim 0.26$ at the electroweak scale, it follows that the β -function is negative. The recent RGE analysis in the NNLO approximation [49] shows that the scale Λ where λ becomes negative is between 10^7 GeV to 10^{15} GeV at the 3σ level. The main uncertainty comes from the top quark mass, α_s , and the theoretical uncertainties in QCD corrections. When the mass of the top quark is measured with the accuracy of about 30 MeV at the ILC, the cut-off scale of the SM can be much better determined, as exhibited by Fig. 1.6.

With a Standard Model Higgs mass of 126 GeV, the central value of λ is negative at the Planck scale. Therefore, the electroweak vacuum is not stable in the Standard Model unless new physics enters below the Planck scale. However, if we only require that the electroweak vacuum is metastable,

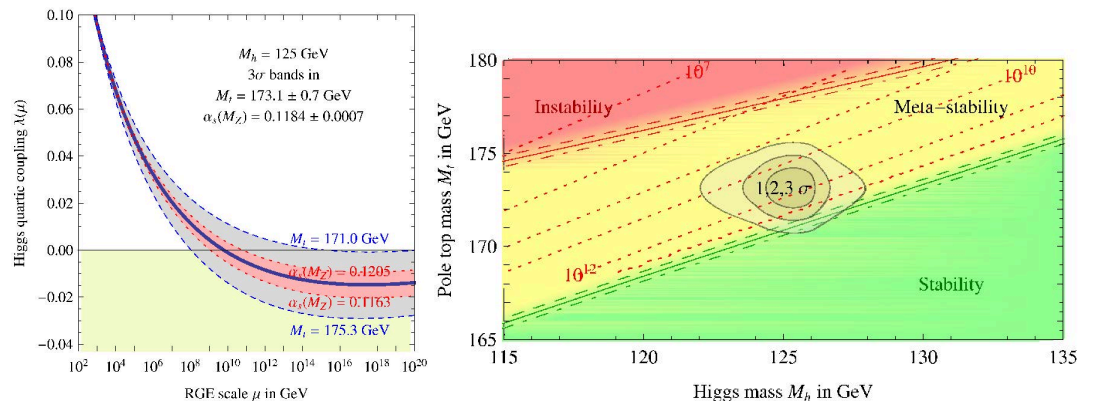


Figure 1.6. *Left:* RG evolution of λ varying M_t and α_s by $\pm 3\sigma$. *Right:* Regions of absolute stability, metastability and instability of the SM vacuum in the M_t - M_h plane in the region of the preferred experimental range of M_h and M_t (the gray areas denote the allowed region at 1, 2, and 3σ). The three boundaries lines correspond to $\alpha_s(M_Z) = 0.1184 \pm 0.0007$, and the grading of the colors indicates the size of the theoretical error. The dotted contour-lines show the instability scale Λ in GeV assuming $\alpha_s(M_Z) = 0.1184$.

with a lifetime considerably longer than the age of the Universe, then Fig. 1.6 indicates that the Standard Model can be valid with no new physics required all the way up to the Planck scale.

Finally, note that the bound from vacuum stability is largely relaxed when extended Higgs sectors are considered where the lightest scalar behaves like the SM Higgs boson [50, 51]. For example, if we consider the scalar sector with two Higgs doublets, the cut off scale where the vacuum stability is violated can be easily above the Planck scale. Due to the loop contribution of extra scalar fields, the beta-function of the quartic coupling constant of the SM-like Higgs boson is in general larger than that in the SM. Therefore, the cutoff scale is higher than that of the SM.

1.3 The two-Higgs-doublet model (2HDM)

Given that there are multiple generations of quarks and leptons, it is reasonable to consider the possibility that the Higgs sector of electroweak theory is also non-minimal. The introduction of the two-Higgs doublet extension of the Standard Model (2HDM) [52] was motivated for various reasons over the years. It was initially introduced to provide a possible new source of CP violation mediated by neutral scalars [53]. Subsequently, the 2HDM was studied for phenomenological reasons, as it provides for new scalar degrees of freedom including a charged Higgs pair, a neutral CP-odd Higgs scalar in the case of a CP-conserving scalar potential and neutral scalars of indefinite CP in the case of a CP-violating scalar potential and/or vacuum [31]. These features yield new phenomenological signals for the production and decay of fundamental spin-0 particles.

Today, the main motivation for the 2HDM is connected with models of TeV-scale supersymmetry. Such models provide the only natural framework for weakly-coupled fundamental scalar particles (for further details, see Section 1.6). In particular, the minimal supersymmetric extension of the Standard Model (MSSM) requires a Higgs sector with at least two Higgs doublet fields. The MSSM Higgs sector is a 2HDM that is highly constrained by supersymmetry. The structure of the MSSM Higgs sector will be explored further in Section 1.3.10.

The most general version of the 2HDM, which contains all possible renormalizable terms (mass terms and interactions) allowed by the electroweak gauge invariance, is not phenomenologically viable due to the presence of Higgs–quark Yukawa interaction terms that lead to tree-level Higgs-mediated flavor changing neutral currents (FCNCs) [54, 55]. Such effects are absent in the MSSM Higgs sector due to the constraints imposed by supersymmetry on the Yukawa interactions. In non-supersymmetric versions of the 2HDM, one can also naturally avoid FCNCs by imposing certain simple discrete symmetries on the the scalar and fermion fields, as discussed in Section 1.3.7. These symmetries reduce the parameter freedom of the 2HDM and automatically eliminate the dangerous FCNC interactions. Nevertheless, it is instructive to examine the structure of the most general 2HDM, as constrained versions of the 2HDM can then be examined as limiting cases of the most general 2HDM.

1.3.1 Model-independent treatment

The scalar fields of the 2HDM are complex SU(2) doublet, hypercharge-one fields, Φ_1 and Φ_2 , where the corresponding vevs are $\langle \Phi_i \rangle = v_i$, and $v^2 \equiv |v_1|^2 + |v_2|^2 = (174 \text{ GeV})^2$ is fixed by the observed W mass, $m_W = gv/\sqrt{2}$. The most general renormalizable SU(2)×U(1) scalar potential is given by

$$\mathcal{V} = m_{11}^2 \Phi_1^\dagger \Phi_1 + m_{22}^2 \Phi_2^\dagger \Phi_2 + [m_{12}^2 \Phi_1^\dagger \Phi_2 + \text{h.c.}] + \frac{1}{2} \lambda_1 (\Phi_1^\dagger \Phi_1)^2 + \frac{1}{2} \lambda_2 (\Phi_2^\dagger \Phi_2)^2 + \lambda_3 (\Phi_1^\dagger \Phi_1) (\Phi_2^\dagger \Phi_2) + \lambda_4 (\Phi_1^\dagger \Phi_2) (\Phi_2^\dagger \Phi_1) + \left\{ \frac{1}{2} \lambda_5 (\Phi_1^\dagger \Phi_2)^2 + [\lambda_6 (\Phi_1^\dagger \Phi_1) + \lambda_7 (\Phi_2^\dagger \Phi_2)] \Phi_1^\dagger \Phi_2 + \text{h.c.} \right\}. \quad (1.27)$$

In the most general 2HDM, the fields Φ_1 and Φ_2 are indistinguishable. Thus, it is always possible to define two orthonormal linear combinations of the two doublet fields without modifying any prediction of the model. Performing such a redefinition of fields leads to a new scalar potential

with the same form as eq. (1.27) but with modified coefficients. This implies that the coefficients that parameterize the scalar potential in eq. (1.27) are not directly physical [56].

To obtain a scalar potential that is more closely related to physical observables, one can introduce the so-called *Higgs basis* in which the redefined doublet fields (denoted below by H_1 and H_2 have the property that H_1 has a non-zero vev whereas H_2 has a zero vev [57]. In particular, we define new Higgs doublet fields:

$$H_1 = \begin{pmatrix} H_1^+ \\ H_1^0 \end{pmatrix} \equiv \frac{v_1^* \Phi_1 + v_2^* \Phi_2}{v}, \quad H_2 = \begin{pmatrix} H_2^+ \\ H_2^0 \end{pmatrix} \equiv \frac{-v_2 \Phi_1 + v_1 \Phi_2}{v}. \quad (1.28)$$

It follows that $\langle H_1^0 \rangle = v$ and $\langle H_2^0 \rangle = 0$. The Higgs basis is uniquely defined up to an overall rephasing, $H_2 \rightarrow e^{i\chi} H_2$ (which does not alter the fact that $\langle H_2^0 \rangle = 0$). In the Higgs basis, the scalar potential is given by [56, 57]:

$$\mathcal{V} = Y_1 H_1^\dagger H_1 + Y_2 H_2^\dagger H_2 + [Y_3 H_1^\dagger H_2 + \text{h.c.}] + \frac{1}{2} Z_1 (H_1^\dagger H_1)^2 + \frac{1}{2} Z_2 (H_2^\dagger H_2)^2 + Z_3 (H_1^\dagger H_1) (H_2^\dagger H_2) + Z_4 (H_1^\dagger H_2) (H_2^\dagger H_1) + \left\{ \frac{1}{2} Z_5 (H_1^\dagger H_2)^2 + [Z_6 (H_1^\dagger H_1) + Z_7 (H_2^\dagger H_2)] H_1^\dagger H_2 + \text{h.c.} \right\}, \quad (1.29)$$

where Y_1, Y_2 and Z_1, \dots, Z_4 are real and uniquely defined, whereas Y_3, Z_5, Z_6 and Z_7 are complex and transform under the rephasing of H_2 ,

$$[Y_3, Z_6, Z_7] \rightarrow e^{-i\chi} [Y_3, Z_6, Z_7] \quad \text{and} \quad Z_5 \rightarrow e^{-2i\chi} Z_5. \quad (1.30)$$

After minimizing the scalar potential, $Y_1 = -Z_1 v^2$ and $Y_3 = -Z_6 v^2$. This leaves 11 free parameters: 1 vev, 8 real parameters, $Y_2, Z_{1,2,3,4}, |Z_{5,6,7}|$, and two relative phases.

If Φ_1 and Φ_2 are indistinguishable fields, then observables can only depend on combinations of Higgs basis parameters that are independent of χ . Symmetries, such as discrete symmetries or supersymmetry, can distinguish between Φ_1 and Φ_2 , which then singles out a specific physical basis for the Higgs fields, and can yield additional observables such as $\tan \beta \equiv |v_2|/|v_1|$ in the MSSM.

In the general 2HDM, the physical charged Higgs boson is the charged component of the Higgs-basis doublet H_2 , and its mass is given by

$$m_{H^\pm}^2 = Y_2 + Z_3 v^2. \quad (1.31)$$

The three physical neutral Higgs boson mass-eigenstates are determined by diagonalizing a 3×3 real symmetric squared-mass matrix that is defined in the Higgs basis [57, 58]

$$\mathcal{M}^2 = 2v^2 \begin{pmatrix} Z_1 & \text{Re}(Z_6) & -\text{Im}(Z_6) \\ \text{Re}(Z_6) & \frac{1}{2}(Z_{345} + Y_2/v^2) & -\frac{1}{2}\text{Im}(Z_5) \\ -\text{Im}(Z_6) & -\frac{1}{2}\text{Im}(Z_5) & \frac{1}{2}(Z_{345} + Y_2/v^2) - \text{Re}(Z_5) \end{pmatrix}, \quad (1.32)$$

where $Z_{345} \equiv Z_3 + Z_4 + \text{Re}(Z_5)$. The diagonalizing matrix is a 3×3 real orthogonal matrix that depends on three angles: θ_{12}, θ_{13} and θ_{23} . Under the rephasing $H_2 \rightarrow e^{i\chi} H_2$ [58],

$$\theta_{12}, \theta_{13} \text{ are invariant, and } \theta_{23} \rightarrow \theta_{23} - \chi. \quad (1.33)$$

By convention, we choose

$$-\frac{1}{2}\pi \leq \theta_{12}, \theta_{13} < \frac{1}{2}\pi. \quad (1.34)$$

It is convenient to define invariant combinations of θ_{12} and θ_{13} , denoted by q_{k1} and q_{k2} in Table 1.3 below, where $k = 1, 2, 3$ corresponds to the associated neutral Higgs mass eigenstate h_k [58].

Table 1.3. Invariant combinations of neutral Higgs mixing angles θ_{12} and θ_{13} , where $c_{ij} \equiv \cos \theta_{ij}$ and $s_{ij} \equiv \sin \theta_{ij}$.

k	q_{k1}	q_{k2}
1	$c_{12}c_{13}$	$-s_{12} - ic_{12}s_{13}$
2	$s_{12}c_{13}$	$c_{12} - is_{12}s_{13}$
3	s_{13}	ic_{13}

The physical neutral Higgs states ($h_{1,2,3}$) are then given by:

$$h_k = \frac{1}{\sqrt{2}} \left\{ q_{k1}^* (H_1^0 - v) + q_{k2}^* H_2^0 e^{i\theta_{23}} + \text{h.c.} \right\}. \quad (1.35)$$

It is convenient to choose the mass ordering of the states such that $m_1 < m_{2,3}$. The mass ordering fixes the neutral Higgs mixing angles θ_{12} and θ_{13} . Although the explicit formulae for the Higgs masses and mixing angles are quite complicated, there are numerous relations among them which take on rather simple forms. The following results are noteworthy [58, 59]:

$$2Z_1 v^2 = m_1^2 c_{12}^2 c_{13}^2 + m_2^2 s_{12}^2 c_{13}^2 + m_3^2 s_{13}^2, \quad (1.36)$$

$$2\text{Re}(Z_6 e^{-i\theta_{23}}) v^2 = c_{13} s_{12} c_{12} (m_2^2 - m_1^2), \quad (1.37)$$

$$2\text{Im}(Z_6 e^{-i\theta_{23}}) v^2 = s_{13} c_{13} (c_{12}^2 m_1^2 + s_{12}^2 m_2^2 - m_3^2), \quad (1.38)$$

$$2\text{Re}(Z_5 e^{-2i\theta_{23}}) v^2 = m_1^2 (s_{12}^2 - c_{12}^2 s_{13}^2) + m_2^2 (c_{12}^2 - s_{12}^2 s_{13}^2) - m_3^2 c_{13}^2, \quad (1.39)$$

$$\text{Im}(Z_5 e^{-2i\theta_{23}}) v^2 = s_{12} c_{12} s_{13} (m_2^2 - m_1^2). \quad (1.40)$$

If we also define the physical charged Higgs state by $H^\pm = e^{\pm i\theta_{23}} H_2^\pm$, then all the Higgs mass eigenstate fields (h_1 , h_2 , h_3 and H^\pm) are invariant under the rephasing $H_2 \rightarrow e^{i\chi} H_2$. Thus, we have established a second well-defined basis of the general 2HDM, which corresponds to the mass-eigenstate basis for the neutral Higgs bosons.

1.3.2 Constraints on 2HDM scalar potential parameters

The assumption of tree-level unitarity in the scattering of longitudinal gauge bosons yields via the equivalence theorem upper bounds on the quartic couplings of the scalar potential. The bounds are rather simple when expressed in the Higgs basis. For example, the following bounds obtained in Ref. [59] are based on single channel scattering processes,

$$\begin{aligned} |Z_1| < 4\pi, \quad |Z_3| < 8\pi, \quad |Z_3 + Z_4| < 8\pi, \quad |\text{Re}(Z_5 e^{-2i\theta_{23}})| < 2\pi, \\ |\text{Im}(Z_5 e^{-2i\theta_{23}})| < 8\pi, \quad |\text{Re}(Z_6 e^{-i\theta_{23}})| < 2\pi, \quad |\text{Im}(Z_6 e^{-i\theta_{23}})| < \frac{8}{3}\pi. \end{aligned} \quad (1.41)$$

There are no unitarity restrictions at tree-level on Z_2 and Z_7 as these quantities are absent from the neutral scalar mass matrix. One can obtain somewhat improved tree-level bounds by considering multi-channel scattering processes and analyzing the eigenvalues of the corresponding amplitude matrices. If the $|Z_i|$ are too large, then the scalar sector becomes strongly coupled, and the tree-level unitarity bounds become suspect. Nevertheless, it is common practice to consider weakly-coupled scalar sectors, in which case one should not allow any of the $|Z_i|$ to become too large. For practical purposes, we shall assume that $|Z_i| \lesssim 2\pi$, in order to maintain unitarity and perturbativity of tree-level amplitudes.

Additional constraints on the 2HDM scalar potential parameters arise from the analysis of precision electroweak observables, which are sensitive to Higgs bosons via loop corrections to Standard

Model processes. The S , T , and U parameters, introduced by Peskin and Takeuchi [60], are independent ultraviolet-finite combinations of radiative corrections to gauge boson two-point functions (the so-called “oblique” corrections). The parameter T is related to the well known ρ -parameter of electroweak physics [61] by $\rho - 1 = \alpha T$. The oblique parameters can be expressed in terms of the transverse part of the gauge boson two-point functions. For example,

$$\alpha T \equiv \frac{\Pi_{WW}^{\text{new}}(0)}{m_W^2} - \frac{\Pi_{ZZ}^{\text{new}}(0)}{m_Z^2}, \quad (1.42)$$

where $\alpha \equiv e^2/(4\pi)$ is the electromagnetic coupling defined in the $\overline{\text{MS}}$ scheme evaluated at m_Z . The $\Pi_{V_a V_b}^{\text{new}}$ are the new physics contributions to the one-loop $V_a - V_b$ vacuum polarization functions (where $V = W$ or Z). New physics contributions are defined as those that enter relative to the Standard Model with the Higgs mass fixed to its observed value. The definition of the two other oblique parameters S and U can be found in Ref. [29].

Explicit expressions for S , T and U in the general 2HDM have been written down and the numerical contributions of the 2HDM states (relative to that of the SM) to the oblique parameters in the 2HDM have been studied in Refs. [59, 62, 63, 64]. The general conclusion is that corrections to S and U due to the contribution of the Higgs sector are small, consistent with the present experimental limits. However, the contributions to T may or may not be significant depending on the amount of custodial symmetry breaking introduced by the 2HDM scalar potential. Indeed, in Ref. [59] it is shown that a custodial symmetric scalar potential is one in which CP is conserved and in addition, the following condition is satisfied,

$$Z_4 = \begin{cases} \varepsilon_{56}|Z_5|, & \text{for } Z_6 \neq 0, \\ \varepsilon_{57}|Z_5|, & \text{for } Z_7 \neq 0, \\ \pm|Z_5|, & \text{for } Z_6 = Z_7 = 0, \end{cases} \quad (1.43)$$

where the two sign factors, ε_{56} and ε_{57} are defined by:

$$\varepsilon_{56} = Z_5^* Z_6^2 = \varepsilon_{56} |Z_5| |Z_6|^2, \quad \varepsilon_{57} = Z_5^* Z_7^2 = \varepsilon_{57} |Z_5| |Z_7|^2. \quad (1.44)$$

Note that since the scalar potential is assumed to be CP conserving (otherwise the custodial symmetry is violated), it follows that $\text{Im}(Z_5^* Z_6^2) = \text{Im}(Z_5^* Z_7^2) = 0$. Hence ε_{56} and ε_{57} are real numbers of unit modulus.

A numerical study shows that the 2HDM contribution to T is within the experimentally measured bounds as long as there is not a significant mass splitting between the charged Higgs boson and the heavy neutral Higgs bosons. Such mass splittings would require rather large values of some of the scalar quartic couplings (which would be approaching their unitarity limits).

1.3.3 Tree-level Higgs boson couplings—the general case

The interactions of the Higgs bosons with the gauge bosons and the Higgs self-interactions, when computed in the Higgs basis, can be expressed in terms of the parameters Z_i , θ_{12} , θ_{13} and θ_{23} [58]. In fact, the only combinations that appear will be invariant with respect to the rephasing $H_2 \rightarrow e^{i\chi} H_2$ (since observables cannot depend on the arbitrary angle χ). Indeed, the interaction terms will depend on the invariant quantities q_{k1} and q_{k2} defined in Table 1.3 and on invariant combinations of the Z_i and $e^{-i\theta_{23}}$.

The interactions of the Higgs bosons and vector bosons of the Standard Model are given by:

$$\mathcal{L}_{VVH} = \left(gm_W W_\mu^+ W^{\mu-} + \frac{g}{2c_W} m_Z Z_\mu Z^\mu \right) q_{k1} h_k, \quad (1.45)$$

$$\begin{aligned} \mathcal{L}_{VVHH} = & \left[\frac{1}{4} g^2 W_\mu^+ W^{\mu-} + \frac{g^2}{8c_W^2} Z_\mu Z^\mu \right] h_k h_k \\ & + \left[\frac{1}{2} g^2 W_\mu^+ W^{\mu-} + e^2 A_\mu A^\mu + \frac{g^2}{c_W^2} \left(\frac{1}{2} - s_W^2 \right)^2 Z_\mu Z^\mu + \frac{2ge}{c_W} \left(\frac{1}{2} - s_W^2 \right) A_\mu Z^\mu \right] H^+ H^- \\ & + \left\{ \left(\frac{1}{2} eg A^\mu W_\mu^+ - \frac{g^2 s_W^2}{2c_W} Z^\mu W_\mu^+ \right) q_{k2} H^- h_k + \text{h.c.} \right\}, \end{aligned} \quad (1.46)$$

$$\begin{aligned} \mathcal{L}_{VHH} = & \frac{g}{4c_W} \epsilon_{jkl} q_{\ell 1} Z^\mu h_j \overleftrightarrow{\partial}_\mu h_k - \frac{1}{2} g \left[iq_{k2} W_\mu^+ H^- \overleftrightarrow{\partial}^\mu h_k + \text{h.c.} \right] \\ & + \left[ie A^\mu + \frac{ig}{c_W} \left(\frac{1}{2} - s_W^2 \right) Z^\mu \right] H^+ \overleftrightarrow{\partial}_\mu H^-, \end{aligned} \quad (1.47)$$

where $s_W \equiv \sin \theta_W$, $c_W \equiv \cos \theta_W$, and the sum over pairs of repeated indices $j, k = 1, 2, 3$ is implied.

The trilinear Higgs self-interactions are given by

$$\begin{aligned} \mathcal{L}_{3h} = & -\frac{v}{\sqrt{2}} h_j h_k h_\ell \left[q_{j1} q_{k1} q_{\ell 1} Z_1 + q_{j2} q_{k2}^* q_{\ell 1} (Z_3 + Z_4) + q_{j1} \text{Re}(q_{k2} q_{\ell 2} Z_5 e^{-2i\theta_{23}}) \right. \\ & \left. + 3q_{j1} q_{k1} \text{Re}(q_{\ell 2} Z_6 e^{-i\theta_{23}}) + \text{Re}(q_{j2}^* q_{k2} q_{\ell 2} Z_7 e^{-i\theta_{23}}) \right] \\ & + \sqrt{2} v h_k H^+ H^- \left[q_{k1} Z_3 + \text{Re}(q_{k2} e^{-i\theta_{23}} Z_7) \right], \end{aligned} \quad (1.48)$$

where there is an implicit sum over repeated indices. Note that the complex $Z_{5,6,7}$ are always paired with the correct power of $e^{-i\theta_{23}}$ such that the corresponding product is invariant under the rephasing of H_2 . Finally, for completeness, the quadrilinear Higgs self-interactions are exhibited,

$$\begin{aligned} \mathcal{L}_{4h} = & -\frac{1}{8} h_j h_k h_l h_m \left[q_{j1} q_{k1} q_{\ell 1} q_{m1} Z_1 + q_{j2} q_{k2} q_{\ell 2}^* q_{m2}^* Z_2 + 2q_{j1} q_{k1} q_{\ell 2} q_{m2}^* (Z_3 + Z_4) \right. \\ & \left. + 2q_{j1} q_{k1} \text{Re}(q_{\ell 2} q_{m2} Z_5 e^{-2i\theta_{23}}) + 4q_{j1} q_{k1} q_{\ell 1} \text{Re}(q_{m2} Z_6 e^{-i\theta_{23}}) + 4q_{j1} \text{Re}(q_{k2} q_{\ell 2} q_{m2}^* Z_7 e^{-i\theta_{23}}) \right] \\ & - \frac{1}{2} h_j h_k H^+ H^- \left[q_{j2} q_{k2}^* Z_2 + q_{j1} q_{k1} Z_3 + 2q_{j1} \text{Re}(q_{k2} Z_7 e^{-i\theta_{23}}) \right] - \frac{1}{2} Z_2 H^+ H^- H^+ H^-. \end{aligned} \quad (1.49)$$

It is remarkable how compact the expressions are for the Higgs boson interactions when written explicitly in terms of invariant quantities that can be directly related to observables.

We next turn to the Higgs-fermion Yukawa couplings. For simplicity, we focus on the interaction of the Higgs bosons with three generations of quarks. The corresponding interactions with leptons are easily obtained from the latter by the appropriate substitutions. One starts out initially with a Lagrangian expressed in terms of the scalar doublet fields Φ_i ($i = 1, 2$) and interaction-eigenstate quark fields. After electroweak symmetry breaking, one can transform the scalar doublets into the

Higgs basis fields H_1 and H_2 . At the same time, one can identify the 3×3 quark mass matrices. By redefining the left and right-handed quark fields appropriately, the quark mass matrices are transformed into diagonal form, where the diagonal elements are real and non-negative. The resulting Higgs–quark Yukawa couplings are given by [59]

$$-\mathcal{L}_Y = \bar{U}_L(\kappa^U H_1^{0\dagger} + \rho^U H_2^{0\dagger})U_R - \bar{D}_L K^\dagger(\kappa^U H_1^- + \rho^U H_2^-)U_R \\ + \bar{U}_L K(\kappa^D H_1^+ + \rho^D H_2^+)D_R + \bar{D}_L(\kappa^D H_1^0 + \rho^D H_2^0)D_R + \text{h.c.}, \quad (1.50)$$

where $U = (u, c, t)$ and $D = (d, s, b)$ are the mass-eigenstate quark fields, K is the CKM mixing matrix and κ and ρ are 3×3 Yukawa coupling matrices. Note that $Q_{R,L} \equiv P_{R,L}Q$, where $Q = U$ or D and $P_{R,L} \equiv \frac{1}{2}(1 \pm \gamma_5)$ are the right and left handed projection operators, respectively.

By setting $H_1^0 = v$ and $H_2^0 = 0$, one can relate κ^U and κ^D to the diagonal quark mass matrices M_U and M_D , respectively,

$$M_U = v\kappa^U = \text{diag}(m_u, m_c, m_t), \quad M_D = v\kappa^{D\dagger} = \text{diag}(m_d, m_s, m_b). \quad (1.51)$$

However, the complex matrices ρ^Q ($Q = U, D$) are unconstrained. Moreover,

$$\rho^Q \rightarrow e^{-i\chi} \rho^Q, \quad (1.52)$$

under the rephasing $H_2 \rightarrow e^{i\chi} H_2$.

The Yukawa coupling of the Higgs doublets to the leptons can be similarly treated by replacing $U \rightarrow N$, $D \rightarrow E$, $M_U \rightarrow 0$, $M_D \rightarrow M_E$ and $K \rightarrow \mathbb{1}$, where $N = (\nu_e, \nu_\mu, \nu_\tau)$, $E = (e, \mu, \tau)$ and M_E is the diagonal charged lepton mass matrix.

To obtain the physical Yukawa couplings of the Higgs boson, one must relate the Higgs basis scalar fields to the Higgs mass-eigenstate fields. This yields the physical Higgs–quark Yukawa couplings,

$$-\mathcal{L}_Y = \frac{1}{\sqrt{2}} \bar{D} \sum_{k=1}^3 \left\{ q_{k1} \frac{M_D}{v} + q_{k2} [e^{i\theta_{23}} \rho^D]^\dagger P_R + q_{k2}^* e^{i\theta_{23}} \rho^D P_L \right\} D h_k \\ + \frac{1}{\sqrt{2}} \bar{U} \sum_{k=1}^3 \left\{ q_{k1} \frac{M_U}{v} + q_{k2}^* e^{i\theta_{23}} \rho^U P_R + q_{k2} [e^{i\theta_{23}} \rho^U]^\dagger P_L \right\} U h_k \\ + \left\{ \bar{U} [K [e^{i\theta_{23}} \rho^D]^\dagger P_R - [e^{i\theta_{23}} \rho^U]^\dagger K P_L] D H^+ + \text{h.c.} \right\}. \quad (1.53)$$

The combinations $e^{i\theta_{23}} \rho^U$ and $e^{i\theta_{23}} \rho^D$ that appear in the interactions above are invariant under the rephasing of H_2 .

Note that no $\tan \beta$ parameter appears above! This is because $\tan \beta$ is the absolute value of the ratio of the two neutral Higgs vevs defined with respect to some arbitrary basis of the scalar doublets. But, since the two Higgs doublet fields are identical at this stage, there is no physical principle that singles out a particular basis. Indeed, physical observables cannot depend on the choice of basis. Hence, $\tan \beta$ is an unphysical parameter. In contrast, all parameters that appear in eq. (1.53) are physical and can be directly related to some observable.

It is convenient to rewrite the Higgs–fermion Yukawa couplings in terms of the following two 3×3 hermitian matrices that are invariant with respect to the rephasing of H_2 ,

$$\rho_R^Q \equiv \frac{v}{2} M_Q^{-1/2} \left\{ e^{i\theta_{23}} \rho^Q + [e^{i\theta_{23}} \rho^Q]^\dagger \right\} M_Q^{-1/2}, \quad \text{for } Q = U, D, \\ \rho_I^Q \equiv \frac{v}{2i} M_Q^{-1/2} \left\{ e^{i\theta_{23}} \rho^Q - [e^{i\theta_{23}} \rho^Q]^\dagger \right\} M_Q^{-1/2}, \quad \text{for } Q = U, D. \quad (1.54)$$

Then, the Yukawa couplings take the following form:

$$\begin{aligned}
-\mathcal{L}_Y = & \frac{1}{v\sqrt{2}} \bar{D} \sum_{k=1}^3 M_D^{1/2} \left\{ q_{k1} \mathbf{1} + \text{Re}(q_{k2}) \rho_R^D + \text{Im}(q_{k2}) \rho_I^D + i\gamma_5 (\text{Im}(q_{k2}) \rho_R^D - \text{Re}(q_{k2}) \rho_I^D) \right\} M_D^{1/2} D h_k \\
& + \frac{1}{v\sqrt{2}} \bar{U} \sum_{k=1}^3 M_U^{1/2} \left\{ q_{k1} \mathbf{1} + \text{Re}(q_{k2}) \rho_R^U + \text{Im}(q_{k2}) \rho_I^U + i\gamma_5 (\text{Im}(q_{k2}) \rho_R^U - \text{Re}(q_{k2}) \rho_I^U) \right\} M_U^{1/2} U h_k \\
& + \frac{1}{v} \left\{ \bar{U} [K M_D^{1/2} (\rho_R^D - i\rho_I^D) M_D^{1/2} P_R - M_U^{1/2} (\rho_R^U - i\rho_I^U) M_U^{1/2} K P_L] D H^+ + \text{h.c.} \right\}, \quad (1.55)
\end{aligned}$$

where $\mathbf{1}$ is the 3×3 identity matrix. The appearance of unconstrained complex 3×3 Yukawa matrices $\rho_{R,I}^Q$ in eq. (1.55) indicates the presence of potential flavor-changing neutral Higgs–quark interactions. If the off-diagonal elements of $\rho_{R,I}^Q$ are unsuppressed, they will generate tree-level Higgs-mediated FCNCs that are incompatible with the strong suppression of FCNCs observed in nature.

1.3.4 Tree-level Higgs boson couplings—the CP-conserving case

It is instructive to consider the case of a CP-conserving Higgs scalar potential. If CP is *explicitly* conserved, then there exists a basis for the scalar fields in which all the parameters of the scalar potential are simultaneously real. Such a basis (if it exists) is called a real basis. If in addition the vacuum conserves CP, then a real basis exists in which the vevs are simultaneously real. In this case, a real Higgs basis exists that is unique up to a redefinition of $H_2 \rightarrow -H_2$. Thus, without loss of generality, we can adopt a convention in which the sign of Z_6 or Z_7 is fixed to be either positive or negative.

Having chosen a real Higgs basis, one can diagonalize the neutral Higgs mass matrix given in eq. (1.32). One immediately finds two neutral CP-even scalars, h and H (with $m_h < m_H$) with squared-masses,

$$m_{H,h}^2 = \frac{1}{2} \left\{ Y_2 + (Z_{345} + 2Z_1)v^2 \pm \sqrt{[Y_2 + (Z_{345} - 2Z_1)v^2]^2 + 16Z_6^2 v^4} \right\}, \quad (1.56)$$

where $Z_{345} \equiv Z_3 + Z_4 + Z_5$ (since Z_5 is real by assumption), and a CP-odd scalar A , with squared-mass

$$m_A^2 = Y_2 + (Z_3 + Z_4 - Z_5)v^2. \quad (1.57)$$

Only one neutral Higgs mixing angle θ_{12} is required, since $\theta_{13} = 0$ and $e^{i\theta_{23}} = \text{sgn } Z_6$. It is conventional to rotate from the Higgs basis to an arbitrary basis by an angle β . In this basis, the conventionally defined Higgs mixing angle α is related to θ_{12} by,

$$\alpha = \beta - \theta_{12} - \frac{1}{2}\pi. \quad (1.58)$$

The quantity $\beta - \alpha = \theta_{12} + \frac{1}{2}\pi$ is clearly independent of the choice of basis used to define β . In this notation, we have

$$\cos \theta_{12} = \sin(\beta - \alpha), \quad \sin \theta_{12} = -\cos(\beta - \alpha) \text{sgn } Z_6, \quad (1.59)$$

where $0 \leq \beta - \alpha < \pi$ [in light of eq. (1.34)]. Eqs. (1.36) and (1.37) yield

$$\cos^2(\beta - \alpha) = \frac{2Z_1 v^2 - m_1^2}{m_2^2 - m_1^2}, \quad (1.60)$$

$$\sin(\beta - \alpha) \cos(\beta - \alpha) = -\frac{2Z_6 v^2}{m_2^2 - m_1^2}. \quad (1.61)$$

It is convenient to adopt a convention where $Z_6 > 0$ in which case we can take $\theta_{23} = 0$. In this convention, eq. (1.61) implies that the sign of $\cos(\beta - \alpha)$ is negative (since by assumption, $0 \leq \sin(\beta - \alpha) \leq 1$ and $m_2 > m_1$). The corresponding invariant combinations of neutral Higgs mixing angles given in Table 1.3 simplify as shown in Table 1.4 below.

Table 1.4. Invariant combinations of Higgs mixing angles in the CP-conserving case, where $c_{\beta-\alpha} \equiv \cos(\beta - \alpha)$ and $s_{\beta-\alpha} \equiv \sin(\beta - \alpha)$, in a convention where $Z_6 > 0$. These are obtained from Table 1.3 by setting $\theta_{12} = \beta - \alpha - \frac{1}{2}\pi$ and $\theta_{13} = 0$.

k	q_{k1}	q_{k2}
1	$s_{\beta-\alpha}$	$c_{\beta-\alpha}$
2	$-c_{\beta-\alpha}$	$s_{\beta-\alpha}$
3	0	i

Using the results of Table 1.4 and identifying $h_1 = h$, $h_2 = -H$ and $h_3 = A$ to match the standard conventions of the CP-conserving 2HDM, we can obtain from eqs. (1.45)–(1.49) and eq. (1.55) the complete list of Higgs couplings in the CP-conserving case. The properties of the three-point and four-point Higgs boson-vector boson couplings are conveniently summarized by listing the couplings that are proportional to either $s_{\beta-\alpha}$ or $c_{\beta-\alpha}$, and the couplings that are independent of $\beta - \alpha$ [31]:

$\cos(\beta - \alpha)$	$\sin(\beta - \alpha)$	angle-independent
HW^+W^-	hW^+W^-	—
HZZ	hZZ	—
ZAh	ZAH	ZH^+H^- , γH^+H^-
$W^\pm H^\mp h$	$W^\pm H^\mp H$	$W^\pm H^\mp A$
$ZW^\pm H^\mp h$	$ZW^\pm H^\mp H$	$ZW^\pm H^\mp A$
$\gamma W^\pm H^\mp h$	$\gamma W^\pm H^\mp H$	$\gamma W^\pm H^\mp A$
—	—	$VV\phi\phi$, $VVAA$, VVH^+H^-

(1.62)

where $\phi = h$ or H and $VV = W^+W^-$, ZZ , $Z\gamma$ or $\gamma\gamma$. Note in particular that *all* vertices in the theory that contain at least one vector boson and *exactly one* non-minimal Higgs boson state (H , A or H^\pm) are proportional to $\cos(\beta - \alpha)$. This can be understood as a consequence of unitarity sum rules which must be satisfied by the tree-level amplitudes of the theory [27, 28, 65, 66].

1.3.5 The decoupling/alignment limit of the 2HDM

Many models of extended Higgs sectors possess a decoupling limit, in which there exists one scalar whose properties coincide with those of the Standard Model Higgs boson [67]. The decoupling limit of the 2HDM corresponds to the limiting case in which the Higgs doublet H_2 (in the Higgs basis) receives a very large mass and is therefore decoupled from the theory. This can be achieved by assuming that $Y_2 \gg v^2$ and $|Z_i| \lesssim \mathcal{O}(1)$ for all i [58, 68]. The effective low energy theory consists of a single Higgs doublet field (namely, H_1), corresponding to the Higgs sector of the Standard Model. The alignment limit of the 2HDM corresponds to the limiting case in which the mixing of the two Higgs doublet fields H_1 and H_2 (in the Higgs basis) is suppressed [69]. This can be achieved by assuming that $|Y_3| \ll 1$ [which implies that $|Z_6| \ll 1$ via the scalar potential minimum conditions given below eq. (1.30)]. In both the decoupling and alignment limits, the neutral Higgs mass eigenstate is approximately given by $\sqrt{2} \text{Re}(H_1^0 - v)$, and its couplings approach those of the Standard Model (SM) Higgs boson. In this section, we provide a general analysis of the decoupling/alignment limit of the 2HDM following the work of Ref. [70].

It is convenient to order the neutral scalar masses such that $m_1 \leq m_{2,3}$ and define the invariant

Higgs mixing angles accordingly. If we identify h_1 as the SM-like Higgs boson so that

$$\frac{g_{h_1 VV}}{g_{h_{\text{SM}} VV}} = c_{12}c_{13} \simeq 1, \quad \text{where } V = W \text{ or } Z, \quad (1.63)$$

then it follows that $s_{12}, s_{13} \ll 1$. Thus, in the decoupling/alignment limit, eqs. (1.37) and (1.38) yield [58]:

$$s_{12} \equiv \sin \theta_{12} \simeq \frac{2 \operatorname{Re}(Z_6 e^{-i\theta_{23}}) v^2}{m_2^2 - m_1^2} \ll 1, \quad (1.64)$$

$$s_{13} \equiv \sin \theta_{13} \simeq -\frac{2 \operatorname{Im}(Z_6 e^{-i\theta_{23}}) v^2}{m_3^2 - m_1^2} \ll 1. \quad (1.65)$$

In addition, eq. (1.40) implies that one additional small quantity characterizes the decoupling/alignment limit,

$$\operatorname{Im}(Z_5 e^{-2i\theta_{23}}) \simeq \frac{(m_2^2 - m_1^2) s_{12} s_{13}}{v^2} \simeq -\frac{2 \operatorname{Im}(Z_6^2 e^{-2i\theta_{23}}) v^2}{m_3^2 - m_1^2} \ll 1. \quad (1.66)$$

Note that in the decoupling/alignment limit, eq. (1.39) yields

$$m_2^2 - m_3^2 \simeq 2 \operatorname{Re}(Z_5 e^{-2i\theta_{23}}) v^2. \quad (1.67)$$

In the decoupling limit, $m_1^2 \simeq 2Z_1 v^2 \ll m_2^2, m_3^2, m_{H^\pm}^2$, which guarantees that eqs. (1.64)–(1.66) are satisfied. In addition, $m_2^2 - m_3^2 \simeq m_{H^\pm}^2 - m_3^2 = \mathcal{O}(v^2)$. That is, the mass splittings among the heavy Higgs states are of order v^2/m_3 . In the alignment limit, $|Z_6| \ll 1$ ensures that eqs. (1.64)–(1.66) are satisfied. We again find that $m_1^2 \simeq Z_1 v^2$, but with no requirement that h_2, h_3 and H^\pm must be significantly heavier than h_1 . The couplings of h_1 to the vector bosons and fermions and the Higgs self-couplings in the approach to the decoupling/alignment limit are exhibited in Table 1.5.

Table 1.5. 2HDM couplings of the SM-like Higgs boson $h \equiv h_1$ normalized to those of the SM Higgs boson, in the decoupling/alignment limit. In the Higgs couplings to vector bosons, $VV = W^+W^-$ or ZZ . In the Higgs self-couplings, $Z_{6R} \equiv \operatorname{Re}(Z_6 e^{-i\theta_{23}})$ and $Z_{6I} \equiv \operatorname{Im}(Z_6 e^{-i\theta_{23}})$. For the fermion couplings, D is a column vector of three down-type fermion fields (either down-type quarks or charged leptons) and U is a column vector of three up-type quark fields. The 3×3 hermitian matrices, ρ_R^Q and ρ_I^Q (where $Q = U$ or D) are defined in eq. (1.54). The normalization of the pseudoscalar coupling of the Higgs boson h to fermions is relative to the corresponding scalar coupling to fermions.

Higgs interaction	2HDM coupling	decoupling/alignment limit
hVV	$c_{12}c_{13}$	$1 - \frac{1}{2}s_{12}^2 - \frac{1}{2}s_{13}^2$
hhh	see eq. (1.48)	$1 - 3(s_{12}Z_{6R} - s_{13}Z_{6I})/Z_1$
$hhhh$	see eq. (1.49)	$1 - 4(s_{12}Z_{6R} - s_{13}Z_{6I})/Z_1$
$h\bar{D}D$	$c_{12}c_{13}\mathbb{1} - s_{12}\rho_R^D - c_{12}s_{13}\rho_I^D$	$\mathbb{1} - s_{12}\rho_R^D - s_{13}\rho_I^D$
$ih\bar{D}\gamma_5 D$	$s_{12}\rho_I^D - c_{12}s_{13}\rho_R^D$	$s_{12}\rho_I^D - s_{13}\rho_R^D$
$h\bar{U}U$	$c_{12}c_{13}\mathbb{1} - s_{12}\rho_R^U - c_{12}s_{13}\rho_I^U$	$\mathbb{1} - s_{12}\rho_R^U - s_{13}\rho_I^U$
$ih\bar{U}\gamma_5 U$	$-s_{12}\rho_I^U + c_{12}s_{13}\rho_R^U$	$-s_{12}\rho_I^U + s_{13}\rho_R^U$

If the scalar potential is CP-conserving, then in the conventions established above, $\theta_{13} = \theta_{23} = 0$ and Z_6 is real and positive. In this case eqs. (1.65) and (1.66) are automatically satisfied. The decoupling/alignment limit is then achieved when eq. (1.64) is satisfied. Using eq. (1.61), the decoupling/alignment limit corresponds to [68]:

$$\cos(\beta - \alpha) \simeq -\frac{2Z_6 v^2}{m_H^2 - m_h^2} \ll 1. \quad (1.68)$$

In this limit, the neutral Higgs masses are given by,

$$m_h^2 \simeq 2Z_1 v^2, \quad m_{H,A}^2 \simeq Y_2 + (Z_3 + Z_4 \pm Z_5)v^2. \quad (1.69)$$

In the 2HDM with a CP-conserving scalar potential, the couplings of h to the vector bosons and fermions and the Higgs self-couplings in the approach to the decoupling/alignment limit are exhibited in Table 1.6. Note that if the Yukawa coupling matrices ρ^U and/or ρ^D are complex, then small CP-violating pseudoscalar couplings of the SM-like Higgs boson to fermion pairs will be present, suppressed by a factor of $c_{\beta-\alpha}$.

Table 1.6. 2HDM couplings of the SM-like Higgs boson h normalized to those of the SM Higgs boson, in the decoupling/alignment limit. The hH^+H^- coupling given below is normalized to the SM hhh coupling. The scalar Higgs potential is taken to be CP-conserving. For the fermion couplings, D is a column vector of three down-type fermion fields (either down-type quarks or charged leptons) and U is a column vector of three up-type quark fields. The 3×3 hermitian matrices, ρ_R^Q and ρ_I^Q (where $Q = U$ or D) are defined in eq. (1.54). The normalization of the pseudoscalar coupling of the Higgs boson h to fermions is relative to the corresponding scalar coupling to fermions.

Higgs interaction	2HDM coupling	decoupling/alignment limit
hVV	$s_{\beta-\alpha}$	$1 - \frac{1}{2}s_{\beta-\alpha}^2$
hhh	see eq. (1.48)	$1 + 3(Z_6/Z_1)c_{\beta-\alpha}$
hH^+H^-	see eq. (1.48)	$\frac{1}{3} [(Z_3/Z_1) + (Z_7/Z_1)c_{\beta-\alpha}]$
$hhhh$	see eq. (1.49)	$1 + 4(Z_6/Z_1)c_{\beta-\alpha}$
$h\bar{D}D$	$s_{\beta-\alpha}\mathbb{1} + c_{\beta-\alpha}\rho_R^D$	$\mathbb{1} + c_{\beta-\alpha}\rho_R^D$
$ih\bar{D}\gamma_5 D$	$c_{\beta-\alpha}\rho_I^D$	$c_{\beta-\alpha}\rho_I^D$
$h\bar{U}U$	$s_{\beta-\alpha}\mathbb{1} + c_{\beta-\alpha}\rho_R^U$	$\mathbb{1} + c_{\beta-\alpha}\rho_R^U$
$ih\bar{U}\gamma_5 U$	$c_{\beta-\alpha}\rho_I^U$	$c_{\beta-\alpha}\rho_I^U$

The 2HDM couplings of H and A in the decoupling/alignment limit are also noteworthy. The couplings to vector boson pairs and fermion pairs are displayed in Table 1.7. The pattern of Higgs couplings noted in eq. (1.62) indicate that all couplings that involve at least one vector boson and exactly one of the non-minimal Higgs states (H , A or H^\pm) is suppressed by a factor of $c_{\beta-\alpha}$ in the decoupling/alignment limit.

Table 1.7. 2HDM couplings of H and A normalized to those of the SM Higgs boson, in the decoupling/alignment limit. The Hhh coupling given below is normalized to the SM hhh coupling. The scalar Higgs potential is taken to be CP-conserving. In the convention of $Z_6 > 0$, we identify $H \equiv -h_2$ and $A \equiv h_3$. See caption to Table 1.6.

Higgs interaction	2HDM coupling	decoupling/alignment limit
HW^+W^-, HZZ	$c_{\beta-\alpha}$	$c_{\beta-\alpha}$
Hhh	see eq. (1.48)	$-Z_6/Z_1 + [1 - \frac{2}{3}(Z_{345}/Z_1)]c_{\beta-\alpha}$
$H\bar{D}D$	$c_{\beta-\alpha}\mathbb{1} - s_{\beta-\alpha}\rho_R^D$	$c_{\beta-\alpha}\mathbb{1} - \rho_R^D$
$iH\bar{D}\gamma_5 D$	$s_{\beta-\alpha}\rho_I^D$	ρ_I^D
$H\bar{U}U$	$c_{\beta-\alpha}\mathbb{1} - s_{\beta-\alpha}\rho_R^U$	$c_{\beta-\alpha}\mathbb{1} - \rho_R^U$
$iH\bar{U}\gamma_5 U$	$-s_{\beta-\alpha}\rho_I^U$	$-\rho_I^U$
AW^+W^-, AZZ	0	0
$h_3\bar{D}D$	ρ_I^D	ρ_I^D
$iA\bar{D}\gamma_5 D$	ρ_R^D	ρ_R^D
$A\bar{U}U$	ρ_I^U	ρ_I^U
$iA\bar{U}\gamma_5 U$	$-\rho_R^U$	$-\rho_R^U$

For completeness we note that it may be possible to identify the SM-like Higgs boson with $h_2 = -H$. In this case, we have $c_{\beta-\alpha} \simeq 1$ and $s_{\beta-\alpha} \ll 1$, in order to achieve a SM-like HVV

coupling. In this case, eq. (1.61) yields

$$s_{\beta-\alpha} \simeq -\frac{2Z_6 v^2}{m_H^2 - m_h^2} \ll 1. \quad (1.70)$$

This cannot be satisfied in the decoupling limit, since by assumption we are identifying H with the SM-like Higgs boson, with $m_H > m_h$. However, eq. (1.70) can be satisfied in the alignment limit where $Z_6 \ll 1$. The corresponding neutral Higgs masses are:

$$m_H^2 = 2Z_1 v^2, \quad m_{h,A}^2 = Y_2 + (Z_3 + Z_4 \pm Z_5)v^2, \quad (1.71)$$

which requires that $2Z_1 v^2 > Y_2 + (Z_3 + Z_4 + Z_5)v^2$ (since $m_h < m_H$). In order for this interpretation to be viable, one must check that the other Higgs states would have not been discovered at LEP. Although it is not yet possible to fully rule out this case, we shall not consider it further here.

1.3.6 Higgs production at the ILC

In the CP-conserving 2HDM, the neutral Higgs bosons are produced via Higgsstrahlung and fusion processes as in the SM. In these production mechanisms, the CP-even Higgs bosons are produced via the coupling to gauge bosons. Consequently, the production cross section of h and H via these processes are simply given by

$$\sigma_{2\text{HDM}}(h) = \sigma_{\text{SM}}(h) \sin^2(\beta - \alpha), \quad (1.72)$$

$$\sigma_{2\text{HDM}}(H) = \sigma_{\text{SM}}(h) \cos^2(\beta - \alpha). \quad (1.73)$$

In the decoupling regime where $\sin^2(\beta - \alpha) \simeq 1$ and $\cos^2(\beta - \alpha) \ll 1$, the production cross section of h is similar to that of the Higgs boson in the SM, while that of H is small. The production of the CP-odd Higgs boson A via Higgsstrahlung or gauge boson fusion is highly suppressed since the A does not couple to weak gauge boson pairs at tree-level.

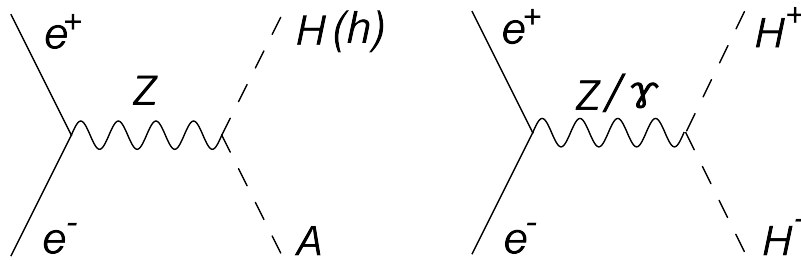


Figure 1.7. Pair production diagrams for neutral and charged Higgs bosons.

In addition, H (or h) and A are pair produced via the couplings HAZ and hAZ , as shown in Fig. 1.7 (Left). In light of eq. (1.62), the corresponding cross-sections are proportional to $\sin^2(\beta - \alpha)$ and $\cos^2(\beta - \alpha)$, respectively. In the decoupling regime, where $\sin^2(\beta - \alpha) \simeq 1$, the HA production is maximal. In Fig. 1.8 (Left), the production cross section of $e^+e^- \rightarrow Z^* \rightarrow HA$ is shown as a function of m_A , assuming $m_A = m_H$ for $\sqrt{s} = 250$ and 500 GeV. In these pair production mechanisms, the mass reach is kinematically limited by $\sqrt{s}/2$. Beyond the threshold of pair production, single production processes $e^+e^- \rightarrow f\bar{f}H$ ($f\bar{f}A$) could be used although the cross sections are rather small due to the limited phase space.

Charged Higgs bosons are produced in pairs via $e^+e^- \rightarrow H^+H^-$ as long as it is kinematically allowed as illustrated in Fig. 1.7 (Right). In Fig. 1.8 (Right), the production cross section of $e^+e^- \rightarrow Z^*(\gamma) \rightarrow H^+H^-$ is shown as a function of m_{H^\pm} for $\sqrt{s} = 300, 500, 800$ and 1000 GeV.

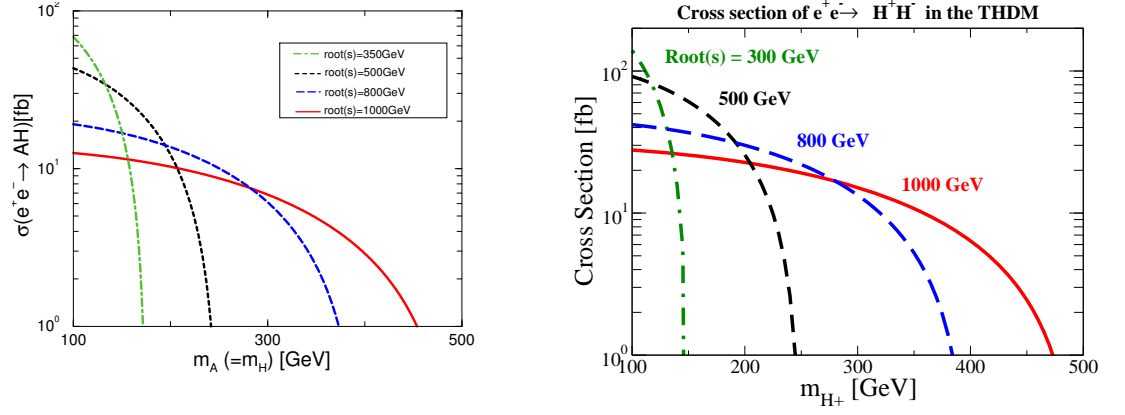


Figure 1.8. Production cross sections of $e^+e^- \rightarrow H^+H^-$ and $e^+e^- \rightarrow AH$

The associated production process, $e^+e^- \rightarrow H^\pm W^\mp$, is highly suppressed in the 2HDM due to the absence of a $H^\pm W^\mp Z$ vertex at tree level. Therefore, this process is especially sensitive to charged Higgs bosons in extended Higgs sectors with exotic scalar fields in a triplet or septet representation, where a tree-level $H^\pm W^\mp Z$ vertex is present.

If $m_{H^\pm} > \frac{1}{2}\sqrt{s}$, then pair production of charged Higgs bosons is not kinematically allowed. In this case, single charged Higgs boson production processes such as $e^+e^- \rightarrow \tau\nu H^\pm$, $e^+e^- \rightarrow csH^\pm$ and $e^+e^- \rightarrow tbH^\pm$ can be studied, although the cross sections for these processes are rather small, typically 0.1 fb or less.

The production of multiple Higgs boson states can in principle probe many of the Higgs self-coupling parameters and allow for a (partial) reconstruction of the Higgs potential. The mechanisms for double Higgs and triple Higgs production in high energy e^+e^- collisions have been considered in Refs. [71, 72, 73, 74, 75, 76].

1.3.7 Special forms for the Higgs-fermion Yukawa interactions

In the most general 2HDM, there is no reason why the matrices ρ_R^Q and ρ_L^Q , which appear in the Higgs-fermion Yukawa interactions [cf. eq. (1.55)], should be approximately diagonal, as required by the absence of large FCNCs (mediated by tree-level neutral Higgs exchange) in the data. Indeed in the general case, the diagonal structure of ρ_R^Q and ρ_L^Q is not stable with respect to radiative corrections, so that imposing such a condition requires an artificial fine-tuning of parameters. However, for special forms for the Higgs-fermion Yukawa interactions, it turns out that the matrices ρ_R^Q and ρ_L^Q are automatically diagonal, due to the presence of a symmetry that guarantees that the diagonal structure is radiatively stable. In this case, tree-level Higgs mediated FCNCs are "naturally" absent (in the same way that tree-level FCNCs mediated by Z -exchange are absent due to the GIM mechanism [77]).

In a general extended Higgs model, tree-level Higgs mediated FCNCs are absent if for some choice of basis of the scalar fields, at most one Higgs multiplet is responsible for providing mass for quarks or leptons of a given electric charge [54, 55]. This Glashow-Weinberg-Pascos (GWP) condition can be imposed by a symmetry principle, which guarantees that the absence of tree-level Higgs mediated FCNCs is natural. By an appropriate choice of symmetry transformation laws for the fermions and the Higgs scalars, the resulting Higgs-fermion Yukawa interactions take on the required form in some basis. The symmetry also restricts the form of the Higgs scalar potential in the same basis.

Applying these considerations to the 2HDM, consider the Higgs-quark Yukawa interactions in

the Φ_1 – Φ_2 basis,

$$\begin{aligned}
-\mathcal{L}_Y = & \bar{U}_L \Phi_a^0 h_a^U U_R - \bar{D}_L K^\dagger \Phi_a^- h_a^U U_R + \bar{U}_L K \Phi_a^+ h_a^D D_R + \bar{D}_L \Phi_a^0 h_a^D D_R \\
& + \bar{N}_L \Phi_a^+ h_a^L E_R + \bar{E}_L \Phi_a^0 h_a^L E_R + \text{h.c.},
\end{aligned} \tag{1.74}$$

where we have made explicit both the couplings to the quarks and leptons. In eq. (1.74), $h^{U,D,L}$ are 3×3 Yukawa coupling matrices and there is an implicit sum over $a = 1, 2$. The GWP condition can be implemented in four different ways [78, 79]:

1. Type-I Yukawa couplings: $h_1^U = h_1^D = h_1^L = 0$,
2. Type-II Yukawa couplings: $h_1^U = h_2^D = h_2^L = 0$.
3. Type-X Yukawa couplings: $h_1^U = h_1^D = h_2^L = 0$,
4. Type-Y Yukawa couplings: $h_1^U = h_2^D = h_1^L = 0$.

The four types of Yukawa couplings can be implemented by a discrete symmetry as shown in Table 1.8.

Table 1.8. Four possible \mathbb{Z}_2 charge assignments that forbid tree-level Higgs-mediated FCNC effects in the 2HDM. [80].

	Φ_1	Φ_2	U_R	D_R	E_R	U_L, D_L, N_L, E_L
Type I	+	−	−	−	−	+
Type II (MSSM like)	+	−	−	+	+	+
Type X (lepton specific)	+	−	−	−	+	+
Type Y (flipped)	+	−	−	+	−	+

The imposition of the discrete symmetry also restricts the form of the Higgs scalar potential given in eq. (1.27) by setting $m_{12}^2 = \lambda_6 = \lambda_7 = 0$. In this case, one can always rephase Φ_1 such that λ_5 is real, in which case the scalar potential is CP-conserving. Moreover, assuming that a $U(1)_{\text{EM}}$ -conserving potential minimum exists, the corresponding vacuum is CP-conserving, corresponding to real vacuum expectation values, $v_i \equiv \langle \Phi_i^0 \rangle$. Thus, the parameter

$$\tan \beta \equiv \frac{v_2}{v_1}, \tag{1.75}$$

is now meaningful since it refers to vacuum expectation values with respect to the basis of scalar fields where the discrete symmetry has been imposed. By convention, we shall take $0 \leq \beta \leq \frac{1}{2}\pi$, in which case $\tan \beta$ is non-negative. This can be achieved by redefining $\Phi_2 \rightarrow -\Phi_2$ if $\tan \beta$ is negative. However, such a redefinition would also reverse the signs of Z_6 and Z_7 . Thus, by adopting the convention that $\tan \beta$ is non-negative, we can no longer choose the convention where, say, $Z_6 > 0$. Indeed, in a convention where $\tan \beta$ and $\sin(\beta - \alpha)$ are non-negative, both Z_6 and $\cos(\beta - \alpha)$ can be of either sign [subject to the constraint that $Z_6 \cos(\beta - \alpha) < 0$ due to eq. (1.61)].

It is straightforward to evaluate the $\rho_{R,I}^Q$ for the Type-I and Type-II Higgs-quark Yukawa couplings. Using the corresponding results for the $\rho_{R,I}^Q$, the couplings of h , H and A are easily obtained from Tables 1.6 and 1.7.

1. Type-I: $\rho_R^D = \rho_R^U = \mathbb{1} \cot \beta$, $\rho_I^D = \rho_I^U = 0$.

$$\begin{aligned}
h\bar{D}D, h\bar{U}U : & \quad \frac{\cos \alpha}{\sin \beta} = s_{\beta-\alpha} + c_{\beta-\alpha} \cot \beta, \\
H\bar{D}D, H\bar{U}U : & \quad \frac{\sin \alpha}{\sin \beta} = c_{\beta-\alpha} - s_{\beta-\alpha} \cot \beta, \\
iA\bar{D}\gamma_5 D : & \quad \cot \beta, \\
iA\bar{U}\gamma_5 U : & \quad -\cot \beta.
\end{aligned} \tag{1.76}$$

$$2. \text{ Type-II: } \rho_R^D = -\mathbb{1} \tan \beta, \quad \rho_R^U = \mathbb{1} \cot \beta, \quad \rho_I^D = \rho_I^U = 0.$$

$$\begin{aligned} h\bar{D}D &: -\frac{\sin \alpha}{\cos \beta} = s_{\beta-\alpha} - c_{\beta-\alpha} \tan \beta, \\ h\bar{U}U &: \frac{\cos \alpha}{\sin \beta} = s_{\beta-\alpha} + c_{\beta-\alpha} \cot \beta, \\ H\bar{D}D &: \frac{\cos \alpha}{\cos \beta} = c_{\beta-\alpha} + s_{\beta-\alpha} \tan \beta, \\ H\bar{U}U &: \frac{\sin \alpha}{\sin \beta} = c_{\beta-\alpha} - s_{\beta-\alpha} \cot \beta, \\ iA\bar{D}\gamma_5 D &: -\tan \beta, \\ iA\bar{U}\gamma_5 U &: -\cot \beta. \end{aligned} \quad (1.77)$$

Likewise, the charged Higgs Yukawa couplings to quarks are given by

$$-\mathcal{L}_Y \ni \frac{\sqrt{2}}{v} \cot \beta \left(\bar{U} [KM_D P_R - M_U K P_L] D H^+ + \text{h.c.} \right), \quad \text{Type-I,} \quad (1.78)$$

$$-\mathcal{L}_Y \ni -\frac{\sqrt{2}}{v} \left(\bar{U} [KM_D P_R \tan \beta - M_U K P_L \cot \beta] D H^+ + \text{h.c.} \right), \quad \text{Type-II,} \quad (1.79)$$

where $M_{U,D}$ are the diagonal up-type and down-type 3×3 quark mass matrices and K is the CKM mixing matrix. The Type-I [Type-II] neutral and charged Higgs Yukawa coupling to quarks also apply to Type-X [Type-Y], respectively.

Following the prescription below eq. (1.52), the charged Higgs Yukawa coupling to leptons are obtained from the couplings to quarks given above by replacing $U \rightarrow N$, $D \rightarrow E$, $M_U \rightarrow 0$, $M_D \rightarrow M_E$ and $K \rightarrow \mathbb{1}$. The Type-I [Type-II] neutral and charged Higgs Yukawa coupling to leptons also apply to Type-Y [Type-X], respectively. The neutral Higgs Yukawa couplings to quarks and leptons (relative to the corresponding couplings of the SM Higgs boson) are conveniently summarized in Table 1.9 for the four possible implementations of the GWP condition.

Table 1.9. Higgs–fermion couplings in the 2HDM subject to the \mathbb{Z}_2 symmetries given in Table 1.8. The couplings listed below are normalized relative to the SM Higgs couplings $h_{\text{SM}}\bar{U}U$, $h_{\text{SM}}\bar{D}D$, and $h_{\text{SM}}\bar{E}E$.

	$h\bar{U}U$ ξ_h^u	$h\bar{D}D$ ξ_h^d	$h\bar{E}E$ ξ_h^e	$H\bar{U}U$ ξ_H^u	$H\bar{D}D$ ξ_H^d	$H\bar{E}E$ ξ_H^e	$iA\bar{U}\gamma_5 U$ ξ_A^u	$iA\bar{D}\gamma_5 D$ ξ_A^d	$iA\bar{E}\gamma_5 E$ ξ_A^e
Type I	$\frac{\cos \alpha}{\sin \beta}$	$\frac{\cos \alpha}{\sin \beta}$	$\frac{\cos \alpha}{\sin \beta}$	$\frac{\sin \alpha}{\sin \beta}$	$\frac{\sin \alpha}{\sin \beta}$	$\frac{\sin \alpha}{\sin \beta}$	$-\cot \beta$	$\cot \beta$	$\cot \beta$
Type II	$\frac{\cos \alpha}{\sin \beta}$	$-\frac{\sin \alpha}{\cos \beta}$	$-\frac{\sin \alpha}{\cos \beta}$	$\frac{\sin \alpha}{\sin \beta}$	$\frac{\cos \alpha}{\cos \beta}$	$\frac{\cos \alpha}{\cos \beta}$	$-\cot \beta$	$-\tan \beta$	$-\tan \beta$
Type X	$\frac{\cos \alpha}{\sin \beta}$	$\frac{\cos \alpha}{\sin \beta}$	$-\frac{\sin \alpha}{\cos \beta}$	$\frac{\sin \alpha}{\sin \beta}$	$\frac{\sin \alpha}{\sin \beta}$	$\frac{\cos \alpha}{\cos \beta}$	$-\cot \beta$	$\cot \beta$	$-\tan \beta$
Type Y	$\frac{\cos \alpha}{\sin \beta}$	$-\frac{\sin \alpha}{\cos \beta}$	$\frac{\cos \alpha}{\sin \beta}$	$\frac{\sin \alpha}{\sin \beta}$	$\frac{\cos \alpha}{\cos \beta}$	$\frac{\sin \alpha}{\sin \beta}$	$-\cot \beta$	$-\tan \beta$	$\cot \beta$

In implementing the \mathbb{Z}_2 discrete symmetries given in Table 1.8, we noted above that the parameters of the scalar Higgs potential are restricted such that $m_{12}^2 = \lambda_6 = \lambda_7 = 0$ in the basis in which the discrete symmetry is manifest. However, these latter conditions can be slightly relaxed by taking $m_{12}^2 = 0$ (while maintaining $\lambda_6 = \lambda_7 = 0$). In this case, the discrete symmetry is softly broken by a dimension-two term in the scalar potential (while it is respected by all dimension-four terms of the Lagrangian). In a 2HDM of this type, Higgs–mediated FCNCs are still absent at tree-level, but can be generated at the one-loop level. Since the neutral Higgs Yukawa couplings are suppressed by fermion masses, one can check that sensible parameter regimes exist in which the radiatively generated FCNCs in this model are sufficiently suppressed so as not to be in conflict with experimental data.

The existence of a softly-broken \mathbb{Z}_2 symmetry that imposes $\lambda_6 = \lambda_7 = 0$ in some basis yields

the following constraint on the Higgs basis scalar potential parameters:

$$(Z_6 + Z_7)(Z_2 - Z_1)(Z_1 + Z_2 - 2Z_{345}) + (Z_6 - Z_7) [(Z_2 - Z_1)^2 - 4(Z_6 + Z_7)^2] = 0,$$

where $Z_{345} \equiv Z_3 + Z_4 + Z_5$. The parameter β is also determined

$$\tan 2\beta = \frac{2(Z_6 + Z_7)}{Z_2 - Z_1}. \quad (1.80)$$

The case of $Z_1 = Z_2$ and $Z_6 = -Z_7$ must be treated separately. In this case, a \mathbb{Z}_2 symmetry governing the quartic terms of the scalar potential is automatically present, and the corresponding value of β is determined from the following quadratic equation,

$$(Z_1 - Z_{345}) \tan 2\beta + 2Z_6(1 - \tan^2 2\beta) = 0. \quad (1.81)$$

In the constrained 2HDMs considered in this subsection, there are a number of benefits in allowing for a soft breaking of the \mathbb{Z}_2 discrete symmetry, which permits a nonzero m_{12}^2 in the basis where $\lambda_6 = \lambda_7 = 0$. First, this allows us to treat the MSSM Higgs sector, which employs the Type-II Higgs–fermion Yukawa couplings as a consequence of supersymmetry rather than a \mathbb{Z}_2 discrete symmetry. Second, the 2HDM with a soft breaking of the \mathbb{Z}_2 discrete symmetry possesses a decoupling limit (which corresponds to large m_{12}^2). If $m_{12}^2 = 0$, no decoupling limit exists since the scalar potential minimum conditions imply that $Y_2 \sim \mathcal{O}(Z_i v^2)$. Thus, in this latter case, a SM-like Higgs boson emerges only in the alignment limit. Finally, taking $m_{12}^2 \neq 0$ allows for a new source of CP-violation in the Higgs sector. One can check [68] that the Higgs scalar potential is explicitly CP-violating if $\text{Im}[(m_{12}^2)^2 \lambda_5^*] \neq 0$. If the scalar potential is explicitly CP-conserving, then one can rephase the scalar fields such that m_{12}^2 and λ_5 are real. In this case spontaneous CP-violation can occur if $0 < |m_{12}^2| < 2\lambda_5 |v_1| |v_2|$, in which case the minimum of the scalar potential yields a relative phase $\langle \Phi_1^\dagger \Phi_2 \rangle = |v_1| |v_2| e^{i\xi}$, where $\cos \xi = m_{12}^2 / (2\lambda_5 |v_1| |v_2|)$.

The decays of the Higgs bosons in the constrained 2HDM depend on the Type of Yukawa interactions. When $\sin(\beta - \alpha) = 1$, the decay pattern of h is the same as those in the Standard Model at tree level. When $\sin(\beta - \alpha)$ differs from 1, the couplings of h will deviate from Standard Model expectations. In particular, the couplings of h to down-type quarks and leptons will differ from those of the SM with a pattern of deviations that strongly depends on the Type of Yukawa Interactions. The precision measurement of these coupling make it possible to discriminate among the various Types of Yukawa interactions of the 2HDM.

On the other hand, the decay patterns of H , A , and H^\pm can vary over a large range [79, 80, 81, 82]. Figure 1.9 shows the decay branching ratios of H , A and H^\pm as a function of $\tan \beta$ for Type I, II, X and Y Yukawa couplings for Higgs boson masses of 200 GeV and $\sin(\beta - \alpha) = 1$ for $m_H = m_A = m_{H^\pm} = 200$ GeV. The decay pattern of H is typically similar to that of A , but with some important exceptions. In the Type I 2HDM, the amplitudes for the fermionic and the gg decays mode of H , A and H^\pm are all proportional to $\cot \beta$. Consequently the corresponding branching ratios are roughly independent of $\tan \beta$. The slight difference between the branching ratios for $H, A \rightarrow \gamma\gamma$ can be attributed to the existence of the $H^+ H^-$ coupling to H (the corresponding coupling to A is absent due to the assumed CP conservation), which governs the charged Higgs loop contribution to $H \rightarrow \gamma\gamma$. In Figure 1.10, the similar figures of the decay branching ratios of H , A and H^\pm to those in Fig. 1.9 are shown for $\sin(\beta - \alpha) = 1$ for $m_H = m_A = m_{H^\pm} = 400$ GeV. The two-body decays $H/A \rightarrow t\bar{t}$ are now kinematically allowed in this case.

In general, the complexity of the H , A , H^\pm decay schemes in the various Types of Yukawa interactions make it difficult to determine the underlying model unless these scalars are created

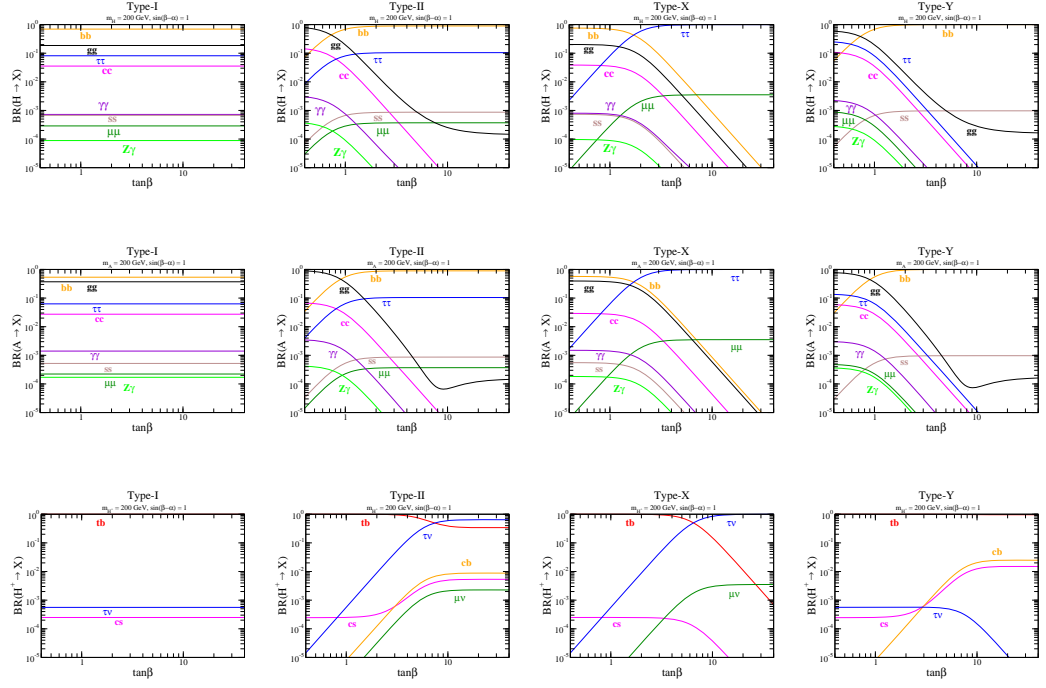


Figure 1.9. Decay branching ratios of H , A and H^\pm in the four different Types of 2HDM as a function of $\tan \beta$ for $m_H = m_A = m_{H^\pm} = 200$ GeV. The SM-like limit $\sin(\beta - \alpha) = 1$ is taken.

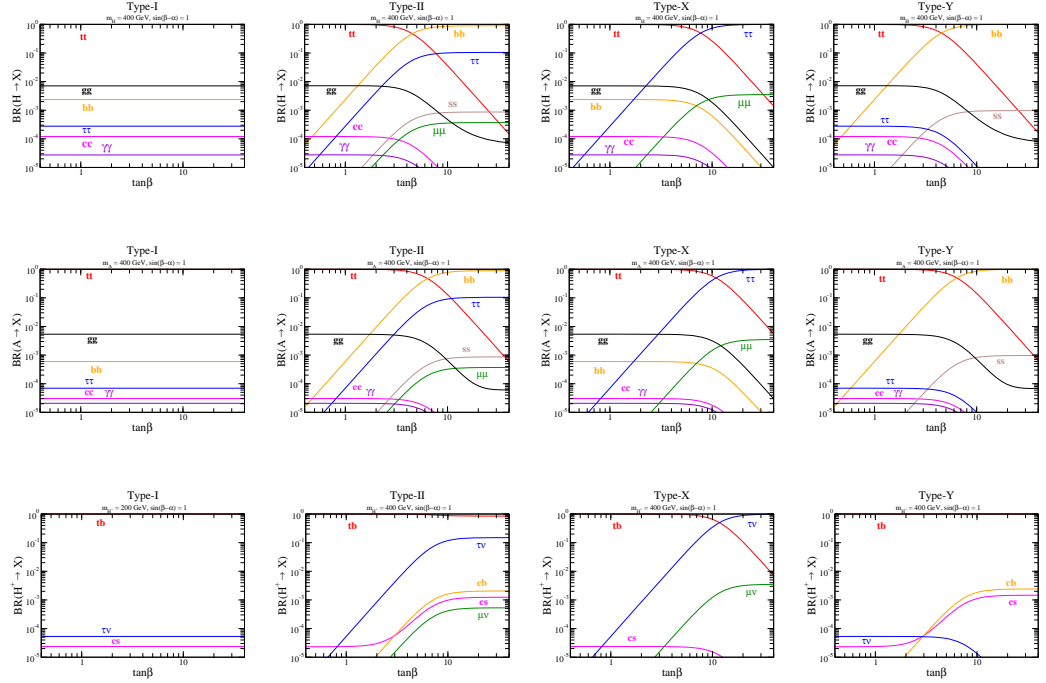


Figure 1.10. Decay branching ratios of H , A and H^\pm in the four different Types of 2HDM as a function of $\tan \beta$ for $m_H = m_A = m_{H^\pm} = 400$ GeV. The SM-like limit $\sin(\beta - \alpha) = 1$ is taken.

through a simple and well-characterized pair-production reaction. Thus, even if these scalars are discovered at the LHC, it will be important to study them via the pair-production process at the ILC.

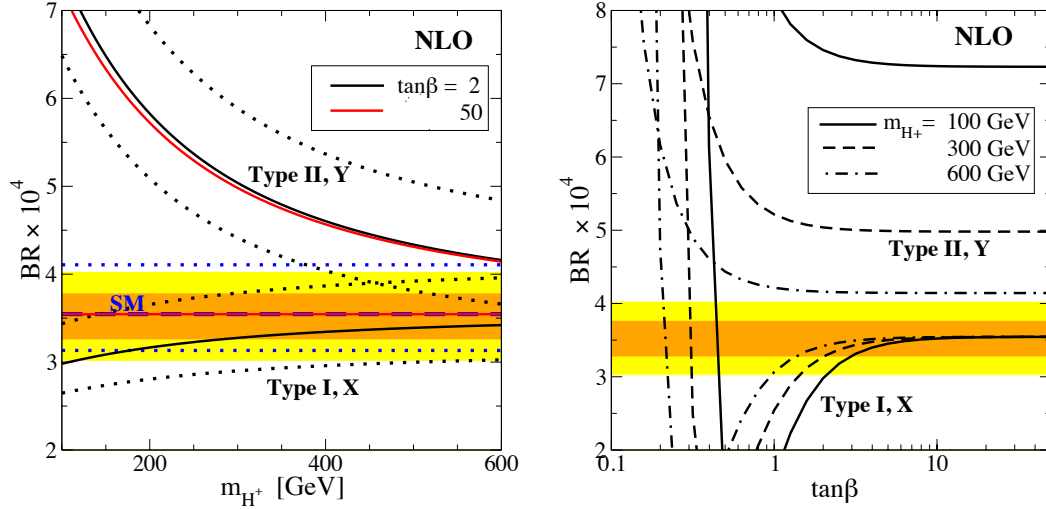


Figure 1.11. Predictions of the decay branching ratio for $b \rightarrow s\gamma$ are shown at the NLO approximation as a function of m_{H^\pm} and $\tan\beta$. The dark (light) shaded band represents 1σ (2σ) allowed region of current experimental data. In the left panel, solid (dashed) curves denote the prediction for $\tan\beta = 2$ (50) in various 2HDMs. In the right panel, solid, dashed and dot-dashed curves are those for $m_{H^\pm} = 100, 300$ and 600 GeV, respectively.

1.3.8 Constraints due to flavor physics

Indirect contributions of Higgs bosons to precisely measurable observables can be used to constrain extended Higgs sectors. In this section, we summarize the experimental bounds from flavor experiments on the constrained 2HDMs introduced in Section 1.3.7. These bounds arise primarily due to tree-level or loop diagrams that contain the charged Higgs boson. The corresponding amplitudes involve the Yukawa interactions and hence strongly depend on which Type of 2HDM is employed.

It is well known that the charged Higgs boson mass in the Type-II 2HDM is stringently constrained by the precision measurements of the radiative decay of $b \rightarrow s\gamma$ [83]. The process $b \rightarrow s\gamma$ receives contributions from the W boson loop and the charged Higgs boson loop in the 2HDM. It is noteworthy that these two contributions always constructively interfere in the Type-II (Type-Y) 2HDM, whereas this is not the case in the Type-I (Type-X) 2HDM [79, 80, 81, 82]. In Fig. 1.11 [79], we show the branching ratio of $B \rightarrow X_s\gamma$ for each Type of 2HDM as a function of m_{H^\pm} (left-panel) and $\tan\beta$ (right-panel), which are evaluated at the next-to-leading order (NLO) following the formulas in Ref. [84]. The SM prediction at the NLO is also shown for comparison. The theoretical uncertainty is about 15% in the branching ratio (as indicated by dotted curves in Fig. 1.11), which mainly comes from the pole mass of charm quark $m_c^{\text{pole}} = 1.67 \pm 0.07$ GeV [85]. (Note that Ref. [84] quotes and error in m_c^{pole} of about 7%, which then leads to a smaller theoretical uncertainty in the branching ratio for $b \rightarrow s\gamma$.) The experimental bounds of the branching ratio are also indicated, where the current world average value is given by $\text{BR}(B \rightarrow X_s\gamma) = (3.52 \pm 0.23 \pm 0.09) \times 10^{-4}$ [86]. One can see from Fig. 1.11 that the branching ratio in the Type-I (Type-X) 2HDM lies within the 2σ experimental error in all the regions of m_{H^\pm} indicated for $\tan\beta \gtrsim 2$, while that in the Type-II (Type-Y) 2HDM is far from the value indicated by the data for a light charged Higgs boson region ($m_{H^\pm} \lesssim 200$ GeV). In the right figure, a cancellation occurs in the Type-I (Type-X) 2HDM since there are destructive interferences between the W boson and the H^\pm contributions. The results of these figures indicate that the $B \rightarrow X_s\gamma$ experimental results still permit a light charged Higgs boson in the Type-I (Type-X) 2HDM. We note that in the MSSM the chargino contribution can

compensate the charged Higgs boson contribution [87, 88]. This cancellation weakens the limit on m_{H^\pm} from $b \rightarrow s\gamma$ in the Type-II 2HDM, and allows a light charged Higgs boson as in the Type-I (Type-X) 2HDM. At the NNLO approximation, the branching ratio for $b \rightarrow s\gamma$ has been evaluated in the SM in Refs. [89, 90, 91]. The predicted value at the NNLO approximation is less than that at the NLO approximation over a wide range of renormalization scales. The branching ratio for $b \rightarrow s\gamma$ in the Standard Model is $(3.15 \pm 0.23) \times 10^{-4}$ [89], and a lower bound for m_{H^\pm} , after adding the NLO charged Higgs contribution, is found to be $m_{H^\pm} \gtrsim 380$ GeV (95% CL) in the Type-II (Type-Y) 2HDM [83]. (Note that the calculation of Refs. [90, 91] for the NNLO branching ratio in the SM yields $(2.98 \pm 0.26) \times 10^{-4}$, and the corresponding charged Higgs mass bound is somewhat relaxed.) On the other hand, in the Type-I (Type-X) 2HDM, although the branching ratio becomes smaller as compared to the NLO evaluation, no serious bound on m_{H^\pm} can be found for $\tan\beta \gtrsim 2$. Therefore, the charged Higgs boson mass is not expected to be strongly constrained in the Type-I (Type-X) 2HDM even at the NNLO, and the conclusion that the Type-I (Type-X) 2HDM is favored for $m_{H^\pm} \lesssim 200$ GeV based on the NLO analysis should not be changed.

The decay $B \rightarrow \tau\nu$ has been examined in the Type-II 2HDM in Refs. [92, 93]. The data for $\text{BR}(B^+ \rightarrow \tau^+\nu_\tau) = (1.65 \pm 0.34) \times 10^{-4}$ are obtained at the B factories [85]. The decay branching ratio can be written as [93]

$$\frac{\mathcal{B}(B^+ \rightarrow \tau^+\nu_\tau)_{\text{2HDM}}}{\mathcal{B}(B^+ \rightarrow \tau^+\nu_\tau)_{\text{SM}}} \simeq \left(1 - \frac{m_B^2}{m_{H^\pm}^2} \xi_A^d \xi_A^e\right)^2, \quad (1.82)$$

where coefficients ξ_A^d and ξ_A^e are defined in Table 1.9. In Fig. 1.12, the allowed region from the experimental $B \rightarrow \tau\nu$ results is shown in the Type-II 2HDM. The dark (light) shaded region denotes

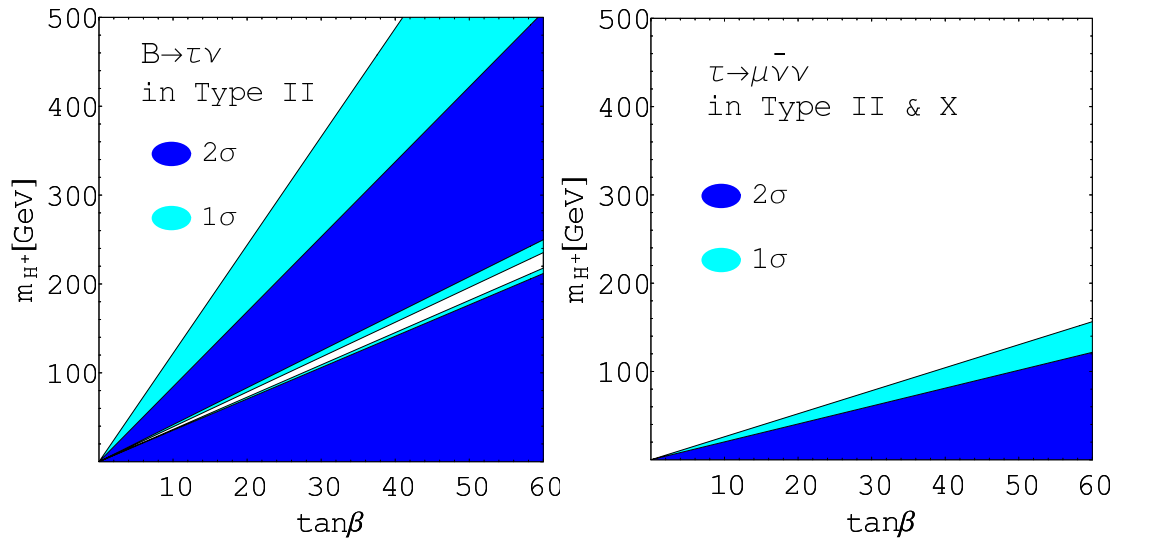


Figure 1.12. Bounds from $B \rightarrow \tau\nu$ (left panel) and tau leptonic decay (right panel) on m_{H^\pm} as a function of $\tan\beta$ are shown. The dark (light) shaded region corresponds to the 2σ (1σ) exclusion of these experimental results. In the Type-II 2HDM the wide parameter space is constrained by $B \rightarrow \tau\nu$, while only the tau leptonic decays are important for the Type-X 2HDM.

the 2σ (1σ) exclusion from the $B \rightarrow \tau\nu$ measurements. The process is important only in the Type-II 2HDM at large values of $\tan\beta$. The other Types of Yukawa interactions are not constrained by this process.

The rate for the leptonic decay of the tau lepton, $\tau \rightarrow \mu\bar{\nu}\nu$, can deviate from the SM value due to the presence of a light charged Higgs boson [94]. The partial decay rate is approximately expressed as [93]

$$\frac{\Gamma_{\tau \rightarrow \mu\bar{\nu}\nu}^{\text{2HDM}}}{\Gamma_{\tau \rightarrow \mu\bar{\nu}\nu}^{\text{SM}}} \simeq 1 - \frac{2m_\mu^2}{m_{H^\pm}^2} \xi_A^{e^2} \kappa \left(\frac{m_\mu^2}{m_\tau^2} \right) + \frac{m_\mu^2 m_\tau^2}{4m_{H^\pm}^4} \xi_A^{e^4}, \quad (1.83)$$

where the function $\kappa(x)$ is defined by

$$\kappa(x) = \frac{1 + 9x - 9x^2 - x^3 + 6x(1+x)\ln x}{1 - 8x + 8x^3 - x^4 - 12x^2 \ln x}. \quad (1.84)$$

In the Type-II (Type-X) 2HDM, the leptonic Yukawa interaction can be enhanced in the large $\tan\beta$ region. Hence, both model Types are weakly constrained by tau decay data, as indicated in Fig. 1.12.

The precision measurement of the muon anomalous magnetic moment can yield a mass bound on the Higgs boson in the SM [95, 96]. This constraint can be applied to models with additional interactions such as the 2HDM [97, 98, 99]. At the one-loop level, the 2HDM contribution is given by

$$\delta a_\mu^{1\text{-loop}} \simeq \frac{G_F m_\mu^4}{4\pi^2 \sqrt{2}} \left[\sum_{\phi^0=h,H} \frac{\xi_{\phi^0}^{e^2}}{m_{\phi^0}^2} \left(\ln \frac{m_{\phi^0}^2}{m_\mu^2} - \frac{7}{6} \right) + \frac{\xi_A^{e^2}}{m_A^2} \left(-\ln \frac{m_A^2}{m_\mu^2} + \frac{11}{6} \right) - \frac{\xi_A^{e^2}}{6m_{H^\pm}^2} \right]. \quad (1.85)$$

This process is also purely leptonic and only yields milder bounds on the Higgs boson masses for very large $\tan\beta$ values in the Type-II (Type-X) 2HDM. No effective bound on the Type-I (Type-Y) 2HDM is obtained. It is also known that the two-loop (Barr-Zee type) diagram can significantly affect a_μ [100]. The contribution from this class of diagrams is only important for large $\tan\beta$ values with smaller Higgs boson masses in the Type-II 2HDM. For the other Types of 2HDM, a much less effective bound on the parameter space is obtained.

The $B^0 - \bar{B}^0$ mass differences, ΔM_{B_d} and ΔM_{B_s} , are sensitive to charged Higgs exchange via box-type diagrams in which top quarks are also exchanged. The data exclude relatively large top Yukawa couplings that are proportional $m_t \cot\beta$ for smaller charged Higgs boson masses. This constraint is common among the four Types of 2HDMs. In light of the current data for ΔM_{B_d} , $\tan\beta < 1$ is ruled out for $m_{H^\pm} < 500$ GeV at 95 % C.L. [101]

All the important constraints on the parameter space for each Type of 2HDM are summarized in Fig. 1.13, where excluded regions from the data of $\text{BR}(B \rightarrow X_s \gamma)$, Δ_{0-} , ΔM_{B_d} , $B_u \rightarrow \tau\nu_\tau$, $B \rightarrow D\tau\nu_\tau$, $K \rightarrow \mu\nu_\mu$, $D_s \rightarrow \tau\nu_\tau$, and $D_s \rightarrow \mu\nu_\mu$ are plotted in the $(m_{H^+}, \tan\beta)$ plane [101]. Here, we have included among the list of flavor observables the degree of isospin asymmetry in the exclusive decay mode $B \rightarrow K^* \gamma$, defined as [102, 103]

$$\Delta_{0-} \equiv \frac{\Gamma(\bar{B}^0 \rightarrow \bar{K}^{*0}) - \Gamma(\bar{B}^- \rightarrow \bar{K}^{*-})}{\Gamma(\bar{B}^0 \rightarrow \bar{K}^{*0}) + \Gamma(\bar{B}^- \rightarrow \bar{K}^{*-})}. \quad (1.86)$$

The exclusion of low $\tan\beta < 1$ in all four model Types for $m_{H^+} < 500$ GeV, arises as a result of three observables: $\text{BR}(B \rightarrow X_s \gamma)$, Δ_{0-} , and ΔM_{B_d} . The constraints at low $\tan\beta$ are similar between the model Types, since the couplings to the up-type quarks are universal. In the Type I 2HDM, a value of $\tan\beta > 1$ signals the decoupling of one Higgs doublet from the whole fermion sector. In Type II and Type III (=Type Y), which share the same coupling pattern for the quarks, there exists a $\tan\beta$ -independent lower limit of $m_{H^+} \gtrsim 300$ GeV imposed by $\text{BR}(B \rightarrow X_s \gamma)$. (This latter constraint

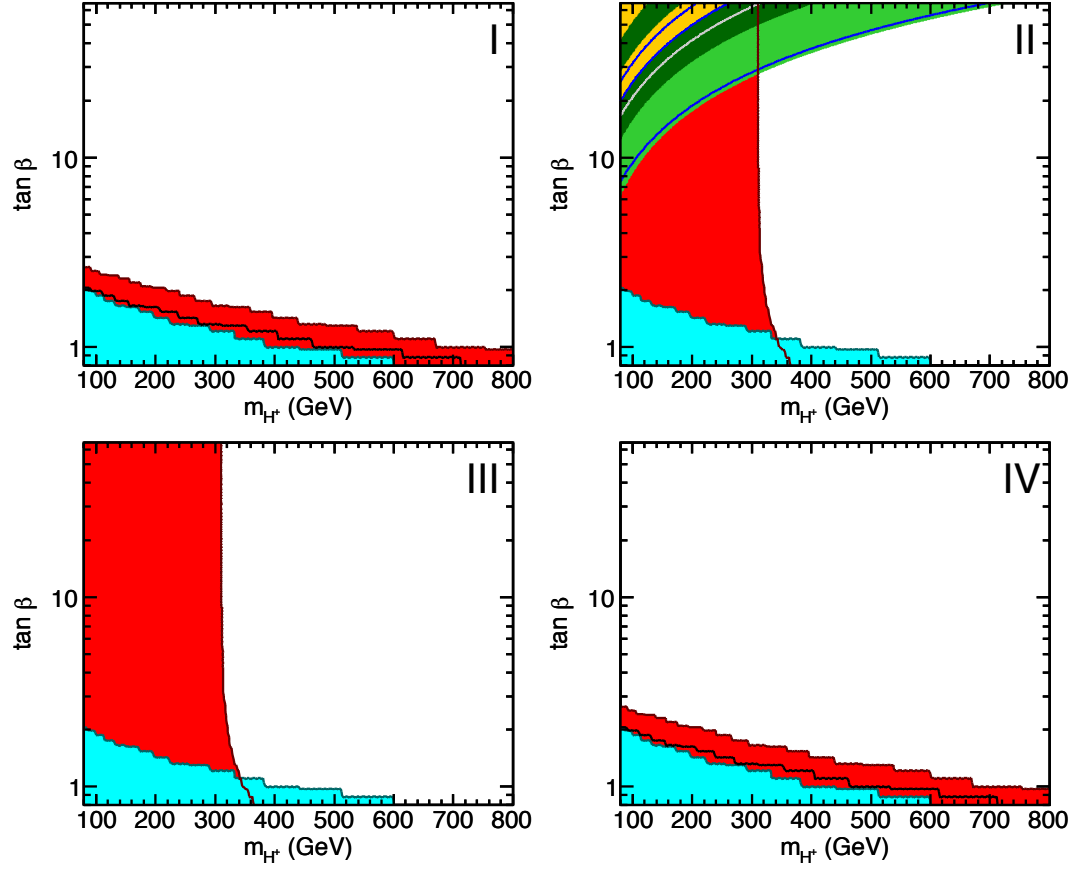


Figure 1.13. Excluded regions of the $(m_{H^+}, \tan \beta)$ parameter space for Z_2 -symmetric 2HDM Types. The Type Y and X models [cf. Table 1.8] are denoted above by Type III and IV, respectively. The color coding is as follows: $\text{BR}(B \rightarrow X_s \gamma)$ (red), Δ_{0-} (black contour), ΔM_{B_d} (cyan), $B_u \rightarrow \tau \nu_\tau$ (blue), $B \rightarrow D \tau \nu_\tau$ (yellow), $K \rightarrow \mu \nu_\mu$ (gray contour), $D_s \rightarrow \tau \nu_\tau$ (light green), and $D_s \rightarrow \mu \nu_\mu$ (dark green).

is now somewhat more stringent in light of Ref. [83].) No generic lower limit on m_{H^+} is found in Type I and Type IV (=Type X) models. Constraints for high $\tan \beta$ are only obtained in the Type II model. This can be understood by noting that the leptonic and semi-leptonic observables require $\tan \beta$ -enhanced couplings $\lambda_{dd} \lambda_{\ell\ell} \sim \tan^2 \beta \gg 1$ ($d = d, s, b$) for the contributions to be interesting. In the Type III (=Type Y) and the Type IV (=Type X) 2HDMs, these couplings are instead always $\lambda_{dd} \lambda_{\ell\ell} = -1$, while in Type I they are proportional to $\cot^2 \beta$.

Finally, recently current data from BaBar of the $\bar{B} \rightarrow D \tau \bar{\nu}$ and $\bar{B} \rightarrow D^* \tau \bar{\nu}$ slightly deviate from the SM predictions by 2.0σ and 2.7σ , respectively [104]. Moreover, these data are also inconsistent with the Type-I (X) and Type-II (Y) 2HDMs, since both decay rates, which depend on the charged Higgs mass, cannot be explained simultaneously for the same value of m_{H^\pm} . However, these data can be compatible in the context of a more general 2HDM with unconstrained Higgs-quark Yukawa interactions [105]. Meanwhile, there is no confirmation yet of the BaBar results for $\bar{B} \rightarrow D \tau \bar{\nu}$ and $\bar{B} \rightarrow D^* \tau \bar{\nu}$ from the BELLE collaboration. Thus, it is certainly premature to claim a definitive deviation from the predictions of the Standard Model as well as all 2HDMs with Types I, II, X, or Y Yukawa interactions.

1.3.9 The inert 2HDM

The inert 2HDM is one of the simplest extensions of the Standard Model [106, 107]. The inert 2HDM is defined as a Type-I model in which the \mathbb{Z}_2 discrete symmetry is imposed in the Higgs basis. The \mathbb{Z}_2 charge assignments for the inert 2HDM are given in Table 1.10. In particular, the Higgs basis field H_2 , which has no vev, is odd under the discrete symmetry. As a result of this discrete symmetry, $Y_3 = Z_6 = Z_7 = 0$ and there are no Yukawa couplings of H_2 to fermions.

Table 1.10. The \mathbb{Z}_2 charge assignments that define the Inert 2HDM, where H_1 and H_2 are the Higgs doublet fields in the Higgs basis.

	H_1	H_2	U_R	D_R	E_R	U_L, D_L, N_L, E_L
Type I Inert	+	−	−	−	−	+

Since $Z_6 = 0$, we are in the exact alignment limit, in which $h = \sqrt{2} \text{Re}(H_1^0 - v)$ is a mass-eigenstate whose couplings are equivalent to those of the SM Higgs bosons. We also identify

$$\Phi_2 = \begin{pmatrix} H^+ \\ (H + iA)/\sqrt{2} \end{pmatrix}, \quad (1.87)$$

where H , A and H^+ are the other Higgs mass eigenstates. The \mathbb{Z}_2 discrete symmetry is unbroken in the vacuum since $\langle H_2^0 \rangle = 0$. Thus, there are no couplings involving an odd number of H , A and H^\pm fields. In particular, the lightest inert particle (LIP) will be absolutely stable and is a potential dark matter candidate [106, 108, 109, 110]. In addition, the inert 2HDM has rich phenomenological features. For example, the dark matter could play a critical role in the breaking of the electroweak symmetry [111] and the triggering of the electroweak phase transition [112]. One can also add a \mathbb{Z}_2 -odd right-handed neutrino to the model thereby providing a mechanism for generating the light neutrino masses at the one loop level [113].

The scalar potential for the inert 2HDM is given (in the Higgs basis) by eq. (1.28) with $Y_3 = Z_6 = Z_7 = 0$. One can always rephase $H_2 \rightarrow e^{i\chi} H_2$ such that the one potentially complex parameter, Z_5 is real. Indeed, the sign of Z_5 is not physical, since the sign can be flipped by redefining $H_2 \rightarrow iH_2$. Thus the Higgs sector of the inert 2HDM is CP-conserving and depends on seven real parameters $\{Y_1, Y_2, Z_1, Z_2, Z_3, Z_4, |Z_5|\}$. The potential minimum condition is given by $Y_1 = -Z_1 v^2$. Using eqs. (1.31) and (1.32), it follows that the physical Higgs masses are given by

$$m_h^2 = 2Z_1 v^2, \quad (1.88)$$

$$m_{H,A}^2 = Y_2 + (Z_3 + Z_4 \pm |Z_5|)v^2, \quad (1.89)$$

$$m_{H^\pm}^2 = Y_2 + Z_3 v^2, \quad (1.90)$$

Here, we have adopted a notation in which h corresponds to the scalar whose properties are precisely those of the SM Higgs boson. No mass ordering of h and H is assumed. Indeed, eqs. (1.60) and (1.61) imply that either $\cos(\beta - \alpha) = 0$ if h is identified as h_1 or $\sin(\beta - \alpha) = 0$ if h is identified as h_2 . In either case, this is the exact alignment limit with h identified as the SM Higgs boson.

Moreover, we have used the notation H and A above for the CP-even and odd bosons from the inert sector. However, an examination of the couplings of H and A implies only that H and A have CP-quantum numbers of opposite sign. However, one cannot assign a unique CP-quantum number to H and A separately. (For further details, see Ref. [59].) The couplings of the inert scalars to the gauge bosons and Higgs bosons are easily obtained by setting $\cos(\beta - \alpha) = 0$ [$\sin(\beta - \alpha) = 0$] if one identifies the SM Higgs boson with h_1 [h_2].

If we require that all scalar squared masses are positive, with $v^2 = -Y_1/Z_1$, then it follows

that [107]

$$Y_1 < 0, \quad Z_1 Y_2 > Z_3 Y_1, \quad Z_1 Y_2 > (Z_3 + Z_4 \pm |Z_5|) Y_1. \quad (1.91)$$

If we also require that the scalar potential is bounded from below (vacuum stability), then the following additional constraints must be satisfied [107]

$$Z_1 > 0, \quad Z_2 > 0, \quad Z_3 > -(Z_1 Z_2)^{1/2}, \quad Z_3 + Z_4 \pm |Z_5| > -(Z_1 Z_2)^{1/2}. \quad (1.92)$$

If one associates the dark matter with an electrically neutral LIP then $m_{H^\pm} > m_{H,A}$, which yields [114]

$$Z_4 < |Z_5|. \quad (1.93)$$

Finally, one can impose the conditions of perturbativity [106] which can be used to restrict the magnitudes of the Z_i .

The seven parameters of the Higgs potential can be replaced by the vev v , four masses of the Higgs boson and the inert scalars, $(m_h, m_{H^\pm}, m_H, m_A)$, the two of the scalar self-couplings Z_2 and Z_3 . For example, we can use this set of input parameters to compute $Y_1 = -\frac{1}{2}m_h^2$, $Y_2 = m_{H^\pm}^2 - Z_3 v^2$, $Z_1 v^2 = \frac{1}{2}m_h^2$, $Z_4 v^2 = \frac{1}{2}(m_H^2 + m_A^2) - m_{H^\pm}^2$ and $|Z_5|v^2 = \frac{1}{2}|m_H^2 - m_A^2|$.

Collider phenomenology of the inert scalars in the inert 2HDM has been studied in Refs. [106, 110, 115, 116]. In Ref. [116], experimental bounds on the inert scalar masses are obtained by using the experimental results at the LEP collider [117, 118, 119]. At the LHC, even though the parameter regions where the inert scalars could be discovered have been suggested [109, 120, 121], a detailed search for the inert scalars and a determination of their masses and quantum numbers would be difficult.

The ILC phenomenology for the inert scalars has been considered in Ref. [122]. Without loss of generality, we assume in what follows that $m_H < m_A$. Four benchmark points for the mass spectrum of inert scalars are listed in Table 1.11, which satisfy all available theoretical and phenomenological constraints. In the four benchmark points, the mass of H is fixed to 65 GeV, so that it does not permit the invisible decay of the SM Higgs boson, $h \rightarrow HH$. While a mass of H up to ~ 80 GeV is consistent with the dark matter relic abundance analysis [108, 109, 110], the collider phenomenology does not change qualitatively by varying m_H in this range.

In Table 1.11, the cross sections of HA production and H^+H^- production at $\sqrt{s} = 250$ GeV and 500 GeV are shown. The production cross sections of the inert scalars are large enough to be tested at the ILC. The cross section of HA production can take the largest value, i.e. 186 fb at $\sqrt{s} = 190$ GeV, 78 fb at $\sqrt{s} = 280$ GeV, and 46 fb at $\sqrt{s} = 350$ GeV for cases (I, III), (II), and (IV), respectively. The cross section of H^+H^- production can take the largest value, i.e. 96 fb at $\sqrt{s} = 380$ GeV and 53 fb at $\sqrt{s} = 500$ GeV for cases (I, II) and (III, IV), respectively. At $\sqrt{s} = 1$ TeV, they are about 10 fb and 20 fb for HA production and H^+H^- production for all the four benchmark points, respectively. For cases (II, IV), H^\pm decays into $W^\pm H$ predominantly, where we admit the W -boson to be off-shell if $m_{H^\pm} - m_H < m_W$. For cases (I) and (III), $H^\pm \rightarrow W^\pm A$ decay would be sizable as well, with the branching ratios about 32% and 27%, respectively. The decay of the A -boson is dominated by $A \rightarrow Z^{(*)}H$.

Table 1.11. Masses of inert scalars and ILC cross sections for our four benchmark points.

	Inert scalar masses			ILC cross sections [$\sqrt{s} = 250$ GeV (500 GeV)]	
	m_H [GeV]	m_A [GeV]	m_{H^\pm} [GeV]	$\sigma_{e^+e^- \rightarrow HA}$ [fb]	$\sigma_{e^+e^- \rightarrow H^+H^-}$ [fb]
(I)	65.	73.	120.	152. (47.)	11. (79.)
(II)	65.	120.	120.	74. (41.)	11. (79.)
(III)	65.	73.	160.	152. (47.)	0. (53.)
(IV)	65.	160.	160.	17. (35.)	0. (53.)

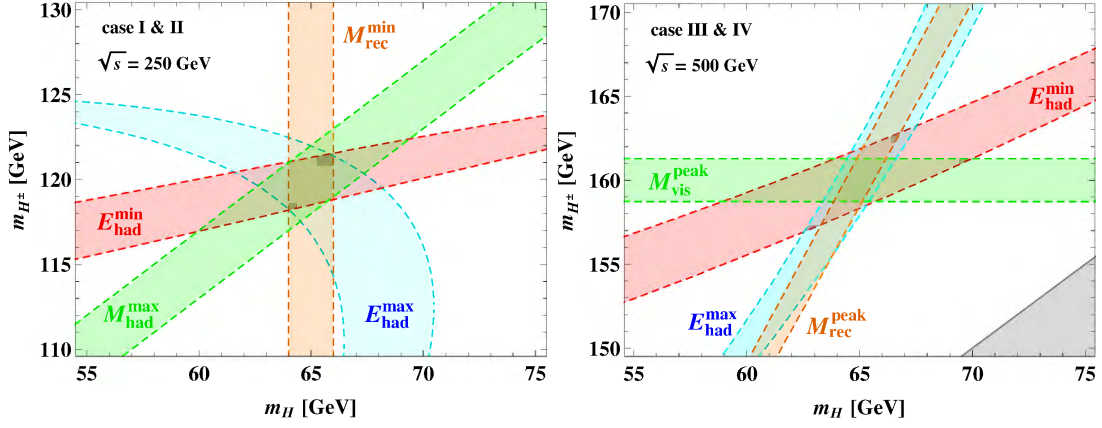


Figure 1.14. Determinations of m_{H^\pm} and m_H by the four observables are illustrated in the left [right] panel for the cases (I, II) [(III, IV)] at $\sqrt{s} = 250$ GeV [500 GeV]. Each observable is assumed to be measured in ± 2 GeV accuracy.

In the left panel of Fig. 1.14, the expected accuracy of mass determination by the measurements of the four observables for cases (I) and (II) at $\sqrt{s} = 250$ GeV is shown [122]. The four bands are plotted in the (m_H, m_{H^\pm}) plane by assuming that these four quantities are measured in ± 2 GeV accuracy (without any systematic shifts). The accuracy of the m_{H^\pm} (m_H) determination would be ± 2 GeV (± 1 GeV). In the right panel of Fig. 1.14, the four bands are plotted in the (m_H, m_{H^\pm}) plane by assuming that the four observables are measured within the ± 2 GeV accuracy. By combining the four measurements with the uncertainty of ± 2 GeV, m_{H^\pm} and m_H can be determined in ± 1 GeV accuracy. The determination of m_A can also be achieved by combining the observables in the process $e^+e^- \rightarrow HA$. However, at $\sqrt{s} = 250$ GeV and $\sqrt{s} = 500$ GeV, since the two constraints are very similar, these masses cannot be determined at one point. In this case, one requires a fixed value of m_H in the process $e^+e^- \rightarrow H^+H^-$ as an input to determine m_A . Then, the expected accuracy of the mass determination is ± 3 GeV for the measurement of the observables in ± 2 GeV accuracy.

The scenarios discussed above provide examples of parameter regions of the inert 2HDM that cannot be detected at the LHC but can be probed in detail at the ILC.

1.3.10 The MSSM Higgs sector

In the minimal supersymmetric extension of the Standard Model (MSSM) [see Ref. [123] for a review and references], all Standard Model particles are accompanied by an associated supersymmetric partner whose spin differs by half a unit. However, adding a doublet hypercharge-one higgsino superpartner would yield a gauge anomaly, rendering the theory mathematically inconsistent. In the MSSM, this problem is overcome by considering the supersymmetric extension of a two-Higgs doublet model, where the two Higgs doublets possess hypercharges ± 1 , respectively. As a result, the corresponding two higgsino superpartners of opposite hypercharge form a vector representation of spin-1/2 fermions, and the gauge anomalies resulting from the higgsinos cancel exactly.

The Higgs sector of the MSSM is a 2HDM, whose Yukawa couplings and scalar potential are constrained by supersymmetry (SUSY). Instead of employing to hypercharge-one scalar doublets $\Phi_{1,2}$, it is more convenient to introduce a $Y = -1$ doublet $H_d \equiv i\sigma_2 \Phi_1^*$ and a $Y = +1$ doublet $H_u \equiv \Phi_2$:

$$H_d = \begin{pmatrix} H_d^1 \\ H_d^2 \end{pmatrix} = \begin{pmatrix} \Phi_1^{0*} \\ -\Phi_1^- \end{pmatrix}, \quad H_u = \begin{pmatrix} H_u^1 \\ H_u^2 \end{pmatrix} = \begin{pmatrix} \Phi_2^+ \\ \Phi_2^0 \end{pmatrix}. \quad (1.94)$$

The notation $H_{u,d}$ is motivated by the form of Higgs Yukawa Lagrangian,

$$\mathcal{L}_{\text{Yukawa}} = -h_u^{ij}(\bar{u}_R^i u_L^j H_u^2 - \bar{u}_R^i d_L^j H_u^1) - h_d^{ij}(\bar{d}_R^i d_L^j H_d^1 - \bar{d}_R^i u_L^j H_d^2) + \text{h.c.}, \quad (1.95)$$

which arises as a consequence of supersymmetry. That is, the neutral Higgs field H_u^2 couples exclusively to up-type quarks and the neutral Higgs field H_d^1 couples exclusively to down-type quarks.

In particular, the so-called *wrong Higgs interactions* [124],

$$\mathcal{L}_{\text{wrong Higgs}} = -h_u'^{ij} (\bar{u}_R^i u_L^j H_d^{1*} + \bar{u}_R^i d_L^j H_d^{2*}) - h_d'^{ij} (\bar{d}_R^i d_L^j H_u^{2*} + \bar{d}_R^i u_L^j H_u^{1*}) + \text{h.c.}, \quad (1.96)$$

are not supersymmetric (due to the appearance of the complex-conjugated scalar fields in the terms exhibited explicitly above). Thus, the MSSM Higgs sector possesses Type-II Yukawa couplings as a consequence of supersymmetry (and not a \mathbb{Z}_2 discrete symmetry as discussed in Section 1.3.7.)

The Higgs potential of the MSSM is:

$$V = (m_d^2 + |\mu|^2) H_d^{i*} H_d^i + (m_u^2 + |\mu|^2) H_u^{i*} H_u^i - b (\epsilon^{ij} H_d^i H_u^j + \text{h.c.}) + \frac{1}{8} (g^2 + g'^2) [H_d^{i*} H_d^i - H_u^{j*} H_u^j]^2 + \frac{1}{2} g^2 |H_d^{i*} H_u^i|^2, \quad (1.97)$$

where $\epsilon^{12} = -\epsilon^{21} = 1$ and $\epsilon^{11} = \epsilon^{22} = 0$, and the sum over repeated indices is implicit. In eq. (1.97), μ is a supersymmetric Higgsino mass parameter and m_d^2 , m_u^2 , b are soft-supersymmetry-breaking squared-mass parameters. The quartic Higgs couplings are related to the SU(2) and U(1)_Y gauge couplings as a consequence of SUSY.

After minimizing the Higgs potential, the neutral components of the Higgs fields (in an appropriately chosen phase convention) acquire real positive vevs: $\langle H_d^0 \rangle = v_d$ and $\langle H_u^0 \rangle = v_u$, where $v^2 \equiv v_d^2 + v_u^2 = 2m_W^2/g^2 = (174 \text{ GeV})^2$. The ratio of the two vevs is

$$\tan \beta \equiv \frac{v_u}{v_d}, \quad 0 \leq \beta \leq \frac{1}{2}\pi. \quad (1.98)$$

In the Higgs basis, the phase of H_2 can be chosen such that Z_5 , Z_6 and Z_7 are real. In particular,

$$\begin{aligned} Z_1 = Z_2 &= \frac{1}{4}(g^2 + g'^2) \cos^2 2\beta, & Z_3 &= Z_5 + \frac{1}{4}(g^2 - g'^2), & Z_4 &= Z_5 - \frac{1}{2}g^2, \\ Z_5 &= \frac{1}{4}(g^2 + g'^2) \sin^2 2\beta, & Z_7 &= -Z_6 = \frac{1}{4}(g^2 + g'^2) \sin 2\beta \cos 2\beta, \end{aligned} \quad (1.99)$$

in the notation of Section 1.3.1. The existence of a Higgs basis where Z_5 , Z_6 and Z_7 are simultaneously real implies that the tree-level MSSM Higgs sector is CP-conserving. Thus the neutral Higgs mass-eigenstates are states of definite CP.

The five physical Higgs particles consist of a charged Higgs pair

$$H^\pm = H_d^\pm \sin \beta + H_u^\pm \cos \beta, \quad (1.100)$$

with squared mass given by $m_{H^\pm}^2 = m_A^2 + m_W^2$, one CP-odd scalar

$$A^0 = \sqrt{2} (\text{Im } H_d^0 \sin \beta + \text{Im } H_u^0 \cos \beta), \quad (1.101)$$

with squared mass given by $m_A^2 = 2b/\sin 2\beta$, and two CP-even scalars

$$\begin{aligned} h^0 &= \sqrt{2} [-(\text{Re } H_d^0 - v_d) \sin \alpha + (\text{Re } H_u^0 - v_u) \cos \alpha], \\ H^0 &= \sqrt{2} [(\text{Re } H_d^0 - v_d) \cos \alpha + (\text{Re } H_u^0 - v_u) \sin \alpha], \end{aligned}$$

where we have now labeled the Higgs fields according to their electric charge. The angle α arises when the CP-even Higgs squared-mass matrix (in the H_d^0 — H_u^0 basis) is diagonalized to obtain the physical CP-even Higgs states. Equivalently, one can perform the diagonalization of the CP-even Higgs squared-mass matrix in the Higgs basis, in which case the corresponding diagonalization angle

is given by $\alpha - \beta$. All Higgs masses and couplings can be expressed in terms of two parameters usually chosen to be m_A and $\tan \beta$.

The CP-even Higgs bosons h and H are eigenstates of the squared-mass matrix, which in the Higgs basis is given by

$$\mathcal{M}_e^2 = \begin{pmatrix} m_Z^2 \cos^2 2\beta & -m_Z^2 \sin 2\beta \cos 2\beta \\ -m_Z^2 \sin 2\beta \cos 2\beta & m_A^2 + m_Z^2 \sin^2 2\beta \end{pmatrix}. \quad (1.102)$$

The eigenvalues of \mathcal{M}_e^2 are the squared-masses of the two CP-even Higgs scalars

$$m_{H,h}^2 = \frac{1}{2} \left(m_A^2 + m_Z^2 \pm \sqrt{(m_A^2 + m_Z^2)^2 - 4m_Z^2 m_A^2 \cos^2 2\beta} \right), \quad (1.103)$$

and α is given by

$$\cos 2\alpha = -\cos 2\beta \frac{m_A^2 - m_Z^2}{m_H^2 - m_h^2}, \quad \sin 2\alpha = -\sin 2\beta \frac{m_A^2 + m_Z^2}{m_H^2 - m_h^2}. \quad (1.104)$$

Conventionally, one takes $0 \leq \beta \leq \frac{1}{2}\pi$ and $-\frac{1}{2}\pi \leq \alpha \leq 0$. It follows that [cf. eqs. (1.60) and (1.61)]:

$$\cos^2(\beta - \alpha) = \frac{m_Z^2 \cos^2 2\beta - m_h^2}{m_H^2 - m_h^2}, \quad (1.105)$$

$$\cos(\beta - \alpha) \sin(\beta - \alpha) = \frac{m_Z^2 \sin 2\beta \cos 2\beta}{m_H^2 - m_h^2}. \quad (1.106)$$

Note that $0 \leq \beta - \alpha < \pi$ so that $0 \leq \sin(\beta - \alpha) \leq 1$ and the sign of $\cos(\beta - \alpha)$ is given by the sign of $\sin 4\beta$.

The tree-level mass of the lightest CP-even Higgs boson of the MSSM is bounded,

$$m_h \leq m_Z |\cos 2\beta| \leq m_Z. \quad (1.107)$$

This inequality arises because all Higgs self-coupling parameters of the MSSM are related to the squares of the electroweak gauge couplings. However, radiative corrections can boost the upper bound of the lightest CP-even Higgs mass above its tree level bound of m_Z . The leading effects of the radiative corrections will be discussed further below.

The tree-level couplings of the MSSM Higgs bosons are those of a CP-conserving 2HDM with Type-II Higgs–fermion Yukawa couplings. For example, the Higgs couplings to gauge boson pairs ($V = W$ or Z) are given by

$$g_{hVV} = g_V m_V s_{\beta-\alpha}, \quad g_{HVV} = g_V m_V c_{\beta-\alpha}, \quad (1.108)$$

where $g_V \equiv \sqrt{2}m_V/v$. There are no tree-level couplings of A or H^\pm to VV . The couplings of V to two neutral Higgs bosons (which must have opposite CP-quantum numbers) are denoted by $g_{\phi AZ}(p_\phi - p_A)$, where $\phi = h$ or H and the momenta p_ϕ and p_A point into the vertex, and

$$g_{hAZ} = \frac{g c_{\beta-\alpha}}{2 \cos \theta_W}, \quad g_{HAZ} = -\frac{g s_{\beta-\alpha}}{2 \cos \theta_W}. \quad (1.109)$$

The properties of the three-point and four-point Higgs boson–vector boson couplings are conveniently summarized in eq. (1.62) by listing the couplings that are proportional to either $\sin(\beta - \alpha)$ or $\cos(\beta - \alpha)$ or are angle-independent. Finally, the couplings of the MSSM Higgs bosons to quarks are given in eqs. (1.77) and (1.79) [with the corresponding coupling to leptons obtained by the substitutions

specified below eq. (1.79)].

The decoupling behavior of the MSSM Higgs sector is exhibited in the limit of $m_A \gg m_Z$, where the corresponding tree-level squared-masses of the Higgs bosons are given by:

$$\begin{aligned} m_h^2 &\simeq m_Z^2 \cos^2 2\beta, \\ m_H^2 &\simeq m_A^2 + m_Z^2 \sin^2 2\beta, \\ m_{H^\pm}^2 &= m_A^2 + m_W^2. \end{aligned} \quad (1.110)$$

Since $\sin(\beta - \alpha) \simeq 1$ and $m_H \simeq m_A$ in the decoupling limit, eq. (1.106) yields

$$\cos(\beta - \alpha) = \frac{m_Z^2 \sin 4\beta}{2m_A^2} + \mathcal{O}\left(\frac{m_Z^4}{m_A^4}\right). \quad (1.111)$$

Note that eq. (1.111) follows from the corresponding 2HDM result given by eq. (1.68) when Z_6 is given by its supersymmetric value [cf. eq. (1.99)].

As expected, in the decoupling limit $m_A \simeq m_H \simeq m_{H^\pm}$, up to corrections of $\mathcal{O}(m_Z^2/m_A)$, and $\cos(\beta - \alpha) = 0$ up to corrections of $\mathcal{O}(m_Z^2/m_A^2)$. In general, in the limit of $\cos(\beta - \alpha) \rightarrow 0$, all the h^0 couplings to SM particles approach their SM limits. In particular, if λ_V is a Higgs coupling to vector bosons and λ_t [λ_b] are Higgs couplings to up-type [down-type] fermions, then

$$\frac{\lambda_V}{[\lambda_V]_{\text{SM}}} = \sin(\beta - \alpha) = 1 + \mathcal{O}\left(\frac{m_Z^4}{m_A^4}\right), \quad (1.112)$$

$$\frac{\lambda_t}{[\lambda_t]_{\text{SM}}} = 1 + \mathcal{O}\left(\frac{m_Z^2 \cos^2 \beta \cos 2\beta}{m_A^2}\right). \quad (1.113)$$

$$\frac{\lambda_b}{[\lambda_b]_{\text{SM}}} = 1 + \mathcal{O}\left(\frac{m_Z^2 \sin^2 \beta \cos 2\beta}{m_A^2}\right). \quad (1.114)$$

Note that the approach to decoupling is fastest in the case of the hVV couplings and slowest in the case of the hbb couplings at large $\tan \beta$ (where the corresponding trigonometric factor in eq. (1.114) is maximal). This implies that at large $\tan \beta$, a precision measurement of the $h^0 b\bar{b}$ coupling provides the greatest sensitivity to m_A [125].

When radiative corrections are incorporated, additional parameters of the supersymmetric model enter via virtual loops. The impact of these corrections can be significant [126, 127, 128]. For example, the tree-level prediction for the upper bound of the lightest CP -even Higgs mass, given by eq. (1.107)[129, 130, 131], can be substantially modified when radiative corrections are included. The qualitative behavior of these radiative corrections can be most easily seen in the large top squark mass limit. Denoting the geometric mean of the two top squark squared masses by $M_S^2 \equiv M_{\tilde{t}_1}^2 M_{\tilde{t}_2}^2$ and assuming that $m_A > m_Z$ and that the top squark mass splitting is small compared to M_S , the predicted upper bound for m_h (which reaches its maximum at large $\tan \beta$ and $m_A \gg m_Z$) is approximately given by

$$m_h^2 \lesssim m_Z^2 \cos^2 2\beta + \frac{3g^2 m_t^4}{8\pi^2 m_W^2} \left[\ln\left(\frac{M_S^2}{m_t^2}\right) + \frac{X_t^2}{M_S^2} \left(1 - \frac{X_t^2}{12M_S^2}\right) \right], \quad (1.115)$$

where $X_t \equiv A_t - \mu \cot \beta$ is the top squark mixing factor.

A more complete treatment of the radiative corrections [132, 133, 134] shows that eq. (1.115) somewhat overestimates the true upper bound of m_h . These more refined computations, which incorporate renormalization group improvement and the leading two-loop (and even some three-loop) contributions, yield $m_h \lesssim 130$ GeV (with an accuracy of a few GeV) for $m_t = 173$ GeV and $M_S \lesssim 2$ TeV. The observed Higgs mass of 126 GeV is consistent with this bound.

Radiative corrections also can have an important impact on the MSSM Higgs couplings. Although radiatively-corrections to couplings generically tend to be at the few-percent level, there is some potential for significant effects. In certain cases, radiative corrections are enhanced for values of $\tan\beta \gg 1$. In addition, CP-violating effects induced by complex SUSY-breaking parameters that enter in loops, can yield new effects in the Higgs sector not present at tree-level.

One leading correction of note is the renormalization of the mixing angle α . This modifies the quantity $\cos(\beta - \alpha)$ which governs the decoupling limit and plays a critical role in the couplings of the Higgs bosons. Employing the same approximations used in obtaining eq. (1.115), one finds that eq. (1.105) is modified by replacing the tree-level bound, $m_Z^2 \cos^2 \beta$, with the radiatively-corrected bound given in eq. (1.115), and replacing m_h and m_H with the corresponding loop-corrected masses.

However, this approximation can still miss some important loop contributions that can drastically alter the tree-level results. Let M_{SUSY} characterize the mass scale of SUSY-breaking (or equivalently, the masses of the superpartners that appear in the loops that contribute to the radiative corrections). If $M_{\text{SUSY}} \gg m_A$, then one can integrate out the superpartners that appear in the loops and obtain an effective low-energy theory that is equivalent to the most general 2HDM. In this effective 2HDM, the supersymmetric value of Z_6 given in eq. (1.99) is modified by radiative corrections. In certain special regions of the MSSM parameter space, the radiative corrections are $\tan\beta$ -enhanced and can approximately cancel out the tree-level value for a particular (large) value of $\tan\beta$, leaving $Z_6 \simeq 0$. This is the alignment limit (which is not possible in the MSSM Higgs sector at tree-level) and yields $\cos(\beta - \alpha) \simeq 0$ in light of eq. (1.68). In this case, the lightest CP-even Higgs boson is very SM-like, whereas the other Higgs bosons of the model need not be significantly heavier.

Moreover, the supersymmetric Yukawa couplings given in eq. (1.95) are modified by the radiative corrections, $h_q \rightarrow h_q + \delta h_q$ ($q = u, d$). In particular, since the effective 2HDM below the SUSY-breaking scale does not respect supersymmetry, the wrong-Higgs Yukawa interactions given in eq. (1.96) are also generated by the radiative corrections; the corresponding Yukawa couplings will be denoted by $h'_q \equiv \Delta h_q$. Of particular interest are the wrong Higgs Yukawa couplings to bottom quarks,

$$\Delta h_b \simeq h_b \left[\frac{2\alpha_s}{3\pi} \mu M_3 \mathcal{I}(M_{\tilde{b}_1}, M_{\tilde{b}_2}, M_g) + \frac{h_t^2}{16\pi^2} \mu A_t \mathcal{I}(M_{\tilde{t}_1}, M_{\tilde{t}_2}, \mu) \right],$$

where, M_3 is the Majorana gluino mass, μ is the supersymmetric Higgs-mass parameter, and $\tilde{b}_{1,2}$ and $\tilde{t}_{1,2}$ are the mass-eigenstate bottom squarks and top squarks, respectively. The loop integral is given by

$$\mathcal{I}(a, b, c) = \frac{a^2 b^2 \ln(a^2/b^2) + b^2 c^2 \ln(b^2/c^2) + c^2 a^2 \ln(c^2/a^2)}{(a^2 - b^2)(b^2 - c^2)(a^2 - c^2)}. \quad (1.116)$$

In the limit where at least one of the arguments of $\mathcal{I}(a, b, c)$ is large,

$$\mathcal{I}(a, b, c) \sim 1/\max(a^2, b^2, c^2). \quad (1.117)$$

Thus, in the limit where $M_3 \sim \mu \sim A_t \sim M_{\tilde{b}} \sim M_{\tilde{t}} \sim M_{\text{SUSY}} \gg m_Z$, the one-loop contributions to Δh_b do *not* decouple.

The wrong-Higgs couplings yield $\tan\beta$ -enhanced modifications of some physical observables. After expressing the Higgs doublet fields H_d and H_u in terms of the physical Higgs mass-eigenstates, one can identify the the b -quark mass,

$$m_b = h_b v \cos\beta \left(1 + \frac{\delta h_b}{h_b} + \frac{\Delta h_b \tan\beta}{h_b} \right) \equiv h_b v \cos\beta (1 + \Delta_b), \quad (1.118)$$

which defines the quantity Δ_b . In the limit of large $\tan\beta$ the term proportional to δh_b can be

neglected, in which case,

$$\Delta_b \simeq \frac{\Delta h_b}{h_b} \tan \beta. \quad (1.119)$$

Thus, Δ_b is $\tan \beta$ -enhanced if $\tan \beta \gg 1$. As previously noted, Δ_b survives in the limit of large M_{SUSY} ; this effect does not decouple.

From the effective Yukawa Lagrangian, one can obtain the couplings of the physical Higgs bosons to third generation fermions. For example, the one-loop corrections can generate measurable shifts in the decay rate for $h^0 \rightarrow b\bar{b}$,

$$g_{h^0 b\bar{b}} = -\frac{gm_b}{2m_W} \frac{\sin \alpha}{\cos \beta} \left[1 + \frac{1}{1 + \Delta_b} \left(\frac{\delta h_b}{h_b} - \Delta_b \right) (1 + \cot \alpha \cot \beta) \right]. \quad (1.120)$$

At large $\tan \beta \sim 20\text{--}50$, Δ_b can be as large as 0.5 in magnitude and of either sign, leading to a significant enhancement or suppression of the Higgs decay rate to $b\bar{b}$.

If $m_A \sim \mathcal{O}(M_{\text{SUSY}})$, then below the scale of supersymmetry-breaking one must also integrate out the second Higgs doublet (in the Higgs basis). In this case, the low-energy effective Higgs theory is a one-Higgs doublet model, and thus $g_{h^0 b\bar{b}}$ must approach its SM value. Indeed in this limit,

$$1 + \cot \alpha \cot \beta = -\frac{2m_Z^2}{m_A^2} \cos 2\beta + \mathcal{O}\left(\frac{m_Z^4}{m_A^4}\right).$$

Thus the previously non-decoupling SUSY radiative corrections decouple for $m_A \gg m_Z$ as expected.

The one-loop corrected effective Higgs-fermion Lagrangian can exhibit CP-violating effect due to possible CP-violating phases in μ , A_t and M_3 . This leads to mixed-CP neutral Higgs states and CP-violating couplings. This is the so-called CPX scenario of the MSSM. In the limit of $m_{H^\pm} \ll M_{\text{SUSY}}$, the effective low-energy theory is the most general CP-violating 2HDM. Thus, the model-independent treatment of the general 2HDM is applicable. Further details on the CPX scenario can be found in Refs. [135, 136, 137, 138].

1.4 Other extended Higgs sectors

1.4.1 Constraints from the tree-level rho parameter

Apart from the part of the SM that is governed by the gauge principle, there is no theoretical principle for fixing the number of Higgs scalars. Indeed, there are a variety of possibilities for non-minimal Higgs sectors that are consistent with phenomenological requirements. We have already treated in detail the two-Higgs doublet extension of the SM in Section 1.3. However, it is also possible that the Higgs sector contains additional Higgs doublets and/or one or more non-doublet representations.

A very strong constraint on exotic Higgs sectors derives from the electroweak rho parameter whose experimental value is very close to unity. The current value for the rho parameter is given by $\rho = 1.0008^{+0.0017}_{-0.0007}$ [29]. In the SM, the rho parameter is exactly unity at the tree level,

$$\rho = \frac{m_W^2}{m_Z^2 \cos^2 \theta} = 1. \quad (1.121)$$

Moreover, including radiative corrections, the SM with the Higgs boson mass of 126 GeV yields a value of ρ that is consistent with the experimentally measure value [30]. Models with only Higgs doublets and singlets do not spoil the tree-level prediction of $\rho = 1$. However, the addition of scalars that transform under higher dimensional representations generally violate the tree-level prediction of $\rho = 1$.

In a general $SU(2) \times U(1)$ model with n scalar multiplets ϕ_i with isospin T_i and hypercharge Y_i , the rho parameter is given at the tree level by [31]

$$\rho = 1 + \frac{\sum_i [4T_i(T_i + 1) - 3Y_i^2] |v_i|^2 c_i}{\sum_i 2Y_i^2 |v_i|^2}, \quad (1.122)$$

where

$$c_i = \begin{cases} 1, & (T, Y) \in \text{complex representation,} \\ \frac{1}{2}, & (T, Y = 0) \in \text{real representation.} \end{cases} \quad (1.123)$$

For a Higgs sector composed of complex ($c = 1$) hypercharge-1 Higgs doublets ($T = 1/2$ and $Y = 1$), it follows that $\rho = 1$, independently of the value of the vacuum expectation value v . One can also add an arbitrary number of Higgs singlets ($T = Y = 0$) without changing the value of ρ . To automatically have $\rho = 1$ independently of the Higgs vevs, one must satisfy the Diophantine equation [139],

$$(2T + 1)^2 - 3Y^2 = 1, \quad (1.124)$$

for non-negative integer values of $(2T, Y)$. The smallest nontrivial solution beyond the complex $Y = 1$ Higgs doublet is a complex Higgs septet with $T = 3$ and $Y = 4$.

For extended Higgs sectors with multiplets that do not satisfy eq. (1.124), the tree-level value for ρ will generally differ from 1. In order to be consistent with the rho parameter data, there are two possible strategies. First, one can fine-tune the values of the vevs v_i such that $\rho = 1$. This may require some vevs to be significantly smaller than 174 GeV, or it may require an unnatural cancellation of terms in the numerator of the second term in eq. (1.122). As an example of the first strategy, consider the effect of adding to the Standard Model an extra hypercharge-two complex scalar triplet field $\phi_2 = \Delta$ ($T_2 = 1, Y_2 = 2$), which has been employed for generating the neutrino mass by the so-called type-II seesaw mechanism [37]. Denoting the vev of the neutral component of the scalar triplet by v_Δ , eq. (1.122) yields

$$\rho = \frac{1 + 2v_\Delta^2/v^2}{1 + 4v_\Delta^2/v^2}. \quad (1.125)$$

Therefore, there is a strong upper bound for v_Δ (\lesssim a few GeV) in light of the rho parameter data.

Second, one can make a clever choice of Higgs multiplets such that the required cancellation of terms in the numerator of the second term in eq. (1.122) appears to be natural. The simplest example of this mechanism is the Georgi-Machacek model [140], which consists of the SM hypercharge-one complex scalar doublet $\Phi(T = \frac{1}{2}, Y = 1)$, a complex hypercharge-two scalar triplet $\Delta(T = 1, Y = 2)$ and a real scalar triplet $\xi(T = 1, Y = 0)$. Suppose that the vevs of the neutral fields of the two scalar triplets are equal, $v_\Delta = v_\xi$, which can be arranged with a special choice of the scalar potential parameters corresponding to an enhanced $SU(2)_L \times SU(2)_R$ global symmetry. In this case, it is easy to check that eq. (1.122) yields $\rho = 1$ independently of the value of the vev of the scalar doublet, v_Φ , and the common value of the triplet vevs, $v_\Delta = v_\xi$. Indeed $v_\Delta/v_\Phi \sim 1$ is phenomenologically viable, which would lead to a very different phenomenology than the simple doublet plus triplet model considered above. However, since the enhanced $SU(2)_L \times SU(2)_R$ global symmetry of the scalar potential is not respected by the hypercharge gauge interactions and the Yukawa interactions, the condition that $v_\Delta = v_\xi$ is not stable under radiative corrections and therefore must be considered as a tuning of parameters [141].

1.4.2 An upper bound for the Higgs coupling to vector boson pairs

Consider a CP-conserving extended Higgs sector that has the property that $\rho = 1$ and no tree-level $ZW^\pm\phi^\mp$ couplings (where ϕ^\pm are physical charged scalars that might appear in the scalar spectrum). Then it follows that [28]

$$\sum_i g_{\phi_i VV}^2 = g^2 m_W^2 = g_{h_{SM} VV}^2, \quad m_W^2 g_{\phi_i ZZ} = m_Z^2 g_{\phi_i WW}, \quad (1.126)$$

where the sum is taken over all neutral CP-even scalars ϕ_i and h_{SM} is the Higgs boson of the SM. In this case, it follows that $g_{\phi_i VV} \leq g_{h_{SM} VV}$ for all i . Models that contain only scalar singlets and doublets satisfy the requirements stated above and hence respect the sum rule and the coupling relation given above. However, it is possible to violate $g_{\phi_i VV} \leq g_{h_{SM} VV}$ and $m_W^2 g_{\phi_i ZZ} = m_Z^2 g_{\phi_i WW}$ if tree-level $ZW^\pm\phi^\mp$ and/or $\phi^{++}W^-W^-$ couplings are present [28, 142, 143]. A more general sum rule is:

$$\sum_i g_{\phi_i VV}^2 = g^2 m_W^2 + \sum_k |g_{\phi_k^{++}W^-W^-}|^2. \quad (1.127)$$

The Georgi-Machacek model provides an instructive example [140, 144, 145]. This model consists of a complex Higgs doublet with $Y = 1$, a complex Higgs triplet with $Y = 2$ and a real Higgs triplet with $Y = 0$, with doublet vev v_Φ and triplet vevs $v_\Delta = v_\xi$, such that $v^2 = v_\Phi^2 + 8v_\Delta^2$.

It is convenient to write [145]

$$c_H \equiv \cos \theta_H = \frac{v_\Phi}{\sqrt{v_\Phi^2 + 8v_\Delta^2}},$$

and $s_H \equiv \sin \theta_H = (1 - c_H^2)^{1/2}$. Then, the following couplings are noteworthy:

$$\begin{aligned} H_1^0 W^+ W^- : & \quad g c_H m_W, & H_1'^0 W^+ W^- : & \quad \sqrt{8/3} g m_W s_H, \\ H_5^0 W^+ W^- : & \quad \sqrt{1/3} g m_W s_H, & H_5^{++} W^- W^- : & \quad \sqrt{2} g m_W s_H. \end{aligned}$$

$H_1'^0$ and H_5^0, H_5^{++} have no coupling to fermions, whereas the H_1^0 coupling to fermions is given by

$$H_1^0 f \bar{f} : \quad \frac{g m_f}{2 m_W c_H}.$$

Table 1.12. The deviations in the Higgs boson couplings from the SM values in various extended Higgs sectors. ϕ , Δ , ξ and φ_7 are respectively denoted as Higgs fields with $(T, Y)=(1/2, 1)$, $(1, 2)$, $(1, 0)$ and $(3, 4)$. In the second and third column, v_X is the vev of the Higgs field X . The mixing angle α is defined for each extended Higgs sector in Ref. [143].

Model	$\tan \beta$	$\tan \beta'$	c_{hWW}	c_{hZZ}
$\phi_1 + \phi_2$ (2HDM)	v_{ϕ_2}/v_{ϕ_1}	v_{ϕ_2}/v_{ϕ_1}	$\sin(\beta - \alpha)$	$\sin(\beta - \alpha)$
$\phi + \Delta$ (cHTM)	$\sqrt{2}v_{\Delta}/v_{\phi}$	$2v_{\Delta}/v_{\phi}$	$\cos \beta \cos \alpha + \sqrt{2} \sin \beta \sin \alpha$	$\cos \beta' \cos \alpha + 2 \sin \beta' \sin \alpha$
$\phi + \xi$ (rHTM)	$2v_{\xi}/v_{\phi}$	-	$\cos \beta \cos \alpha + 2 \sin \beta \sin \alpha$	$\cos \alpha$
$\phi + \Delta + \xi$ (GM model)	$2\sqrt{2}v_{\Delta}/v_{\phi}$	$2\sqrt{2}v_{\Delta}/v_{\phi}$	$\cos \beta \cos \alpha + \frac{2\sqrt{6}}{3} \sin \beta \sin \alpha$	$\cos \beta \cos \alpha + \frac{2\sqrt{6}}{3} \sin \beta \sin \alpha$
$\phi + \varphi_7$	$4v_{\varphi_7}/v_{\phi}$	$4v_{\varphi_7}/v_{\phi}$	$\cos \beta \cos \alpha + 4 \sin \beta \sin \alpha$	$\cos \beta \cos \alpha + 4 \sin \beta \sin \alpha$

In general H_1^0 and $H_1'^0$ can mix.

In the absence of H_1^0 – $H_1'^0$ mixing and $c_H = 1$, we see that the couplings of H_1^0 match those of the SM. In contrast, in the case of $s_H = \sqrt{3/8}$, the $H_1'^0$ coupling to W^+W^- matches that of the SM. Nevertheless, this does not saturate the $\Phi_i WW$ sum rule! Moreover, it is possible that the $H_1'^0 W^+W^-$ coupling is *larger* than gm_W , without violating the $\Phi_i WW$ sum rule. Including H_1^0 – $H_1'^0$ mixing allows for even more baroque possibilities not possible in a multi-doublet extension of the SM. Deviations above the $h_{\text{SM}} VV$ coupling by as much as 10% or more are possible. Thus we have demonstrated the possibility that

$$g_{\phi VV}^2 > g_{h_{\text{SM}} VV}^2, \quad (1.128)$$

in Higgs sectors with exotic (larger than doublet) Higgs representations.

In Table 1.12, the deviations in the Higgs boson couplings from the SM values are listed in various extended Higgs sectors (further details are given in Ref. ([143])). Moreover, except for the case of the 2HDM, the couplings of the SM like Higgs boson with the weak gauge bosons shown in Table 1.12 can be greater than 1. At the ILC the hVV couplings can be measured at the percent level. Therefore, even if extra Higgs bosons are not discovered directly, a Higgs sector with exotic multiplets can be distinguished via the precision measurement of the hVV coupling.

1.4.3 Adding Higgs singlets

The introduction of an additional Higgs singlet field to the SM Higgs sector does not affect $\rho = 1$, and does not generate any flavor changing Higgs-mediated neutral current processes as it does not couple to quarks, leptons and gauge bosons. For example, such a singlet field has been introduced in new physics models with an extra U(1) gauge symmetry, where the U(1) boson couples to B–L [146]. A neutral singlet scalar field is also employed in the Next-to-Minimal supersymmetric extension of the Standard Model (NMSSM) along with the second doublet field required in SUSY [147].

The existence of a singlet field $\phi_2 = S$ ($T_2 = 0$, $Y_2 = 2$) only change the Higgs boson couplings via mixing of the singlet and doublet Higgs fields. In the model with only one additional neutral singlet scalar field to the SM, S and Φ can be parameterized as

$$\Phi = \begin{pmatrix} \omega^+ \\ v + (\phi + i\chi)/\sqrt{2} \end{pmatrix}, \quad S = v_S + \phi_S \quad (1.129)$$

where $v = 174$ GeV, and v_S is the vev of S . The two CP-even mass eigenstates h and H are defined by

$$h = \phi \cos \theta - \phi_S \sin \theta, \quad H = \phi \sin \theta + \phi_S \cos \theta. \quad (1.130)$$

In models with an extra U(1) gauge boson, this boson absorbs the CP-odd component χ_S via the Higgs mechanism. The difference from the SM is just one additional CP-even scalar boson H . There is no physical charged scalar state in this model. All of the SM fields obtain mass from the vev, v , while the couplings of h and H are obtained by the replacement of $\phi_{\text{SM}} \rightarrow h \cos \theta + H \sin \theta$ in the Standard Model Lagrangian.

In the decoupling region $\theta \sim 0$, h is the SM-like Higgs boson with its couplings reduced from their SM values by $\cos \theta \sim 1 - \theta^2/2$. On the other hand, when $\tan \theta \sim \mathcal{O}(1)$, both h and H behave as SM-like Higgs bosons, sharing the SM couplings to gauge bosons and fermions. If h and H are almost degenerate in mass, the two bosons might appear as a single SM Higgs boson in the LHC experiments. At the ILC, by tagging the Higgs mass in $e^+e^- \rightarrow Z + (h, H)$ by the invariant mass recoiling against the Z , the two Higgs bosons could be better separated. The ILC phenomenology of the Higgs sector in the minimal B-L model is surveyed in Ref. [148].

1.4.4 Adding Higgs triplets

Triplet Higgs fields are introduced in several new physics models. An example of these models is the Higgs sector with the SM Higgs doublet Φ with an additional triplet Δ with $T_2 = 1, Y_2 = 2$. If Δ carries the lepton number of 2, it can couple to leptons by

$$\mathcal{L}_Y = h_{ij} \bar{L}^{ic} i\tau_2 \Delta L_L^j + \text{h.c.} \quad (1.131)$$

If Δ obtains the vev that is proportional to the explicit violation term for the lepton number in the Higgs sector, then a neutrino mass matrix is generated,

$$\mathcal{M}_{ij} = \sqrt{2} h_{ij} v_\Delta. \quad (1.132)$$

The Higgs fields Φ and Δ are expressed in terms of component fields as

$$\Phi = \begin{pmatrix} \omega^+ \\ v_\Phi + (\phi + i\chi)/\sqrt{2} \end{pmatrix}, \quad \Delta = \begin{pmatrix} \Delta^+/\sqrt{2} & \Delta^{++} \\ v_\Delta + (\delta + i\eta)/\sqrt{2} & -\Delta^+/\sqrt{2} \end{pmatrix}, \quad (1.133)$$

where v_Φ and v_Δ are vevs of Φ and Δ . The physical scalar states are two CP-even (h and H), a CP-odd (A), a singly charged pair (H^\pm) and a doubly charged pair ($H^{\pm\pm}$), which are derived from the component fields by diagonalizing the squared-mass matrices with the mixing angles α , β_0 and β_\pm as

$$\begin{aligned} h &= \phi \cos \alpha + \delta \sin \alpha, & H &= -\phi \sin \alpha + \delta \cos \alpha, \\ A &= -\chi \sin \beta_0 + \eta \cos \beta_0, & H^\pm &= -\phi^\pm \sin \beta_\pm + \Delta^\pm \cos \beta_\pm, & H^{++} &= \Delta^{++}. \end{aligned} \quad (1.134)$$

In light of the constraint from the rho parameter, $v_\Delta \ll v$ must be taken, and then the masses of the scalar bosons are given by

$$m_h^2 \simeq 2\lambda_1 v^2, \quad m_{H^{++}}^2 - m_{H^+}^2 \simeq m_{H^+}^2 - m_A^2, \quad m_H^2 \simeq m_A^2, \quad (1.135)$$

with $\alpha \ll 1$, $\beta_0 \ll 1$, and $\beta_\pm \ll 1$, where λ_1 represents the quartic coupling constant of the doublet field. Therefore, h behaves as the SM Higgs boson, and the others scalar states satisfy the relations among the masses given in eq. (1.135).

The most interesting characteristic feature in this model is the existence of doubly charged Higgs bosons $H^{\pm\pm}$. Its discovery would be a direct probe of the exotic Higgs sectors. In general, doubly charged Higgs fields can arise from the singlet with $Y = 4$, the doublet with $Y = 3$ and the triplet

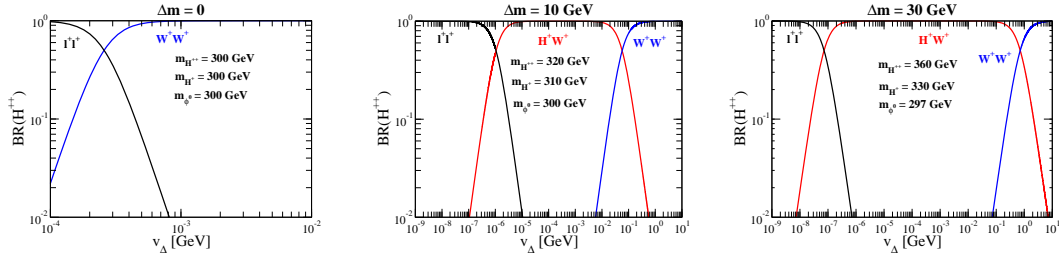


Figure 1.15. Decay branching ratio of H^{++} as a function of v_{Δ} . In the left figure, $m_{H^{++}}$ is fixed to be 300 GeV, and Δm is taken to be zero. In the middle figure, $m_{H^{++}}$ is fixed to be 320 GeV, and Δm is taken to be 10 GeV. In the right figure, $m_{H^{++}}$ is fixed to be 360 GeV, and Δm is taken to be 30 GeV.

with $Y = 2$. In the model with an additional triplet field, the doubly charged Higgs bosons $H^{\pm\pm}$ can decay into $\ell^{\pm}\ell^{\pm}$, $H^{\pm}W^{\pm}$ and $W^{\pm}W^{\pm}$ depending on the magnitude of v_{Δ} [149]. In Fig. 1.15, the branching ratios are shown as a function of the vacuum expectation value of the triplet field, v_{Δ} , for the cases with the mass difference $\Delta m = m_{H^{++}} - m_{H^+} = 0, 10$ GeV and 30 GeV [150]. When v_{Δ} is smaller than 10^{-3} GeV, the dilepton decay $H^{\pm\pm} \rightarrow \ell^{\pm}\ell^{\pm}$ is dominant. The signal directly shows the existence of the doubly charged scalar boson with lepton number 2, which can be a strong evidence for the neutrino mass generation via Eq. (1.132). At the LHC, the current search results for $H^{\pm\pm}$ using this decay mode gives the lower bound on the mass of $m_{H^{++}} > 400$ GeV [151, 152].

In contrast, when v_{Δ} is sufficiently larger than 10^{-3} GeV, the diboson decay $H^{\pm\pm} \rightarrow W^{\pm}W^{\pm}$ becomes dominant. In this case, the signal can also be same sign four leptons, but its rate is reduced by the branching ratios of leptonic decays of W s. The current lower bound from this final state is only $m_{H^{++}} > 60$ GeV at 95% CL from data at the LHC with 5 fb^{-1} [153] as exhibited in Fig. 1.16. This bound is greatly relaxed as compared to the dilepton decay scenario. By the extrapolation of the data to 20 fb^{-1} with the same collision energy, the lower limit is estimated to be 85 GeV.

If there is a mass difference between $H^{\pm\pm}$ and H^{\pm} , the parameter region where $H^{\pm\pm}$ can mainly decay into $H^{\pm}W^{\pm}$ appears. For example, for $v_{\Delta} = 1$ GeV with a mass difference $\Delta m = m_{H^{++}} - m_{H^+} \sim 10$ GeV, the decay into H^+W^+ dominates for a wide range of v_{Δ} . In this case, H^{++} could be identified through its cascade decay. If there is a mass difference with the opposite

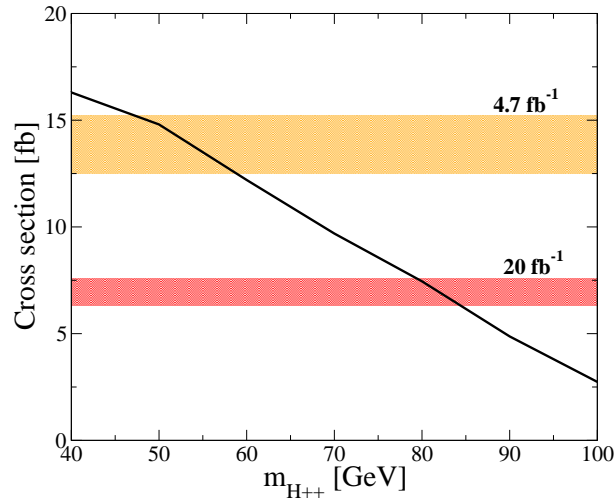


Figure 1.16. The signal cross section after the $M_{\ell\ell}$ cut as a function of $m_{H^{++}}$ with the collision energy to be 7 TeV. The light (dark) shaded band shows the 95% CL (expected) upper limit for the cross section from the data for the $\mu^+\mu^+$ channel with the integrate luminosity to be 4.7 fb^{-1} (20 fb^{-1}).

sign, $\Delta m \sim -10$ GeV for $v_\Delta \sim 1$ GeV, $H^{\pm\pm} \rightarrow W^+W^+$ is dominant.

There are wide regions of parameter space where the diboson decay is dominant. In this case, a relatively light $H^{\pm\pm}$ with a mass of few 100 GeV is expected to be still allowed even after the LHC run at 14 TeV with an integrated luminosity with 3000 fb^{-1} . The $H^{\pm\pm}$ can be pair produced at the ILC with $\sqrt{s} = 250$ GeV or 500 GeV, and a doubly-charged Higgs signal can be easily detected.

1.4.5 The NMSSM Higgs sector

The minimal Higgs sector required for an anomaly-free supersymmetric extension of the Standard Model consists of two Higgs doublets as described in Section 1.3.10. But, the Higgs sector of the MSSM has a number of troubling features. First, the Higgs-Higgsino Lagrangian contains a dimensionful parameter μ , which in principle can be arbitrarily large. However, phenomenological considerations require this parameter to be no larger than a typical supersymmetry-breaking mass parameter, which should be of $\mathcal{O}(1 \text{ TeV})$ or less in order to provide a natural explanation for the origin of the scale of electroweak symmetry breaking (EWSB). Second, the coefficients of the quartic terms of the MSSM Higgs potential are fixed by the $\text{SU}(2) \times \text{U}(1)$ gauge couplings g and g' . This is the origin of the tree-level bound $m_h \leq m_Z$, and implies that radiative corrections due to loops of top-quarks must be large enough to explain the observed mass of $m_h \simeq 126$ GeV. This in turn requires rather large top squark masses and/or mixing, which pushes at least one of the top squark masses to values above 1 TeV. Indeed, there is already considerable tension in the MSSM between achieving a large enough Higgs mass while maintaining a natural explanation of the EWSB scale.

In the NMSSM, one add an additional complex singlet scalar field S to the MSSM Higgs sector. A comprehensive review of the NMSSM can be found in Refs. [147, 154]. The additional degrees of freedom of the NMSSM Higgs sector provide an opportunity for ameliorating some of the troubling features of the MSSM Higgs sector. In the NMSSM, one can set $\mu = 0$ and generate an effective μ parameter dynamically that is proportional to the vacuum expectation value of S . Thus, a phenomenologically acceptable NMSSM Higgs sector exist that contains no new fundamental dimensionful parameters. Second, the NMSSM scalar potential contains a new quartic term proportional to a dimensionless parameter λ that is independent of gauge couplings. Thus, the mass of the observed Higgs boson now depends on an unknown coupling, and it is significantly easier to achieve the observed mass of $m_h \simeq 126$ GeV without extremely large top squark masses and/or mixing. As a result, the flexibility of the additional degrees of freedom of the NMSSM can (somewhat) reduce the tension with naturalness as compared with the MSSM.

In this section, we briefly review the structure of the Higgs sector of the NMSSM. We first consider the general NMSSM (sometimes called the GNMSSM [155]), in which all possible terms of dimension-four or less are allowed in the Higgs Lagrangian. The Higgs potential of the GNMSSM is:

$$\begin{aligned}
 V = & (m_d^2 + |\mu + \lambda S|^2) H_d^{i*} H_d^i + (m_u^2 + |\mu + \lambda S|^2) H_u^{i*} H_u^i - b(\epsilon^{ij} H_d^i H_u^j + \text{h.c.}) \\
 & + m_s^2 |S|^2 + (\xi_s S + \frac{1}{2} b_s S^2 + \frac{1}{3} \kappa A_\kappa S^3 - \lambda A_\lambda S \epsilon^{ij} H_d^i H_u^j + \text{h.c.}) \\
 & |\xi + \mu_s S + \kappa S^2 - \lambda \epsilon^{ij} H_d^i H_u^j|^2 + \frac{1}{8} (g^2 + g'^2) [H_d^{i*} H_d^i - H_u^{j*} H_u^j]^2 + \frac{1}{2} g^2 |H_d^{i*} H_u^i|^2,
 \end{aligned} \tag{1.136}$$

where μ and μ_s are the supersymmetric Higgsino mass parameters, λ and κ are dimensionless supersymmetric scalar self-interaction parameters, m_d^2 , m_u^2 , b , b_s and ξ are soft-supersymmetry-breaking squared-mass parameters, A_κ and A_λ are soft-supersymmetry-breaking mass parameters, and ξ_s is a soft-supersymmetry-breaking cubed-mass parameter.

To eliminate the supersymmetric preserving mass parameters, one can impose a discrete \mathbb{Z}_3 symmetry, such that the scalar potential is invariant under $\{H_d, H_u, S\} \rightarrow \omega \{H_d, H_u, S\}$ with $\omega^3 = 1$ and $\omega \neq 1$. In this case we have $\mu = \mu_s = b = b_s = \xi = \xi_s = 0$, and the scalar potential is

specified in terms of two supersymmetric dimensionless parameters, λ and κ , and five dimensionful supersymmetry-breaking parameters, m_d^2 , m_u^2 , m_s^2 , A_λ and A_κ . This model is often referred to simply as the NMSSM (more accurately, it is also called as the \mathbb{Z}_3 -invariant NMSSM).

Unlike the MSSM, the tree-level (G)NMSSM allows for the possibility of CP-violation in the Higgs sector. For simplicity, we shall assume in the following that the (G)NMSSM scalar potential is CP-conserving, and take all scalar potential parameters and vacuum expectation values to be real,

$$\langle H_d^0 \rangle = v_d, \quad \langle H_u^0 \rangle = v_u, \quad \langle S \rangle = v_s. \quad (1.137)$$

In this case, the scalar spectrum consists of three CP-even neutral scalars, two CP-odd neutral scalars and a pair of charged Higgs scalars H^\pm . It is again convenient to go to the Higgs basis in which linear combinations of the two doublet fields, denoted by H_1 and H_2 , are defined such that $\langle H_1^0 \rangle = v = 174 \text{ GeV}$ and $\langle H_2^0 \rangle = 0$, where $v^2 \equiv v_u^2 + v_d^2$. In this basis, the squared-mass matrix of the CP-even neutral Higgs bosons is given by

$$\mathcal{M}_e^2 = \begin{pmatrix} m_Z^2 \cos^2 2\beta + \lambda^2 v^2 \sin^2 2\beta & -(m_Z^2 - \lambda^2 v^2) \sin 2\beta \cos 2\beta & M_{e13}^2 \\ -(m_Z^2 - \lambda^2 v^2) \sin 2\beta \cos 2\beta & m_A^2 + m_Z^2 \sin^2 2\beta & M_{e23}^2 \\ M_{e13}^2 & M_{e23}^2 & M_{e33}^2 \end{pmatrix}, \quad (1.138)$$

where

$$m_A^2 \equiv \frac{2[b + \lambda(\mu_s v_s + \xi) + \lambda v_s(A_\lambda + \kappa v_s)]}{\sin 2\beta}, \quad (1.139)$$

and M_{e13}^2 , M_{e23}^2 and M_{e33}^2 can be expressed in terms of the scalar potential parameters (explicit expressions can be found in Ref. [155]). The parameter m_A^2 is no longer the squared-mass of the CP-odd Higgs boson. Rather, it is a diagonal element of the CP-odd Higgs squared-mass matrix,

$$\mathcal{M}_o^2 = \begin{pmatrix} m_A^2 & M_{o12}^2 \\ M_{o12}^2 & M_{o22}^2 \end{pmatrix}, \quad (1.140)$$

where M_{o12}^2 and M_{o22}^2 can be expressed in terms of the scalar potential parameters (explicit expressions can be found in Ref. [155]). The squared-masses of the neutral Higgs bosons are obtained by computing the eigenvalues of \mathcal{M}_e^2 and \mathcal{M}_o^2 . Finally, the charged Higgs mass is given by

$$m_{H^\pm}^2 = m_W^2 + m_A^2 - \lambda^2 v^2. \quad (1.141)$$

The phenomenology of the GNMSSM is richer than that of the MSSM due to the additional Higgs states and the larger parameter space. The simplest scenario is an MSSM-like scenario in which either M_{e33}^2 and M_{o22}^2 are large and/or M_{e13}^2 , M_{e23}^2 and M_{o12}^2 are small. In this case, the mixing of the singlet and doublet Higgs components is suppressed and two of the three CP-even Higgs bosons are governed by the 2×2 block obtained from the first two rows and columns of \mathcal{M}_e^2 , while the doublet-like CP-odd Higgs boson has mass m_A . Nevertheless, the MSSM squared-mass relations are corrected by terms of $\mathcal{O}(\lambda^2 v^2)$. Using eq. (1.138), it follows that the CP-even Higgs squared-mass inequality given by eq. (1.115) is modified to [156],

$$m_h^2 \leq m_Z^2 \cos^2 2\beta + \lambda^2 v^2 \sin^2 2\beta + \frac{3g^2 m_t^4}{8\pi^2 m_W^2} \left[\ln \left(\frac{M_S^2}{m_t^2} \right) + \frac{X_t^2}{M_S^2} \left(1 - \frac{X_t^2}{12M_S^2} \right) \right], \quad (1.142)$$

which includes the leading one-loop radiative correction. Whereas the bound is saturated at large $\tan \beta$ in the MSSM (where $\lambda = 0$), we see that in the NMSSM it is possible to have a SM-like Higgs boson with a mass of 126 GeV for relatively modest values of $\tan \beta$ if λ is sufficiently large. Indeed,

in contrast to the MSSM, one does not need as large a boost from the radiative corrections, which means that lower top squark masses are allowed given the observed Higgs mass (thereby lessening the tension with naturalness). Typically, the region of interest corresponds to $\tan\beta \sim 2$ and $\lambda \sim 0.7$. For values of $\lambda > 0.7$, the scalar self-coupling running parameter $\lambda(Q)$ blows up at scales below the Planck scale. Although such a scenario is not consistent with perturbative unification, it does lead to some interesting model building opportunities for a highly natural Higgs boson with a mass of 126 GeV over a wide range of parameters [157].

The scalar states that are dominantly singlet can only couple to gauge bosons and fermions through the small doublet admixture in their wave functions. Thus, these states are very difficult to produce and observe at the ILC. One possible exception to this statement occurs in the limit where both the mixing terms M_{e13}^2 , M_{e23}^2 and M_{o12}^2 are small, and the diagonal elements of the CP-even and/or CP-odd scalar squared-mass matrices are also small. In this case, the lightest scalar particles of the Higgs spectrum can be dominantly singlet. This leaves open the possibility that the decay channels $h \rightarrow h_1 h_1$ and/or $h \rightarrow a_1 a_1$ are allowed, where h is identified as the observed SM-like Higgs boson and h_1 and a_1 are the light dominantly singlet CP-even and CP-odd scalar states. These light states would then decay dominantly via their small scalar doublet admixtures into a pair of the heaviest fermions that are kinematically allowed. There are some experimental limits to this scenario due to searches at LEP, Tevatron and LHC, but allowed regions of the (G)NMSSM parameter space with light singlet-like scalars still persist.

Finally, it is possible that the mixing between singlet and doublet components is not particularly small. In this case, one can still find parameter regimes (e.g. large m_A) in which the lightest CP-even state is dominantly doublet and SM-like (to be identified with the observed Higgs boson), while the heavier states are admixtures of doublet and singlet states. In this scenario, all Higgs states are in play and can be studied at the ILC if their masses are less than half the center-of-mass energy.

1.5

Model-independent treatments of Higgs properties

In the quest for identifying the underlying physics of electroweak symmetry breaking it will be crucial to study the properties of the observed signal at 126 GeV with high precision, taking into account also the limits from Higgs searches in other regions of the parameter space. Besides the interpretation of the experimental results in specific models, it is also useful to express the properties of the Higgs sector in terms of less model-dependent parameterizations. For the observed signal at 126 GeV this refers in particular to its mass, spin, CP properties and couplings.

While the mass can be determined in an essentially model-independent way, and the spin quantum number for a single resonance can be obtained from confronting distinct hypotheses for different spin states with the data (see below), the determination of CP properties and couplings is more involved. An observed state can in general consist of any admixture of CP-even and CP-odd components. Testing the distinct hypotheses of a pure CP-even and a pure CP-odd state can therefore only be a first step in determining the CP properties of a new particle. While it is an obvious goal to extract information on the couplings of the discovered state to other particles, some care is necessary regarding the actual definition of those couplings. It would be tempting to treat the couplings in a certain model, for instance the SM, as independent free parameters and perform a fit to the experimental data. This is not possible, however, once (electroweak) higher-order corrections are taken into account, since model-specific relations between the couplings and the other parameters of the theory are required to ensure properties like UV-finiteness and gauge cancellations.

Moreover, modifying a certain coupling as compared to its form in the SM will in general change both the overall coupling strength and the tensor structure of the coupling. The latter implies a modification of the CP properties of the considered state. As a consequence, in general the

determination of couplings cannot be treated separately from the determination of the CP properties.

Accordingly, in order to analyze the coupling properties of the discovered state a well-defined framework is required where the state-of-the art predictions within the SM (or any other reference model), including all relevant higher-order corrections, are supplemented by a parameterization of possible deviations of the couplings from their reference values (including also possible changes of the tensor structure). If one assumes that effects of new physics occur only at rather high scales, such that the contributions of heavy degrees of freedom can be systematically integrated out, such a framework can be formulated with the help of an effective Lagrangian.

1.5.1 Effective Lagrangian treatments

Assuming that effects of new light particles in loops are absent, physics beyond the Standard Model (BSM) can be described via an effective Lagrangian in terms of the SM fields. This approach has been pioneered in Ref. [158], where a list of operators of dimensions 5 and 6 in the linear parameterization of the Higgs sector with a Higgs doublet has been provided. Those higher-dimensional operators arise from integrating out the contributions of heavy degrees of freedom. Restricting to operators of up to dimension 6 that are relevant for Higgs physics, such an effective Lagrangian has the general form

$$\mathcal{L}_{\text{eff}} = \mathcal{L}_{\text{SM}}^{(4)} + \frac{1}{\Lambda^2} \sum_k \alpha_k \mathcal{O}_k, \quad (1.143)$$

where $\mathcal{L}_{\text{SM}}^{(4)}$ is the SM Lagrangian, $\mathcal{O}_k \equiv \mathcal{O}_k^{d=6}$ denotes dimension-6 operators, α_k the corresponding Wilson coefficients, and Λ is the scale of new physics.

Taking into account all dimension-6 operators that are in accordance with gauge invariance leads to a rather large number of operators. A minimal complete basis can be constructed using the equations of motions to eliminate redundant operators [159]. Proposals that are suitable for the analysis of the upcoming data at the LHC are currently under discussion, (e.g., see Ref. [47] and references therein). For the analysis of the LHC results up to 2012 an “interim framework” has been adopted that is based on a simplified approach using “leading order inspired” scale factors κ_i [47, 160]. In particular, in order to make use of reinterpretations of searches that have been performed within the context of the SM, in this approach only overall changes in the coupling strengths are considered, while effects that change kinematic distributions are not taken into account.

1.5.2 Simplified approach for the analysis of Higgs couplings

The searches for a SM-like Higgs carried out at the LHC so far have mainly focused on the production processes gluon fusion, $gg \rightarrow H$, weak-boson fusion, $qq' \rightarrow qq'H$, associated production with W or Z , $q\bar{q} \rightarrow WH/ZH$, and associated production with a top-quark pair, $q\bar{q}/gg \rightarrow t\bar{t}H$. The searches were based on the decay channels $\gamma\gamma$, $ZZ^{(*)}$, $WW^{(*)}$, $b\bar{b}$ and $\tau^+\tau^-$. The couplings involved in those processes have been analyzed in an “interim framework” under the following simplifying assumptions [47, 160]:

- The observed signal is assumed to correspond to a single narrow resonance. The case of several, possibly overlapping, resonances is not considered.
- The zero-width approximation is assumed for this state. This implies that all channels can be decomposed into a production cross section times a decay branching ratio.
- Only modifications of coupling strengths, i.e. of absolute values of couplings, are considered. No modifications of the tensor structure as compared to the SM case are taken into account. This means in particular that the observed state is assumed to be a CP-even scalar.

In order to parameterize possible deviations from the SM predictions in this framework scale factors κ_i are introduced. The scale factors κ_i are defined in such a way that the cross sections σ_{ii} or

the partial decay widths Γ_{ii} associated with the SM particle i scale with the factor κ_i^2 when compared to the corresponding SM prediction. For a process $ii \rightarrow H \rightarrow jj$ the application of the scale factors results in the term $\kappa_i^2 \kappa_j^2 / \kappa_H^2$ relative to the SM prediction, where κ_H^2 denotes the scale factor for the total width of the observed signal.

By construction, the SM predictions according to the current state-of-the-art, i.e. including the available higher-order corrections, are recovered if all $\kappa_i = 1$. Since higher-order corrections in general do not factorize with respect to the rescalings, the theoretical accuracy degrades for $\kappa_i \neq 1$. This is a drawback of this simplified framework in comparison to the effective Lagrangian approach discussed above, where possible deviations from the SM predictions are parameterized in a more systematic way.

For loop-induced processes such as $gg \rightarrow H$ and $H \rightarrow \gamma\gamma$ the scale factors κ_g and κ_γ are in general treated as free parameters. If on the other hand one assumes that there are no contributions of BSM particles to the loops, those scale factors can be related to the scale factors of the corresponding SM particles in the loop, e.g. $\kappa_\gamma = \kappa_\gamma(\kappa_b, \kappa_t, \kappa_\tau, \kappa_W, m_H)$ in this approximation.

The total width Γ_H is the sum of all Higgs partial widths. The corresponding scale factor κ_H^2 , i.e. $\Gamma_H = \kappa_H^2 \Gamma_H^{\text{SM}}$, in general needs to be treated as a free parameter. Under the assumption that no additional BSM Higgs decay modes (into either invisible or undetectable final states) contribute to the total width and making additional approximations for the scale factors of the currently undetectable decay modes into SM particles, e.g. $\kappa_c = \kappa_t$, $\kappa_s = \kappa_b$ etc., the scale factor κ_H^2 can be related to the scale factors of the partial widths of the different decay modes in the SM,

$$\kappa_H^2 = \kappa_H^2(\kappa_j, m_H), \quad (1.144)$$

where $j = W, Z, b, \tau, \dots$

Within this interim framework, several benchmark parameterizations have been considered. Since the available data do not permit a measurement of the total width Γ_H , in general it is not possible to directly determine scale factors κ_i , but one is limited to determining ratios of scale factors of the form $\kappa_i \kappa_j / \kappa_H$. If one assumes that no BSM Higgs decay modes contribute to the total width and using the approximations mentioned above for the currently undetectable SM modes, one can relate κ_H to the other scale factors as given in eq. (1.144), which makes an absolute determination of the κ_i possible (a milder assumption that also allows to constrain the total width is to assume $\kappa_W \leq 1$ and $\kappa_Z \leq 1$ [47, 161]).

For the experimental analyses up to now often benchmark parameterizations with two free parameters have been used. In particular, a parameterization in terms of a common scale factor for the couplings to fermions, κ_F , and a common scale factor for the couplings to W and Z , κ_V , has been considered, where $\kappa_F = \kappa_t = \kappa_b = \kappa_\tau$ and $\kappa_V = \kappa_W = \kappa_Z$. Besides assuming that all couplings to fermions and the couplings to W and Z can be scaled with a universal factor, in this case it is furthermore assumed that contributions of BSM particles to the loop-induced processes are absent and that the contributions to the total width can be approximated according to eq. (1.144). The most general parameterization that has been investigated up to now involves the parameters $\kappa_V, \kappa_t, \kappa_b, \kappa_\tau, \kappa_g, \kappa_\gamma$ [23].

1.6

Alternative approaches to electroweak symmetry breaking dynamics

In the Standard Model, electroweak symmetry is broken by perturbative scalar dynamics. The scalar potential exhibits a minimum at a non-zero value for the neutral component of a hypercharge one, complex doublet of scalar fields. The scalar fields are elementary (not composite) degrees of freedom, at least at energy scales of order 1 TeV and below. In all extensions of the Higgs sector discussed previously in this document, the elementarity of the scalar fields is maintained and the weakly-coupled nature of the scalar dynamics is preserved.

The Standard Model cannot be a fundamental theory of elementary particle interactions to arbitrarily high energy scales. At Planck scale energies ($M_{\text{PL}} \simeq 10^{19}$ GeV), gravitational phenomena at the microscopic scale can no longer be neglected. Indeed, other new scales of fundamental physics may exist between the scale of electroweak symmetry breaking (EWSB) of order $v = 174$ GeV and the Planck scale, e.g. the grand unification scale, the seesaw scale (that governs right-handed neutrinos and is responsible for generating mass for the light neutrinos) and the mass scale associated with dark matter.

In the Standard Model, the scale of EWSB is not protected by any known symmetry. Thus, it is deeply puzzling how the EWSB scale can be stable with respect to the Planck scale (and other high energy scales if they exist). An equivalent statement is that there is no mechanism in the Standard Model that can keep the mass of an elementary scalar field much lighter than the highest fundamental mass scale of the theory, Λ . That is, the natural value for the squared-mass of the scalar is [162]

$$m_h^2 \sim \frac{g^2}{16\pi^2} \Lambda^2, \quad (1.145)$$

where g is the coupling of the scalar to other sectors of the theory. That is, the scale of EWSB and the attendant Higgs mass is extremely *unnatural* if $\Lambda \gg \mathcal{O}(1 \text{ TeV})$. Only if $\Lambda \sim 1 \text{ TeV}$ do we have a chance of providing a natural mechanism for the EWSB dynamics [163].

The quest for a natural theory of EWSB is one of the motivations for TeV-scale supersymmetry [164, 165, 166, 167, 168, 169]. In this framework, elementary scalars are related by supersymmetry to elementary fermionic superpartners. The fermion masses can be naturally small due to weakly broken chiral symmetries, which in turn protects the masses of the scalar partners. In theories of TeV-scale supersymmetry, we identify Λ with the scale of supersymmetry breaking. Ideally, this scale should be no larger than of $\mathcal{O}(1 \text{ TeV})$. The fact that supersymmetry has not yet been discovered at the LHC provides some tension for natural EWSB in the supersymmetric framework. A pedagogical review of alternative EWSB scenarios can be found in Ref. [170]. In this section, we shall briefly consider non-supersymmetric approaches that could provide a natural explanation for EWSB dynamics.

One of the first leading contenders for a natural theory of EWSB dynamics was technicolor. (Reviews and references can be found in Refs. [171, 172, 173].) In this approach, EWSB was generated by the condensation of bilinears of new fermion fields. No elementary scalar fields were needed, and the naturalness problem associated with them was avoided. Unfortunately, this approach was ultimately unsuccessful. Apart from the fact that it was very difficult to generate a realistic fermion mass spectrum (which required additional new dynamics beyond the introduction of technicolor and the associated techniquarks), the constraints of the precision electroweak observables were extremely difficult to accommodate. The discovery of Higgs boson with Standard Model like properties may have provided the final nail in the coffin (although not all technicolor proponents have conceded [174, 175]). Any theory of EWSB dynamics must explain the presence of a weakly-coupled SM-like Higgs boson whose mass is considerably smaller than $\mathcal{O}(1 \text{ TeV})$.

1.6.1 The Higgs boson as a pseudo-Goldstone boson

Apart from supersymmetry, there is a known mechanism that can yield naturally light elementary scalars. When a continuous global symmetry is broken, one of the consequences is an exactly massless Goldstone boson. If this global symmetry is now explicitly broken, the would-be Goldstone boson acquires a mass proportional to the strength of the symmetry breaking. This is a mechanism for producing naturally light scalars—pseudo-Goldstone bosons whose masses are generated by small symmetry-breaking effects [176].

Thus, perhaps the Higgs boson is in fact a pseudo-Goldstone boson (PGB) generated by strong dynamics associated with scale of new physics Λ [177, 178]. Even though the tree-level mass of the PGB can be significantly smaller than Λ , one-loop corrections to the PGB squared-mass due to the new physics at the scale Λ will still be quadratically sensitive to Λ . This would imply that $\Lambda \sim \mathcal{O}(1 \text{ TeV})$, which is in conflict with precision electroweak observables that do not show any sign of strongly-coupled new physics effects at a mass scale of order 1 TeV.

By a clever construction, one can overcome this last objection by arranging to have the quadratic sensitivity at one loop ameliorated by a cancellation of contributions to the one-loop radiative corrections. The quadratic sensitivity will persist at two-loops, but the presence of the extra loop factor would imply that $\Lambda \sim \mathcal{O}(10 \text{ TeV})$, which is no longer in conflict with precision electroweak observables. This is precisely the mechanism employed by the little Higgs Models [179]. In this framework, the Higgs boson is a PGB associated with the explicit breaking of some global symmetry. But in this case, the global symmetry becomes exact when two different interactions separately vanish (this phenomenon is known as collective symmetry breaking). That is, the lightness of the Higgs boson mass is doubly protected. Indeed, at one loop the quadratic sensitivity of the Higgs squared-mass to Λ vanishes due to the cancellation between Standard Model particles and partner particles of the same spin (in contrast to supersymmetry where the cancellation is due to partners that differ by a half a unit of spin). For example, the top quark must be accompanied by new fermionic top partners whose masses should be of order 1 TeV. Likewise, such models typically include additional gauge bosons, which are partners of the W^\pm and Z .

Numerous realizations of little Higgs models can be found in the literature [180, 181, 182]. The challenge of precision electroweak observables is still present but can be overcome by introducing a discrete T -parity [183, 184] (whose consequences are similar to that of R -parity in supersymmetry models). The presence of new physics (such as top partners and new gauge bosons) can modify the properties of the 126 GeV Higgs boson and provide additional constraints on model building.

An alternative approach for constructing Higgs bosons as PGBs arises in composite models of Higgs bosons [177, 178]. A pedagogical review of the recent progress in developing realistic models of this type can be found in Ref. [185]. Such models often arise as low-energy effective theories of models constructed in higher dimensions of spacetime, where the Higgs boson degree of freedom is identified as the fifth component of a five-dimensional gauge field. (A recent review of this mechanism, called gauge-Higgs unification, can be found in Ref. [186].) In this approach, $f \sim \mathcal{O}(1 \text{ TeV})$ characterizes the scale of new strong interactions that produce the PGB when some larger global symmetry (in which the Standard Model gauge group is embedded) is broken. The effective cutoff of the theory is $\Lambda \sim 4\pi f \sim 10 \text{ TeV}$. The natural value for the Higgs mass is a few hundred GeV, so some amount of tuning is required to identify the Higgs boson of these models with the 126 GeV Higgs boson. Typically, deviations from SM Higgs properties are expected at the 10% level or higher due to the composite nature of the Higgs state. Moreover, such approaches typically predict the existence of other composite resonant states with masses below 1 TeV, which can be searched for at the LHC [187]. These class of models are best studied using the effective Lagrangian analysis of Section 1.5.1.

1.6.2 The Higgs boson as a dilaton

A massless scalar can also arise due to the spontaneous breaking of conformal symmetry. In this case, the corresponding massless Goldstone boson is called a dilaton. If there is a small explicit breaking of conformal symmetry, the corresponding dilaton will be light. So perhaps the Higgs boson can be identified as the dilaton of a broken conformal symmetry. Indeed, if one sets the Higgs potential of the Standard Model to zero, then the Standard Model is classically scale invariant. The Higgs field can take on any value (without costing energy at the classical level). If the Higgs field assumes a nonzero value, then both the electroweak symmetry and the conformal invariance is broken. In this case, the Higgs boson is identified as the dilaton of spontaneously broken conformal symmetry. (In practice, the resulting Higgs boson is not massless due to quantum effects that break the conformal symmetry due to the conformal anomaly.) Models of this type have been recently reviewed in Ref. [188].

It is not clear whether a theoretically consistent model of this type exists. One would have to demonstrate that given a model with spontaneously broken conformal symmetry with a flat direction for the dilaton, a suitable weak explicit breaking of that symmetry can be introduced that picks out a unique vacuum and generates a small mass for the dilaton. Identifying the breaking scale f with the scale of EWSB v , it then follows that the leading couplings of the dilaton to SM fermions is m_f/v and to SM bosons is m_b^2/v which matches precisely with the couplings of the SM Higgs boson. However, there could be corrections to the one-loop couplings of the dilaton to gluons and photons that depend in a model-independent way on the details of the conformal sector, which would yield deviations from the expected one-loop couplings of the SM Higgs boson [189]. The most significant difference between a SM Higgs boson and a dilaton Higgs boson would be found in the triple and quartic Higgs self-couplings. All these deviations can be parameterized via the effective Lagrangian treatment of Section 1.5.1.

In models where $f \neq v$, the dilaton is a scalar distinct from the Higgs boson. This would yield a phenomenology quite distinctive from that of a typical extended Higgs sector [190]. However, such an approach would not provide any fundamental understanding of how the SM Higgs boson mass remains significantly smaller than the higher energy scale that define this theory.

1.7 Probing the properties of the signal at 126 GeV

After the spectacular discovery of a signal at 126 GeV in the Higgs searches at the LHC [19, 20], it is critically important to determine the properties of the new state as comprehensively and as accurately as possible. This information will provide crucial input for identifying the nature of the electroweak symmetry-breaking mechanism.

1.7.1 Present status and prospects for the upcoming LHC runs

We briefly discuss here the present status and the prospects for the upcoming LHC runs. We keep this discussion at a rather qualitative level. For a more quantitative treatment we refer to the latest results from ATLAS and CMS (see in particular [21, 22, 23, 24] and references therein) and the future projections that have been made under various assumptions.

The determination of the mass of the new particle is already at the level of a precision measurement with the 2012 data, driven by the $\gamma\gamma$ and $ZZ^* \rightarrow 4\ell$ channels. The accuracy will further improve with increasing statistics, requiring however a careful treatment of systematic effects.

Concerning the spin of the discovered particle, the observation in the $\gamma\gamma$ channel rules out the possibility of a $J = 1$ state as a consequence of the Landau–Yang theorem [191, 192]. It should be mentioned that there are two caveats to this argument. First, the Landau–Yang theorem strictly applies to an on shell resonance, so that the $J = 1$ hypothesis can be excluded only by making an additional small-width assumption [193]. Second, the decay product could in principle consist of

two pairs of boosted photons each misinterpreted as a single photon. Nevertheless, assuming that the discovered state corresponds to a single resonance rather than to several overlapping resonances corresponding to different spin states, the spin of the discovered particle can be determined by discriminating between the distinct hypotheses for spin 0, (1), 2 states. Some care is necessary in modeling possible incarnations of the spin 2 hypothesis in order to make sure that the discriminating power of the analysis actually refers to the spin properties rather than to some unphysical behavior of the spin 2 implementation. The experimental results obtained up to now are well compatible with the spin 0 hypothesis [22, 24], and there is growing evidence against the alternative hypotheses.

The determination of the CP properties of the observed state is a much more difficult task, since the observed state could in principle consist of any admixture of CP-even and CP-odd components. The analyses so far are mainly based on observables involving the coupling of the new state to two gauge bosons, HVV , where $V = W, Z$, in particular $H \rightarrow ZZ^* \rightarrow 4\ell$. The angular and kinematic distributions in these processes will only provide sensitivity for a discrimination between CP-even and CP-odd properties if a possible CP-odd component A of the new state couples with sufficient strength to WW and ZZ . However, in many models of physics beyond the SM there is no lowest-order coupling between a pseudoscalar A and a pair of gauge bosons, so that the AVV coupling is strongly suppressed compared to the coupling of the CP-even component. In this case, the angular and kinematic distributions will show essentially no deviations from the expectations of a pure CP-even state, even if the state had a sizable CP-odd component. The difference between a pure CP-even state and a state that is a mixture of CP-even and CP-odd components would rather manifest itself as a reduction of the total rate. However, such a reduction in rate could be caused by other effects (and there could even be a compensation with other contributions leading to an enhancement of the rate). The couplings of the Higgs boson to fermions offer a more democratic test of its CP nature, since in this case the CP-even and odd components can have the same magnitude.

Using the results of the $H \rightarrow ZZ^* \rightarrow 4\ell$ channel to discriminate between the distinct hypotheses of a pure CP-even and a pure CP-odd state has led to a growing evidence against the pure CP-odd hypothesis. Furthermore, first results of more general analyses that take into account the possibility of a CP-admixture have been obtained. As explained above, in the channels involving the HVV coupling the effects of even a large CP-admixture can be heavily suppressed as a consequence of a small coupling of the CP-odd component to gauge bosons.

Concerning the determination of the couplings and the total width of the observed particle, a modification of a coupling will give rise to a change in the tensor structure and thus in the CP properties. The determination of coupling and CP properties are therefore closely related. For the analysis of the data taken at the LHC so far, an “interim framework” (described in Section 1.5.2) has been introduced for determining coupling properties. In this framework, it is assumed that only the overall coupling strength gets modified while the tensor structure of the different couplings is the same as in the SM. In this way, results for scale factors κ_i (or, with fewer assumptions, ratios of scale factors) have been obtained under certain assumptions, as discussed in Section 1.5.2. At the present level of accuracy, these analyses do not show a significant deviation from the SM predictions (the SM case corresponds to $\kappa_i = 1$ for all scale factors). Projections for future accuracies of the scale factors κ_i have also been discussed. The reported projections [194] should be interpreted with some care given the fact that one of the goals of the analyses during the next run of the LHC will be to go beyond the “interim framework” used for the definition of the κ_i in order to obtain more general results with less theoretical assumptions (see Section 1.5.1).

The self-coupling HHH will be very difficult to access at the LHC, even with the integrated luminosities obtainable at the high-luminosity upgraded LHC. The prospects are even worse for the quartic self-coupling $HHHH$.

The total decay width for a light Higgs boson with a mass in the observed range is not expected to be directly observable at the LHC. The predicted total width of the Standard Model Higgs boson is about 4 MeV, which is several orders of magnitude smaller than the LHC experimental mass resolution. Furthermore, as all LHC channels rely on the identification of Higgs decay products, the total Higgs width cannot be measured in those analyses without additional assumptions. More sensitive constraints on the total width than the ones limited by the experimental mass resolution can be expected from the analysis of interference effects between signal and background [195, 196, 197, 198, 199]. The limited access to the total width at the LHC implies that without further assumptions only ratios of couplings can be determined rather than the absolute values of the couplings.

In summary, while the experimental information obtained so far about the signal at 126 GeV is compatible with the expectations for the Higgs boson of the SM, a large variety of other interpretations of the discovered particle is also possible, corresponding to very different underlying physics. Some scenarios of this kind have been discussed in the previous sections. These include the possibility that the observed state is composite or that it is an admixture or shares properties with other scalar states of new physics. Extended Higgs sectors are a simplest alternatives to the SM Higgs boson. In this context the signal at 126 GeV can be interpreted as the lightest state of an extended Higgs sector, but interpretations involving at least one lighter Higgs state below 126 GeV, having significantly suppressed couplings to gauge bosons as compared to the SM case, are also possible. The sensitivity for discriminating among the different possible interpretations correlates with the achievable precision in confronting the experimental results with the theory predictions.

1.7.2 Experimental precision required to discriminate between different possible interpretations

If the observed signal at about 126 GeV is interpreted as the lightest state of an extended Higgs sector, this interpretation typically refers to the decoupling region of the respective model, where the lightest state has SM-like properties, while the heavier Higgs states decouple from the gauge bosons of the SM. A concrete example of this kind is the MSSM, where solely from the measured mass value of about 126 GeV important constraints can be inferred if the signal is interpreted in terms of the light CP-even Higgs boson h . Requiring the prediction for the mass of the light CP-even Higgs boson, m_h , to be compatible with the measured mass value of about 126 GeV leads to a lower bound of about 200 GeV on the mass of the CP-odd Higgs boson, m_A , if the masses of the superpartners are in the TeV range [200]. The value of m_A is therefore much larger than m_Z in this case, which corresponds to the decoupling region of the MSSM. This implies that the properties of the state at 126 GeV are expected to be SM-like, and that one generically would not have expected any deviations from SM-like properties in the LHC measurements of the new resonance carried out so far.

In the actual decoupling limit, the couplings of the light Higgs state to SM particles are exactly the same as for the SM Higgs. Of course, even if the couplings to SM particles were very close to the SM values, there could still be deviations from the SM predictions in the branching ratios and the total width if there is a significant branching ratio into invisible BSM particles. The deviations of the Higgs couplings from the SM limit depend on the mass scale of the new physics. In general 2HDM-type models (including the case of the MSSM) one typically expects deviations from the SM predictions at the percent level for BSM particles in the TeV range. In this context, one expects the largest deviations to occur in the couplings to fermions that get their mass from the Higgs doublet with the smaller vacuum expectation value. For example, within the MSSM this refers in particular to the couplings to $b\bar{b}$ and $\tau^+\tau^-$ [2, 125]. The couplings to W and Z are usually less affected by deviations from the decoupling limit. This can be illustrated in a general 2HDM by the feature that the deviation of the HVV coupling ($V = W, Z$) from its SM values behaves quadratically in an expansion of the deviation term, while the couplings to fermions behave linearly, as discussed

in Section 1.3.5. The loop-induced couplings $H\gamma\gamma$ and Hgg can be significantly affected by the presence of relatively light BSM particles in the loops. See Refs. [2, 201] for a discussion of other electroweak symmetry breaking scenarios.

Examples of the coupling patterns in specific models are discussed in the following section.

1.7.3 Examples of analyses in different models

The decays of the Higgs bosons in the 2HDM depend on the Type of Yukawa interactions. In the decoupling/alignment limit where $\sin(\beta - \alpha) = 1$, all the tree-level couplings of h coincide with those in the SM, as discussed in Section 1.3.5. However at the loop level, the effects of the additional Higgs bosons H , A and H^\pm can generate deviations in the h couplings from the SM predictions in the alignment limit if the masses of the additional Higgs boson are not significantly heavier than the mass of the external particles. When $\sin(\beta - \alpha)$ is slightly smaller than 1, the couplings of h to various SM particles can differ from the SM predictions by mixing effects in addition to the loop corrections due to extra fields. The gauge couplings hVV ($VV = WW$ and ZZ) are modified by the factor $\sin(\beta - \alpha)$ relative to the SM values, and Yukawa interactions of h differ from the SM predictions by the factors given in Table 1.9. The pattern of deviation in Yukawa couplings strongly depends on the Type of Yukawa Interactions in the 2HDM. Therefore, we can basically separate the type of an extended Higgs sector by precision measurements of the couplings of h at the ILC.

For example, we discuss here the deviations from the SM of the Yukawa couplings of h in 2HDMs with a softly broken \mathbb{Z}_2 discrete symmetry, which is imposed to avoid tree-level Higgs-mediated flavor changing neutral currents. The Yukawa interactions of the SM-like Higgs boson (h) are given by

$$\mathcal{L}_{\text{Yukawa}}^{2\text{HDM}} = - \sum_f \frac{m_f}{v} \xi_h^f \bar{f} f h, \quad (1.146)$$

where the scaling factors ξ_h^f are displayed in Table 1.9. The scaling parameters for the gauge couplings to h are given by $\kappa_V = \sin(\beta - \alpha)$, while those for the Yukawa interactions are given by $\kappa_f = \xi_h^f$ for $f = u, d, \ell$. The pattern in deviations for each coupling is different among the various Types of Yukawa interactions.

In Fig. 1.17, the scale factors $\kappa_f = \xi_h^f$ in the 2HDM with a softly broken \mathbb{Z}_2 symmetry are plotted on the κ_ℓ - κ_d plane and the κ_ℓ - κ_u plane as a function of $\tan\beta$ and $\kappa_V = \sin(\beta - \alpha)$ with $\cos(\beta - \alpha) \leq 0$. The points and the dashed curves denote changes of $\tan\beta$ by steps of one. The scaling factor κ_V for the Higgs-gauge-gauge couplings is taken to be $\kappa_V^2 = 0.99, 0.95$ and 0.90 . For $\kappa_V = 1$, all the scaling factors for the couplings of h to SM particles become unity. In Fig. 1.17, the current LHC constraints and the expected LHC and ILC sensitivities for κ_d and κ_ℓ at 68.27 % C.L. are also shown. For the current LHC constraints (LHC30), we take the numbers from the universal fit in Eq. (18) of Ref. [202],

$$\epsilon_b = -0.23 \pm 0.31, \quad \epsilon_\tau = +0.00 \pm 0.19, \quad \rho = \begin{pmatrix} 1 & 0.45 \\ 0.45 & 1 \end{pmatrix} \quad (1.147)$$

where $\kappa_x = 1 + \epsilon_x$. Those including ϵ_t are not provided in Ref. [202], because the uncertainties are much larger than unity. For the future LHC sensitivities (LHC300 and LHC3000), the expectation numbers are taken from the Scenario 1 in Table. 1 of Ref. [203]. The central values and the correlations are assumed to be the same as in LHC30 (although in practice, the correlations would change at a collision energy of $\sqrt{s} = 14$ TeV). The ILC sensitivities are based on the numbers in Table. 2.6 in Ref. [2]. The same central values and no correlation are assumed for the plots of ILC sensitivity curves. Therefore, by precisely measuring the couplings of h at the ILC, one can detect deviations from the SM. Those deviations can then be used to discriminate among the various types

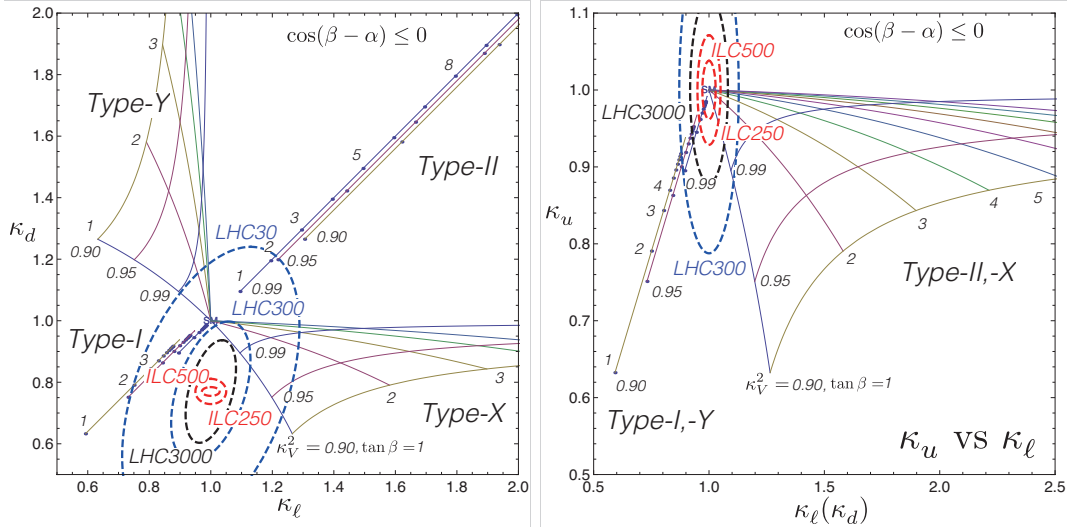


Figure 1.17. The deviation in $\kappa_f = \xi_h^f$ in the 2HDM with Type I, II, X and Y Yukawa interactions are plotted as a function of $\tan\beta = v_2/v_1$ and $\kappa_V = \sin(\beta - \alpha)$ with $\cos(\beta - \alpha) \leq 0$. For the sake of clarity of illustration, several lines with $\kappa_x = \kappa_y$ are shifted slightly so as to be separately visible. The points and the dashed curves denote changes of $\tan\beta$ by one steps. The scaling factor for the Higgs-gauge-gauge couplings is taken to be $\kappa_V^2 = 0.99, 0.95$ and 0.90 . For $\kappa_V = 1$, all the scaling factors with SM particles become unity. The current LHC constraints, expected LHC and ILC sensitivities on (left) κ_d and κ_ℓ and (right) κ_u and κ_ℓ are added.

of extended Higgs sectors by fingerprinting predictions in each model with the precision data of the h coupling measurement.

The behavior of the scaling factors depends on the structure of the extended Higgs sector. For example, a model with mixing of the SM-like Higgs boson with a singlet Higgs field predicts a universal suppression of the SM-like Higgs couplings, $\kappa_F = \kappa_V = \cos\alpha$, where α is the mixing angle between the doublet field and the singlet field. In contrast, $\kappa_F \neq \kappa_V$ in more complicated extended Higgs models such as the 2HDM, the Georgi-Machacek model [140] and doublet-septet model [142, 143]. The scaling factors for these models are summarized in Table. 1.13 . Note that in exotic models with higher representation scalar fields such as the Georgi-Machacek model and doublet-septet model, κ_V can be greater than 1 as already discussed in Section 1.4.2, which is the clear signature of these exotic Higgs sectors.

Table 1.13. Scaling factors in models with universal Yukawa coupling constants.

	Doublet-Singlet	2HDM-I	Georgi-Machacek	Doublet-Septet
$\tan\beta$	—	v_2/v_1'	$v_2/(2\sqrt{2}v_3)$	$v_2/(4v_7)$
ξ_h^f	c_α	$\frac{c_\alpha}{s_\beta}$	$\frac{c_\alpha}{s_\beta}$	$\frac{c_\alpha}{s_\beta}$
ξ_h^V	c_α	$s_{\beta-\alpha} (= s_\beta c_\alpha - c_\beta s_\alpha)$	$s_\beta c_\alpha - \frac{2\sqrt{6}}{3} c_\beta s_\alpha$	$s_\beta c_\alpha - 4c_\beta s_\alpha$

In Fig. 1.18, the predictions for the scale factors of the universal Yukawa coupling κ_F and the gauge coupling κ_V are plotted in the doublet-singlet model, the Type-I 2HDM, the Georgi-Machacek model and the doublet-septet model for each set of $\tan\beta$ and α . The current LHC constraints, expected LHC and ILC sensitivities for κ_F and κ_V at 68.27 % C.L. are also shown. By precision measurements of κ_V and κ_F one can discriminate among exotic models. The central values of the contours correspond to the SM prediction. For the contours for LHC 300 and LHC 3000, κ_τ is used for the scaling factor of the Yukawa coupling, which exhibits the best sensitivity among the fermionic channels. For the contours for ILC250 and ILC500, the scaling factors are chosen as $(\kappa_V, \kappa_F) = (\kappa_Z, \kappa_b)$ without making combinations.

When κ_V is slightly different from unity, we can obtain the upper bound on the mass scale of the second Higgs boson. Extended Higgs sectors usually contain additional mass parameters which

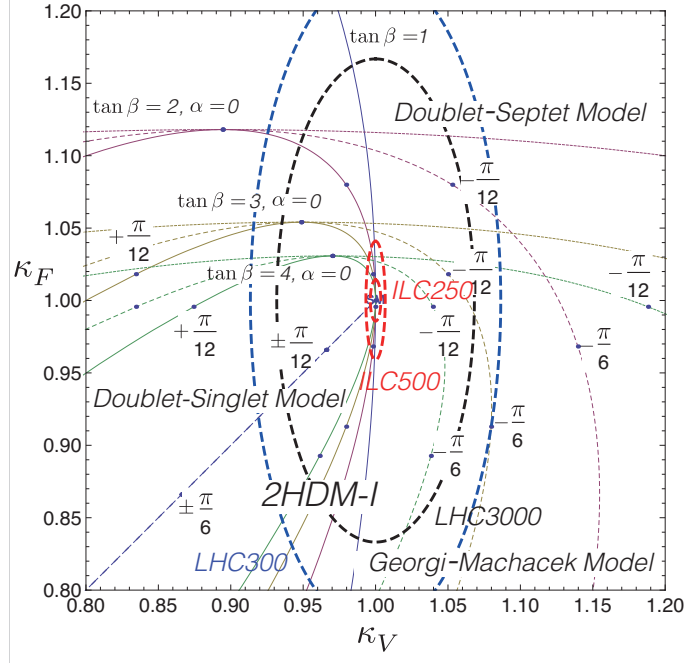


Figure 1.18. The scaling factors in models with universal Yukawa couplings.

are irrelevant to electroweak symmetry breaking. The mass of the second Higgs boson then is a free parameter and can be taken to be very heavy, so that all the couplings of the lightest Higgs boson h coincide with the SM value at tree level. Although we cannot predict the mass of the second Higgs boson, when the coupling hVV is slightly different from the SM prediction, the upper bound on the heavy Higgs mass scale can be theoretically obtained as a function of κ_V by using the properties of the SM-like Higgs boson and the constraint from vacuum stability and perturbative unitarity.

In the case of the 2HDM with a softly-broken discrete \mathbb{Z}_2 symmetry, the vacuum stability bound is given by [107]

$$\lambda_1 > 0, \quad \lambda_2 > 0, \quad \sqrt{\lambda_1 \lambda_2} + \lambda_3 + \min\{0, \lambda_4 + \lambda_5, \lambda_4 - \lambda_5\} > 0. \quad (1.148)$$

The unitarity bounds are obtained by imposing the conditions, $|x_i| < \frac{1}{2}$, where the x_i are the eigenvalues of the s -wave amplitude matrix for the elastic scattering of two scalar states. They are calculated in Ref. [204],

$$x_1^\pm = \frac{1}{16\pi} \left[\frac{3}{2}(\lambda_1 + \lambda_2) \pm \sqrt{\frac{9}{4}(\lambda_1 - \lambda_2)^2 + (2\lambda_3 + \lambda_4)^2} \right], \quad (1.149)$$

$$x_2^\pm = \frac{1}{16\pi} \left[\frac{1}{2}(\lambda_1 + \lambda_2) \pm \sqrt{\frac{1}{4}(\lambda_1 - \lambda_2)^2 + \lambda_4^2} \right], \quad (1.150)$$

$$x_3^\pm = \frac{1}{16\pi} \left[\frac{1}{2}(\lambda_1 + \lambda_2) \pm \sqrt{\frac{1}{4}(\lambda_1 - \lambda_2)^2 + \lambda_5^2} \right], \quad (1.151)$$

$$x_4 = \frac{1}{16\pi}(\lambda_3 + 2\lambda_4 - 3\lambda_5), \quad x_5 = \frac{1}{16\pi}(\lambda_3 - \lambda_5), \quad (1.152)$$

$$x_6 = \frac{1}{16\pi}(\lambda_3 + 2\lambda_4 + 3\lambda_5), \quad x_7 = \frac{1}{16\pi}(\lambda_3 + \lambda_5), \quad x_8 = \frac{1}{16\pi}(\lambda_3 + \lambda_4). \quad (1.153)$$

In Fig. 1.19, an upper limit on the mass of the second lightest Higgs boson is shown in the 2HDM with a softly broken \mathbb{Z}_2 discrete symmetry. Regions on the left side of each curve are the allowed regions by the constraints from unitarity and vacuum stability in the (M, κ_V^2) plane for each fixed value of $\tan \beta$. We take $M = m_A = m_H = m_{H^\pm}$. If the equality of the heavier Higgs masses

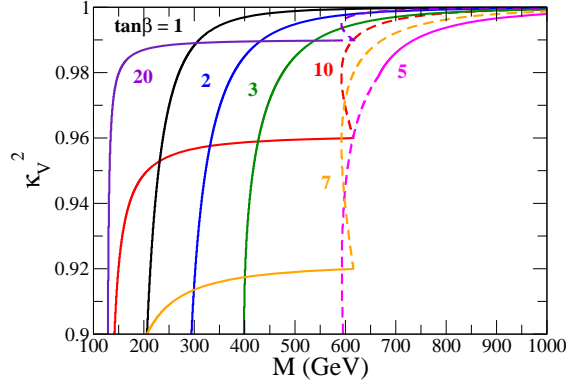


Figure 1.19. Regions inside the curves are allowed by the constraints from unitarity and vacuum stability in the (M, κ_V^2) plane for each fixed value of $\tan\beta$. We take $M = m_A = m_H = m_{H^+}$. The solid and dashed curves correspond to the boundaries of the exclusion regions due to vacuum stability and unitarity, respectively.

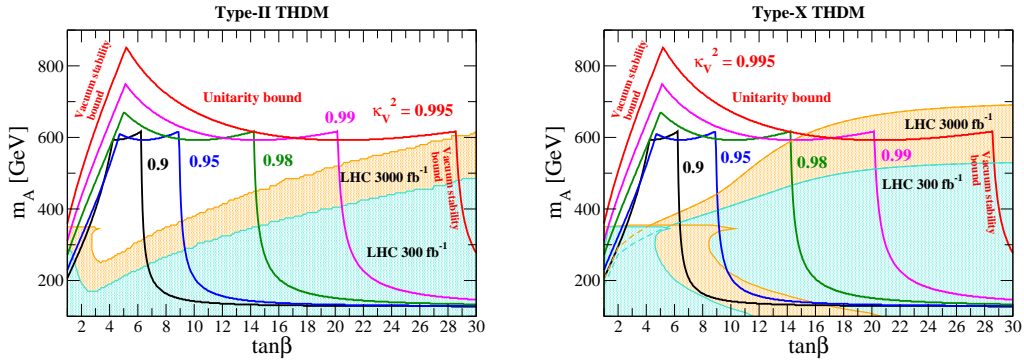


Figure 1.20. Regions below the curves are allowed by the constraints from unitarity and vacuum stability in the $(\tan\beta, m_A)$ plane for each fixed value of κ_V^2 for $M = m_A = m_H = m_{H^+}$ in the Type II and Type X 2HDMs. Expected excluded areas of the parameter space are also shown by blue (orange) shaded regions from the gluon fusion production and associate production of A and H with bottom quarks and tau leptons at the LHC with the collision energy to be 14 TeV with an integrated luminosity of 300 fb^{-1} (3000 fb^{-1}).

is relaxed, then the bound on the mass of the second lightest Higgs boson is typically stronger. The solid and dashed curves correspond to the boundaries of the exclusion regions due to vacuum stability and unitarity, respectively.

In Fig. 1.20, the upper bound on the mass of the additional Higgs bosons are shown as a function of $\tan\beta$ for each fixed value of $\kappa_V^2 = \sin^2(\beta - \alpha)$ under the constraints of perturbative unitarity and vacuum stability [107, 204]. The expected discovery regions at LHC with 300 fb^{-1} and 3000 fb^{-1} are also shown assuming a Type-II Yukawa interaction and a Type-X Yukawa interaction. These discovery regions are obtained from the analysis of the tau lepton decay of H and A from gluon fusion production processes and associate production processes with the bottom quarks and tau leptons,

$$gg \rightarrow \phi^0 \rightarrow \tau^+ \tau^-, \quad (1.154)$$

$$gg \rightarrow b\bar{b}\phi^0 \rightarrow b\bar{b}\tau^+ \tau^-, \quad (1.155)$$

$$gg \rightarrow \tau^+ \tau^- \phi^0 \rightarrow \tau^+ \tau^- \tau^+ \tau^-, \quad (1.156)$$

where ϕ^0 represents H or A . The cross section is obtained by rescaling the values of gluon fusion cross section for h_{SM} at 14 TeV from Ref. [205], and the signal and background analysis in the MSSM

given in Ref. [206] is used. The signal significance \mathcal{S} is computed by rescaling the results to the case of the 2HDMs, and the expected excluded regions are obtained by requiring that $\mathcal{S} > 2$.

For moderate values of $\tan\beta$, it may not be possible to detect the second lightest Higgs boson of the 2HDM at the LHC. In this case, it is important to determine the mass scale of the second Higgs boson in an indirect way. For example, it is possible to measure κ_V at the ILC with a precision at the one percent level or better. If κ_V is found to be slightly different from unity at the ILC at the percent level, then the upper bound on the heavy Higgs mass scale can be obtained from perturbative unitarity. If the deviation is a few percent, these upper bounds are above the discovery reach at LHC with 300 fb^{-1} in wide region of $\tan\beta$ in both Type-II and Type-X 2HDMs. At the LHC with 3000 fb^{-1} , regions with relatively large $\tan\beta$ can be surveyed. The ILC with a center-of-mass energy of 1 TeV can directly survey the extra Higgs bosons with masses less than 500 GeV for relatively low $\tan\beta$ regions, where the LHC cannot detect them.

1.7.4 The hhh coupling and electroweak baryogenesis

How accurately we should measure the hhh coupling?

Given a sufficient accuracy of the hhh coupling measurement, one can test certain scenarios of electroweak baryogenesis. The matter anti-matter asymmetry in our Universe cannot be explained within the Standard Model of particle physics. In particular, the baryon-to-photon ratio is given by $n_b/n_\gamma \simeq (5.1\text{--}6.5) \times 10^{-10}$ at 95 % CL [207], where n_b is the difference in the number density between baryons and anti-baryons and n_γ is the photon number density. In order to generate the baryon asymmetry from a baryon number symmetric initial state, three conditions first given by Sakharov must be satisfied [208]. The electroweak gauge theory can satisfy these conditions by employing sphaleron processes at high temperatures, C and CP violation in the theory and the strongly first order phase transition of the electroweak symmetry. The mechanism of baryogenesis using such a scenario is called electroweak baryogenesis [44, 45, 209], which directly relates to the Higgs sector. Electroweak baryogenesis is especially attractive because of its testability at collider experiments.

In the SM, this scenario is already excluded by the data [44, 45]. The simplest viable model is the 2HDM [210], which provides additional CP violating phases and a sufficiently strong first order electroweak phase transition compatible with the 126 GeV SM-like Higgs boson due to the loop effect of the extra Higgs bosons. One of the interesting phenomenological predictions for such a scenario is a large deviation in the triple Higgs boson coupling [46, 211]. The requirement of a sufficiently strong first order phase transition results in a large deviation in the triple Higgs boson coupling as seen in Fig. 1.21. This suggests that the electroweak baryogenesis scenario can be tested by measuring the

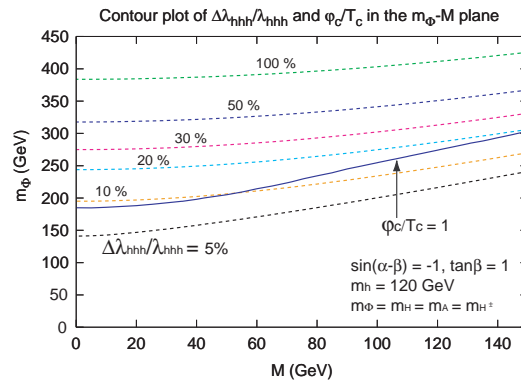


Figure 1.21. The region of strong first order phase transition ($\phi_c/T_c > 1$) required for successful electroweak baryogenesis and the contour plot of the deviation in the triple Higgs boson coupling from the SM prediction [46], where m_Φ represents the common mass of H , A and H^\pm and M is the soft-breaking mass of the \mathbb{Z}_2 discrete symmetry in the Higgs potential.

hhh coupling with a 10% accuracy.

An analysis of the first order phase transition has also been performed in Ref. [211] using a simple Higgs potential with higher order operators where similar deviations in the hhh coupling are predicted. Moreover, the correlation between the condition of strong first order phase transition and the deviation in the hhh coupling from the SM prediction can be seen in various extended Higgs models. Therefore, measuring the hhh coupling accurately is a useful probe of the class of models of electroweak baryogenesis.

The measurement of the hhh coupling for $m_h \simeq 126$ GeV is very challenging at the LHC and even at the high luminosity upgrade of the LHC. At the ILC, the hhh coupling can be measured via $e^+e^- \rightarrow Zhh$ and $e^+e^- \rightarrow hh\nu\bar{\nu}$. As indicated in Chapter 9, for the combined data taken at the ILC with $\sqrt{s} = 250$ with 1150 fb^{-1} and 500 GeV with 1600 fb^{-1} , the hhh coupling can be measured with an accuracy of about 46%. By adding additional data from a run of $\sqrt{s} = 1$ TeV with 2500 fb^{-1} , one can determine the hhh coupling to an accuracy of about 13%. Therefore, the scenario for electroweak baryogenesis would be testable by measuring the triple Higgs boson coupling at the ILC.

1.7.5 Value added by the ILC Higgs program post-LHC

What will be the value added by the ILC Higgs program in the context of the current and future results from the LHC? We provide a qualitative assessment of this question in this section.

The ILC will provide crucial information for identifying the underlying nature of electroweak symmetry breaking. In particular, high-precision measurements of the properties of the signal observed at 126 GeV will be performed at the ILC. For example, for the Higgs couplings to gauge bosons and fermions, one typically expects an order of magnitude improvement from the ILC measurements as compared to the ultimate LHC precision. This expected accuracy provides a high sensitivity for discriminating among possible realizations of electroweak symmetry breaking, such as effects of an extended Higgs sector, of additional states of new physics or deviations in the couplings from the respective SM values that would occur in case the observed signal is a composite state.

Besides those quantitative improvements, the ILC Higgs program will also give rise to crucial qualitative improvements in studying the properties of the observed signal. In particular, the Higgsstrahlung process $e^+e^- \rightarrow ZH$ provides the unique opportunity to make absolute measurements of Higgs couplings in a model-independent way. The clean experimental environment and the relatively low SM cross sections for background processes allow $e^+e^- \rightarrow ZH$ events to be selected based on the identification of two oppositely charged leptons with invariant mass consistent with m_Z . The remainder of the event, i.e. the Higgs decay, is not considered in the event selection.

Because only the properties of the dilepton system are used in the selection, this decay-mode independent measurement provides an absolute determination of the Higgsstrahlung cross section. Subsequently, by identifying the individual final states for different Higgs and Z decay modes, absolute measurements of the Higgs boson branching fractions can be made. Moreover, the ILC provides a unique sensitivity to invisible decay modes of the observed signal. If dark matter consists of a particle (or more than one) with a mass that is less than half the mass of the observed signal, there could be a significant branching ratio of the discovered state at 126 GeV into a pair of dark matter particles. If an invisible decay mode is detected, this could be the first hint for the production of dark matter in collider experiments.

Furthermore, the absolute measurements of the Higgs boson branching ratios imply that the ILC can provide an absolute measurement of the total width a model-independent way. This can be accomplished using the relationship between the total and partial decay widths, for example

$$\Gamma_H = \frac{\Gamma(H \rightarrow WW^*)}{\text{BR}(H \rightarrow WW^*)}, \quad (1.157)$$

where Γ_H denotes the total width. The partial width $\Gamma(H \rightarrow WW^*)$ can be determined from the measurement of the HWW coupling obtained from the fusion process $e^+e^- \rightarrow H\nu\bar{\nu}$. When combined with the direct measurement of $\text{BR}(H \rightarrow WW^*)$, the total Higgs width can be inferred.

The measurement of the Higgs trilinear self-coupling is of particular importance, since it provides direct access to the form of the Higgs potential that gives rise to electroweak symmetry breaking. This measurement is therefore crucial for experimentally establishing the scalar dynamics of electroweak symmetry breaking. As mentioned above, the measurement of the Higgs trilinear self-coupling will be extremely challenging at the LHC even with 3000fb^{-1} of data. This is due to the complexity of the final state and the smallness of the cross sections. At the ILC the processes $e^+e^- \rightarrow ZHH$ and $e^+e^- \rightarrow HH\nu\bar{\nu}$ provide sensitivity to the trilinear self-coupling given sufficiently high luminosity.

Besides a high-precision determination of the properties of the observed signal at 126 GeV, the ILC has also a high physics potential in the direct search for additional states of an extended Higgs sector. The search capacity of the ILC for the pair production of heavy Higgs states is expected to be close to the kinematic limit of $\frac{1}{2}\sqrt{s}$. An extended Higgs sector could however also contain at least one state that is *lighter* than 126 GeV with significantly suppressed couplings to gauge bosons as compared to the case of a SM-like Higgs. The search for such a light Higgs state in the mass range between 60 GeV and 100 GeV is very challenging in the standard search channels at the LHC. In contrast, at the ILC there will be a high sensitivity for probing scenarios of this kind.

Chapter 2

ILC Accelerator Parameters and Detector Concepts

2.1	ILC Accelerator Parameters
2.1.1	TDR Baseline ILC 250 - 500 GeV

The International Linear Collider (ILC) is a high-luminosity linear electron-positron collider based on 1.3 GHz superconducting radio-frequency (SCRF) accelerating technology. Its center-of-mass-energy range is 200–500 GeV (extendable to 1 TeV). A schematic view of the accelerator complex, indicating the location of the major sub-systems, is shown in Fig. 2.1:

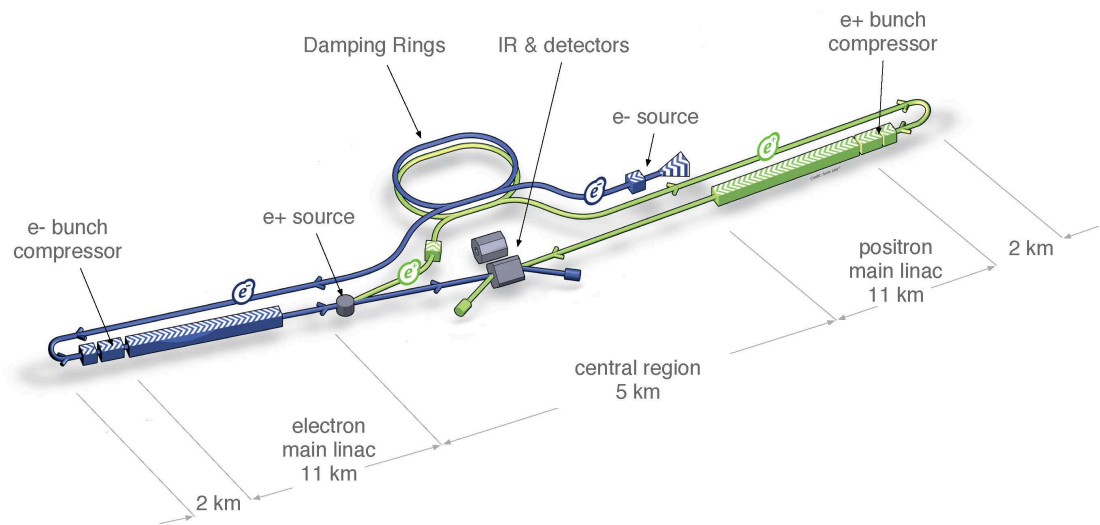


Figure 2.1. Schematic layout of the ILC, indicating all the major subsystems (not to scale).

- a polarized electron source based on a photocathode DC gun;
- a polarized positron source in which positrons are obtained from electron-positron pairs by converting high-energy photons produced by passing the high-energy main electron beam through an undulator;
- 5 GeV electron and positron damping rings (DR) with a circumference of 3.2 km, housed in a common tunnel;
- beam transport from the damping rings to the main linacs, followed by a two-stage bunch-compressor system prior to injection into the main linac;
- two 11 km main linacs, utilizing 1.3 GHz SCRF cavities operating at an average gradient of 31.5 MV/m, with a pulse length of 1.6 ms;

- two beam-delivery systems, each 2.2 km long, which bring the beams into collision with a 14 mrad crossing angle, at a single interaction point which can be occupied by two detectors in a so-called “push-pull” configuration.

The total footprint of the ILC complex is ~ 31 km long. The electron source, positron source (including an independent low-powered auxiliary source), and the electron and positron damping rings are centrally located around the interaction region (IR) in the Central Region. The damping-ring complex is displaced laterally to avoid interference with the detector hall. The electron and positron sources themselves are housed in the same (main accelerator) tunnels as the beam-delivery systems, which reduces the overall cost and size of the central-region underground construction.

The top-level parameters for the baseline operational range of center-of-mass energies from 250 to 1000 GeV were set in close discussion with the physics community that will exploit the ILC. The baseline performance requirements thus obtained have been optimized with respect to cost, physics performance and risk. All have been either directly demonstrated, or represent justifiable extrapolations from the current state of the art. Table 2.1 shows the parameters for several center-of-mass energies, including possible upgrades and staging.

The parameters in Table 2.1 represent relatively conservative operating points resulting from optimization subject to the constraints imposed by the various accelerator sub-systems. For example, the bunch charge, bunch spacing and the total number of bunches in the damping rings are limited by various instability thresholds (most notably the electron cloud in the positron ring), realistic rise-times for the injection and extraction kickers, and the desire to minimize the circumference of the rings. Secondly, the maximum length of the beam pulse is constrained to ~ 1.6 ms, which is routinely achieved in the available 1.3 GHz 10 MW multi-beam klystrons and modulators. The beam current is further constrained by the need to minimize the number of klystrons (peak power) and higher-order modes (cryogenic load and beam dynamics). Dynamic cryogenic load (refrigeration) is also a cost driver, which limits the repetition rate of the machine. Thirdly, both the electron and positron sources constrain the achievable beam current and total charge: For the laser-driven photocathode polarized electron source, the limits are set by the laser; for the undulator-based positron source, the limits are set by the power deposition in the photon target. The beam pulse length is further constrained by the achievable performance of the warm RF capture sections (both sources). Finally, at the interaction point, single-bunch parameters are limited by the strong beam-beam effects and requirements on both the beam-beam backgrounds and beam stability.

Table 2.1. Summary table of the 250–500 GeV baseline and luminosity and energy upgrade parameters. Also included is a possible 1st stage 250 GeV parameter set (half the original main linac length)

			Baseline 500 GeV Machine			1st Stage	L Upgrade	E_{CM} Upgrade	
			250	350	500	250	500	A 1000	B 1000
Center-of-mass energy	E_{CM}	GeV							
Collision rate	f_{rep}	Hz	5	5	5	5	5	4	4
Electron linac rate	f_{linac}	Hz	10	5	5	10	5	4	4
Number of bunches	n_b		1312	1312	1312	1312	2625	2450	2450
Bunch population	N	$\times 10^{10}$	2.0	2.0	2.0	2.0	2.0	1.74	1.74
Bunch separation	Δt_b	ns	554	554	554	554	366	366	366
Pulse current	I_{beam}	mA	5.8	5.8	5.8	5.8	8.8	7.6	7.6
Main linac average gradient	G_a	MV m ⁻¹	14.7	21.4	31.5	31.5	31.5	38.2	39.2
Average total beam power	P_{beam}	MW	5.9	7.3	10.5	5.9	21.0	27.2	27.2
Estimated AC power	P_{AC}	MW	122	121	163	129	204	300	300
RMS bunch length	σ_z	mm	0.3	0.3	0.3	0.3	0.3	0.250	0.225
Electron RMS energy spread	$\Delta p/p$	%	0.190	0.158	0.124	0.190	0.124	0.083	0.085
Positron RMS energy spread	$\Delta p/p$	%	0.152	0.100	0.070	0.152	0.070	0.043	0.047
Electron polarization	P_-	%	80	80	80	80	80	80	80
Positron polarization	P_+	%	30	30	30	30	30	20	20
Horizontal emittance	$\gamma\epsilon_x$	μm	10	10	10	10	10	10	10
Vertical emittance	$\gamma\epsilon_y$	nm	35	35	35	35	35	30	30
IP horizontal beta function	β_x^*	mm	13.0	16.0	11.0	13.0	11.0	22.6	11.0
IP vertical beta function	β_y^*	mm	0.41	0.34	0.48	0.41	0.48	0.25	0.23
IP RMS horizontal beam size	σ_x^*	nm	729.0	683.5	474	729	474	481	335
IP RMS vertical beam size	σ_y^*	nm	7.7	5.9	5.9	7.7	5.9	2.8	2.7
Luminosity	L	$\times 10^{34} \text{ cm}^{-2} \text{ s}^{-1}$	0.75	1.0	1.8	0.75	3.6	3.6	4.9
Fraction of luminosity in top 1%	$L_{0.01}/L$		87.1%	77.4%	58.3%	87.1%	58.3%	59.2%	44.5%
Average energy loss	δ_{BS}		0.97%	1.9%	4.5%	0.97%	4.5%	5.6%	10.5%
Number of pairs per bunch crossing	N_{pairs}	$\times 10^3$	62.4	93.6	139.0	62.4	139.0	200.5	382.6
Total pair energy per bunch crossing	E_{pairs}	TeV	46.5	115.0	344.1	46.5	344.1	1338.0	3441.0

Table 2.2. ILC Higgs factory operational modes

			1st Stage Higgs Factory	Baseline ILC, after Lumi Upgrade	High Rep Rate Operation
Center-of-mass energy	E_{CM}	GeV	250	250	250
Collision rate	f_{rep}	Hz	5	5	10
Electron linac rate	f_{linac}	Hz	10	10	10
Number of bunches	n_b		1312	2625	2625
Pulse current	I_{beam}	mA	5.8	8.75	8.75
Average total beam power	P_{beam}	MW	5.9	10.5	21
Estimated AC power	P_{AC}	MW	129	160	200
Luminosity	L	$\times 10^{34} \text{ cm}^{-2}\text{s}^{-1}$	0.75	1.5	3.0

2.1.2 Luminosity and Energy Upgrade Options

The ILC TDR outlines two upgrades. One is the luminosity upgrade to double the average beam power by adding RF to the linacs. The second is the energy upgrade to double the center of mass energy to 1 TeV by extending the main linacs. The latter will require substantial additional tunnel construction and the upgraded 1 TeV machine will consume more electrical power. The TDR also describes a possible first stage 250 GeV center of mass energy Higgs Factory. These options are included in Table 2.1.

Two additional options should be considered [212]. The first is operation at 250 GeV center of mass energy following the baseline luminosity upgrade. The second is the potential for operation at 1.5 TeV center of mass energy. The latter is briefly mentioned in the ILC cover letter submission to the European Strategy Preparatory Group [213]. Here we only consider the luminosity upgrade at 250 GeV center of mass energy. For operation at 250 GeV, a second step may be considered in which the collider is operated at 10 Hz, instead of 5 Hz, with an average beam power equivalent to that shown in the L Upgrade 500 column in Table 2.1. It is assumed in what follows that the full Baseline 500 and L Upgrade 500 have been completed. At that point, if the main linac gradient is reduced to half of nominal, the repetition rate can be doubled without substantially increasing the overall average power consumption (in a scheme quite similar to that adopted for the electron linac at center of mass energy below 300 GeV). Naturally, the average beam power is also the same as the L Upgrade 500 beam power. This second step scheme allows the ILC Light Higgs Factory luminosity to be increased by a factor four from $0.75 \times 10^{34} \text{ cm}^{-2}\text{s}^{-1}$ to $3.0 \times 10^{34} \text{ cm}^{-2}\text{s}^{-1}$. Table 2.2 and Fig. 2.2 summarize the primary parameters for these three ILC operational modes.

The main impact of low energy ten Hz collision rate operation is on the injector systems: these must be able to cope with high repetition rate operation without any reduction in gradient, as is presently conceived only for the electron side (see [3], Part II, Section 2.2.2, page 9). Furthermore, the positron source undulator must be able to produce adequate positrons using only the nominal 125 GeV luminosity-production electron beam. The latter may require further development of superconducting helical undulator technology as the helix pitch should be reduced from the present 12 cm (as demonstrated in Ref. [3], Part I, Section 4.3.2, page 129) to 0.9 cm without reducing the peak field. It is possible that a longer undulator with ILC TDR parameters would be adequate. Alternatively, an intermediate solution could be considered with a reduced positron yield and possibly higher electron beam energy. For the latter additional electrical power would be required and the e^+/e^- beams might not have equal energy. This does not pose a problem for machine operation in principle but requires study. In addition, the positron injector system would be operated at 10 Hz, full gradient, requiring about two times more RF power and cryogenic capacity. Because of the low center of mass energy positron scheme, this aspect of electron injector operation is already accounted

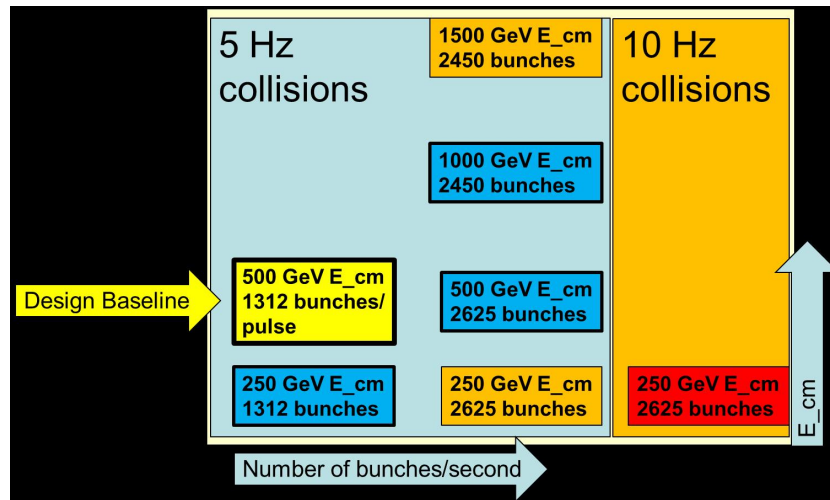


Figure 2.2. ILC Stages and Upgrades. The baseline design (yellow) is fully optimized and represents the starting point for evaluating options. Three options (1st stage, L upgrade and TeV upgrade) are described in the TDR (blue). A further 3 options are mentioned here (orange and red).

in the TDR.

2.1.3 Gamma-Gamma Option

High energy photon-photon collisions can be achieved by integrating high average power short-pulse lasers to the Linear Collider, enabling an expanded physics program for the facility including:

- Single Higgs production sensitive to charged particles of arbitrary mass
- Greater reach for single production of supersymmetric Higgs bosons, H and A
- Probe of CP nature of the observed Higgs bosons through control of the polarization of the Compton photons that define the initial state
- Anomalous couplings in single and double W boson production
- Potential production of supersymmetric particles in electron-gamma collisions

The technology required to realize a photon linear collider continues to mature. Compton back-scattering technology is being developed worldwide for light source applications and high average power lasers continue to advance for Inertial Confinement Fusion.

Compton scattering can transfer $\sim 80\%$ of the incident electron energy to the backscattered photons when a 1 micron wavelength laser pulse is scattered from a 250 GeV electron beam. A laser pulse of 5 Joules, compressed to 1 ps width and focused to a diffraction limited spot can convert most of the incoming electrons in a bunch to high energy photons. An enormous amount of average laser power is required to provide 15,000 laser pulses per second to match the electron beam structure. Since most of the laser energy goes unused in the Compton process the required energy can be greatly reduced if the laser pulses can be recirculated.

A design of a recirculating cavity [214] was created in 2001 which takes advantage of the long inter-bunch spacing in the superconducting machine to recirculate the laser pulses around the outside of the detector. Calculations showed that the required laser power could be reduced by a factor of 300 in this design. Recent studies have shown that a laser with sufficient phase stability to drive such a cavity is achievable with current technology. The available power saving for a recirculating system depends on the achievable cavity size that determines the number of times a laser pulse could be reused in a single electron bunch train.

Implementation of the photon collider option has several requirements for both the detector and the electron accelerator. Apertures must be opened in the forward part of the detector to allow

Table 2.3. Energy and luminosity scenarios assumed in this paper.

Nickname	Ecm(1) (GeV)	Lumi(1) (fb ⁻¹)	+	Ecm(2) (GeV)	Lumi(2) (fb ⁻¹)	+	Ecm(3) (GeV)	Lumi(3) (fb ⁻¹)	Runtime (yr)	Wall Plug E (MW-yr)
ILC(250)	250	250							1.1	130
ILC(500)	250	250		500	500				2.0	270
ILC(1000)	250	250		500	500		1000	1000	2.9	540
ILC(LumUp)	250	1150		500	1600		1000	2500	5.8	1220

the laser pulses to reach the Interaction Point and be focused a few millimeters before the electron beams collide. The electron beam will be left with an enormous energy spread after the Compton backscatter and a large crossing angle will be required in order to allow sufficient aperture for the spent beam to be extracted. Finally, the photon collider option will require its own beam dump design in order to handle the photon beam which will have about 50% of the final beam energy.

Compton backscattering for the creation of MeV gamma-ray light sources is a world-wide activity. The basic techniques of bringing an electron beam and a laser pulse into collision is independent of the electron beam energy and these facilities are providing vital experience in the development of these techniques for the linear collider. These facilities are also developing the technology for recirculating laser pulses which will be critical to achieve a cost effective solution for the photon linear collider. Current MeV gamma-ray sources include the ThomX[215] machine at LAL, the LUCX[216] machine at KEK and the T-REX[217] machine at LLNL. The MightyLaser collaboration is developing a four mirror recirculating cavity for the demonstration of Compton backscattering at ATF[218].

While the photon linear collider has always been envisioned as a later stage to the basic linear collider program there may be advantages to considering it as a first stage. The photon collider requires an electron linear collider to drive it but it does not require positrons and it does not require flat electron beams at the Interaction Point in order to reduce the beamstrahlung. This opens up the possibility of creating a first stage linear collider without a positron source. The creation of a low-emittance RF electron gun, might also create the possibility of eliminating the damping rings in the first stage. Consideration of a dedicated photon collider Higgs factory as a first stage to the linear collider program is motivated by the discovery of a low mass Higgs boson at the LHC.

2.1.4 Energy/Luminosity Running Scenarios

It is of interest to consider the evolution of ILC Higgs physics results over time given the ILC machine parameters defined in Table 2.1 and Table 2.2. Taking eighteen years as a reasonable ILC lifetime, and using the concept of a Snowmass Year where an accelerator is assumed to run at its nominal luminosity for one-third of the time, we assume that the ILC runs for a total of 18×10^7 seconds at nominal luminosity during its life. Without optimization we make the simple assumption that we run for 3×10^7 s at the baseline luminosity at each of the center of mass energies 250, 500, and 1000 GeV, in that order. Following those runs we go back and run for 3×10^7 s at the upgraded luminosity at each of the three center of mass energies.

To avoid a proliferation of table entries, most results are only presented for the four different combinations of energy and luminosity listed in Table 2.3. Each scenario corresponds to the accumulated luminosity at different points in time. In the summary chapter, however, we present results for some alternative scenarios where, for example, runs at center of mass energies of 250 and 500 GeV take place at the upgraded luminosity before any runs at 1000 GeV.

2.2 Detector Concepts

2.2.1 ILD

The ILD detector is a multi-purpose detector. It has been designed for optimal particle-flow (PFA) performance and high precision vertexing and tracking performance. The tracking system consists of a high-precision pixel vertex detector, silicon trackers and a time-projection chamber. The calorimeter system consists of highly segmented electro-magnetic calorimeter and hadron calorimeter. They are placed inside a 3.5 Tesla solenoid magnet and achieves high precision measurements of particle flows, track momentum and vertexes. On the outside of the magnet coil, the iron return yoke is instrumented as a muon system and as a tail catcher calorimeter. The forward region is covered by 2 layers of pixel and 5 layers of silicon strip tracker. Calorimeter system covers down to 5 mrad from the outgoing beam except the hole for the in-coming beam due to 14 mrad crossing angle. The quadrant view of the ILD detector is shown in Fig.2.3. Further detail of the detector will be found in the reference[5].

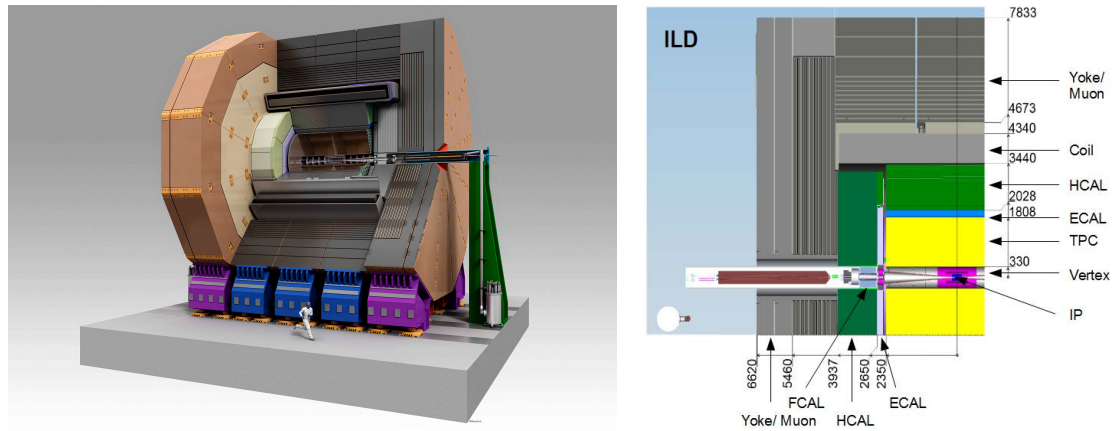


Figure 2.3. The ILD detector, showing (left) an isometric view on the platform, and (right) a quadrant view.

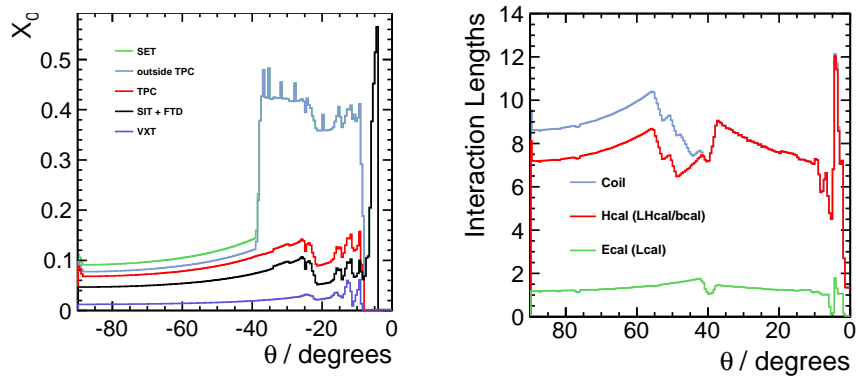
The ILC beam operates at 5 Hz, with 1 msec of beam collision period followed by 199 msec quiet period. This unique beam pulse structure allows data acquisition without a hard ware trigger and lower power consumption electronics system by adapting the pulsed operation of read out electronics. The requirement of the electronics system cooling is moderate and a thin detector system could be realized.

Particle flow requires a thin tracker, to minimize interactions before the calorimeters and thick calorimeters to fully absorb the showers. Thin vertex detector, as well as the small beam pipe radius, helps a precise vertex reconstruction even for low momentum tracks. Figure.2.4 (left) shows the material in the detector in radiation lengths up to the end of the tracking system. The amount of material up to the end of the tracking is mostly below 10% for the full solid angle. The right-hand plot shows the total interaction length including hadron calorimeter, showing a calorimeter coverage by 7 interaction length of coverage in almost all solid angle

For the ILC TDR study, we have developed a realistic detector simulation model. In the model, we have implemented materials for electronics, cooling system, and support structure based on the ILD baseline design in order to evaluate the detector performance as realistically as possible. The simulated data were analyzed with a realistic tracking software, (Marlin tracking packages[219]), particle flow analysis(PandoraPFANew[220]), flavor tagging analysis(LCFIPlus[221]). In physics event analysis, background events as low P_T hadronic background due to collisions of bremsstrahlung or beamstrahlung photons and low energy electron/positron backgrounds hitting beam calorimeter were overlaid on signal events.

Figure 2.4

Left: Average total radiation length of the material in the tracking detectors as a function of polar angle. Right: Total interaction length in the detector up to the end of the calorimeter system and including the coil.



According to the performance study using $e^+e^- \rightarrow q\bar{q}$ events and single μ events, we have obtained the jet energy resolution (90% truncated RMS error) of below 4solid angle and the momentum resolution of $\sigma_{P_T} = 2 \times 10^{-5} \text{ GeV}^{-1}$ for high momentum tracks. From the study using $e^+e^- \rightarrow t\bar{t}$ events, the average track reconstruction efficiency of 99.7% for tracks greater than 1 GeV across the entire polar angle range has been achieved. For $e^+e^- \rightarrow q\bar{q}$ events at 91 GeV, b -quark(c -quark) tagging purity at 60% efficiency was about 100% (60%).

2.2.2 SiD

SiD is a general-purpose detector designed to perform precision measurements at a Linear Collider[5, 222]. It satisfies the challenging detector requirements for physics at the ILC. SiD is the result of many years of creative design by physicists and engineers, backed up by a substantial body of past and ongoing detector research and development. While each component has benefitted from continual development, the SiD design integrates these components into a complete system for excellent measurements of jet energies, based on the Particle Flow Algorithm (PFA) approach, as well as of charged leptons, photons and missing energy. The use of robust silicon vertexing and tracking makes SiD applicable to a wide range of energies from a Higgs factory to beyond 1 TeV. SiD has been designed in a cost-conscious manner, with the compact design that minimizes the volumes of high-performing, high-value, components, while maintaining critical levels of performance. The restriction on dimensions is offset by the relatively high central magnetic field from a superconducting solenoid.

SiD is a compact detector based on a powerful silicon pixel vertex detector, silicon tracking, silicon-tungsten electromagnetic calorimetry (ECAL) and highly segmented hadronic calorimetry (HCAL). SiD also incorporates a high-field solenoid, iron flux return, and a muon identification system (see Fig. 2.5).

The choice of silicon detectors for tracking and vertexing ensures that SiD is robust with respect to beam backgrounds or beam loss, provides superior charged-particle momentum resolution, and eliminates out-of-time tracks and backgrounds. The main tracking detector and calorimeters are “live” only during each single bunch crossing, so beam-related backgrounds and low- p_T backgrounds from $\gamma\gamma \rightarrow \text{hadrons}$ processes will be reduced to the minimum possible levels. The SiD calorimetry is optimized for excellent jet-energy measurement using the PFA technique. The complete tracking and calorimeter systems are contained within a superconducting solenoid, which has a 5 T field strength, enabling the overall compact design. The coil is located within a layered iron structure that returns the magnetic flux and is instrumented to allow the identification of muons.

The tracking system is a key element as the particle-flow algorithm requires excellent tracking with superb efficiency and good two-particle separation. The requirements for precision measurements, in particular in the Higgs sector, place high demands on the momentum resolution at the level of

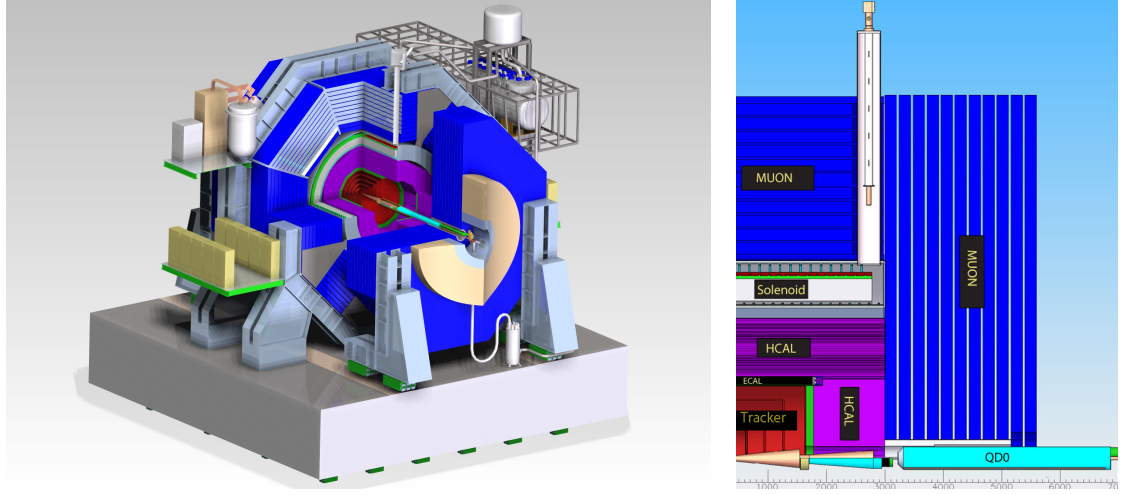


Figure 2.5. The SiD detector, showing (left) an isometric view on the platform, and (right) a quadrant section. Colour coding: tracking (red), ECAL (green), HCAL (violet) and the flux return (blue).

$\delta(1/p_T) \sim 2\text{--}5 \times 10^{-5} (\text{GeV}/c)^{-1}$ and the material budget of the tracking system. Highly efficient tracking is achieved using the pixel detector and main tracker to recognize and measure prompt tracks.

The SiD vertex detector uses a barrel and disk layout. The barrel section consists of five silicon pixel layers with a pixel size of $20 \times 20 \mu\text{m}^2$. The forward and backward regions each have four silicon pixel disks. In addition, there are three silicon pixel disks at a larger distance from the interaction point to provide uniform coverage for the transition region between the vertex detector and the outer tracker. This configuration provides for very good hermeticity with uniform coverage and guarantees excellent charged-track pattern-recognition capability and impact-parameter resolution over the full solid angle. The vertex detector design relies on power pulsing during bunch trains to minimize heating and uses forced air for its cooling. The main tracker technology of choice is silicon-strip sensors arrayed in five nested cylinders in the central region with an outer cylinder radius of 1.25 m and four disks in each of the endcap regions. The geometry of the endcaps minimizes the material budget to enhance forward tracking. The detectors are single-sided silicon sensors with a readout pitch of $50 \mu\text{m}$.

The choice of PFA imposes a number of basic requirements on the calorimetry. The central calorimeter system must be contained within the solenoid in order to reliably associate tracks to energy deposits. The electromagnetic and hadronic sections must have imaging capabilities that allow both efficient track-following and correct assignment of energy clusters to tracks. These requirements imply that the calorimeters must be finely segmented both longitudinally and transversely.

The combined ECAL and HCAL systems consist of a central barrel part and two endcaps, nested inside the barrel. The entire barrel system is contained within the volume of the cylindrical superconducting solenoid. The electromagnetic calorimeter has silicon active layers between tungsten absorber layers. The active layers use $3.5 \times 3.5 \text{ mm}^2$ hexagonal silicon pixels, which provide excellent spatial resolution. The structure has 30 layers in total, the first 20 layers having a thinner absorber than the last ten layers. This configuration is a compromise between cost, electromagnetic shower radius, sampling frequency, and shower containment. The total depth of the electromagnetic calorimeter is 26 radiation lengths (X_0) and one nuclear interaction length. The hadronic calorimeter has a depth of 4.5 nuclear interaction lengths, consisting of alternating steel plates and active layers. The baseline choice for the active layers is the glass resistive-plate chamber with an individual readout segmentation of $10 \times 10 \text{ mm}^2$. Two special calorimeters are foreseen in the very forward region: LumiCal for precise measurement, and BeamCal for fast estimation, of the luminosity.

The SiD superconducting solenoid is based on the CMS solenoid design philosophy and construction techniques, using a slightly modified CMS conductor as its baseline design. Superconducting strand count in the coextruded Rutherford cable was increased from 32 to 40 to accommodate the higher 5 T central field. The flux-return yoke is instrumented with position sensitive detectors to serve as both a muon filter and a tail catcher. The SiD Muon System baseline design is based on scintillator technology, using extruded scintillator readout with wavelength-shifting fiber and SiPMs. Simulation studies have shown that nine or more layers of sensitive detectors yield adequate energy measurements and good muon-detection efficiency and purity.

A large fraction of the software for the generation, simulation and reconstruction is shared between the detector concepts. The SiD detector is fully implemented and simulated using SLIC, which is based on GEANT4. The background originating from incoherent pair interactions and from $\gamma\gamma \rightarrow \text{hadrons}$ for one bunch crossing is fully taken into account by the simulation. The events are then passed through the reconstruction software suite, which encompasses digitization, tracking, vertexing and the Pandora PFA algorithm. The material budget of the simulated tracker and the simulated tracking performance for single particles are shown in Fig. 2.6.

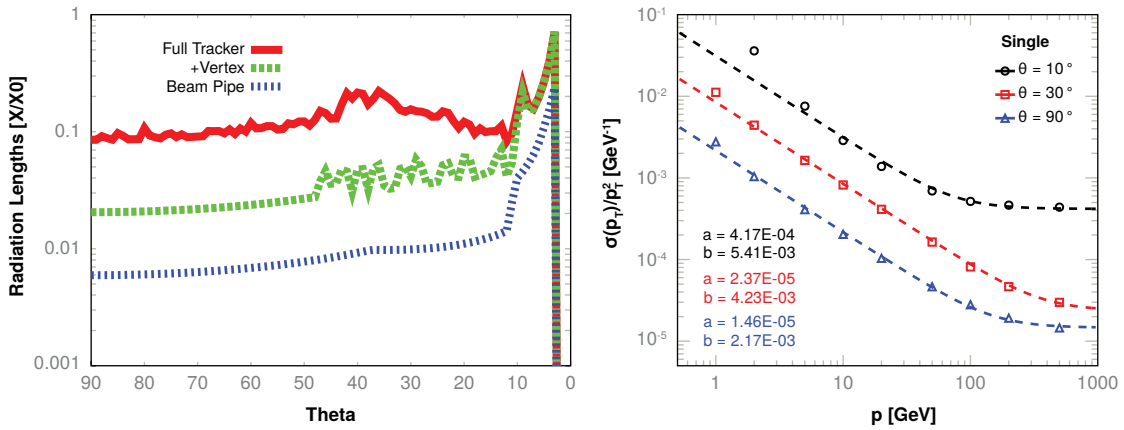


Figure 2.6. Left: SiD Tracker Material budget in terms of X_0 . Right: the normalised transverse momentum resolution for single-muon events.

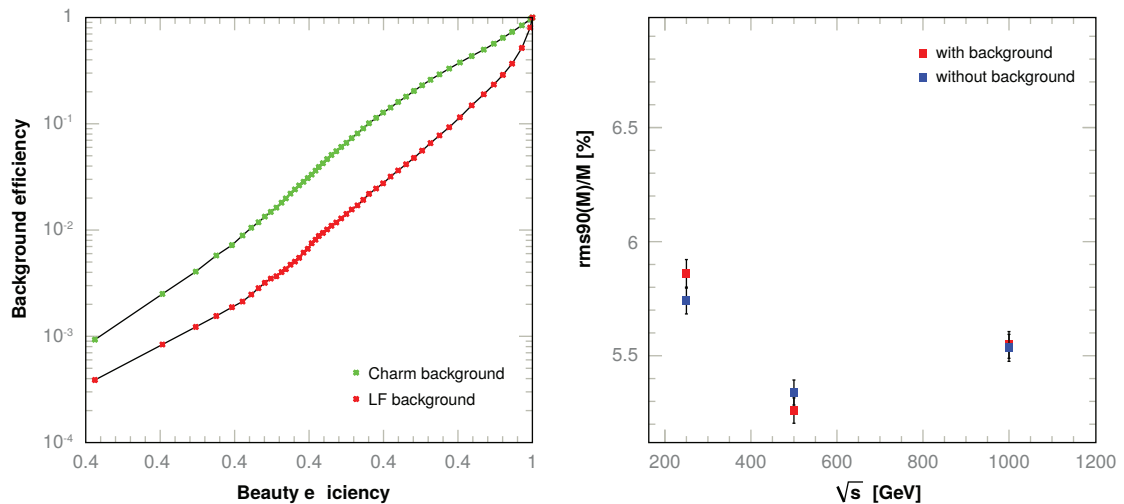


Figure 2.7. Left: Mis-identification efficiency of light quark (red points) and c quark events (green points) as b quark jets versus the b identification efficiency in di-jet events at $\sqrt{s} = 91 \text{ GeV}$ including background from $\gamma\gamma \rightarrow \text{hadrons}$ and incoherent pairs. Right: Mass resolution of reconstructed ZZ events with and without the backgrounds from $\gamma\gamma \rightarrow \text{hadrons}$ and incoherent pairs at different values of \sqrt{s} .

The material budget of the entire tracking system is less than $0.2 X_0$ down to very low angles. The

current design achieves an asymptotic momentum resolution of $\delta(1/p_T) = 1.46 \times 10^{-5} (\text{GeV}/c)^{-1}$ and an transverse impact parameter resolution better than $2\mu\text{m}$. The ability to tag bottom and charm decays with high purity has been a driving factor in the design of the vertex detector. Figure 2.7 (left) illustrates the capability of the SiD to separate b-quarks also in the presence of the full beam background.

Besides the detector performance, sophisticated reconstruction algorithms are necessary to obtain a jet-energy resolution that allows the separation of hadronic W and Z decays. To avoid a bias from possible tails, the rms_{90} value is computed to describe the energy or mass resolution of a particle-flow algorithm. It is defined as the standard deviation of the distribution in the smallest range that contains 90% of the events. Figure 2.7 (right) shows the mass resolution of reconstructed Z bosons in $e^+e^- \rightarrow ZZ$ events at different collision energies, where one Z decays to neutrinos, the other to two light quarks that give rise to two jets.

2.3 Systematic Errors

Most of the errors quoted in this document include statistical errors only. For the three baseline luminosity scenarios this is an excellent approximation of the total error. For the luminosity upgrade scenario, however, some thought has to be given to systematic errors.

2.3.1 Flavor Tagging

2.3.1.1 Introduction

We give a ballpark estimate of the systematic uncertainties arising from b tagging in the context of the Higgs branching ratio measurements. The strategy is to employ control samples to evaluate the b tagging efficiencies as well as the fake rate due to non- b jets (primarily c jets) passing the b tag requirements. For the former, we give an estimate using a b jet rich sample selecting the $ZZ \rightarrow \ell\ell b\bar{b}$ process. For the latter, we use the $WW \rightarrow \ell\nu qq$ process to obtain a control sample containing very few b jets in the event. We then evaluate the impact on the uncertainties of $BR(h \rightarrow b\bar{b})$ assuming a center-of-mass energy of $\sqrt{s} = 250$ GeV and an integrated luminosity of $\mathcal{L} = 250 \text{ fb}^{-1}$ (nominal ILC case) with an extrapolation to $\mathcal{L} = 1150 \text{ fb}^{-1}$ for the high luminosity ILC case.

For the b tagging efficiency points, we use the following two points in our estimates $\epsilon = 80\%$ and 50% with the c and uds fake rate summarized in Tab. 2.4, which are read off from Fig. 2.8 which shows the signal and background efficiencies obtained using LCFIPlus.

Table 2.4. b tagging working points and fake rate for $e^+e^- \rightarrow q\bar{q}$ samples at $\sqrt{s} = 91.2$ GeV using LCFIPlus.

b tag efficiency	c fake rate	q fake rate
80%	8%	0.8%
50%	0.13%	0.05%

2.3.1.2 Estimate of b tag efficiency using $ZZ \rightarrow \ell^+\ell^-b\bar{b}$

The signal efficiency is assumed to be 50%, by noting that the analysis will be very similar to the $e^+e^- \rightarrow Zh \rightarrow \ell\ell qq$ analysis[223]. Background efficiency from the WW process is assumed to be 1%, which should be a conservative estimate. The sample after the first b tag is used as the control

Table 2.5. Selection table for the ZZ analysis. The b tag is applied to one of the two jets.

Process	Before selection	After selection	Tag b ($\epsilon = 50\%$)
$ZZ \rightarrow \ell\ell b\bar{b}$	30000	15000	7500
$ZZ \rightarrow \ell\ell cc$	24000	12000	14
$ZZ \rightarrow \ell\ell qq$	86000	43000	22
$WW \rightarrow \ell\nu cs$	1.3×10^6	13000	13
$WW \rightarrow \ell\nu ud$	1.3×10^6	13000	7

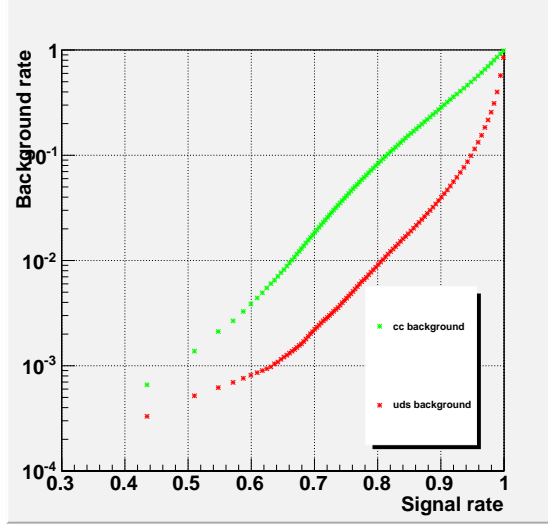


Figure 2.8. b tagging efficiencies versus background efficiencies for $e^+e^- \rightarrow q\bar{q}$ samples at $\sqrt{s} = 91.2$ GeV using LCFIPlus.

sample.

We apply the b tagging with varying efficiencies to our control sample. Since our sample achieves a purity of over 99%, we can safely neglect the contribution of fake b jets in our estimate of b tagging efficiencies. We use the standard recipe for computing the selection efficiencies and use the uncertainty from the binomial distribution $\sqrt{p(1-p)/N}$ where $N = 7500$ and p is chosen for the varying efficiencies. The results are summarized in Tab. 2.6. We therefore conclude that the

Table 2.6. Expected b -tagging uncertainties at various selection efficiencies.

Efficiency	Uncertainty
80%	0.46%
70%	0.53%
60%	0.57%
50%	0.58%

uncertainty in the b tagging efficiency is around 0.3%. Since the uncertainty scales to the statistics of the control samples, it goes down to around 0.15% in the high luminosity ILC case.

2.3.1.3 Estimate of b tagging fake rate using the $WW \rightarrow \ell\nu qq$ process

Here we assume a selection efficiency of 10% for $WW \rightarrow \ell\nu qq$ events. The selection for this process could proceed by selecting an isolated lepton with tight lepton identification criteria and no more than one isolated lepton with loose lepton identification criteria. We assume that the dominant background in this case will be due to $ZZ \rightarrow \tau\tau b\bar{b}$ events where one τ will result in hadronic jets while the other τ undergoes one-prong leptonic decay.

Table 2.7. Summary of selection for the fake rate measurement. Here the b tag selection is such that one of the two jets will pass the b tag requirement at the specified efficiency.

Process	Before selection	After selection	b tag ($\epsilon_b = 80\%$)	b tag ($\epsilon_b = 50\%$)
$WW \rightarrow \ell\nu cs$	1.3×10^6	1.3×10^5 (10%)	11310 (8.7%)	234 (0.18%)
$WW \rightarrow \ell\nu ud$	1.3×10^6	1.3×10^5 (10%)	2080 (1.6%)	130 (0.1%)
$ZZ \rightarrow \tau\tau b\bar{b}$	8500	85 (1%)	82 (96%)	64 (75%)

We give an estimate of the fake rate as follows. The contribution of the fake rate from $WW \rightarrow \ell\nu cs$ will be dominated by c jets as we can infer from Tab. 2.4. As the uncertainty for this number, we take the number of $WW \rightarrow \ell\nu ud$ events as the full uncertainty, which should be a very

conservative estimate. This gives 20% (100%) as the relative uncertainty in the fake rate for the case of $\epsilon_b = 80\%$ (50%).

2.3.1.4 Estimate of branching ratio systematic uncertainty

We now translate these results into the Higgs branching ratio analysis. We take the nominal Higgs branching ratios of $BR(h \rightarrow b\bar{b}) = 58\%$ and $BR(h \rightarrow c\bar{c}) = 2.9\%$. For the b tagging working point of $\epsilon_b = 80\%$, the fake rate from c jet is around $\epsilon_c = 8 \pm 2\%$ including the uncertainty which was just estimated. Applying this b tag gives $BR(h \rightarrow b\bar{b}) \cdot \epsilon_b = 46.4 \pm 0.14\%$ and $BR(h \rightarrow c\bar{c}) \cdot \epsilon_c = 0.23 \pm 0.06\%$ where we took 0.3% as the relative uncertainty in ϵ_b and 20% for the uncertainty in ϵ_c . Similarly for the $\epsilon_b = 50\%$ working point, we compute $BR(h \rightarrow b\bar{b}) \cdot \epsilon_b = 29.0 \pm 0.09\%$ and $BR(h \rightarrow c\bar{c}) \cdot \epsilon_c = 0.038 \pm 0.038\%$, where we took 0.3% as the relative uncertainty in ϵ_b and 100% for the uncertainty in ϵ_c .

We conclude that despite the large relative uncertainty in c jet tagging, the overall uncertainty is dominated by the uncertainty in b jet tagging due to the small $h \rightarrow c\bar{c}$ branching ratio. It is estimated that the uncertainty in the b tagging efficiency in the observable $\sigma(e^+e^- \rightarrow Zh) \cdot BR(h \rightarrow b\bar{b})$ is at the 0.3% level in the nominal ILC and at the 0.15% level in the ILC luminosity upgrade case. Prospects for improving these numbers include refined selection of the control samples (before the first b tagging) and the addition of other ZZ and $Z\gamma$ modes which will require background estimates with an actual simulation analysis. Moving up to $\sqrt{s} = 350$ GeV provides additional clean control samples from fully leptonic top pair decays $e^+e^- \rightarrow t\bar{t} \rightarrow b\bar{b}\nu\bar{\nu}$.

2.3.1.5 Summary and prospects

We put forth a ballpark argument for the b tagging systematic uncertainty in the context of the Higgs branching ratio measurement. Our preliminary findings are that the dominant contribution comes from the uncertainty in the estimate of the b efficiency, which is at the level of 0.3% (nominal ILC) / 0.15% (high luminosity ILC) when applied to the Higgs branching ratio measurement. This number is expected to improve by including additional modes. The contribution from the fake rate is found to be negligible. It is highly desired to refine these estimates using a proper simulation study including all background processes.

2.3.2 Luminosity

The number of Bhabha events per bunch crossing for a detector with minimum and maximum polar angle coverage θ_{min} and θ_{max} (in mrad) is:

$$N = 0.5\text{pb} \frac{L}{R} \int_{\theta_{min}}^{\theta_{max}} \frac{d\cos\theta}{\sin^4\theta/2} \sim 6 \times 10^{-6} \left(\frac{1}{\theta_{min}^2} - \frac{1}{\theta_{max}^2} \right)$$

for $\sqrt{s} = 0.5$ TeV, $L = 2 \times 10^{34} \text{cm}^{-2}\text{s}^{-1}$, and bunch crossing rate $R = 1.4 \times 10^4 \text{s}^{-1}$. Our goal is to measure the luminosity normalization with an accuracy of several 10^{-4} for $\sqrt{s} = 0.5$ TeV. To do this one needs $\approx 10^8$ events collected over $\approx 10^7$ s, or about ten events per second. One can then calculate the absolute luminosity with $\approx 10\%$ statistical error every several minutes during the run. With a bunch crossing rate of $1.4 \times 10^4 \text{s}^{-1}$, we need $> 10^{-3}$ events per bunch crossing. To achieve this statistical accuracy, we start the fiducial region for the precision luminosity measurement well away from the beamstrahlung pair edge at $\theta = 20$ mrad, with a fiducial region beginning at $\theta_{min} = 46$ mrad, which gives $\approx 2 \times 10^{-3}$ events per bunch crossing.

Since the Bhabha cross section is $\sigma \sim 1/\theta^3$, the luminosity precision can be expressed as

$$\frac{\Delta L}{L} = \frac{2\Delta\theta}{\theta_{min}},$$

Table 2.8. Systematic errors assumed throughout the paper.

	Baseline	LumUp
luminosity	0.1%	0.05%
polarization	0.1%	0.05%
b-tag efficiency	0.3%	0.15%

where $\Delta\theta$ is a systematic error (bias) in polar angle measurement and $\theta_{min} = 46$ mrad is the minimum polar angle of the fiducial region. Because of the steep angular dependence, the precision of the minimum polar angle measurement determines the luminosity precision. To reach the luminosity precision goal of 10^{-3} , the polar angle must be measured with a precision $\Delta\theta < 0.02$ mrad and the radial positions of the sensors must be controlled within $30\text{ }\mu\text{m}$ relative to the IP.

2.3.3 Polarization

The primary polarization measurement comes from dedicated Compton polarimeters detecting backscattered electrons and positrons. A relative polarization error of 0.1% is expected from implementing polarimeters both upstream and downstream of the Interaction Region. In addition the polarization can be measured directly with physics processes such as $e^+e^- \rightarrow W^+W^-$. Combining the two techniques we assume a polarization systematic error on cross section times branching ratios of 0.1% and 0.05% for the baseline and upgraded luminosities, respectively.

2.3.4 Systematic Error Summary

The systematic errors that are used throughout this paper are summarized in Table 2.8.

Chapter 3

Higgs Mass, ZH Cross Section, Spin and CP

3.1 Higgs Mass and $\sigma(ZH)$ Measurements

The Higgs mass and the total cross section for $e^+e^- \rightarrow Zh$ are measured simultaneously in the process $e^+e^- \rightarrow Zh$, with $Z \rightarrow \mu^+\mu^-$, $Z \rightarrow e^+e^-$, and $Z \rightarrow q\bar{q}$ decays. Here the shape of the distribution of the invariant mass recoiling against the reconstructed Z provides a precise measurement of m_h , while the normalization of the distribution provides the total cross section $\sigma(ZH)$ independently of the Higgs decay mode. In particular, the $\mu^+\mu^-X$ final state provides a particularly precise measurement as the e^+e^-X channel suffers from larger experimental uncertainties due to bremsstrahlung. It should be noted that it is the capability to precisely reconstruct the recoil mass distribution from $Z \rightarrow \mu^+\mu^-$ that defines the momentum resolution requirement for an ILC detector. A measurement using $Z \rightarrow q\bar{q}$ decays appears to only be feasible at $\sqrt{s} \geq 350$ GeV. A study of this channel at $\sqrt{s} = 500$ GeV is presented here.

3.1.1 l^+l^-h at $\sqrt{s} = 250$ GeV

The reconstructed recoil mass distributions, calculated assuming the Zh is produced with four-momentum $(\sqrt{s}, 0)$, are shown in Fig.3.1. In the e^+e^-X channel FSR and bremsstrahlung photons are identified and used in the calculation of the $e^+e^-(n\gamma)$ recoil mass. Fits to signal and background components are used to extract m_h and $\sigma(ZH)$. Based on this model-independent analysis of Higgs production in the ILD detector, it is shown that m_h can be determined with a statistical precision of 40 MeV (80 MeV) from the $\mu^+\mu^-X$ (e^+e^-X) channel. When the two channels are combined an uncertainty of 32 MeV is obtained [224, 225]. The corresponding model independent uncertainty on the Higgs production cross section is 2.6 %. For a luminosity of 1150 fb^{-1} at $\sqrt{s}=250$ GeV (our scenario 4) the uncertainty on the Higgs mass and production cross section drop to 15 MeV and 1.2 %, respectively.

Similar results were obtained from SiD [222]. It should be emphasized that these measurements only used the information from the leptonic decay products of the Z and are independent of the Higgs decay mode. As such this analysis technique could be applied even if the Higgs decayed invisibly and hence allows us to determine the absolute branching ratios including that of invisible Higgs decays.

3.1.2 l^+l^-h at $\sqrt{s} = 500$ GeV

A Higgs recoil mass analysis has been done at $\sqrt{s} = 500$ GeV with ILD full detector simulation. At $\sqrt{s} = 500$ GeV the Zh cross section is about one-third compared to $\sqrt{s} = 250$ GeV. Also there are numerous backgrounds from t -channel processes such as ZZ at $\sqrt{s} = 500$ GeV. Those aspects make the Zh analysis at $\sqrt{s} = 500$ GeV less powerful than at $\sqrt{s} = 250$ GeV; however the result can be combined with the $\sqrt{s} = 250$ result to improve the overall Zh total cross section accuracy.

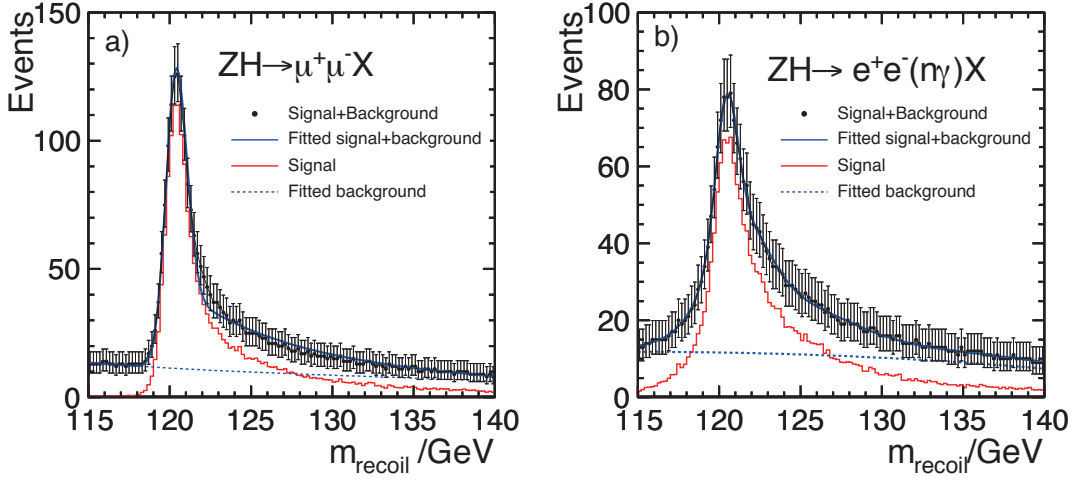


Figure 3.1. Results of the model independent analysis of the Higgsstrahlung process $e^+e^- \rightarrow Zh$ at $\sqrt{s} = 250$ GeV in which (a) $Z \rightarrow \mu^+ \mu^-$ and (b) $Z \rightarrow e^+ e^- (n\gamma)$. The results are shown for $P(e^+, e^-) = (+30\%, -80\%)$ beam polarization.

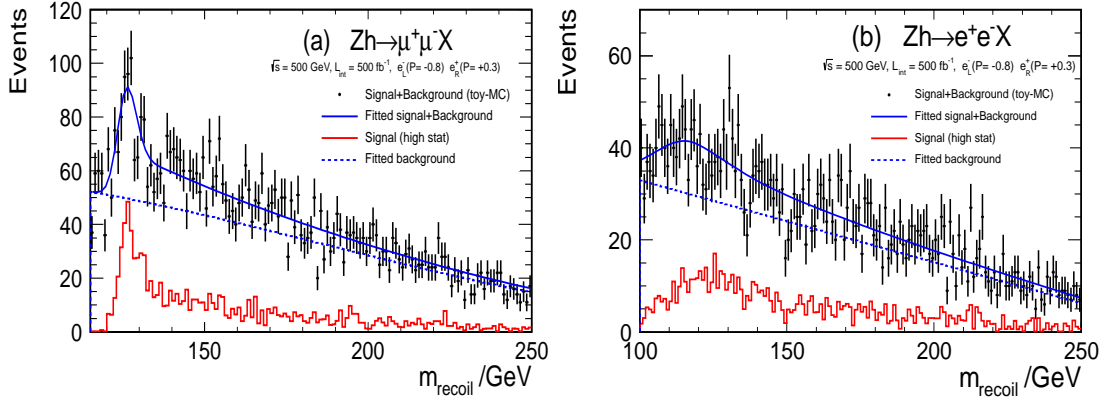


Figure 3.2. Results of the model independent analysis of the Higgs-strahlung process $e^+e^- \rightarrow Zh$ at $\sqrt{s} = 500$ GeV in which (a) $Z \rightarrow \mu^+ \mu^-$ and (b) $Z \rightarrow e^+ e^- (n\gamma)$. The results are shown for $P(e^+, e^-) = (+30\%, -80\%)$ beam polarization.

Firstly, lepton tagging is applied to both the muon and electron channels. For the muon, the cluster energy is required to be smaller than half of the track energy. For the electron, the ratio of the energy deposited in the ECAL to the total calorimeter energy must be greater than 90%, and the cluster energy is required to be between 70% and 140% with respect to the track energy. For the electron channel, all neutral particles with $\cos \theta < 0.99$ with respect to the electron candidate are added to the candidate electron to recover photons from final state radiation and bremsstrahlung. If more than two lepton candidates are found, a pair giving the dilepton mass nearest to the Z mass is selected.

Cuts on the Z mass, recoil mass, and di-lepton p_T are applied. Additional cuts are applied to the acoplanarity of the di-lepton system and the difference between the p_T of the di-lepton and the most energetic neutral particle. Likelihood cuts are applied as the final cuts, with input variables of di-lepton p_T , Z mass, di-lepton $\cos \theta$ and acollinearity of di-lepton.

The resultant recoil mass distributions with fit are shown in Figure 3.2. The cross section error is 6.49% in $\mu\mu h$ channel and 7.10% in $ee h$ channel. The combined resolution for the $Zh \rightarrow \ell\ell h$ at $\sqrt{s} = 500$ GeV is 4.8%.

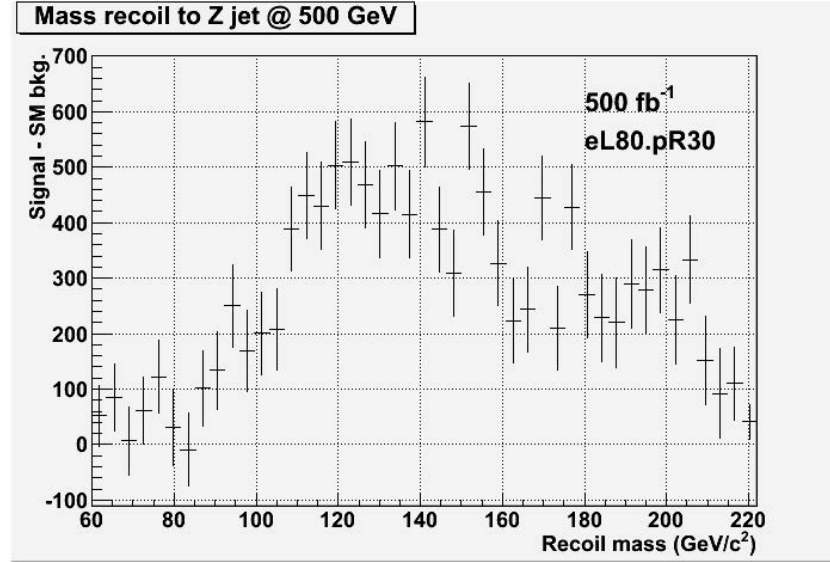


Figure 3.3. The recoil mass of inclusive jet pair after subtracting background processes.

3.1.3 $q\bar{q}h$ at $\sqrt{s} = 500$ GeV

At $\sqrt{s} = 500$ GeV, the total cross section for $e^+e^- \rightarrow q\bar{q}h$ is about 70 fb with an e^-/e^+ beam polarization of $-80\%/+30\%$. About 35k such events are produced for 500 fb^{-1} integrated luminosity. Unlike the situation at $\sqrt{s} = 250$ GeV, the Z and h contain a significant boost at $\sqrt{s} = 500$ GeV and the decay product jets can be unambiguously associated with the parent Z or h boson. The major background processes are 4-fermion W^+W^- , Z^0Z^0 , and 2-fermion $q\bar{q}$.

The energy of the Z from the Zh process is more than 200 GeV, and the two jets from the Z overlap significantly. Therefore, we reconstruct the hadronically decaying Z as a single jet by the k_t jet algorithm with a jet radius of 1.2. From reconstructed jets, candidate jets are preselected by requiring that (1) the jet p_t be greater than 50 GeV, (2) the jet mass be between 70 and 150 GeV/c^2 , and (3) the jet energy be between 210 and 300 GeV.

With a fixed jet radius, both jet mass and jet energy are reduced if some decay products from the Z are outside the jet radius. This effect was corrected by assuming a linear relationship between jet mass and jet energy; in this way a better separation between Z jets and non- Z jets was achieved. For the final selection we required that (1) the corrected jet mass be between 87 and 105 GeV/c^2 , (2) the maximum energy of a photon in the event be less than 100 GeV, (3) the number of particles in the jet be greater than 20, and (4) the jet angle satisfy $|\cos \theta_{jet}| < 0.7$.

The recoil mass distribution of selected events is shown in Fig. 3.3. The figure shows the distribution after subtracting background events. The error bar and the central value of the histogram correspond to the actual event statistics. All standard model processes simulated for the ILC TDR were considered as background. For the number of events with the recoil mass between 100 and 210 GeV/c^2 , S/N is $11113/175437=0.063$. 43% of the backgrounds are due to 4-quark events through ZZ and WW processes. Other 4-fermion processes and 2-fermion hadron events constitute 26% and 27% of background events, respectively. The relative cross section error for 500 fb^{-1} is 3.9%.

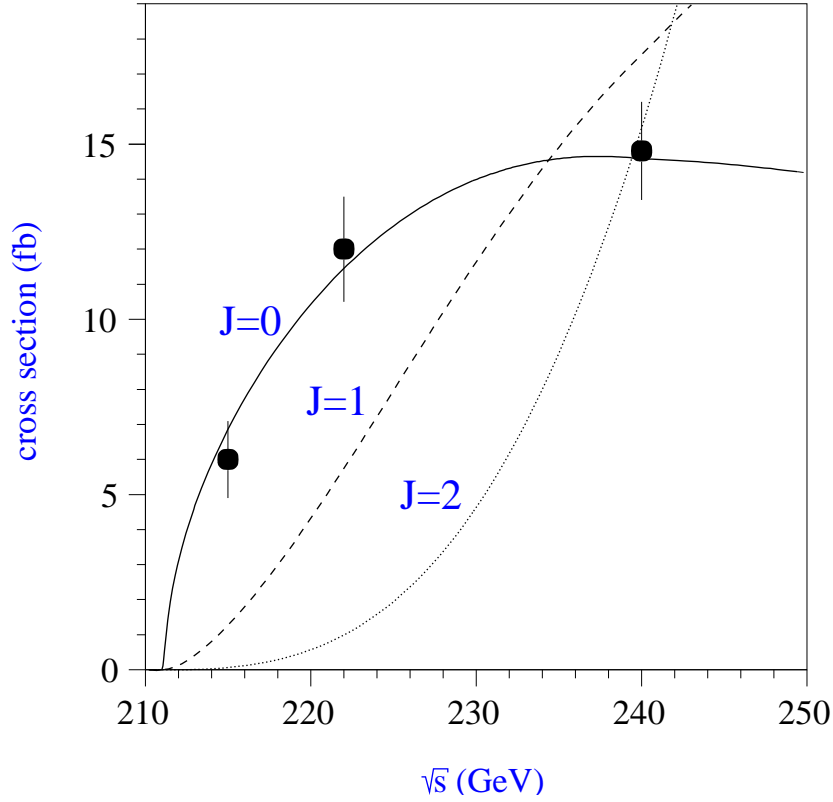


Figure 3.4. Threshold scan of the $e^+e^- \rightarrow Zh$ process for $m_h = 120$ GeV, compared with theoretical predictions for $J^P = 0^+, 1^-,$ and 2^+ [226].

3.2 Higgs Spin Measurement

The threshold behavior of the Zh cross section has a characteristic shape for each spin and each possible CP parity. For spin 0, the cross section rises as β near the threshold for a CP even state and as β^3 for a CP odd state. For spin 2, for the canonical form of the coupling to the energy-momentum tensor, the rise is also β^3 . If the spin is higher than 2, the cross section will grow as a higher power of β . With a three-20 fb^{-1} -point threshold scan of the $e^+e^- \rightarrow Zh$ production cross section we can separate these possibilities [226] as shown in Fig. 3.4. The discrimination of more general forms of the coupling is possible by the use of angular correlations in the boson decay; this is discussed in detail in [227].

At energies well above the Zh threshold, the Zh process will be dominated by longitudinal Z production as implied by the equivalence theorem. The reaction will then behave like a scalar pair production, showing the characteristic $\sim \sin^2 \theta$ dependence if the h particle's spin is zero. The measurement of the angular distribution will hence strongly corroborate that the h is indeed a scalar particle.

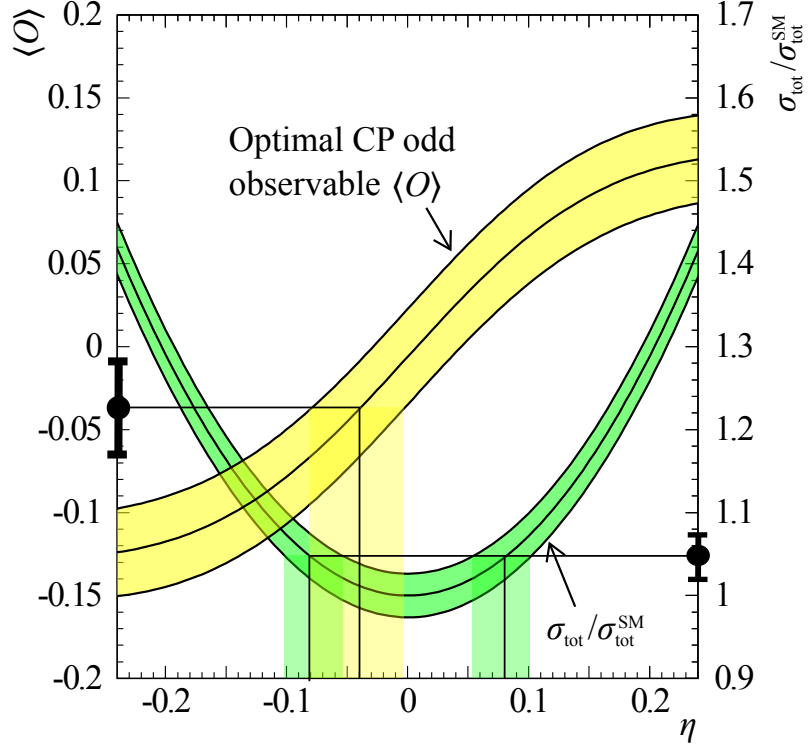


Figure 3.5. Determination of CP -mixing with $1\text{-}\sigma$ bands expected at $\sqrt{s} = 350\text{ GeV}$ and 500 fb^{-1} [228].

3.3 Higgs Sector CP Measurements

3.3.1 Introduction

The analytic power of the ILC is emphasized when we consider more detailed questions. It is possible that the h is not a CP eigenstate but rather a mixture of CP even and CP odd components. This occurs if there is CP violation in the Higgs sector. It is known that CP violation from the CKM matrix cannot explain the cosmological excess of baryons over antibaryons; thus, a second source of CP violation in nature is needed. One possibility is that this new CP violation comes from the Higgs sector and gives rise to net baryon number at the electroweak phase transitions, through mechanisms that we will discuss in Section 9.1 of this report. For these models, the h mass eigenstates can be mainly CP even but contain a small admixture of a CP odd component.

3.3.2 $e^+e^- \rightarrow ZH$

A small CP odd contribution to the hZZ coupling can affect the threshold behavior. The right-hand side of Fig. 3.5 shows the determination of this angle at a center of mass energy of 350 GeV from the value of the total cross section and from an appropriately defined optimal observable [228].

A new result was presented during the Snowmass study [229] for the CP mixing that would appear in the hZZ coupling in both the pp and e^+e^- colliders. The analysis utilized a simplified detector simulation based on the smearing of parton-level information and simply assumed 30% efficiency and 10% background for the signal process: $e^+e^- \rightarrow Zh \rightarrow \mu^+\mu^-b\bar{b}$. From the cross section and the observables concerning the production and decay angles of both the Z and h bosons, the analysis estimated the expected sensitivity to the effective fraction of events due to the CP violating coupling, f_{a3} , which was then translated to that of the corresponding fraction of the anomalous contribution for the Higgs to two vector boson decays, f_{a3}^{dec} , used in earlier CMS studies. If the Zh

cross-section is first measured at the center of mass energy, $\sqrt{s} = 250$ GeV (250 fb^{-1}), and then at 350 (350 fb^{-1}), 500 (500 fb^{-1}), and 1000 GeV (1000 fb^{-1}), f_{a3} can be measured to 0.035, 0.041, and 0.055, respectively, which would translate to precision on f_{a3}^{dec} of 10^{-4} , 4×10^{-5} , and 10^{-5} , respectively. However, the relative contributions of various possible anomalous couplings to the cross section might depend on the underlying dynamics that would appear as form factors in the anomalous couplings and would depend on the virtuality of Z^* . At the ILC, the q^2 dependence can be separated by performing angular analyses separately at different energies since the virtuality of Z^* is fixed at a fixed center-of-mass energy. The expected precision of f_{a3} is in the range of 0.03 - 0.04, being independent of the center-of-mass energy, and translates to 7×10^{-4} to 8×10^{-6} , entering a region sensitive to a possible loop-induced CP-violating contribution.

3.3.3 $H \rightarrow \tau^+ \tau^-$

Tests of mixed CP property using the hZZ coupling may not be the most effective ones, since the CP odd hZZ coupling is of higher dimension and may be generated only through loops. It is more effective to use a coupling for which the CP even and CP odd components are on the same footing. An example is the h coupling to $\tau^+ \tau^-$, given by

$$\Delta \mathcal{L} = -\frac{m_\tau}{v} h \bar{\tau} (\cos \alpha + i \sin \alpha \gamma_5) \tau \quad (3.1)$$

taucouple for a Higgs boson with a CP odd component. The polarizations of the final state τ s can be determined from the kinematic distributions of their decay products; the CP even and odd components interfere in these distributions [230]. In [231], it is estimated that the angle α can be determined to an accuracy of 6° with 1 ab^{-1} at $\sqrt{s} = 350$ GeV in the case of maximal CP mixing, $\alpha = \pi/4$. A similar study has been performed in [232] for a 120 GeV Higgs boson assuming the baseline ILC machine running at $\sqrt{s} = 230$ GeV for an integrated luminosity of 500 fb^{-1} with beam polarizations of $(P_{e^-}, P_{e^+}) = (-0, 8, +0.3)$. A full simulation for the $e^+ e^- \rightarrow Zh \rightarrow \mu^+ \mu^- \tau^+ \tau^-$ mode in the study showed that with an inclusion of other Z decay modes an expected statistical precision of $\Delta\alpha = 0.135$ (i.e. 28 %) could be achieved for $\alpha = -\pi/8$ given the baseline integrated luminosity of 500 fb^{-1} .

3.3.4 $e^+ e^- \rightarrow t\bar{t}H$

In the presence of CP violation, only the CP-even component of the HZZ coupling is projected out in Higgs decays to ZZ . The ZZ couplings of a pure CP-odd A state are zero at tree-level and are generated only through tiny loop corrections.

The decays of the Higgs boson to fermions provide a more democratic probe of its CP nature since, in this case, the CP-even and CP-odd components can have the same magnitude. One therefore needs to look at channels where the Higgs boson is produced and/or decays through these couplings.

A promising production mode for studying the Higgs CP properties is $e^+ e^- \rightarrow t\bar{t}H$. The production of a spin 0 state with arbitrary model-independent CP properties in association with a top quark pair at the ILC was investigated in Ref. [233, 234]. The CP properties of the Higgs coupling to the top quarks were parametrized in a model-independent way by a parameter a for a CP-even Higgs, by a parameter b for a CP-odd Higgs and by simultaneously non-vanishing a and b for a CP-mixed state:

$$C_{ttH} = -ig_{ttH}(a + ib\gamma_5). \quad (3.2)$$

Notice that in the Standard Model, $a = 1$ and $b = 0$.

These parameters were determined by a measurement of the total cross section, the polarization asymmetry of the top quark and the up-down asymmetry of the antitop quark with respect to the

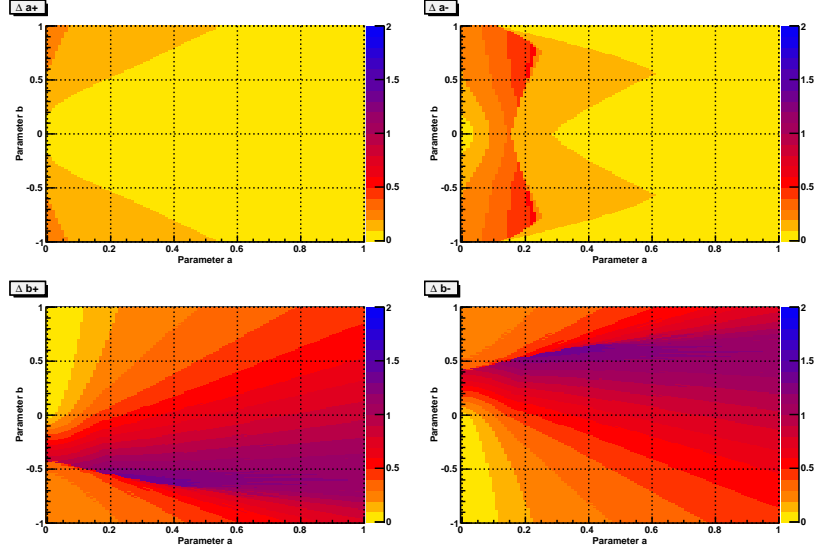


Figure 3.6. Errors Δa^+ (upper left) and Δa^- (upper right) on a as well as Δb^+ (lower left) and Δb^- (lower right) on b , by combining all 3 observables σ, P_t, A_ϕ , at 1σ confidence level for $M_\Phi = 120$ GeV and $\sqrt{s} = 800$ GeV with $\mathcal{L} = 500 \text{ fb}^{-1}$. The electron and positron beams are polarized with $(P_{e^-}, P_{e^+}) = (-0.8, +0.3)$. The colour code indicates the magnitude of the respective error.

top-electron plane. The former two observables are CP-even and can be exploited to distinguish a CP-even from a CP-odd Higgs boson. Since the up-down asymmetry A_ϕ is CP-odd, it can be exploited directly and unambiguously to test CP violation.

The sensitivities to a and b were studied in each observable separately before investigating the combination of all three observables. It was found that the total cross section is most sensitive to a and to some extent to b . The observables P_t and A_ϕ do not exhibit much sensitivity to a and b , although polarization of the initial e^\pm beams slightly improves the sensitivity in case of P_t . The combination of all three observables, however, reduces the error on a for polarized e^\pm beams as shown in Fig. 3.6. If we assume that $a^2 + b^2 = 1$ and parametrize a and b as $a = \cos \phi$ and $b = \sin \phi$, as in eq. (3.1) for $h \rightarrow \tau^+ \tau^-$, then the cross section alone will be a measure of the mixing angle, ϕ . Fig.3.7-(a) shows the $e^+ e^- \rightarrow t \bar{t} h$ cross section as a function of $\sin^2 \phi$ at three different center of mass energies: $\sqrt{s} = 500, 520$, and 1000 GeV. The cross section values are translated into the expected $1\text{-}\sigma$ bounds and shown in Fig.3.7-(b) as a function of $\sin^2 \phi$ for the three energies assuming 500 fb^{-1} for $\sqrt{s} = 500$ and 520 GeV, and the baseline 1 ab^{-1} and the upgraded 2.5 ab^{-1} at $\sqrt{s} = 1 \text{ TeV}$ [235]. The figure tells us that the contribution from the CP-odd component could be constrained to $\sim 5\%$ at $1\text{-}\sigma$.

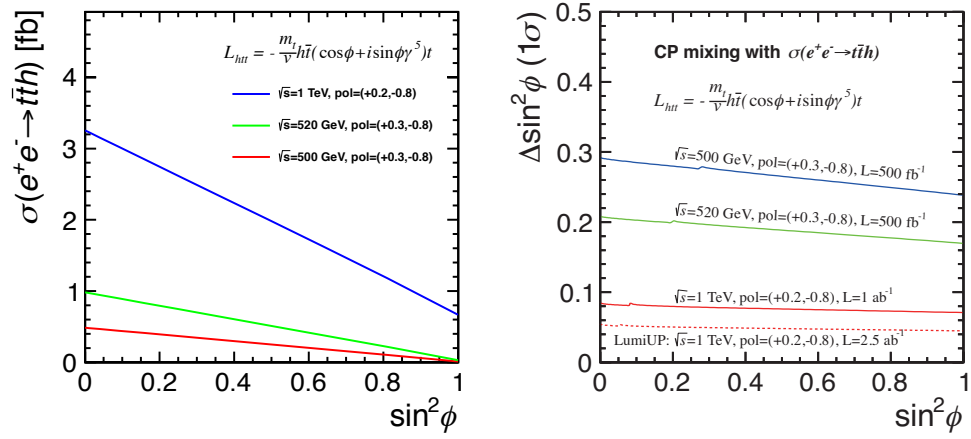


Figure 3.7. (a) $e^+e^- \rightarrow t\bar{t}h$ cross section as a function of $\sin^2 \phi$ at three different center of mass energies: $\sqrt{s} = 500, 520$, and 1000 GeV, (b) the expected 1- σ bound on the CP-odd contribution, $\Delta \sin^2 \phi$, as a function of $\sin^2 \phi$ at the three energies. The corresponding beam polarizations and integrated luminosities are indicated in the figure.

Chapter 4

Cross Section Times Branching Ratio Measurements I

The measurement accuracies of the cross section times branching ratio ($\sigma \cdot BR$) for Higgs decay to $b\bar{b}$, $c\bar{c}$, gg , WW^* and $\tau^+\tau^-$ are described in this chapter.

4.1	$h \rightarrow b\bar{b}, c\bar{c}, gg$
4.1.1	250 GeV and 350 GeV

The measurement accuracies of the cross section times branching ratio $\Delta(\sigma \cdot BR)$ for Higgs decays to $b\bar{b}$, $c\bar{c}$ and gluons were studied in the ILD and SiD LOI's [222, 224] at $\sqrt{s} = 250$ GeV assuming $m_h = 120$ GeV. A comprehensive study at 250 GeV and 350 GeV with $m_h = 120$ GeV was reported in Ref. [236], which is presented below.

At these energies the Higgsstrahlung process ($e^+e^- \rightarrow Zh$) is the dominant contribution to the Higgs production. Therefore, the event signatures of 4-jet($q\bar{q}h$) and 2-lepton (e^+e^- or $\mu^+\mu^-$)+2-jet ($\ell\bar{\ell}h$) were studied in addition to missing energy + 2-jet ($\nu\bar{\nu}h$) events. In the case of the 4-jet analysis, the particles in the event were forcibly clustered to four-jets, from which the dijet pairs for the h and Z candidates were selected as the pairs which minimized the dijet mass χ^2 for Z and h bosons. The background events were rejected by cuts on the number of tracks for each jet, the maximum scaled jet mass (y_{max}) needed to cluster as four jets, the thrust, the thrust angle and the Higgs production angle. The kinematical constraint fit was applied to the four jets to improve background rejection. Finally, the likelihood ratio (LR) was derived from the thrust, $\cos\theta_{thrust}$, the minimum angle between all the jets, the number of particles in the Higgs candidate jets, and the fitted Z and Higgs masses. The cut position to select 4-jet candidates was chosen to maximize the signal significance. The background fractions after all cuts are 80% $q\bar{q}q\bar{q}$ and 20% $q\bar{q}$ at 250 GeV, and 60% $q\bar{q}q\bar{q}$, 30% $q\bar{q}$ and 10% $t\bar{t}$ at 350 GeV

In the case of the 2-lepton + 2-jet mode an event must have an e^+e^- or $\mu^+\mu^-$ pair with mass consistent with the Z , and the mass of everything else must be consistent with the h . Additionally, cuts on the production angle of the Z and the lepton pair recoil mass were applied to improve the signal to noise ratio.

In the analysis of the missing energy+2-jet mode all visible objects were forced into two jets, and the four vector sum of the two jets had to have a P_T and mass consistent with the Higgs. In contrast to the 1 TeV study, the recoil mass calculated from the two jets was required to be consistent with the Z mass because the Higgsstrahlung process is dominant at these energies; in addition this cut was effective in reducing backgrounds from non-Higgs four fermion processes. The likelihood ratio (LR) was formed from the recoil mass, the number of particles, the jet momentum, the jet pair mass and the minimum of the scaled jet mass for forced 2-jet clustering.

With 250 fb⁻¹ at 250 GeV (250 fb⁻¹ at 350 GeV), the signal significance, $S/\sqrt{S+B}$, is 47.9

(66.4) for $\nu\bar{\nu}h$, 32.3(47.1) for $q\bar{q}h$, 22.4(16.7) for e^+e^-h and 28.2 (19.2) for $\mu\bar{\mu}h$.

In order to evaluate the flavor content of the selected events, the flavor likeness of dijet events was calculated by LCFIPlus and fitted by a template consisting of $h \rightarrow b\bar{b}$, $h \rightarrow c\bar{c}$, $h \rightarrow gg$, other Higgs decays and the standard model processes. Pseudo experiments were performed with the fraction of $b\bar{b}$, $c\bar{c}$ and gg as free parameters, and $\Delta\sigma \cdot BR$ was determined by the widths of the fitted distribution. The results are summarized in Table 4.1

Table 4.1. Summary of the sensitivity to $\sigma \cdot BR$ for Higgs decay to $b\bar{b}$, $c\bar{c}$, gg at 250 GeV with 250 fb⁻¹ and $P(e^-)/P(e^+) = -80\%/+30\%$ and 350 GeV with 250 fb⁻¹ and $P(e^-)/P(e^+) = -80\%/+30\%$. $m_h = 120$ GeV was used for this analysis.

Energy	channel	missing+2-jet	4-jet	$e^+e^-+2\text{-jet}$	$\mu^+\mu^-+2\text{-jet}$	Combined
250 GeV	$\frac{\Delta\sigma \cdot BR}{\sigma \cdot BR}(h \rightarrow b\bar{b})$	1.7	1.5	3.8	3.3	1.0
	$\frac{\Delta\sigma \cdot BR}{\sigma \cdot BR}(h \rightarrow c\bar{c})$	11.2	10.2	26.8	22.6	6.9
	$\frac{\Delta\sigma \cdot BR}{\sigma \cdot BR}(h \rightarrow gg)$	13.9	13.1	31.3	33.0	8.5
	$\frac{\Delta\sigma \cdot BR}{\sigma \cdot BR}(h \rightarrow b\bar{b})$	1.4	1.5	5.3	5.1	1.0
350 GeV	$\frac{\Delta\sigma \cdot BR}{\sigma \cdot BR}(h \rightarrow c\bar{c})$	8.6	10.1	30.5	30.9	6.2
	$\frac{\Delta\sigma \cdot BR}{\sigma \cdot BR}(h \rightarrow gg)$	9.2	13.7	35.8	33.0	7.3

The $\sigma \cdot BR$ accuracies for a Higgs with 125 GeV mass were obtained by scaling the number of signal events according to the branching ratio while keeping the number of background events the same. From this extrapolation $\frac{\Delta\sigma \cdot BR}{\sigma \cdot BR}$ for $h \rightarrow b\bar{b}$, $c\bar{c}$, and gg were estimated to be 1.2%, 8.3% and 7.0%, respectively, assuming 250 fb⁻¹ at $\sqrt{s} = 250$ GeV[237].

The $\nu_e\bar{\nu}_e h$ WW -fusion channel was studied in the $h \rightarrow b\bar{b}$ channel at $\sqrt{s} = 250$ GeV using the ILD full simulation[238]. From a χ^2 fit of the missing mass distribution, the contributions from the WW -fusion channel and the Higgsstrahlung channel were separated. A measurement accuracy of $\frac{\Delta\sigma_{\nu\bar{\nu}h} \cdot BR}{\sigma_{\nu\bar{\nu}h} \cdot BR} = 0.11$ was obtained with 250 fb⁻¹ assuming $P(e^-)/P(e^+) = -80\%/+30\%$ and $m_h = 126$ GeV.

4.1.2 500 GeV

The Higgs decay to $b\bar{b}$ in the process $e^+e^- \rightarrow \nu\bar{\nu}h$ at 500 GeV was studied by ILD[238] using full simulation with $m_h = 125$ GeV.

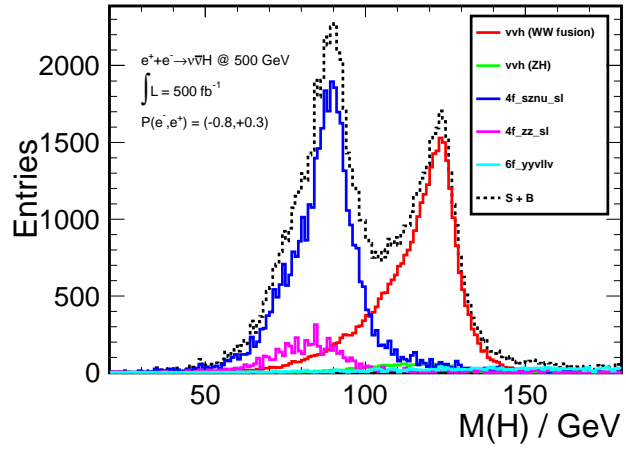
In order to remove piled up background particles, the anti- k_t jet algorithm was employed with the jet size parameter $R = 1.5$. Events with an isolated muon or electron were removed, and events with 2 b -tagged jets were selected. The visible energy and missing P_T were required to be consistent with $\nu\bar{\nu}$ production, and the recoil mass opposite the dijet was required to be greater than 172 GeV to reject $Z \rightarrow \nu\bar{\nu}$ events. The dijet mass distribution for selected events is shown in Figure 4.1.

The signal events were selected with 66% efficiency and a signal-to-noise ratio of 3.7. The main background was $e^+e^- \rightarrow \nu\bar{\nu}Z$, which is labelled as 4f_sznus1 in Figure 4.1. The signal significance for the $h \rightarrow b\bar{b}$ channel was 150 and $\Delta(\sigma \cdot BR)/(\sigma \cdot BR) = 0.667\%$.

The decays $h \rightarrow c\bar{c}$ and gg were studied at 500 GeV[239] using the ILD full simulation samples for the ILC TDR. The analysis strategy is similar to the 1 TeV case in order to select Higgs production via the WW fusion process $e^+e^- \rightarrow \nu_e\bar{\nu}_e h$. However, since no low p_T $\gamma\gamma \rightarrow$ hadron background was overlaid the Durham jet clustering algorithm[240] was applied instead of the k_t algorithm. Events with two jets were selected by cuts on P_T , P_Z , P_{max} , $N_{charged}$ with efficiencies of 57%, 46%, 65% for $h \rightarrow b\bar{b}$, $c\bar{c}$ and gg , respectively. Among the background processes considered, $\nu\bar{\nu}q\bar{q}$ and $\nu\ell q\bar{q}$ were the largest. Flavor composition was determined using the template method described above. The following sensitivities were obtained assuming 500 fb⁻¹ and $P(e^-)/P(e^+) = -80\%/+30\%$: $\Delta(\sigma \cdot BR)/(\sigma \cdot BR) = 0.6\%(b\bar{b})$, 5.2%($c\bar{c}$) and 5.0%(gg). The result can be extrapolated to the case of $m_h = 125$ GeV by scaling the signal yield by the total cross section and the branching ratio:

Figure 4.1

The dijet mass distribution of $e^+e^- \rightarrow \nu\bar{\nu}h \rightarrow \nu\bar{\nu}b\bar{b}$ at $\sqrt{s} = 500$ GeV assuming 500 fb^{-1} , $P(e^-)/P(e^+) = -80\% / +30\%$, and $m_h = 125$ GeV.



$\Delta(\sigma \cdot BR)/(\sigma \cdot BR) = 0.66\%(b\bar{b})$, $6.2\%(c\bar{c})$ and $4.1\%(gg)$. Note that this result for $h \rightarrow b\bar{b}$ is consistent with the dedicated $h \rightarrow b\bar{b}$ study described earlier.

The results from the Zh process were obtained by extrapolating the 250 GeV full simulation results. The number of signal and background events before template fitting were scaled according to the cross section, and then they were extrapolated according to the enhanced statistical significance from the template fitting. As a result, $\frac{\Delta\sigma \cdot BR}{\sigma \cdot BR}$ with 500 fb^{-1} at 500 GeV with $(-80\%, +30\%)$ polarization was estimated to be 1.8%, 13%, and 11% for $h \rightarrow b\bar{b}, c\bar{c}$, and gg respectively.

4.1.3 1 TeV

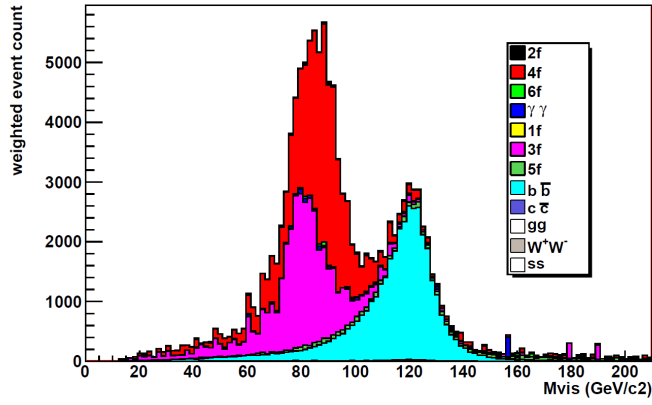
The Higgs decays to $b\bar{b}$, $c\bar{c}$, and gg were studied at 1 TeV as one of the detector benchmark studies for the ILC TDR by the ILD and SiD concept groups. At this energy the Higgs is produced dominantly by the process $e^+e^- \rightarrow \nu\bar{\nu}h$. Therefore, the event signature is a large missing P_T due to un-detected neutrinos and 2 jets from Higgs decays to $b\bar{b}, c\bar{c}$, and gg , with their invariant mass consistent with the Higgs. To minimize the effect of the low P_T hadron events, which are produced at an average rate of 4.1 events per bunch crossing at 1 TeV, both ILD and SiD employed the k_t jet clustering algorithm with a size parameter, R , of 1.5 (1.1 in the case of ILD).

After the jet clustering the candidate 2-jet events were selected by cuts on the visible P_T , visible energy, visible mass, the jet production angles, and the number of tracks. In the case of the SiD analysis, these variables were used to form Fisher Discriminants implemented in TMVA together with the flavor tagging variables for b jets and c jets. Fisher discriminants which maximized the significance for each decay mode were used to obtain the final results. The uncertainties on the cross section times Higgs branching ratios were determined from the numbers of signal and background events passing each selection. A typical Higgs mass distribution in the case of SiD is shown in Figure 4.2.

In the case of the ILD analysis[239], a flavor tagging template fitting was performed to extract $\sigma \cdot BR$ for the different channels. The flavor templates of $h \rightarrow b\bar{b}, c\bar{c}, gg$, and background channels were obtained from the flavor tagging output of the LCFIPlus package. Taking into account the b-tagging efficiency systematic error of 0.3%, the accuracies for 1 ab^{-1} and $P(e^-)/P(e^+) = -80\% / +20\%$ beam polarization were 0.49%, 3.9%, and 2.8% for $h \rightarrow b\bar{b}, c\bar{c}$, and gg respectively. Following the publication of the ILC TDR, improvements to background rejection were developed [237], leading to relative $\sigma \cdot BR$ errors of 0.45%, 3.1%, and 2.3% for $h \rightarrow b\bar{b}, c\bar{c}$, and gg respectively.

Figure 4.2

The visible mass distribution for the $h \rightarrow b\bar{b}$ analysis without the visible mass cut for 500 fb^{-1} and $P(e^-)/P(e^+) = -80\%/+20\%$.



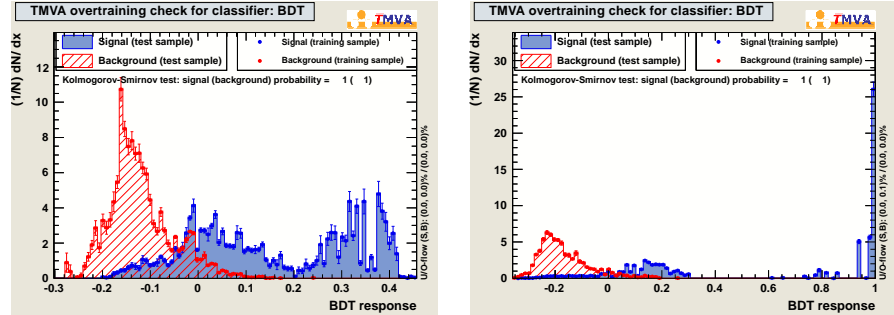
4.2 $h \rightarrow WW^*$

4.2.1 500 GeV

The full simulation study of the process, $e^+e^- \rightarrow \nu\bar{\nu}H \rightarrow \nu\bar{\nu}WW^*$ was performed using the fully hadronic mode of WW^* . In this case the event signature is 4 jets with missing energy and missing momentum and mass consistent with Higgs. The 2 jets from the W^* are soft and the piled up low P_T particles due to $\gamma\gamma$ collisions have to be removed effectively. To this end, a multivariate analysis (MVA) to identify pile up particles was employed using P_T and rapidity. In the case of charged particles, the closest approach to the interaction point along the beam axis (Z_0) was also used to reduce background contamination. Figure 4.3 shows the boosted decision tree (BDT) MVA response for neutral and charged particles.

Figure 4.3

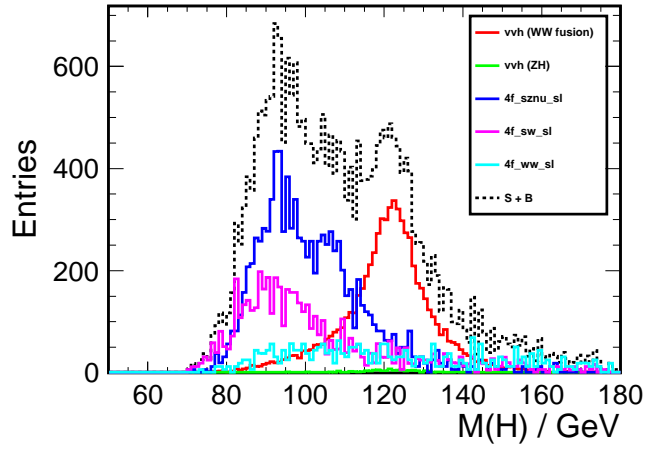
BDT response for particles from $\nu\bar{\nu}h \rightarrow WW^* \rightarrow q\bar{q}q\bar{q}$ events and low P_T hadron background events for neutral particles (left) and charged particles (right).



After rejecting background tracks by the MVA, events with isolated muons or electrons were removed and anti- k_t jet clustering was employed to select 4-jet events. Each jet was required to not be tagged as a b -jet, and one jet pair must have its mass consistent with the W with the other jet pair mass between 11 and 64 GeV. The 4-jet mass distribution for selected events is shown in Figure 4.4.

The signal selection efficiency was about 43%. The major backgrounds were other Higgs decays and the semi-leptonic channels for $e^+e^- \rightarrow ZZ$ or WW . The signal-to-noise ratio was about 1. For 500 fb^{-1} , the signal significance, $S/\sqrt{S+B}$, was 35 and $\Delta(\sigma \cdot BR)/(\sigma \cdot BR) = 2.8\%$. When combined with an analysis of the semileptonic channel for $h \rightarrow WW^*$ [238] the precision improves to $\Delta(\sigma \cdot BR)/(\sigma \cdot BR) = 2.4\%$.

Figure 4.4
4-jet mass distribution
for selected events in
the $h \rightarrow WW^*$ study.



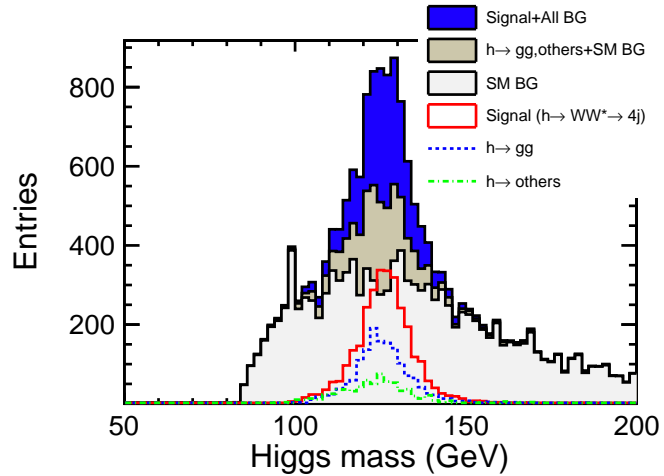
4.2.2 1 TeV

The decay $h \rightarrow WW^*$ was studied at 1 TeV by ILD and SiD for the ILC TDR using the fully hadronic decay mode of WW^* . The signal final state is four jets consistent with WW^* , with total mass consistent with the Higgs mass, and large missing energy and missing transverse momentum.

In the ILD analysis background from pile-up events was removed by employing the k_t jet clustering algorithm with $R = 0.9$ and $N_{jet} = 4$. Further, the Durham algorithm was applied to force the remaining particles to be clustered into four jets, which were paired so that one dijet system had a mass consistent with the W , while the other had a mass between 15 and 60 GeV. To reduce background from $h \rightarrow b\bar{b}$ the b -likeness of each jet was required to be low. The signal selection efficiency was 12.4%, and the remaining major backgrounds were 4-fermions ($e^+e^- \rightarrow \nu\bar{\nu}q\bar{q}$), 3-fermions ($e\gamma \rightarrow \nu q\bar{q}$) and other decay channels of the Higgs. The reconstructed Higgs mass distribution is shown in Figure 4.5.

With 1 ab^{-1} luminosity and a beam polarization of $P(e^-) = -80\%$, $P(e^+) = +20\%$, ILD obtained $\Delta(\sigma \cdot BR)/(\sigma \cdot BR) = 2.5\%$. SiD obtained a similar result. By including the semi-leptonic topology for $h \rightarrow WW^*$, and by using the particle-based MVA technique to better reject pileup, the precision for $h \rightarrow WW^*$ improves to $\Delta(\sigma \cdot BR)/(\sigma \cdot BR) = 1.6\%$ [237].

Figure 4.5
ILD reconstructed
Higgs mass distribu-
tion for the $h \rightarrow WW^*$
analysis in the fully
hadronic decay channel.



4.3 $h \rightarrow \tau^+ \tau^-$ **4.3.1** **250 GeV**

The full simulation samples of the ILD LOI [224] were used for the study of $h \rightarrow \tau^+ \tau^-$ in Ref. [241]. In this study the Higgsstrahlung process ($e^+ e^- \rightarrow Zh$) at $\sqrt{s} = 250$ GeV was considered using $m_h = 120$ GeV and the Z decay modes $Z \rightarrow l^+ l^-$ ($l = e, \mu$) and $Z \rightarrow q\bar{q}$.

In the case of $Z \rightarrow l^+ l^-$, events with an $l^+ l^-$ mass consistent with the Z were selected, where the $l^+ l^-$ tracks were required to come from the IP to reject such tracks from τ decay. Particles other than those from the Z were fed to a tau jet finder, which identified low mass (< 2 GeV) jets using particles within 1 radian of an energetic track. Signal events were required to have a τ^+ , a τ^- and an $l^+ l^-$ recoil mass close to the Higgs mass. The signal events were selected with an efficiency of 47% and 62% for the $e^+ e^-$ and $\mu^+ \mu^-$ channels, respectively. The S/N was 1.43 (1.44) for $e^+ e^-$ ($\mu^+ \mu^-$), and the signal significance was 8.0σ (8.8σ) for the $e^+ e^-$ ($\mu^+ \mu^-$) channel.

In the case of $Z \rightarrow q\bar{q}$, a tau-jet was formed using an energetic track and all particles within 0.2 radians of the energetic track. The mass of a tau-jet was required to be less than 2 GeV, and additional cuts on the τ energy and isolation were applied to reduce mis-identified quark jets. Low energy charged tracks found in a jet were detached one by one until a unit charged jet with 1 or 3 prong charged multiplicity was obtained. Once a tau jet pair was found, the kinematics of the tau jet pair were reconstructed assuming that the visible tau decay products and neutrinos were collinear, and that the missing momentum of the event was generated only by the neutrinos from the tau decays. Following the reconstruction of the two τ jets, $q\bar{q}$ jets were reconstructed by clustering the remaining particles with the Durham jet algorithm. Variables such as jet mass, energy, and production angle were used together with particle multiplicities and the impact parameters of tracks from τ jets to select $Zh \rightarrow q\bar{q}\tau^+\tau^-$ events. The efficiency for signal selection was about 0.24 and the S/N was 1.85. With an integrated luminosity of 250 fb^{-1} , the signal significance was 25.8σ .

If we combine the results for $Z \rightarrow l^+ l^-$ and $Z \rightarrow q\bar{q}$, the significance is 28.4 , which corresponds to a measurement accuracy of $\Delta(\sigma \cdot BR)/(\sigma \cdot BR) = 3.5\%$. Table 4.2 shows the extrapolation of this result to the case of $m_h = 125$ GeV, where it was assumed that the signal selection efficiency is unchanged.

Table 4.2. Relative error on $\sigma \cdot BR$ at $\sqrt{s} = 250$ GeV for $h \rightarrow \tau^+ \tau^-$ assuming $m_h = 125$ GeV, 250 fb^{-1} luminosity and beam polarization $P(e^-) = -80\%$ and $P(e^+) = +30\%$. The results were obtained by scaling the errors for $m_h = 120$ GeV.

$Z \rightarrow e^+ e^-$	$Z \rightarrow \mu^+ \mu^-$	$Z \rightarrow q\bar{q}$	Combined	$\frac{\Delta(\sigma \cdot BR)}{(\sigma \cdot BR)}$
6.8σ	7.4σ	21.9σ	24.1σ	4.2%

4.3.2 **500 GeV**

The decay $h \rightarrow \tau^+ \tau^-$ was studied at $\sqrt{s} = 500$ GeV using the ILD full simulation with $m_h = 125$ GeV [242]. At this energy both Higgsstrahlung and WW fusion processes contribute with comparable weight.

For the Higgsstrahlung process $e^+ e^- \rightarrow Zh \rightarrow q\bar{q}h$, methods similar to those used at $\sqrt{s} = 250$ GeV were employed. A signal efficiency of 21.0% and a precision of $\frac{\Delta(\sigma_{ZH} \cdot BR)}{\sigma_{ZH} \cdot BR} = 5.4\%$ were obtained for $-80\%/+30\%$ e^-/e^+ polarization and 500 fb^{-1} luminosity. Further improvement is expected by including the $Z \rightarrow \ell\bar{\ell}$ mode.

In the WW fusion case $e^+ e^- \rightarrow \nu_e \bar{\nu}_e h \rightarrow \nu_e \bar{\nu}_e \tau^+ \tau^-$, a jet with mass less than 2 GeV was considered a τ jet. The most energetic τ^+ and τ^- were combined as the Higgs boson, and cuts were

applied to the tau pair mass and event missing energy. A signal efficiency of 25% and a precision of $\frac{\Delta(\sigma_{\nu_e \bar{\nu}_e h \cdot BR})}{\sigma_{\nu_e \bar{\nu}_e h \cdot BR}} = 9.0\%$ were obtained for -80%/+30% e^-/e^+ polarization and 500 fb⁻¹ luminosity.

Chapter 5

Cross Section Times Branching Ratio Measurements II

5.1

$h \rightarrow ZZ^*$

A full simulation study of the decay $h \rightarrow ZZ^*$ has been performed using the process $e^+e^- \rightarrow Zh \rightarrow ZZZ^*$ at $\sqrt{s} = 250$ GeV. This decay has a SM branching ratio of 2.7% given the Higgs mass of 125 GeV. The final state is characterized by two on-shell Z bosons and one off-shell Z boson, leading to a variety of combinations of jets, isolated leptons and missing energy. The analysis is directed toward topologies where the Z opposite the Higgs boson decays in any manner $Z \rightarrow q, l, \nu$, while the Higgs decays without missing energy, $h \rightarrow ZZ^* \rightarrow q\bar{q}$ or l^+l^- , $l = e, \mu$. The datasets used for this analysis are shown in Table 5.1.

5.1.1

Event reconstruction for $h \rightarrow ZZ^*$

Events are classified as 6-jet or 4-jet, depending on whether the visible energy in the event is greater or less than 140 GeV; here the term “jet” can also refer to an isolated electron or muon.

In the low visible energy signal events we expect a 4-jet topology if the Z and Z^* decay visibly. One pair of jets must have a mass consistent with the Z mass. Events that have opposite signed electrons or muons with a mass consistent with the Z mass are unlikely to come from the WW background. Because of large missing energy and momentum from the invisible Z decay, it is unlikely that the reconstructed Z bosons are back-to-back and so we cut on the angle between them. Cutting on the number of tracks helps to remove much of the two-photon background.

The high visible energy signal events are largely true six jet events with all Z bosons decaying visibly. Backgrounds that come from ZZ and WW decays can be cut using the Durham jet clustering y_{24} and y_{56} variables. All pairs of jets are tried for the pair most consistent with the mass of the Z . Then from the remaining jets, the next pair most consistent with the mass of the Z is found and the remaining pair is taken as coming from the Z^* . Each Z is then paired with the Z^* to see which one gives a mass most consistent with coming from a 125 GeV Higgs. The analysis then proceeds similarly to the 4 jet analysis using this pair of ZZ^* .

Before applying an MVA selection, preselection cuts are applied separately for $E_{vis} < 140$ GeV and $E_{vis} > 140$ GeV. The preselection cuts exclude regions only where there is almost no signal. Events are preselected based on the Higgs topology being studied using the criteria shown in Table 5.2.

Table 5.1. Simulated data samples used for the $\nu_e \bar{\nu}_e h$ analysis.

Process	$P(e^-)/P(e^+)$	N_{Events}
$f^+ f^- h \rightarrow ZZ^*$	+80%/-30%	120,012
All SM background mix	+80%/-30%	2,058,374

Table 5.2. Overview of the preselections for the different Higgs decay modes. The cuts as well as the efficiencies for signal and background events are shown.

Higgs decay	Preselection cuts	Signal eff.	Background eff.
$h \rightarrow ZZ^*(E_{vis} < 140\text{GeV})$	$25 < p_{vis}^T < 70 \text{ GeV}$ $95. < M_{vis}^{higgs} < 140. \text{ GeV}$ $ \cos(\theta_{jet}) < 0.90$ $N_{PFO} > 5$ $y_{34} > 0.$ $E_Z > 120\text{GeV}$		
$h \rightarrow ZZ^*(E_{vis} > 140\text{GeV})$	$90. < M_{vis}^{higgs} < 160. \text{ GeV}$ $ \cos(\theta_{jet}) < 0.90$ $N_{PFO} > 5$ $y_{34} > 0.$ $E_Z > 120\text{GeV}$ $ \text{thrust} \geq 0.98$		
Both		77%	1.5×10^{-2}

5.1.2 Multi-Variate Analysis

After the preselection, multivariate methods, as implemented in TMVA, are then used to maximize the significance ($S/\sqrt{S+B}$) of the selection. They are trained using 50% of the signal and background events and done separately for the different polarizations and integrated luminosities. The cuts on the Fisher discriminant which maximize the significance for each decay mode are used to obtain the final results. The input variables for the multivariate methods are:

- visible mass of the event
- the visible energy, mass and transverse momentum
- B-Likeness from b-tag flavor tagging values
- C-likeness from c-tag flavor tagging values
- Number of High Energy Electrons
- Higgs Mass = mass of the reconstructed ZZ^*
- reconstructed Z energy
- reconstructed Z^* energy
- cosine of the reconstructed Z polar angle
- cosine of the reconstructed Z^* polar angle
- reconstructed Z mass
- reconstructed Z^* mass
- the angle between the reconstructed Z and Z^* in the plane perpendicular to the beam axis.
- the event thrust magnitude
- number Charged Tracks
- number of identified electrons
- number of identified muons
- Durham jet clustering y_{34} value
- Durham jet clustering y_{56} value
- lepton pair (PDG ID1 = -ID2) mass closest to $m(Z)$

- jet pair mass closest to $m(W)$
- sum of the absolute differences of the best W jet pair mass w.r.t. $m(W)$

The flavor tagging is used as implemented in the LCFIPlus package which uses boosted decision trees on vertexing quantities to determine b-tag and c-tag probabilities for bottom and charm jets respectively. It is trained using samples of four-jet events from $ZZ^* \rightarrow b\bar{b}, c\bar{c}$ and $q\bar{q}$ at $\sqrt{s} = 350$ GeV and the tagging is accordingly applied to all signal and background samples.

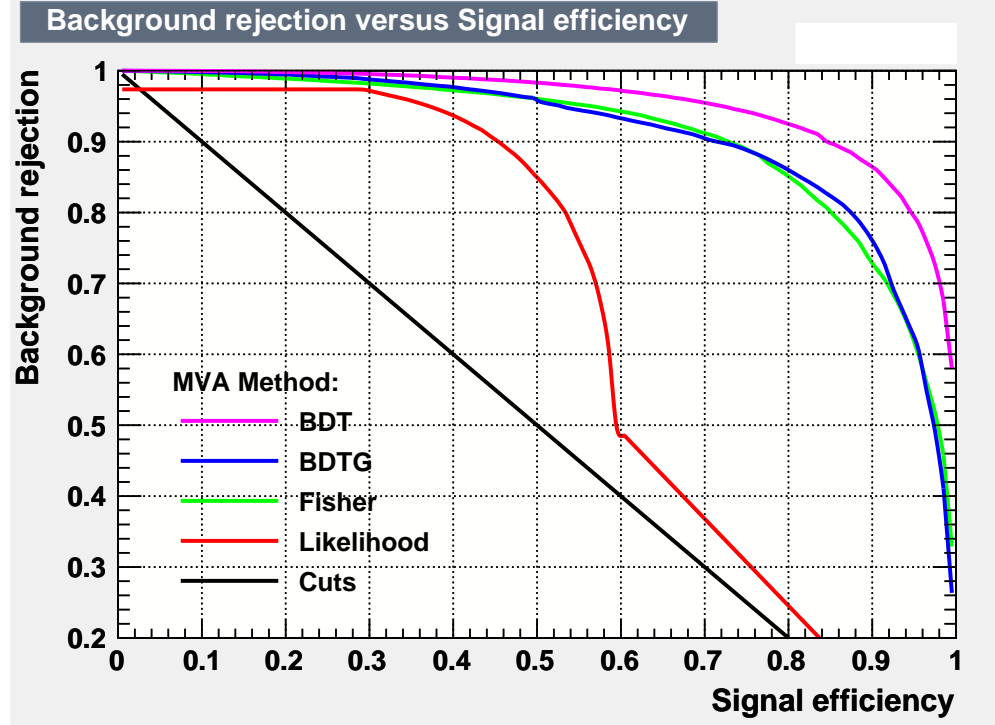


Figure 5.1. Rejection of background vs. signal for selecting Higgs boson decays to ZZ^* from the BDT, BDTG, Fisher, Likelihood and CUTS multivariate methods.

The performance of the various MVA methods is shown in Figure 5.1. It is found that the BDT method significantly out performs the other methods. Plots showing the efficiency and significance curves vs. cuts on the BDT output are shown in Figure 5.2.

The composition of the samples of events passing all selections of the analysis are shown in Table 5.3 for the polarization $P(e^-) = +80\%$, $P(e^+) = -30\%$ and 250 fb^{-1} . The fraction of events passing all selections is 10.8% for the signal and 0.0008% for the background. The significance of the signal after the preselection is 1.0. After applying the cut on the BDT output, the significance is 5.6.

Table 5.3. Composition of the events passing all analysis selections for the polarizations $P(e^-) = +80\%$, $P(e^+) = -30\%$ and an integrated luminosity of 250 fb^{-1} collected by SiD at a center of mass energy of 250 GeV.

	$h \rightarrow ZZ^*$ (%)
$e^+e^- \rightarrow 2 \text{ fermions}$	50
$e^+e^- \rightarrow 4 \text{ fermions}$	462
$e^+e^- \rightarrow 6 \text{ fermions}$	0
$\gamma\gamma \rightarrow X$	0
$\gamma e^\pm \rightarrow X$	0
$e^\pm \gamma \rightarrow X$	0
$qqh \rightarrow ZZ^*$	68
$eeh, \mu\mu h \rightarrow ZZ^*$	24
$\tau\tau h \rightarrow ZZ^*$	3
$\nu\nu h \rightarrow ZZ^*$	49

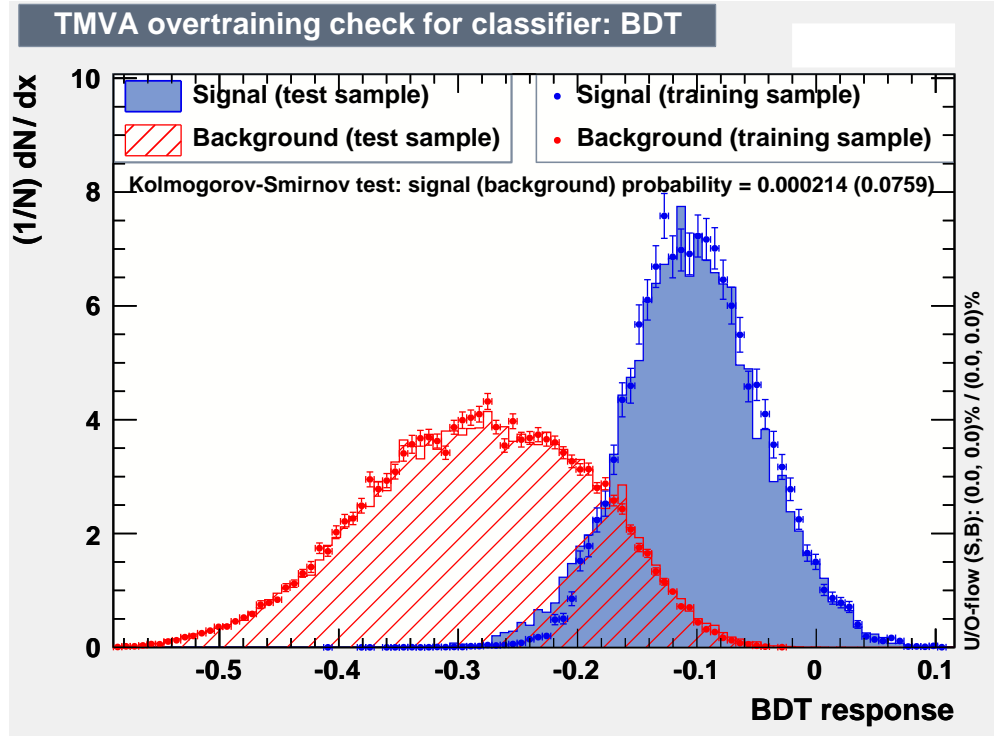


Figure 5.2. The multi-variate BDT output for the signal ($h \rightarrow ZZ^*$) and background for the training samples and test samples (points).

5.1.3 Results for $f^+f^-h \rightarrow ZZ^*$

The uncertainties on the cross sections times Higgs branching fractions, $\Delta(\sigma \times BR)$, are determined from the numbers of signal and background events passing each selection. For 250 fb^{-1} of e^+e^- $P(e^-) = +80\%$, $P(e^+) = -30\%$ 250 GeV collisions in the SiD detector this benchmark indicates that a precision of 18% can be obtained.

5.2 $h \rightarrow \gamma\gamma$

Fast Monte Carlo studies of $e^+e^- \rightarrow Zh \rightarrow f\bar{f}\gamma\gamma$, $f = q, \nu$ at $\sqrt{s} = 250$ GeV [243] and $e^+e^- \rightarrow \nu\bar{\nu}h \rightarrow \nu\bar{\nu}\gamma\gamma$ at $\sqrt{s} = 1000$ GeV [244] have been supplemented recently with a full simulation study of $e^+e^- \rightarrow f\bar{f}h \rightarrow f\bar{f}\gamma\gamma$, $f = q, \nu$ at $\sqrt{s} = 250$ GeV and 500 GeV [245]. These studies indicate that the ILC can measure $\sigma \cdot BR(h \rightarrow \gamma\gamma)$ with an accuracy of 34% using $e^+e^- \rightarrow Zh$ at $\sqrt{s} = 250$ GeV assuming 250 fb^{-1} . The process $e^+e^- \rightarrow \nu\bar{\nu}h \rightarrow \nu\bar{\nu}\gamma\gamma$ yields errors of 23% for 500 fb^{-1} at $\sqrt{s} = 500$ GeV and 8.5% for 1000 fb^{-1} at $\sqrt{s} = 1000$ GeV.

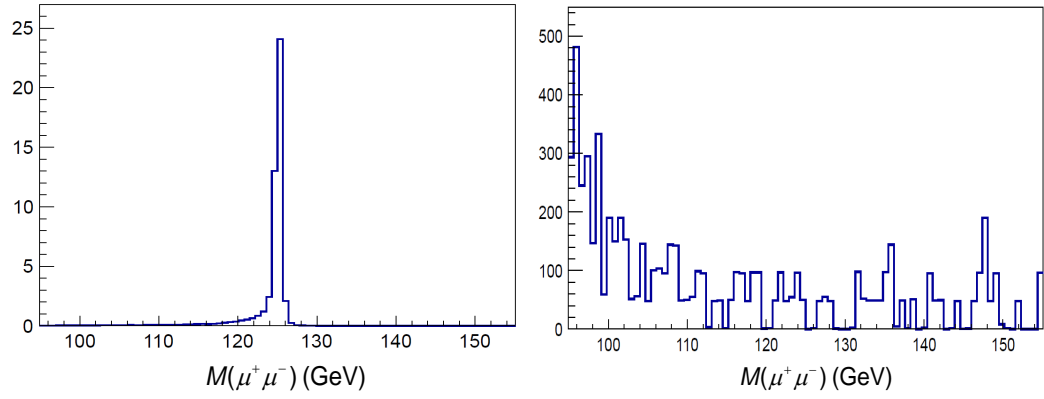


Figure 5.3. Muon pair mass for $e^+e^- \rightarrow \nu\bar{\nu}h \rightarrow \nu\bar{\nu}\mu^+\mu^-$ at $\sqrt{s} = 1000$ GeV (left) and for all Standard Model background (right) following all cuts. The plots are normalized to 1000 fb^{-1} luminosity.

5.3

$h \rightarrow \mu^+ \mu^-$

The decay $h \rightarrow \mu^+ \mu^-$ has been studied using $e^+e^- \rightarrow Zh \rightarrow q\bar{q}\mu^+\mu^-$ at $\sqrt{s} = 250$ GeV [222] and $e^+e^- \rightarrow \nu\bar{\nu}h \rightarrow \nu\bar{\nu}\mu^+\mu^-$ at $\sqrt{s} = 1000$ GeV [5]. This decay has a SM branching ratio of 0.02%. The very small event rate at the ILC can be compensated somewhat by the excellent $\delta(1/p_T) \sim 2\text{--}5 \times 10^{-5} (\text{GeV}/c)^{-1}$ charged particle momentum resolution of the ILD and SiD detectors.

At $\sqrt{s} = 250$ GeV the largest background is $e^+e^- \rightarrow ZZ \rightarrow q\bar{q}\mu^+\mu^-$. Following all cuts an error of 91% for $\sigma \cdot BR(h \rightarrow \mu^+\mu^-)$ was obtained in Ref. [222] for 250 fb^{-1} assuming a 120 GeV Higgs mass. Scaling to a Higgs mass of 125 GeV this error becomes 100%.

Figure 5.3 shows the reconstructed muon pair mass distributions for signal and background after all cuts at $\sqrt{s} = 1000$ GeV. At this center of mass energy the largest backgrounds following all cuts are $e^+e^- \rightarrow \nu_e\bar{\nu}_e\mu^+\mu^-$, $e^+e^- \rightarrow W^+W^- \rightarrow \nu_\mu\bar{\nu}_\mu\mu^+\mu^-$, and $\gamma\gamma \rightarrow W^+W^- \rightarrow \nu_\mu\bar{\nu}_\mu\mu^+\mu^-$. With 1000 fb^{-1} an error of 31% was obtained in Ref. [5].

5.4

Invisible Higgs Decays

The h decay to invisible final states, if any, can be measured by looking at the recoil mass under the condition that nothing observable is recoiling against the Z boson. Higgs portal models predict such decays and provide a unique opportunity to access dark matter particles [246]. The main background is $e^+e^- \rightarrow ZZ$ followed by one Z decaying into a lepton pair or quark pair, and the other into a neutrino pair. With an integrated luminosity of 250 fb^{-1} at $\sqrt{s} = 250$ GeV, the ILC can set a 95% CL limit on the invisible branching ratio of 4.8% using the golden $Z \rightarrow \mu^+\mu^-$ mode alone [247]. Using other modes including $Z \rightarrow q\bar{q}$, we can improve this significantly to 0.9% [248]. Assuming a luminosity of 1150 fb^{-1} at $\sqrt{s} = 250$ GeV the 95% CL limit is 0.4%

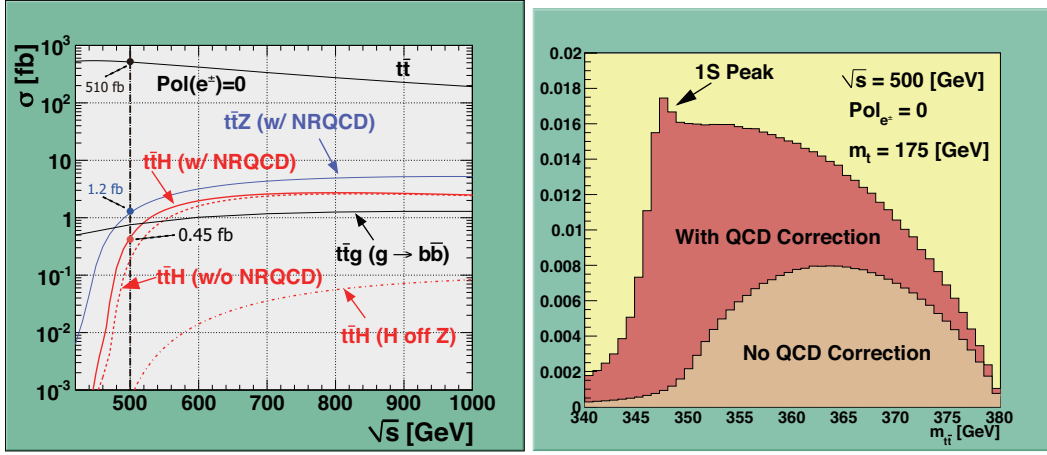


Figure 5.4. Left: Cross section for the $e^+e^- \rightarrow t\bar{t}h$ process as a function of \sqrt{s} , together with those of background processes, $e^+e^- \rightarrow t\bar{t}Z$, $\rightarrow t\bar{t}g^*$, and $\rightarrow t\bar{t}$. Right: The invariant mass distribution of the $t\bar{t}$ system from the $e^+e^- \rightarrow t\bar{t}h$ process with and without the non-relativistic QCD correction.

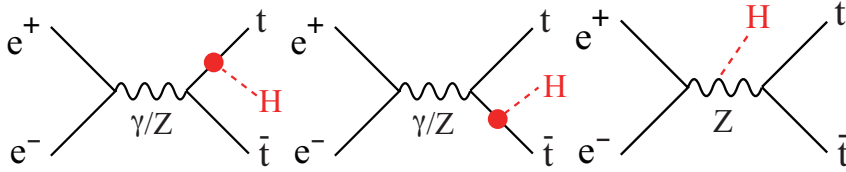


Figure 5.5. Three diagrams contributing to the $e^+e^- \rightarrow t\bar{t}h$ process. The h -off- t or \bar{t} diagrams, (a) and (b), contain the top Yukawa coupling while the h -off- Z diagram (c) does not.

5.5 Top Yukawa Coupling Measurement

The cross section for the process $e^+e^- \rightarrow t\bar{t}h$ is significantly enhanced near the threshold due to the bound-state effects between t and \bar{t} [249, 250, 251, 252, 253, 254, 255]. The effect is made obvious in the right-hand plot of Fig. 5.4. This enhancement implies that the measurement of the top Yukawa coupling might be possible already at $\sqrt{s} = 500$ GeV [256]. A serious simulation study at $\sqrt{s} = 500$ GeV was performed for the first time, with the QCD bound-state effects consistently taken into account for both signal and background cross sections, in [257].

The $e^+e^- \rightarrow t\bar{t}h$ reaction takes place through the three diagrams shown in Fig. 5.5. As shown in Fig. 5.4 (left), the contribution from the irrelevant h -off- Z diagram is negligible at $\sqrt{s} = 500$ GeV, thereby allowing us to extract the top Yukawa coupling g_t by just counting the number of signal events. By combining the 8-jet and 6-jet-plus-lepton modes of $e^+e^- \rightarrow t\bar{t}h$ followed by $h \rightarrow b\bar{b}$, the analysis of [257] showed that a measurement of the top Yukawa coupling to $\Delta g_t/g_t = 14.1\%$ is possible for $m_h = 120$ GeV with polarized electron and positron beams of $(P_{e^-}, P_{e^+}) = (-0.8, +0.3)$ and an integrated luminosity of 500 fb^{-1} . This result obtained with a fast Monte Carlo simulation has just recently been corroborated by a full simulation [258]. When extrapolated to $m_h = 125$ GeV, and taking into account a recent analysis improvement, the corresponding expected precision would be $\Delta g_t/g_t = 14.0\%$.

It should be noted that a small increase in the center of mass energy beyond $\sqrt{s} = 500$ GeV can increase the cross section for $e^+e^- \rightarrow t\bar{t}h$ significantly, as can be seen in Fig. 5.4. By increasing the center of mass energy to $\sqrt{s} = 520$ GeV, for example, the cross section for $e^+e^- \rightarrow t\bar{t}h$ can be doubled and hence the precision can be improved to 9.9% assuming 500 fb^{-1} .

The 14% accuracy on the top quark Yukawa coupling expected at $\sqrt{s} = 500$ GeV can be significantly improved by the data taken at 1000 GeV, thanks to the larger cross section and the less

Figure 5.6
Relevant diagrams
containing the triple
Higgs coupling for
the two processes:
 $e^+e^- \rightarrow Zhh$ (left)
and $e^+e^- \rightarrow \nu_e\bar{\nu}_e hh$.

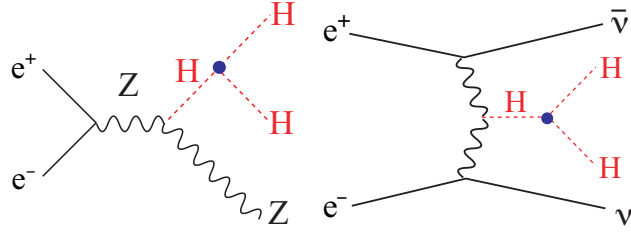
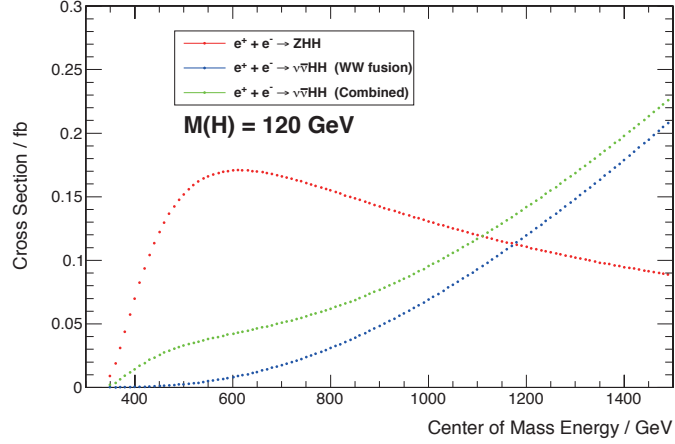


Figure 5.7
Cross sections for
the two processes
 $e^+e^- \rightarrow Zhh$ (left)
and $e^+e^- \rightarrow \nu_e\bar{\nu}_e hh$
as a function of \sqrt{s} for
 $m_h = 120$ GeV.



background from $e^+e^- \rightarrow t\bar{t}$. Fast simulations at $\sqrt{s} = 800$ GeV showed that we would be able to determine the top Yukawa coupling to 6% for $m_h = 120$ GeV, given an integrated luminosity of 1 ab^{-1} and residual background uncertainty of 5% [259, 260]. As described in the Detector Volume of the ILC TDR [5] full simulations just recently completed by SiD and ILD show that the top Yukawa coupling can indeed be measured to a statistical precision of 3.1% for $m_h = 125$ GeV with 1 ab^{-1} .

With luminosities of 1600 fb^{-1} at 500 GeV and 2500 fb^{-1} at 1000 GeV, the statistical precision can be improved to 2.0%.

5.6

Higgs Self Coupling Measurement

The triple Higgs boson coupling can be studied at the ILC through the processes $e^+e^- \rightarrow Zhh$ and $e^+e^- \rightarrow \nu_e\bar{\nu}_e hh$. The relevant Feynman diagrams are shown in Fig. 5.6 [72]. The cross sections for the two processes are plotted as a function of \sqrt{s} for $m_h = 120$ GeV in Fig. 5.7. The cross section reaches its maximum of about 0.18 fb at around $\sqrt{s} = 500$ GeV, which is dominated by the former process.

A full simulation study of the process $e^+e^- \rightarrow Zhh$ followed by $h \rightarrow b\bar{b}$ at $\sqrt{s} = 500$ GeV has recently been carried out using the ILD detector [261]. From the combined result of the three channels corresponding to different Z decay modes, $Z \rightarrow l^+l^-$, $\nu\bar{\nu}$, and $q\bar{q}$, it was found that the process can be detected with an excess significance of $4.5\text{-}\sigma$ and the cross section can be measured to $\Delta\sigma/\sigma = 0.30$ for an integrated luminosity of 1.6 ab^{-1} with beam polarization $(P_{e^-}, P_{e^+}) = (-0.8, +0.3)$. Unlike the $e^+e^- \rightarrow t\bar{t}h$ case, however, the contribution from the background diagrams without the self-coupling is significant and the relative error on the self-coupling λ is $\Delta\lambda/\lambda = 0.49$ with a proper event weighting to enhance the contribution from the self-coupling diagram. When extrapolated to $m_h = 125$ GeV, taking into account a 20% relative improvement expected from a recent preliminary full simulation result including $hh \rightarrow b\bar{b}WW^*$ mode, the precision would be improved to 46%.

At $\sqrt{s} = 1000$ GeV, the $e^+e^- \rightarrow \nu\bar{\nu}hh$ process will become significant [262]. The cross section for this process is only about 0.07 fb^{-1} , but the sensitivity to the self-coupling is potentially higher since the contribution from the background diagrams is smaller, leading to the relation

Table 5.4. Expected accuracies for cross section and cross section times branching ratio measurements for the 125 GeV h boson assuming you run 3×10^7 s at the baseline differential luminosity for each center of mass energy. For invisible decays of the Higgs, the number quoted is the 95% confidence upper limit on the branching ratio.

\sqrt{s} and \mathcal{L} (P_{e-}, P_{e+})	250 fb $^{-1}$ at 250 GeV (-0.8,+0.3)		500 fb $^{-1}$ at 500 GeV (-0.8,+0.3)				1 ab $^{-1}$ at 1 TeV (-0.8,+0.2)		
	Zh	$\nu\bar{\nu}h$	Zh	$\nu\bar{\nu}h$	tth	Zhh	$\nu\bar{\nu}h$	tth	$\nu\bar{\nu}hh$
$\Delta\sigma/\sigma$	2.6%	-	3.0	-	-	42.7%	-	-	26.3%
BR(invis.)	< 0.9 %	-	-	-	-	-	-	-	-
mode	$\Delta(\sigma \cdot BR)/(\sigma \cdot BR)$								
$h \rightarrow b\bar{b}$	1.2%	10.5%	1.8%	0.7%	28%	-	0.5%	6.0%	-
$h \rightarrow c\bar{c}$	8.3%	-	13%	6.2%	-	-	3.1%	-	-
$h \rightarrow gg$	7.0%	-	11%	4.1%	-	-	2.3%	-	-
$h \rightarrow WW^*$	6.4%	-	9.2%	2.4%	-	-	1.6%	-	-
$h \rightarrow \tau^+\tau^-$	4.2%	-	5.4%	9.0%	-	-	3.1%	-	-
$h \rightarrow ZZ^*$	18%	-	25%	8.2%	-	-	4.1%	-	-
$h \rightarrow \gamma\gamma$	34%	-	34%	23%	-	-	8.5%	-	-
$h \rightarrow \mu^+\mu^-$	100%	-	-	-	-	-	31%	-	-

Table 5.5. Expected accuracies for cross section and cross section times branching ratio measurements for the 125 GeV h boson assuming you run 3×10^7 s at the sum of the baseline and upgrade differential luminosities for each center of mass energy. For invisible decays of the Higgs, the number quoted is the 95% confidence upper limit on the branching ratio.

\sqrt{s} and \mathcal{L} (P_{e-}, P_{e+})	1150 fb $^{-1}$ at 250 GeV (-0.8,+0.3)		1600 fb $^{-1}$ at 500 GeV (-0.8,+0.3)				2.5 ab $^{-1}$ at 1 TeV (-0.8,+0.2)		
	Zh	$\nu\bar{\nu}h$	Zh	$\nu\bar{\nu}h$	tth	Zhh	$\nu\bar{\nu}h$	tth	$\nu\bar{\nu}hh$
$\Delta\sigma/\sigma$	1.2%	-	1.7	-	-	23.7%	-	-	16.7%
BR(invis.)	< 0.4 %	-	-	-	-	-	-	-	-
mode	$\Delta(\sigma \cdot BR)/(\sigma \cdot BR)$								
$h \rightarrow b\bar{b}$	0.6%	4.9%	1.0%	0.4%	16%	-	0.3%	3.8%	-
$h \rightarrow c\bar{c}$	3.9%	-	7.2%	3.5%	-	-	2.0%	-	-
$h \rightarrow gg$	3.3%	-	6.0%	2.3%	-	-	1.4%	-	-
$h \rightarrow WW^*$	3.0%	-	5.1%	1.3%	-	-	1.0%	-	-
$h \rightarrow \tau^+\tau^-$	2.0%	-	3.0%	5.0%	-	-	2.0%	-	-
$h \rightarrow ZZ^*$	8.4%	-	14%	4.6%	-	-	2.6%	-	-
$h \rightarrow \gamma\gamma$	16%	-	19%	13%	-	-	5.4%	-	-
$h \rightarrow \mu^+\mu^-$	46.6%	-	-	-	-	-	20%	-	-

$\Delta\lambda/\lambda \simeq 0.85 \times (\Delta\sigma_{\nu\bar{\nu}hh}/\sigma_{\nu\bar{\nu}hh})$, as compared to $\Delta\lambda/\lambda \simeq 1.8 \times (\Delta\sigma_{Zhh}/\sigma_{Zhh})$ for the $e^+e^- \rightarrow Zhh$ process at 500 GeV. The measurement of the self-coupling has been studied at 1 TeV with full simulation. That analysis is described in the Detector Volume of the ILC TDR [5]. The result, for 2.5 ab^{-1} with $(P_{e-}, P_{e+}) = (-0.8, +0.2)$, is $\Delta\lambda/\lambda \simeq 0.16$ for $m_h = 125$ GeV. This has recently been improved to 13% with the inclusion of the $hh \rightarrow b\bar{b}WW^*$ mode [263]. Further improvements would be possible by adding more decay modes and/or improvements in jet clustering ¹.

5.7 Cross Section Times Branching Ratio Summary

The accuracies for all cross section and $\sigma \cdot BR$ measurements considered in this paper are summarized in Table 5.4 and Table 5.5. Table 5.4 shows the accuracies assuming you run 3×10^7 s at the baseline differential luminosity for each of the center of mass energies 250, 500 and 1000 GeV. Table 5.5 gives the accuracies when you add the luminosities of Table 5.4 to 3×10^7 s times the upgraded differential luminosities at each of the three center of mass energies.

¹With perfect jet clustering we expect a 40% relative improvement in the self-coupling precision.

Chapter 6

Higgs Couplings, Total Width and Branching Ratios

6.1 Model Independent Determination of Higgs Couplings

The sigma times branching ratio measurements in the previous chapters imply a very high level of precision for the various Higgs boson couplings. To quantify this we perform a global fit of the Higgs boson couplings and total Higgs width using all the available cross section and cross section times branching ratio data.

Before discussing the global fit in detail, it would be helpful to show an example explaining how we get the absolute couplings and Higgs total width. Let's look at the following four independent measurements:

$$\begin{aligned}
 Y_1 &= \sigma_{ZH} = F_1 \cdot g_{HZZ}^2 \\
 Y_2 &= \sigma_{ZH} \times \text{Br}(H \rightarrow b\bar{b}) = F_2 \cdot \frac{g_{HZZ}^2 g_{Hb\bar{b}}^2}{\Gamma_T} \\
 Y_3 &= \sigma_{\nu\bar{\nu}H} \times \text{Br}(H \rightarrow b\bar{b}) = F_3 \cdot \frac{g_{HWW}^2 g_{Hb\bar{b}}^2}{\Gamma_T} \\
 Y_4 &= \sigma_{\nu\bar{\nu}H} \times \text{Br}(H \rightarrow WW^*) = F_4 \cdot \frac{g_{HWW}^4}{\Gamma_T},
 \end{aligned}$$

where Γ_T is the Higgs total width, g_{HZZ} , g_{HWW} , and $g_{Hb\bar{b}}$ are the couplings of the Higgs to ZZ , WW , and $b\bar{b}$, respectively, and F_1 , F_2 , F_3 , F_4 are calculable quantities. It is straightforward to get the couplings with the following steps:

- i.) from measurement Y_1 we can get the coupling g_{HZZ} .
- ii.) from the ratio Y_2/Y_3 we can get the coupling ratio g_{HZZ}/g_{HWW} .
- iii.) with g_{HZZ} and g_{HZZ}/g_{HWW} , we can get g_{HWW} .
- iv.) once we know g_{HWW} , from measurement Y_4 we can get the Higgs total width Γ_T .
- v.) once we know g_{HZZ} , g_{HWW} and Γ_T , from measurement Y_2 or Y_3 we can get $g_{Hb\bar{b}}$.

This example already gave quite clear synergy between the two main Higgs production channels. The best energy to investigate the Higgsstrahlung production $e^+e^- \rightarrow ZH$ is around 250 GeV, however the $e^+e^- \rightarrow \nu\bar{\nu}H$ at 250 GeV is very small. WW-fusion production will be fully open at 500 GeV with cross section one order of magnitude larger. This is one essential motivation to go to higher energy after running at 250 GeV.

We discuss in detail the model independent fit of the Higgs couplings for the ILC(1000) luminosity scenario. For this scenario the 33 independent $\sigma \times \text{Br}$ measurements in Table 5.4 are used as experimental input. The $\sigma \times \text{Br}$ measurements are labelled with Y_i , $i = 1, 2, \dots, 33$. The predicted values of these measurements as a function of the Higgs couplings are given by $Y'_i = F_i \cdot \frac{g_{HZZ}^2 g_{HXX}^2}{\Gamma_T}$,

Table 6.1. Expected accuracies $\Delta g_i/g_i$ for Higgs boson couplings for a completely model independent fit assuming theory errors of $\Delta F_i/F_i = 0.1\%$

Mode	ILC(250)	ILC(500)	ILC(1000)	ILC(LumUp)
$\gamma\gamma$	18 %	8.4 %	4.0 %	2.4 %
gg	6.4 %	2.3 %	1.6 %	0.9 %
WW	4.8 %	1.1 %	1.1 %	0.6 %
ZZ	1.3 %	1.0 %	1.0 %	0.5 %
$t\bar{t}$	—	14 %	3.1 %	1.9 %
$b\bar{b}$	5.3 %	1.6 %	1.3 %	0.7 %
$\tau^+\tau^-$	5.7 %	2.3 %	1.6 %	0.9 %
$c\bar{c}$	6.8 %	2.8 %	1.8 %	1.0 %
$\mu^+\mu^-$	91 %	91 %	16 %	10 %
$\Gamma_T(h)$	12 %	4.9 %	4.5 %	2.3 %

Table 6.2. Expected accuracies $\Delta g_i/g_i$ for Higgs boson couplings for a completely model independent fit assuming theory errors of $\Delta F_i/F_i = 0.5\%$

Mode	ILC(250)	ILC(500)	ILC(1000)	ILC(LumUp)
$\gamma\gamma$	18 %	8.4 %	4.0 %	2.4 %
gg	6.4 %	2.3 %	1.6 %	0.9 %
WW	4.9 %	1.2 %	1.1 %	0.6 %
ZZ	1.3 %	1.0 %	1.0 %	0.5 %
$t\bar{t}$	—	14 %	3.2 %	2.0 %
$b\bar{b}$	5.3 %	1.7 %	1.3 %	0.8 %
$\tau^+\tau^-$	5.8 %	2.4 %	1.8 %	1.0 %
$c\bar{c}$	6.8 %	2.8 %	1.8 %	1.1 %
$\mu^+\mu^-$	91 %	91 %	16 %	10 %
$\Gamma_T(h)$	12 %	5.0 %	4.6 %	2.5 %

or $Y'_i = F_i \cdot \frac{g_{HWW}^2 g_{HXX}^2}{\Gamma_T}$, $Y'_i = F_i \cdot \frac{g_{Htt}^2 g_{HXX}^2}{\Gamma_T}$, where XX means some specific decay particle from Higgs and F_i is some factor corresponding to the decay. In addition we have one absolute cross section measurement $Y_{34} = \sigma_{ZH}$ which can be predicted as $Y'_{34} = F_{34} \cdot g_{HZZ}^2$. In total we have 34 independent measurements and 10 fit parameters consisting of 9 fundamental couplings HZZ , HWW , $Hb\bar{b}$, $Hc\bar{c}$, Hgg , $H\tau^+\tau^-$, $H\mu\mu$, $Ht\bar{t}$ and $H\gamma\gamma$, and the Higgs total width Γ_T .

The factors F_i can be written

$$F_i = S_i G_i \quad \text{where } S_i = \left(\frac{\sigma_{ZH}}{g_Z^2}\right), \left(\frac{\sigma_{\nu\bar{\nu}H}}{g_W^2}\right), \text{ or } \left(\frac{\sigma_{t\bar{t}H}}{g_t^2}\right), \text{ and } G_i = \left(\frac{\Gamma_i}{g_i^2}\right). \quad (6.1)$$

These are theoretical calculations with parametric and theoretical uncertainties. Because the relevant quantities are ratios of cross sections and partial widths to couplings squared, the total theory errors for S_i , and particularly G_i , should be less than the total theory errors for the corresponding cross sections and partial widths. We believe that a total theory error of 0.5% or less can be achieved for the F_i parameters at the time of ILC running. We quote coupling results assuming total theory errors of $\Delta F_i/F_i = 0.1\%$ and $\Delta F_i/F_i = 0.5\%$.

The fitted couplings and width are obtained by minimizing the chi-square function χ^2 defined by

$$\chi^2 = \sum_{i=1}^{34} \left(\frac{Y_i - Y'_i}{\Delta Y_i} \right)^2, \quad (6.2)$$

where ΔY_i is the square root of the sum in quadrature of the error on the measurement Y_i and the total theory error for Y'_i . The results for theory errors of $\Delta F_i/F_i = 0.1\%$ and $\Delta F_i/F_i = 0.5\%$ are summarized in Table 6.1 and Table 6.2, respectively.

Table 6.3. Summary of expected accuracies for the three cross sections and eight branching ratios obtained from an eleven parameter global fit of all available data.

	ILC(250)	ILC500	ILC(1000)	ILC(LumUp)
process	$\Delta\sigma/\sigma$			
$e^+e^- \rightarrow ZH$	2.6 %	2.0 %	2.0 %	1.0 %
$e^+e^- \rightarrow \nu\bar{\nu}H$	11 %	2.3 %	2.2 %	1.1 %
$e^+e^- \rightarrow t\bar{t}H$	-	28 %	6.3 %	3.8 %
mode	$\Delta\text{Br}/\text{Br}$			
$H \rightarrow ZZ$	19 %	7.5 %	4.2 %	2.4 %
$H \rightarrow WW$	6.9 %	3.1 %	2.5 %	1.3 %
$H \rightarrow b\bar{b}$	2.9 %	2.2 %	2.2 %	1.1 %
$H \rightarrow c\bar{c}$	8.7 %	5.1 %	3.4 %	1.9 %
$H \rightarrow gg$	7.5 %	4.0 %	2.9 %	1.6 %
$H \rightarrow \tau^+\tau^-$	4.9 %	3.7 %	3.0 %	1.6 %
$H \rightarrow \gamma\gamma$	34 %	17 %	7.9 %	4.7 %
$H \rightarrow \mu^+\mu^-$	100 %	100 %	31 %	20 %

6.2 Model Independent Determination of Higgs Cross Sections and Higgs Branching Ratios

Alternatively, in the χ^2 of our global fit, we can define the fit parameters to be the three cross sections σ_{ZH} , $\sigma_{\nu\bar{\nu}H}$, $\sigma_{t\bar{t}H}$, and the eight branching ratios $\text{Br}(H \rightarrow b\bar{b})$, $\text{Br}(H \rightarrow c\bar{c})$, $\text{Br}(H \rightarrow gg)$, $\text{Br}(H \rightarrow WW^*)$, $\text{Br}(H \rightarrow ZZ^*)$, $\text{Br}(H \rightarrow \tau^+\tau^-)$, $\text{Br}(H \rightarrow \mu^+\mu^-)$, $\text{Br}(H \rightarrow \gamma\gamma)$. Taking again the ILC(1000) luminosity scenario as an example, we use the 34 independent cross section and cross section times branching ratio measurements from Table 5.4 and appropriately redefined Y'_i functions to solve for the 11 parameters through the minimization of an alternate χ^2 function. The cross section and branching ratio accuracies for all four of our energy and luminosity scenarios are summarized in Table 6.3.

6.3 Model-Dependent Coupling Parameterizations

While the couplings of the Higgs boson and the total Higgs width can be determined at the ILC without model assumptions, it is sometimes useful to extract couplings from ILC data within the context of certain models. Such analyses makes it easier to compare the experimental precision of the ILC with other facilities, such as the LHC, that cannot determine Higgs couplings in a model independent manner.

6.3.1 Benchmark Parameterizations of the LHC HXSWG

The LHC Higgs Cross Section Working Group (HXSWG) has proposed a series of benchmark Higgs coupling parameterizations [160, 205]. We take as an example the parameterization with seven free parameters $\kappa_g, \kappa_\gamma, \kappa_W, \kappa_Z, \kappa_b, \kappa_t, \kappa_\tau$ and a dependent parameter $\kappa_H(\kappa_i)$ described in Section 10.3.7 of Ref. [205]. In this parameterization 2nd generation fermion Higgs couplings are related to 3rd generation couplings via $\kappa_c = \kappa_t$, $\kappa_\mu = \kappa_\tau$, etc., and the total Higgs width is assumed to be the sum of the partial widths for all Standard model decays. We implement these boundary conditions by adding two new terms to our model independent chisquare function:

$$\chi^2 = \sum_{i=1}^{i=33} \left(\frac{Y_i - Y'_i}{\Delta Y_i} \right)^2 + \left(\frac{\xi_{ct}}{\Delta \xi_{ct}} \right)^2 + \left(\frac{\xi_\Gamma}{\Delta \xi_\Gamma} \right)^2 \quad (6.3)$$

where

$$\xi_{ct} = \kappa_c - \kappa_t = \frac{g_c}{g_c^{SM}} - \frac{g_t}{g_t^{SM}}, \quad \xi_\Gamma = \Gamma_T - \sum_{i=1}^9 \Gamma_i, \quad \text{and} \quad \Gamma_i = G_i \cdot g_i^2. \quad (6.4)$$

Table 6.4. Expected accuracies $\Delta g_i/g_i$ for Higgs boson couplings and the total width $\Gamma_T(h)$ using the seven parameter HXSWG benchmark parameterization described in Section 10.3.7 of Ref. [205] assuming all theory errors are given 0.1%.

Mode	ILC(250)	ILC(500)	ILC(1000)	ILC(LumUp)
$\gamma\gamma$	17 %	8.3 %	3.8 %	2.3 %
gg	6.1 %	2.0 %	1.1 %	0.7 %
WW	4.7 %	0.4 %	0.3 %	0.2 %
ZZ	0.7 %	0.5 %	0.5 %	0.3 %
$t\bar{t}$	6.4 %	2.5 %	1.3 %	0.9 %
$b\bar{b}$	4.7 %	1.0 %	0.6 %	0.4 %
$\tau^+\tau^-$	5.2 %	1.9 %	1.3 %	0.7 %
$\Gamma_T(h)$	9.0 %	1.7 %	1.1 %	0.8 %

Table 6.5. Expected accuracies $\Delta g_i/g_i$ for Higgs boson couplings and the total width $\Gamma_T(h)$ using the seven parameter HXSWG benchmark parameterization described in Section 10.3.7 of Ref. [205] and assuming all theory errors are 0.5%.

Mode	ILC(250)	ILC(500)	ILC(1000)	ILC(LumUp)
$\gamma\gamma$	17 %	8.3 %	3.8 %	2.3 %
gg	6.1 %	2.0 %	1.2 %	0.7 %
WW	4.7 %	0.5 %	0.3 %	0.2 %
ZZ	0.8 %	0.5 %	0.5 %	0.3 %
$t\bar{t}$	6.4 %	2.6 %	1.4 %	0.9 %
$b\bar{b}$	4.7 %	1.0 %	0.6 %	0.4 %
$\tau^+\tau^-$	5.2 %	2.0 %	1.3 %	0.8 %
$\Gamma_T(h)$	9.0 %	1.8 %	1.1 %	0.9 %

The error $\Delta\xi_{ct}$ is obtained by propagating the total theory errors on g_e^{SM} and g_t^{SM} , while the error $\Delta\xi_\Gamma$ is obtained by propagating the errors on G_i :

$$\Delta\xi_\Gamma = \Gamma_{SM} \left[\sum_i \left(\frac{\Delta G_i}{G_i} \right)^2 (BR_i)^2 \right]^{\frac{1}{2}} \approx \Gamma_{SM} \frac{\Delta G}{G} \left[\sum_i (BR_i)^2 \right]^{\frac{1}{2}} \approx 0.63 \Gamma_{SM} \frac{\Delta G}{G}. \quad (6.5)$$

The results for the seven parameters in the HXSWG parameterization are shown in Table 6.4 and Table 6.5 assuming all theory errors are given by $\Delta\xi_{ct} = \Delta G_i/G_i = \Delta F_i/F_i = 0.1\%$ and 0.5% , respectively.

Table 6.6. Expected accuracies for Higgs boson couplings under the assumption of Eqn. (6.6) and assuming LHC results with 300 fb^{-1} are combined with ILC results.

Mode	LHC(300 fb^{-1}) +ILC(250)	LHC(300 fb^{-1}) +ILC(500)	LHC(300 fb^{-1}) +ILC(1000)	LHC(300 fb^{-1}) +ILC(LumUp)
$\gamma\gamma$	4.8 %	4.2 %	3.0 %	2.0 %
gg	3.8 %	1.9 %	1.1 %	0.7 %
WW	1.9 %	0.2 %	0.1 %	0.1 %
ZZ	0.4 %	0.3 %	0.3 %	0.1 %
$t\bar{t}$	12.0 %	9.6 %	2.9 %	1.8 %
$b\bar{b}$	2.8 %	1.0 %	0.6 %	0.3 %
$\tau^+\tau^-$	3.3 %	1.8 %	1.2 %	0.7 %
$c\bar{c}$	5.1 %	2.6 %	1.4 %	0.8 %
$\Gamma_T(h)$	4.7 %	1.6 %	0.9 %	0.5 %

6.3.2 Higgs Couplings to W and Z Bounded by SM Couplings

A different method to fit for Higgs couplings using LHC data is given in Ref. [264], where an effort is made to minimize the model dependence of the coupling fit. Under rather general conditions [28], each scalar with a vev makes a positive contribution to the masses of the W and Z . Since the Higgs couplings to the W and Z also arise from the vev, this implies that the coupling of any single Higgs field is bounded above by the coupling that would give the full mass of the vector bosons. This implies

$$g^2(hWW) \leq g^2(hWW)|_{SM} \quad \text{and} \quad g^2(hZZ) \leq g^2(hZZ)|_{SM} \quad (6.6)$$

Then the measurement of the $\sigma \cdot BR$ for a process such as WW fusion to h with decay to WW^* , which is proportional to $g^4(hWW)/\Gamma_T$, puts an upper limit on Γ_T . This constraint was first applied to Higgs coupling fitting by Dührssen *et al.* [161]. In the literature, this constraint is sometimes applied together with the relation

$$g^2(hWW)/g^2(hZZ) = \cos^2 \theta_w. \quad (6.7)$$

The relation (6.7), however, requires models in which the Higgs is a mixture of $SU(2)$ singlet and doublet fields only, while (6.6) is more general [265]. An estimate of Higgs coupling errors from the LHC under the assumption of Eqn. (6.6) can be found in Ref. [264].

We have carried out a global fit to the ILC measurements under the constraint (6.6) with 9 parameters representing independent Higgs boson couplings to WW , ZZ , $b\bar{b}$, gg , $\gamma\gamma$, $\tau^+\tau^-$, $c\bar{c}$, $t\bar{t}$, and the total Higgs width $\Gamma_T(h)$. The results for the errors on Higgs couplings are shown in Table 6.6. The four columns represent the combination of results from LHC (300 fb^{-1} , 1 detector) [264] and our four ILC luminosity scenarios.

6.4 Effective Higgs Operators

The $h \rightarrow WW^*$ decay provides an interesting opportunity to study its differential width and probe the Lorentz structure of the hWW coupling through angular analyses of the decay products. The relevant part of the general interaction Lagrangian, which couples the Higgs boson to W bosons in a both Lorentz- and gauge-symmetric fashion, can be parameterized as

$$\mathcal{L}_{hWW} = 2m_W^2 \left(\frac{1}{v} + \frac{a}{\Lambda} \right) h W_\mu^+ W^{-\mu} + \frac{b}{\Lambda} h W_{\mu\nu}^+ W^{-\mu\nu} + \frac{\tilde{b}}{\Lambda} h \epsilon^{\mu\nu\sigma\tau} W_{\mu\nu}^+ W_{\sigma\tau}^-, \quad (6.8)$$

where $W_{\mu\nu}^\pm$ is the usual gauge field strength tensor, $\epsilon^{\mu\nu\sigma\tau}$ is the Levi-Civita tensor, v is the VEV of the Higgs field, and Λ is a cutoff scale¹. The real dimensionless coefficients, a , b , and \tilde{b} , are all zero

¹ The Lagrangian (6.8) is not by itself gauge invariant; to restore explicit gauge invariance we must also include the corresponding anomalous couplings of the Higgs boson to Z bosons and photons.

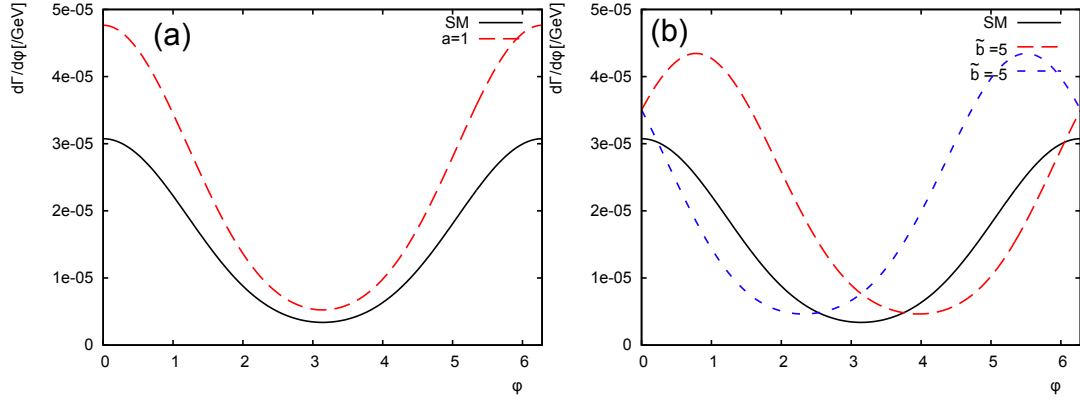
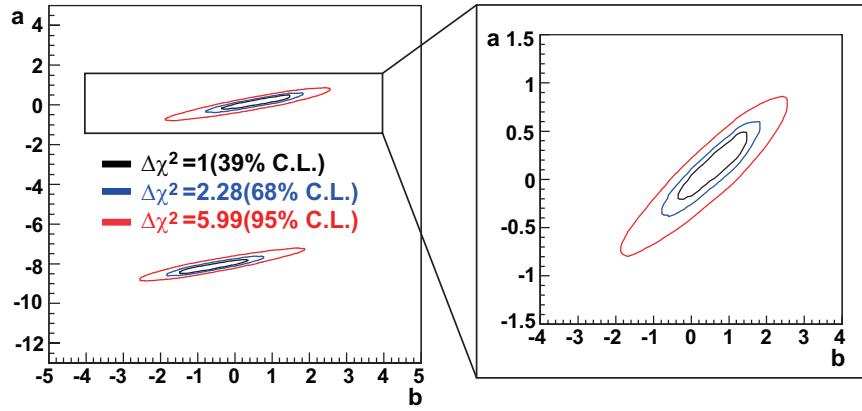


Figure 6.1. Distribution of the angle ϕ between two decay planes of W and W^* from the decay $H \rightarrow WW^* \rightarrow 4j$ with the inclusion of anomalous couplings [266]. (a) The SM curve along with that for $a = 1$, $b = \tilde{b} = 0$, $\Lambda = 1$ TeV; the position of the minimum is the same for both distributions. (b) The SM result with the cases $\tilde{b} = \pm 5$, $a = b = 0$, $\Lambda = 1$ TeV; the position of the minimum is now shifted as discussed in the text. From [266].

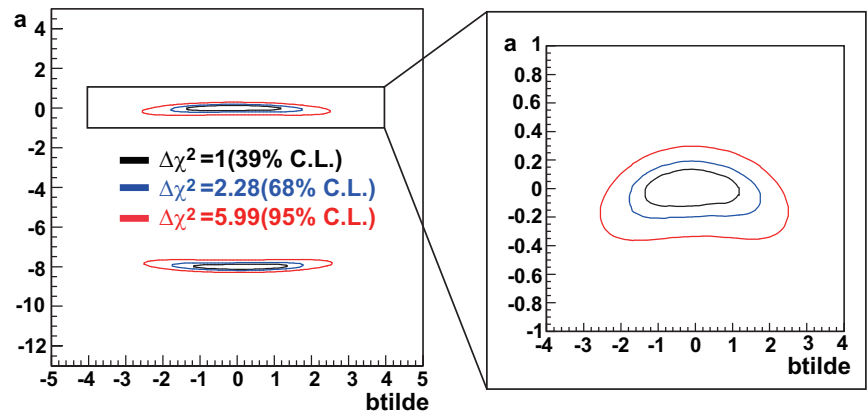
Figure 6.2

Probability contours for $\Delta\chi^2 = 1, 2.28$, and 5.99 in the a - b plane, which correspond to 39%, 68%, and 95% C.L., respectively.



in the Standard Model and measure the anomaly in the hWW coupling, which arise from some new physics at the scale Λ . The coefficient a stands for the correction to the Standard Model coupling. The coefficients b and \tilde{b} parametrize the leading dimension-five non-renormalizable interactions and corresponding to $(\mathbf{E} \cdot \mathbf{E} - \mathbf{B} \cdot \mathbf{B})$ -type CP -even and $(\mathbf{E} \cdot \mathbf{B})$ -type CP -odd contributions. The a coefficient, if nonzero, would modify just the normalization of the Standard Model coupling, while the b and \tilde{b} coefficients would change the angular correlations of the decay planes. This effect is shown in Fig. 6.1 [266]. Nonzero b and \tilde{b} would also modify the momentum distribution of the W boson in the Higgs rest frame. Simultaneous fits to p_W and ϕ_{plane} result in the contour plots in Figs. 6.2 and 6.3.

Figure 6.3
Contours similar to
Fig. 6.2 plotted in the
 a - b plane.



Chapter 7

Non-Minimal Higgs Models

7.1 Direct Production of Non-Minimal Higgs Bosons

The discovery of additional Higgs bosons such as H , A , H^\pm and $H^{\pm\pm}$ would give direct evidence for extended Higgs sector. As discussed in Section 1.3.7 there are many possibilities for the decay branching ratios of these particles. The ongoing searches at LHC rely on specific production and decay mechanisms that occupy only a part of the complete model parameter space. At the ILC, the extended Higgs bosons are produced in electroweak pair production through cross sections that depend only on the $SU(2) \times U(1)$ quantum numbers and the mixing angles. Thus, the reach of the ILC is typically limited to masses less than $\sqrt{s}/2$, but it is otherwise almost uniform over the parameter space.

7.1.1 Neutral Higgs pair production at ILC

The signals from HA production in the $bbbb$ and $bb\tau\tau$ channels, in the context of the MSSM (Type-II 2HDM), was carried out in the studies of Ref. [267, 268]. A rather detailed detector simulation was performed in [268], including all the SM backgrounds at $\sqrt{s} = 500, 800$ and 1000 GeV. Using a kinematical fit which imposes energy momentum conservation and under the assumed experimental conditions, a statistical accuracy on the Higgs boson mass from 0.1 to 1 GeV is found to be achievable. The topological cross section of $e^+e^- \rightarrow HA \rightarrow bbbb$ ($e^+e^- \rightarrow HA \rightarrow \tau\tau bb$) could be determined with a relative precision of 1.5% to 7% (4% to 30%). The width of H and A could also be determined with an accuracy of 20% to 40%, depending on the mass of the Higgs bosons. Figure 7.1 shows, on the left, the $\tau^+\tau^-$ invariant mass obtained by a kinematic fit in $e^+e^- \rightarrow HA \rightarrow b\bar{b}\tau^+\tau^-$ for $m_A = 140$ GeV and $m_H = 150$ GeV, for $\sqrt{s} = 500$ GeV and 500 fb^{-1} [268].

The $\tau^+\tau^-\tau^+\tau^-$ and $\mu^+\mu^-\tau^+\tau^-$ final states would be dominant for the type X (lepton specific) 2HDM. When $\sqrt{s} = 500$ GeV, assuming an integrated luminosity of 500 fb^{-1} , one expects to collect 16,000 (18,000) $\tau^+\tau^-\tau^+\tau^-$ events in the type X (type II) 2HDM, and 110 (60) $\mu^+\mu^-\tau^+\tau^-$ events in the same models, assuming $m_H = m_A = m_{H^\pm} = 130$ GeV, $\sin(\beta - \alpha) = 1$ and $\tan \beta = 10$. These numbers do not change much for $\tan \beta \gtrsim 3$. It is important to recognize that the four-momenta of the τ leptons can be solved by a kinematic fit based on the known center of mass energy and momentum, by applying the collinear approximation to each set of τ lepton decay products [269, 270]. Figure 7.1 shows, on the right, the two dimensional invariant mass distribution of the τ lepton pairs from the neutral Higgs boson decays as obtained with a simulation at 500 GeV in which the masses of the neutral Higgs bosons are taken to be 130 GeV and 170 GeV [271].

In an extended Higgs sector with singlets, it is very common to have lighter Higgs bosons with suppressed couplings to the Z, but which can be seen at an e^+e^- collider either through direct production or by decays of the 125 GeV Higgs boson. A specific NMSSM example that has been studied is the cascade decay $h_1 \rightarrow aa \rightarrow (\tau^+\tau^-)(\tau^+\tau^-)$ at the ILC[272]. In addition to discovery, the masses can be measured to better than 1%.

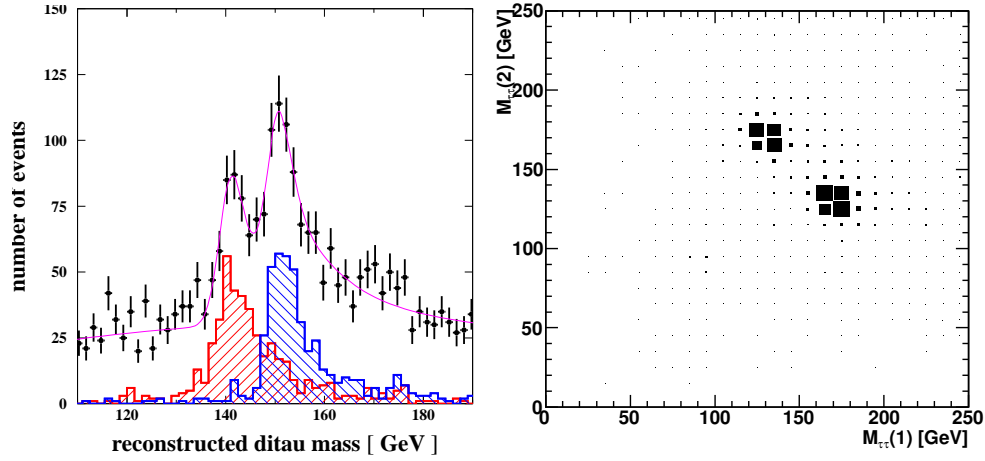


Figure 7.1. Left: Invariant mass reconstruction from the kinematical fit in the process $e^+e^- \rightarrow HA \rightarrow b\bar{b}\tau^+\tau^-$ in the Type-II (MSSM like) 2HDM for $m_A = 140$ GeV and $m_H = 150$ GeV at $\sqrt{s} = 500$ GeV and 500 fb^{-1} [268]. Right: Two dimensional distribution of ditau invariant mass in $e^+e^- \rightarrow HA \rightarrow \tau^+\tau^-\tau^+\tau^-$ in the Type X (lepton specific) 2HDM for $m_A = 170$ GeV and $m_H = 130$ GeV for $\sqrt{s} = 500$ GeV and 500 fb^{-1} [271].

Although the associated Higgs production process $e^+e^- \rightarrow HA$ is a promising one for testing the properties of the extended Higgs sectors, the kinematic reach is restricted by $m_H + m_A < \sqrt{s}$ and is not available beyond this limit. Above the threshold of the HA production, the associated production processes $t\bar{t}\Phi$, $b\bar{b}\Phi$ and $\tau^+\tau^-\Phi$ ($\Phi = h, H, A$) could be used [273, 274]. In particular, for $b\bar{b}\Phi$ and $\tau^+\tau^-\Phi$, the mass reach is extended almost up to the collision energy. The cross sections for these processes are proportional to the Yukawa interaction, so they directly depend on the type of Yukawa coupling in the 2HDM structure. In MSSM or the Type II 2HDM (Type I 2HDM), these processes are enhanced (suppressed) for large $\tan\beta$ values. In Type X 2HDM, only the $\tau^+\tau^-H/A$ channels could be significant while only $b\bar{b}H/A$ channels would be important in Type I and Type Y 2HDMs. These reactions can then be used to discriminate the type of the Yukawa interaction.

7.1.2 Charged Higgs boson production

At the ILC, charged Higgs bosons are produced in pairs in $e^+e^- \rightarrow H^+H^-$ [275]. The cross section is a function only of m_{H^\pm} and is independent of the type of Yukawa interaction in the 2HDM. Therefore, as in the case of the HA production, the study of the final state channels can be used to determine the type of Yukawa interaction. When $m_{H^\pm} > m_t + m_b$, the main decay mode is $t\bar{b}$ in Type I, II and Y, while in Type X the main decay mode is $\tau\nu$ for $\tan\beta > 2$. When H^\pm cannot decay into $t\bar{b}$, the main decay mode is $\tau\nu$ except in Type Y for large $\tan\beta$ values. For $m_{H^\pm} < m_t - m_b$, the charged Higgs boson can also be studied via the decay of top quarks $t \rightarrow bH^\pm$ in 2HDMs except in Type X 2HDM case with $\tan\beta > 2$.

In the MSSM, a detailed simulation study of this reaction has been performed for the final state $e^+e^- \rightarrow H^+H^- \rightarrow t\bar{b}t\bar{b}$ for $m_{H^\pm} = 300$ GeV at $\sqrt{s} = 800$ GeV [276]. The final state is 4 b -jets with 4 non- b -tagged jets. Assuming an integrated luminosity of 1 ab^{-1} , a mass resolution of approximately 1.5% can be achieved (Figure 7.2 (left)). The decay mode $t\bar{b}t\bar{b}$ can also be used to determine $\tan\beta$, especially for relatively small values, $\tan\beta < 5$, where the production rate of the signal strongly depends on this parameter.

The pair production is kinematically limited to relatively light charged Higgs bosons with $m_{H^\pm} < \sqrt{s}/2$. When $m_{H^\pm} > \sqrt{s}/2$, one can make use of the single production processes $e^+e^- \rightarrow t\bar{b}H^+$, $e^+e^- \rightarrow \tau\nu H^+$, $e^+e^- \rightarrow W^-H^+$, $e^+e^- \rightarrow H^+e^-\nu$ and their charge conjugates. The cross sections for the first two of these processes are directly proportional to the square of the Yukawa coupling

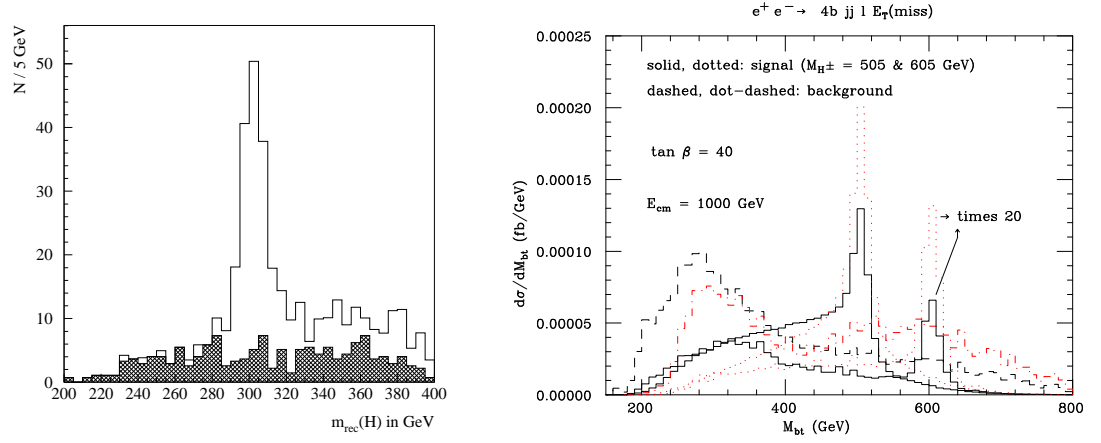
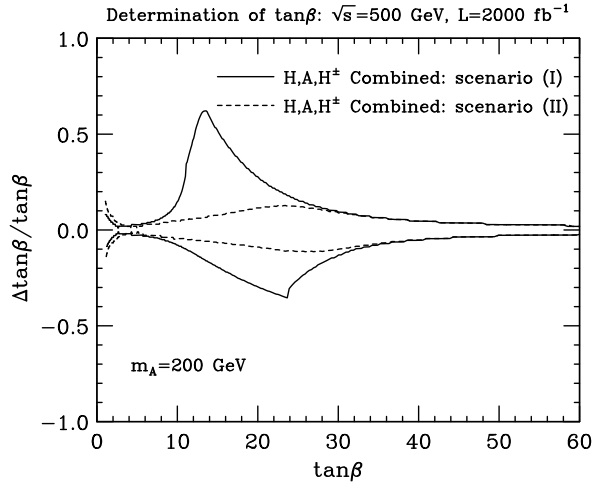


Figure 7.2. Left: Fitted charged Higgs boson mass in $H^+H^- \rightarrow (t\bar{b})(t\bar{b})$ in the MSSM, with $m_{H^\pm} = 300$ GeV, measured at the ILC at CM energy 800 GeV with 1 ab^{-1} of data. The background is shown by the dark histogram [276]. Right: Differential distribution of the reconstructed Higgs mass for the signal $e^+e^- \rightarrow b\bar{t}H^+ + t\bar{b}H^- \rightarrow t\bar{t}b\bar{b}$ and the background $e^+e^- \rightarrow t\bar{t}g^* \rightarrow t\bar{t}b\bar{b}$ in the MSSM or the Type II 2HDM [277].

Figure 7.3
Estimates of the 1σ statistical upper and lower bounds on $\tan\beta$ from ILC measurements, for an MSSM model with $m_{H^\pm} \sim m_A = 200$ GeV, assuming $\sqrt{s} = 500$ GeV and 2000 fb^{-1} of data, from [278]. The quantity plotted is the relative error, $\Delta \tan\beta / \tan\beta$.



constants. The others are one-loop induced. Apart from the pair production rate, these single production processes strongly depend on the type of Yukawa interaction in the 2HDM structure. In general, their rates are small and quickly suppressed for larger values of m_{H^\pm} . They can be used only for limited parameter regions where m_{H^\pm} is just above the threshold for the pair production with very large or low $\tan\beta$ values.

In Ref. [277], a simulation study for the process $e^+e^- \rightarrow t\bar{b}H^- + b\bar{t}H^+ \rightarrow 4b + jj + \ell + p_T^{\text{miss}}$ ($\ell = e, \mu$) has been done for m_{H^\pm} just above the pair production threshold $m_{H^\pm} \simeq \sqrt{s}/2$. It is shown that this process provides a significant signal of H^\pm in a relatively small region just above $\sqrt{s}/2$, for very large or very small values of $\tan\beta$, assuming a high b -tagging efficiency. The reconstructed H^+ mass distribution is shown in the right-hand side of Fig. 7.2.

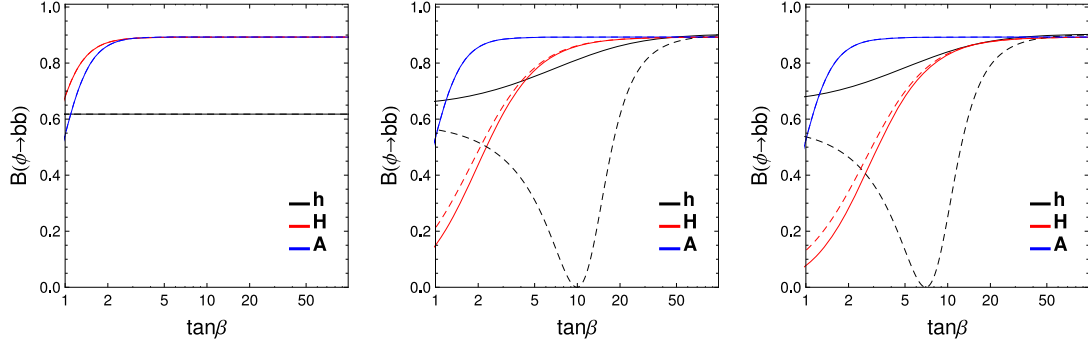


Figure 7.4. The decay branching ratios as a function of $\tan \beta$ for a fixed $\sin^2(\beta - \alpha)$ for $h \rightarrow b\bar{b}$ (black curves), $H \rightarrow b\bar{b}$ (red curves), and $A \rightarrow b\bar{b}$ (blue curves) in the Type-II 2HDM. From left to right, $\sin^2(\beta - \alpha)$ is taken to be 1, 0.99, and 0.98. The solid (dashed) curves denote the case with $\cos(\beta - \alpha) \leq 0$ ($\cos(\beta - \alpha) \geq 0$).

7.2

Measurements of $\tan \beta$ at the ILC

In multi-Higgs models, mixing angles between bosons with the same quantum numbers are important parameters. In the CP-conserving two Higgs doublet model, there are two mixing angles α and β , where α is introduced to diagonalize the mass matrix of the CP-even scalar states, and $\tan \beta$ is defined as the ratio of vacuum expectation values of two Higgs doublets diagonalizing the charged and CP-odd scalar states. All coupling constants associated with the Higgs bosons, i.e. the couplings of h , H , A and H^\pm to gauge bosons, fermions and themselves, depend on these mixing angles.

The information on $\sin(\beta - \alpha)$ ($\cos(\beta - \alpha)$) can be directly extracted from the precision measurement of the couplings of the SM-like boson h (the extra Higgs boson H) to weak gauge bosons, hVV (HVV). At the LHC, the SM-like coupling hVV ($VV = WW$ and ZZ) is being measured, and the current data indicates $\sin^2(\beta - \alpha) \simeq 1$ within the error of order 10-20%. At the ILC, the hWW and hZZ couplings can be measured precisely to the percent level or better.

When $\sin(\beta - \alpha)$ is precisely determined, all the Yukawa couplings $hf\bar{f}$ and $Hf\bar{f}$ are a function of $\tan \beta$, so that one can extract $\tan \beta$ by precise measurements of the Yukawa interactions. The $\tan \beta$ dependences in the Yukawa couplings are different for each type of Yukawa interaction [79, 80, 81, 82]. In the Type-II 2HDM, the $\tan \beta$ dependences are large for Yukawa interactions of H and A with down type fermions such as $Hb\bar{b}$, $Ab\bar{b}$, $H\tau^+\tau^-$ and $A\tau^+\tau^-$ ($Y_{Hb\bar{b}, Ab\bar{b}} \sim m_b \tan \beta$, $Y_{H\tau\tau, A\tau\tau} \sim m_\tau \tan \beta$), while in the Type-X (lepton specific) 2HDM the Yukawa couplings of H or A to charged leptons are sensitive to $\tan \beta$ ($Y_{H\tau\tau, A\tau\tau} \sim m_\tau \tan \beta$).

In Fig. 7.4 the branching ratios of $h \rightarrow b\bar{b}$, $H \rightarrow b\bar{b}$ and $A \rightarrow b\bar{b}$ are shown as a function of $\tan \beta$ for a fixed value of $\sin^2(\beta - \alpha) = 1, 0.99$ and 0.98 in the Type-II 2HDM (MSSM) [279]. In Fig. 7.5, similar figures for the branching ratios of $h \rightarrow \tau^+\tau^-$, $H \rightarrow \tau^+\tau^-$ and $A \rightarrow \tau^+\tau^-$ are shown in the Type-X (lepton specific) 2HDM.

In Refs. [278, 280] methods using the production and decay of the H and A have been studied in the context of the MSSM. Since the masses of the H and A can be measured by the invariant mass distributions in an appropriate decay mode in $e^+e^- \rightarrow HA$, the branching ratios can be predicted as a function of $\tan \beta$. Thus one can extract $\tan \beta$ by measuring the branching ratios of H and A . Since the $\tan \beta$ dependence of the branching ratio is large in small $\tan \beta$ regions, this method is useful for small $\tan \beta$. A second method [280] is based on the measurement of the total decay widths of the H and A . For large $\tan \beta$ values, the total decay widths are dominated by the $b\bar{b}$ and $\tau\tau$ decay modes in the Type-II and Type-X 2HDMs, respectively, whose partial widths are proportional to $(\tan \beta)^2$. Therefore, $\tan \beta$ can be extracted using this method in large $\tan \beta$ regions.

In addition to these two methods, a new method using the precision measurement of the SM-like Higgs boson h has been proposed in Ref. [279]. This can be applied to the case where $\sin^2(\beta - \alpha)$

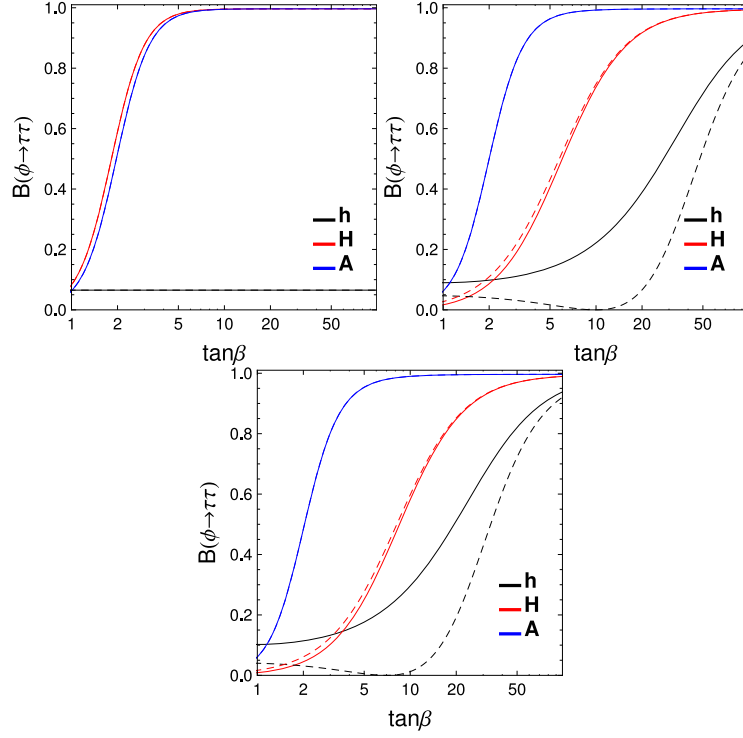


Figure 7.5. The decay branching ratios are shown as a function of $\tan \beta$ with a fixed value of $\sin^2(\beta - \alpha)$ for $h \rightarrow \tau\tau$ (black curves), for $H \rightarrow \tau\tau$ (red curves), and for $A \rightarrow \tau\tau$ (blue curves) in the Type-X 2HDM. From left to right, $\sin^2(\beta - \alpha)$ is taken to be 1, 0.99, and 0.98. The solid (dashed) curves denote the case with $\cos(\beta - \alpha) \leq 0$ ($\cos(\beta - \alpha) \geq 0$).

is smaller than unity through the $\tan \beta$ dependences in the Yukawa couplings for h . In the limit of $\sin^2(\beta - \alpha) = 1$, the Yukawa couplings for the SM-like Higgs boson h are identical to the SM ones, so that there is no $\tan \beta$ dependence in them. However, if $\sin^2(\beta - \alpha)$ turns out to be slightly smaller than unity in future precision measurements, then the Yukawa couplings for h can also depend on $\tan \beta$ significantly. For example, for the Type-II 2HDM

$$Y_{hb\bar{b}} \sim \sin(\beta - \alpha) - \tan \beta \cos(\beta - \alpha), \quad (7.1)$$

$$Y_{h\tau\tau} \sim \sin(\beta - \alpha) - \tan \beta \cos(\beta - \alpha), \quad (7.2)$$

and for the Type-X 2HDM

$$Y_{hb\bar{b}} \sim \sin(\beta - \alpha) + \cot \beta \cos(\beta - \alpha), \quad (7.3)$$

$$Y_{h\tau\tau} \sim \sin(\beta - \alpha) - \tan \beta \cos(\beta - \alpha). \quad (7.4)$$

At the ILC, the main decay modes of h can be measured precisely to the few percent level. The precision measurement of the decay of h can be used to determine $\tan \beta$ for the case with $\sin(\beta - \alpha) < 1$.

In Fig. 7.6, the numerical results for the sensitivities of the $\tan \beta$ measurements are shown for the Type-II 2HDM [279]. The production cross section and the number of the signal events are evaluated for $m_H = m_A = 200$ GeV with $\sqrt{s} = 500$ GeV and $\mathcal{L}_{\text{int}} = 250 \text{ fb}^{-1}$. The acceptance ratio of the $4b$ final states in the $e^+e^- \rightarrow HA$ signal process is set to 50%. The results for the three methods are shown. The results for 1σ (solid) and 2σ (dashed) sensitivities for the branching ratios, the total width of H and A , and the branching ratio of h are plotted in the red, blue and black curves, respectively. The parameter $\sin^2(\beta - \alpha)$ is set to 1 (left), 0.99 (middle) and 0.98 (right) for $\cos(\beta - \alpha) < 0$.

In Fig. 7.7, the sensitivities to $\tan \beta$ are shown for the case of the Type-X 2HDM, where

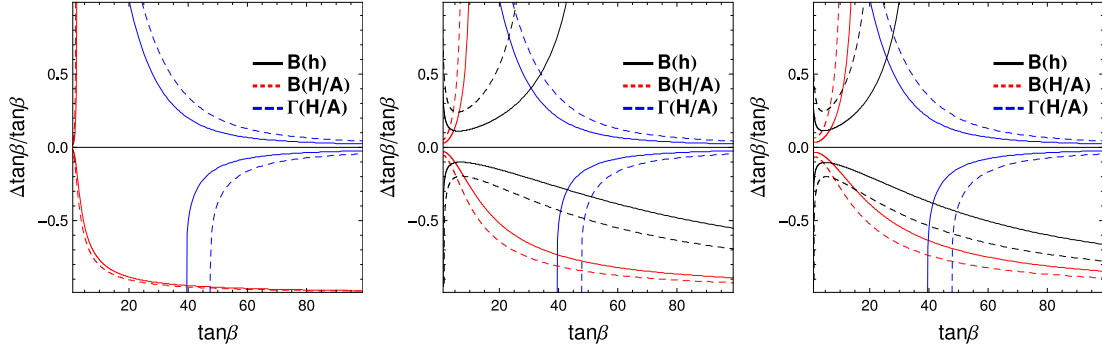


Figure 7.6. Sensitivities to the $\tan \beta$ measurement by the three methods in the Type-II 2HDM. From left to right, $\sin^2(\beta - \alpha)$ is taken to be 1, 0.99, and 0.98, with $\cos(\beta - \alpha) \leq 0$. Estimated $\Delta \tan \beta / \tan \beta$ using the branching ratio of $H/A \rightarrow b\bar{b}$ (red curves), the total width of H/A (blue curves), and the branching ratio of $h \rightarrow b\bar{b}$ (black curves) are plotted as a function of $\tan \beta$. The solid curves stand for 1σ sensitivities, and the dashed curves for 2σ . For HA production, $m_H = m_A = 200$ GeV with $\sqrt{s} = 500$ GeV and $\mathcal{L}_{\text{int}} = 250 \text{ fb}^{-1}$ are assumed. For the $h \rightarrow b\bar{b}$ measurement, $\Delta B/B = 1.3\%$ (1σ) and 2.7% (2σ) are used.

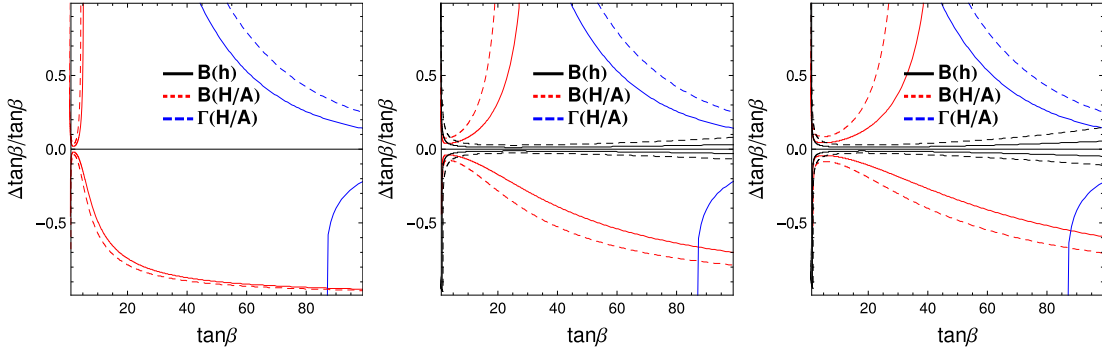


Figure 7.7. The same as FIG. 7.6, but $\tau\tau$ decay modes are used for the analysis in the Type-X 2HDM. From left to right, $\sin^2(\beta - \alpha)$ is taken to be 1, 0.99, and 0.98, with $\cos(\beta - \alpha) \leq 0$. For $B_{\tau\tau}^h$, $\Delta B/B = 2\%$ (1σ) and 5% (2σ) are assumed.

the channels $H \rightarrow \tau^+\tau^-$ and $A \rightarrow \tau^+\tau^-$ are the main decay modes [279]. With or without the assumption of $\sin^2(\beta - \alpha) = 1$, the total width measurement of H and A is a useful probe for the large $\tan \beta$ regions. For the smaller $\tan \beta$ regions, the branching ratio measurement of H and A can probe $\tan \beta$. For $\sin(\beta - \alpha) = 0.99$ and 0.98 , the measurement of the branching ratio of $h \rightarrow \tau^+\tau^-$ can give good $\tan \beta$ sensitivity over a wide range of $\tan \beta$.

Here, comments on the $\tan \beta$ measurements for the other 2HDM types are given. In the Type-I 2HDM, the Yukawa coupling constants are universally changed from those in the SM. In the SM-like limit, $\sin(\beta - \alpha) = 1$, the Yukawa interactions for H and A become weak for $\tan \beta > 1$. As for the $\tan \beta$ measurement at the ILC, the method using the total width of H and A is useless, because the absolute value of the decay width is too small compared to the detector resolution. Without the SM-like limit, the branching ratio measurement of H and A using the fermionic decay modes may be difficult, because the bosonic decay modes $H \rightarrow WW$ and $A \rightarrow Zh$ become important. Furthermore, the decays of h are almost unchanged from the SM because there is no $\tan \beta$ enhancement. Thus, the $\tan \beta$ determination in the Type-I 2HDM seems to be difficult even at the ILC. In the Type-Y 2HDM, the $\tan \beta$ sensitivity at the ILC would be similar to that of the Type-II 2HDM, because the Yukawa interactions of the neutral scalar bosons with the bottom quarks are enhanced by $\tan \beta$ in the same way.

Chapter 8

Gamma-Gamma and e-Gamma Option

Higgs production in $\gamma\gamma$ collisions, first studied in [281, 282, 283], offers a unique capability to measure the two-photon width of the Higgs and to determine its charge conjugation and parity (CP) composition through control of the photon polarization. Both measurements have unique value in understanding the nature of a Higgs boson eigenstate. Photon-photon collisions also offer one of the best means for producing a heavy Higgs boson singly, implying significantly greater mass reach than electron-positron production of a pair of Higgs bosons.

There are many important reasons for measuring the $\gamma\gamma$ coupling of a Higgs boson, generically denoted h . In the Standard Model, the coupling of the Higgs boson, h_{SM} , to two photons receives contributions from loops containing any charged particle whose mass arises in whole or part from the vacuum expectation value (vev) of the neutral Higgs field. In the limit of infinite mass for the charged particle in the loop, the contribution asymptotes to a value that depends on the particle's spin (i.e., the contribution does not decouple). Thus, a measurement of $\Gamma(h_{SM} \rightarrow \gamma\gamma)$ provides the possibility of revealing the presence of arbitrarily heavy charged particles, since in the SM context all particles acquire mass via the Higgs mechanism.¹

Even if there are no new particles that acquire mass via the Higgs mechanism, a precision measurement of $N(\gamma\gamma \rightarrow h \rightarrow X)$ for specific final states X ($X = b\bar{b}, WW^*, \dots$) can allow one to distinguish between a h that is part of a larger Higgs sector and the SM h_{SM} . The ability to detect deviations from SM expectations will be enhanced by combining this with other types of precision measurements for the SM-like Higgs boson. Observation of small deviations would be typical for an extended Higgs sector as one approaches the decoupling limit in which all other Higgs bosons are fairly heavy, leaving behind one SM-like light Higgs boson. In such models, the observed small deviations could then be interpreted as implying the presence of heavier Higgs bosons.

The ability to detect $\gamma\gamma \rightarrow H^0, A^0$ will be of greatest importance if the H^0 and A^0 cannot be detected either at the LHC or in e^+e^- collisions at the ILC. In fact, there is a very significant section of parameter space in the MSSM for which this is the case. The $\gamma\gamma$ collider would also play a very important role in exploring a non-supersymmetric general two-Higgs-doublet model (2HDM) of which the MSSM Higgs sector is a special case.

Once one or several Higgs bosons have been detected, precision studies can be performed. Primary on the list would be the determination of the CP nature of any observed Higgs boson. This and other types of measurements become especially important if one is in the decoupling limit of a 2HDM. The decoupling limit is defined by the situation in which there is a light SM-like Higgs boson, while the other Higgs bosons (H^0, A^0, H^\pm) are heavy and quite degenerate. In the MSSM

¹Loop contributions from charged particles that acquire a large mass from some other mechanism, beyond the SM context, will decouple as $(\text{mass})^{-2}$ and, if there is a SM-like Higgs boson h , $\Gamma(h \rightarrow \gamma\gamma)$ will not be sensitive to their presence.

context, such decoupling is automatic in the limit of large m_{A^0} . In this situation, a detailed scan to separate the H^0 and A^0 would be very important and entirely possible at the $\gamma\gamma$ collider. Further, measurements of relative branching fractions for the H^0 and A^0 to various possible final states would also be possible and reveal much about the Higgs sector model.

8.1 Production Cross Sections and Luminosity Spectra

The gamma-gamma option at the ILC opens a new opportunity for truly high energy two-photon physics that is not limited to the QCD studies performed by most e^+e^- colliders. The production cross sections for charged particles are considerably larger in $\gamma\gamma$ collisions than in e^+e^- enabling the study of new particles above threshold at a higher rate - e.g. WW pair production at 500 GeV is a factor of 20 larger than in e^+e^- . This effect more than offsets that factor of 5 – 10 lower $\gamma\gamma$ luminosity compared to the corresponding e^+e^- collider. Similarly the cross sections for charged scalars, lepton and top pairs are a factor of 5 – 10 higher at a photon collider compensating for the luminosity reduction.

The proposed technique for the gamma-gamma option consists of Compton backscattering a ~ 1 MeV laser photons from the 125-500 GeV electron and positron beams. The backscattered photon receives a large fraction of the incoming electron energy. This is described in detail in [284]. The maximum energy of the generated photons is given by $E_{\gamma}^{max} = xE_e/(1+x)$, where E_e is the electron beam energy and $x = 4E_e E_L \cos^2(\theta/2)/m_e^2 c^4$ with E_L and θ the laser photon energy and angle between the electron and laser beam. The distance from the conversion point to the interaction point is in the range of a few millimeters to a few centimeters. The optimal values of x are around 4.8, yielding $E_{\gamma}^{max} \approx 0.82E_e$, which maximizes the spin-0 luminosity near $E_{\gamma\gamma} = 0.8E_{ee}$, for a particular configuration of beam and laser polarizations as shown in Figure 8.1. The fundamental laser wavelength is determined by available technology and are typically $1.054 \mu m$. For machine energies of $\sqrt{s}=250, 500, 1000$ GeV the corresponding values of x are 2.26, 4.52 and 9.03, respectively. The maximum $E_{\gamma\gamma}$ are 173 GeV, 409 GeV, and 900 GeV with the peak in the spin-0 luminosity somewhat lower. The optimal machine energy (using a $1.054 \mu m$ laser) to study a 126 GeV Higgs-like particle is about 215 GeV with $x = 1.94$. As mentioned above larger values of x are desirable and can be obtained using non-linear optics to triple the laser frequency ² In this case, the optimal machine energy to study a 126 GeV Higgs-like particle is ~ 170 GeV and $x = 4.55$ much closer to the optimal value.

8.2 Higgs Studies

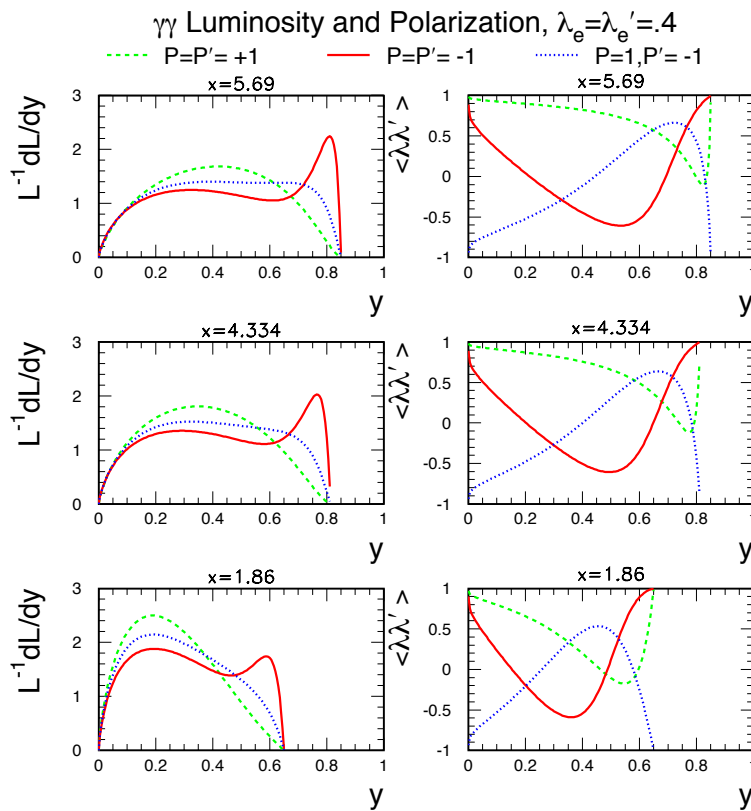
A Standard Model-like Higgs boson h arises in many models containing physics beyond the SM. The $h \rightarrow \gamma\gamma$ coupling receives contributions from loops containing any charged particle whose mass, M , arises in whole or part from the vacuum expectation value of the corresponding neutral Higgs field. When the mass, M , derives in whole or part from the vacuum expectation value (v) of the neutral Higgs field associated with the h , then in the limit of $M \gg m_h$ for the particle in the loop, the contribution asymptotes to a value that depends on the particle's spin (i.e., the contribution does not decouple). As a result, a measurement of $\Gamma(h \rightarrow \gamma\gamma)$ provides the possibility of revealing the presence of heavy charged particles that acquire their mass via the Higgs mechanism.

In addition, we note that $B(h \rightarrow X)$ is entirely determined by the spectrum of particles with mass $< m_h/2$, and is not affected by heavy states with $M > m_h/2$. Consequently, measuring $N(\gamma\gamma \rightarrow h \rightarrow X)$ provides an excellent probe of new heavy particles with mass deriving from the Higgs mechanism.

²The efficiency with which the standard 1.054μ laser beam is converted to 0.351μ is 70%. Thus, roughly 40% more laser power is required in order to retain the subpulse power.

Figure 8.1

The normalized differential luminosity $\frac{1}{\mathcal{L}_{\gamma\gamma}} \frac{d\mathcal{L}_{\gamma\gamma}}{dy}$ and the corresponding $\langle\lambda\lambda'\rangle$ for $\lambda_e = \lambda'_e = .4$ (80% polarization) and three different choices of the initial laser photon polarizations P and P' . The distributions shown are for $\rho^2 \ll 1$ [285, 286]. Results for $x = 5.69$, $x = 4.334$ and $x = 1.86$ are compared.

**Figure 8.2**

Higgs signal and heavy quark backgrounds in units of events per 2 GeV for a Higgs mass of 115 GeV and assuming a running year of 10^7 sec [287].

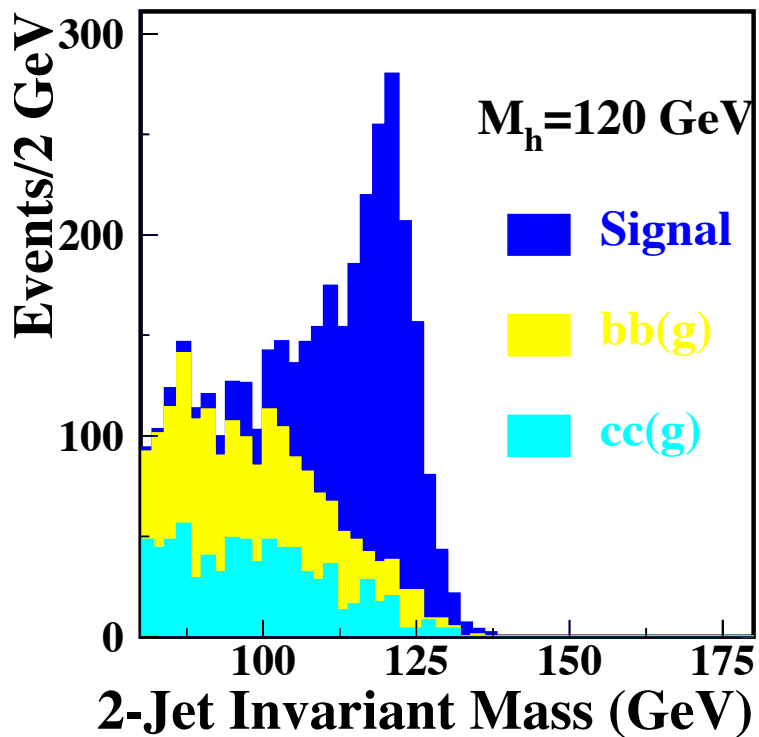
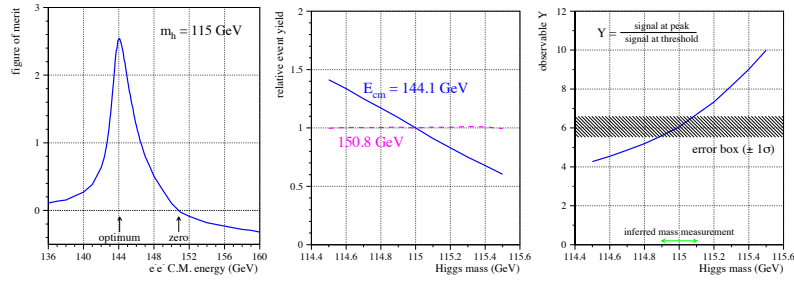


Figure 8.3

(a) A figure of merit quantifying the measurement error on the mass as a function of the e^-e^- center-of-mass energy. The optimum and zero sensitivity points are marked. (b) Relative yield for a 115 GeV Higgs boson at the point of optimum sensitivity and zero sensitivity to m_H . (c) Behavior of the observable Y as a function of m_H , and the projected error.



8.2.1 h_{SM} Mass Measurement

A special feature of the $\gamma\gamma$ collider is the sharp edge of the $\gamma\gamma$ luminosity function, as depicted in Fig. 8.1. The position of this edge can be controlled by changing the electron beam energy. As it sweeps across the threshold for Higgs production, the number of, e.g., $b\bar{b}$ events will increase dramatically. Since the position of this turn-on depends on the Higgs mass, a threshold scan offers the possibility to measure the Higgs mass kinematically, as developed in Ref. [288].

This possibility was studied in the context of CLICHE [287], assuming that the Higgs mass is already known to within a GeV or so. There is a point of optimum sensitivity to the Higgs mass a few GeV below the peak of the cross section. The raw number of events at a single energy cannot be used to measure the mass, however, because the $\gamma\gamma$ partial width cannot be assumed known *a priori*. There is another point, though, close to the maximum of the cross section, at which there is no sensitivity to the Higgs mass, and with maximum sensitivity to $\Gamma_{\gamma\gamma}$, allowing the separation of these two quantities. These points are illustrated in Fig. 8.3. Furthermore, the background can be estimated using data obtained by running below the threshold. To estimate the sensitivity of the yields to m_H , we work with a simple observable based on the ratio of background-subtracted yields at peak and at threshold:

$$Y = \frac{N_{\text{peak}} - N_{\text{below}} \cdot r_p}{N_{\text{threshold}} - N_{\text{below}} \cdot r_t}$$

where N is the number of events in a mass window logged at the peak, on the threshold, and below threshold, and r_p and r_t are scale factors to relate the background data taken below threshold to the expectation at peak and at threshold. We have propagated statistical uncertainties, and, assuming one year of data on peak, half a year on threshold and another half below threshold, we find $\sigma_Y/Y = 0.088$. This translates into an error on the inferred Higgs mass of 100 MeV. A more refined treatment should improve this estimate somewhat. This estimate is obtained using the laser and beam energies proposed for CLIC 1 and the analysis results are similar to those shown in Fig. 8.2. It is still necessary to investigate how sensitive the luminosity function is to the shape of the luminosity curve. It is not sensitive to the electron polarization precision.

8.2.2 Branching Fractions

The precision to which the most important decay modes of a Standard Model Higgs boson can be measured at a gamma-gamma collider are presented in Table 8.1. One of the objectives of a gamma-gamma collider would be to test the Standard Model predictions for Higgs branching fractions and to use measurements of them to distinguish between the Standard Model and its possible extensions, such as the minimal supersymmetric extension of the Standard Model (MSSM) or a more general two-Higgs-doublet model (2HDM).

Table 8.1
Summary of Higgs Branching Fraction and other measurements in 3 years of design luminosity at a Higgs Factory. This study assumed a 120 GeV Standard Model-like Higgs Boson and accelerator parameters as described in [287].

Measurement	Precision
$\Gamma_{\gamma\gamma} \times B(h \rightarrow b\bar{b})$	0.012
$\Gamma_{\gamma\gamma} \times B(h \rightarrow WW)$	0.035
$\Gamma_{\gamma\gamma} \times B(h \rightarrow \gamma\gamma)$	0.121
$\Gamma_{\gamma\gamma} \times B(h \rightarrow ZZ)$	0.064
$\Gamma_{\gamma\gamma} \times B(h \rightarrow \gamma Z)$	0.020
$\Gamma_{\gamma\gamma}^*$	0.021
Γ_{Total}^*	0.13
$m_{h_{SM}} (h \rightarrow \gamma\gamma)$	61 MeV
CP Asymmetry ($h \rightarrow WW$)	0.035-0.040
*Taking $BR(h \rightarrow b\bar{b})$ from e^+e^- running at ILC	

8.2.2.1 $h \rightarrow b\bar{b}$

If there are no new particles that acquire mass via the Higgs mechanism, a precision measurement of $\Gamma(\hat{h} \rightarrow \gamma\gamma)$ can allow one to distinguish between a \hat{h} that is part of a larger Higgs sector and the SM h_{SM} . Figure 8.2 shows the dijet invariant mass distributions for the Higgs signal and for the $b\bar{b}(g)$ and $c\bar{c}(g)$ backgrounds, after all cuts.

Due to the large branching ratio for $H \rightarrow b\bar{b}$ decay for a Higgs mass ~ 115 GeV, this is the main channel for Higgs studies at CLICHE. This channel has received the most attention and the studies are already quite detailed [287, 289]. Our analysis includes perturbative QCD backgrounds, including $\gamma\gamma \rightarrow b\bar{b}(g)$ and $\gamma\gamma \rightarrow c\bar{c}(g)$. The $\bar{q}q$ backgrounds are suppressed by choosing like polarizations for the colliding photons, but this suppression is not so strong when the final states contain additional gluons.

The mass resolution is around 6 GeV with a jet energy resolution of $\sigma_E = 0.6 \times \sqrt{E}$. The distribution in the dijet invariant mass, m_{jets} , for a $m_H = 115$ GeV Higgs found in this study with an integrated luminosity of 200 fb^{-1} is shown in Fig. 8.2. A clear signal peak can be seen above sharply falling backgrounds. Including the three bins nearest to $m_{jets} \sim 115$ GeV, we obtain 4952 signal events and 1100 background events. Thus, the signal-to-background ratio is expected to be 4.5 after all cuts. A feature which is not taken into account in these studies is the pile-up of events from different bunch crossings. Initial studies indicate that pile-up of order 10 bunch crossings degrades the Higgs signal only slightly.

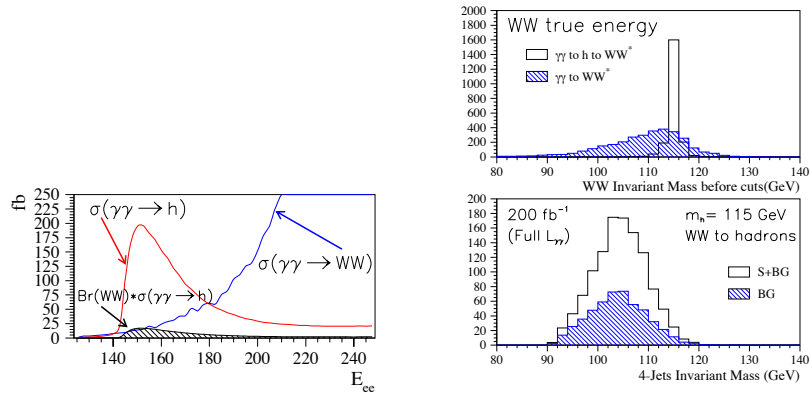
This would yield a measurement of $\Gamma(h_{SM} \rightarrow \gamma\gamma)B(h_{SM} \rightarrow b\bar{b})$ with an accuracy of $\sqrt{S+B}/S \sim 1.2\%$ in 3 years of design luminosity at a Higgs Factory. This study assumed a 120 GeV Standard Model-like Higgs Boson and accelerator parameters as described in [287].

8.2.2.2 $h \rightarrow WW$

Observation of this decay mode is extremely difficult at high-energy $\gamma\gamma$ colliders, because of the large cross section for W pair production. If the $\gamma\gamma$ center-of-mass energy is below the W^+W^- threshold, however, the continuum production of W pairs is greatly reduced, allowing the observation of resonant production through a Higgs boson. The sharp peak in the $\gamma\gamma$ luminosity function seen in Fig. 8.1 plays a key role here. Figure 8.4(a) compares the cross sections for the continuum W pair

Figure 8.4

(a) Cross sections for $\gamma\gamma \rightarrow h$, $\gamma\gamma \rightarrow h \times \text{Br}(h \rightarrow WW)$ for $m_H = 115$ GeV and $\gamma\gamma \rightarrow WW$ production. (b) Comparison of the ideal invariant mass of the WW pairs from signal and background events. (c) Selection of the WW decay mode of the Higgs boson for $m_H = 115$ GeV, running at $E_{CM}(\gamma\gamma) = 115$ GeV at CLICHE.



production with the Higgs resonance curve. As shown, the cross sections for $\sigma(\gamma\gamma \rightarrow W^+W^-)$ and $\text{Br}(h \rightarrow W^+W^-) \times \sigma(\gamma\gamma \rightarrow h)$ are comparable, if $E_{CM}(e^-e^-) = 150$ GeV for a $m_H = 115$ GeV. One significant difference between the two type of events is the energy distribution of the W^+W^- pairs, as illustrated in Figure 8.4(b).

Our study is concentrated on the hadronic decays of the W pairs, applying several kinematic cuts. One pair of jets must reconstruct to the W mass, while the other pair is required to saturate the remaining phase space. This cuts allows us not only to reduce the W^+W^- pairs to those with energy similar to those produced in Higgs events, but also to reject any possible $\gamma\gamma \rightarrow qq(g)$ background. There must be at least four jets in the event and the jet reconstruction efficiency is assumed to be 100%. In contrast to the $h \rightarrow b\bar{b}$ analysis, here we are imposing a $y = 0.003$ cut in the Durham algorithm used in the jet reconstruction. In addition, the transverse momentum is required to be smaller than 0.1. After these cuts we have a 29% reconstruction efficiency. A comparison of the signal and the background after cuts is given in Fig. 8.4(c), which corresponds to a signal-to-background ratio of 1.3, and the statistical precision in the signal rate measurement is expected to be 5%.

The other event topologies (two leptons and missing energy, or one lepton, missing energy and jets) remain to be studied. Techniques similar to those described in [290] may be used. We also believe that the decay $H \rightarrow ZZ, Z\gamma$ might be interesting, despite their relatively small branching ratios.

8.2.2.3 $h \rightarrow \gamma\gamma$

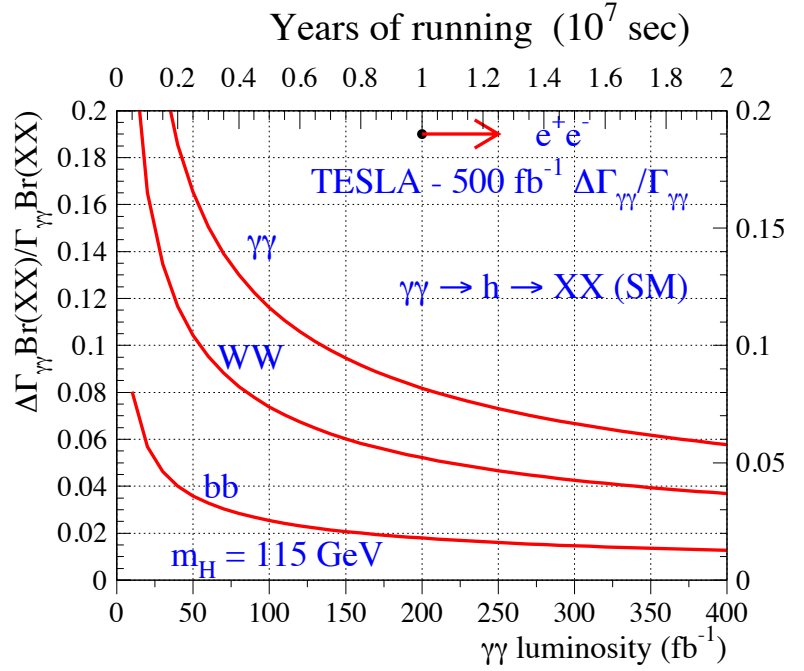
In almost any phenomenological context, the decay $H \rightarrow \gamma\gamma$ is a very rare one. However, the number of Higgs events is large at a $\gamma\gamma$ collider, so an interesting number of $H \rightarrow \gamma\gamma$ events would be produced. Furthermore, the backgrounds are expected to be quite small, below 2 fb [291], since there is no tree-level coupling of photons, and the box-mediated processes are peaked very sharply in the forward direction. A complete background study has not yet been made, but initial estimates indicate that a clear peak in the $\gamma\gamma$ mass distribution should be observable, and we assume here that the background error would be negligible.

The number of events produced in this channel is proportional to $\Gamma_{\gamma\gamma}^2/\Gamma_{\text{total}}$. The quadratic dependence is interesting, because if Γ_{total} could be measured elsewhere, a small error on $\Gamma_{\gamma\gamma}$ would be obtained. Similarly, if $\Gamma_{\gamma\gamma}$ is measured elsewhere, a small error Γ_{total} could be obtained. In Fig. 8.5, we can see that a 10% measurement of $\Gamma_{\gamma\gamma}^2/\Gamma_{\text{total}}$ can be made with less than a year of data taking.

The cleanliness of these events and good energy resolution in the electromagnetic calorimeter would allow for an independent measurement of the Higgs mass. Assuming that the calorimeter energy scales can be sufficiently well calibrated, a resolution better than 100 MeV can be expected.

Figure 8.5

The expected precision in the $h \rightarrow \gamma\gamma$ decay width from direct measurements of $h \rightarrow \gamma\gamma$ for $m_H = 115$ GeV. The precision is less than in the equivalent measurement of $H \rightarrow WW, bb$, but this observable is unique to a low-energy $\gamma\gamma$ collider like CLICHE.



8.2.3 Determining CP Nature of a Higgs Boson

Precision studies of the Standard Model-like Higgs can be performed using the peaked luminosity spectrum (II) with $\sqrt{s} = m_{\text{Higgs}}/y_{\text{peak}}$. These include: determination of CP properties; a detailed scan to separate the H^0 and A^0 when in the decoupling limit of a 2HDM; branching ratios, and the ratio of vacuum expectation values - $\tan \beta$.

Determination of the CP properties of any spin-0 Higgs \hat{h} produced in $\gamma\gamma$ collisions is possible since $\gamma\gamma \rightarrow \hat{h}$ must proceed at one loop, whether \hat{h} is CP-even, CP-odd or a mixture. As a result, the CP-even and CP-odd parts of \hat{h} have $\gamma\gamma$ couplings of similar size. However, the structure of the couplings is very different:

$$\mathcal{A}_{CP=+} \propto \vec{\epsilon}_1 \cdot \vec{\epsilon}_2, \quad \mathcal{A}_{CP=-} \propto (\vec{\epsilon}_1 \times \vec{\epsilon}_2) \cdot \hat{p}_{\text{beam}}. \quad (8.1)$$

By adjusting the orientation of the photon polarization vectors with respect to one another, it is possible to determine the relative amounts of CP-even and CP-odd content in the resonance \hat{h} [292]. If \hat{h} is a mixture, one can use helicity asymmetries for this purpose [230, 292]. However, if \hat{h} is either purely CP-even or purely CP-odd, then one must employ transverse linear polarizations [230, 293].

For a Higgs boson of pure CP, one finds that the Higgs cross section is proportional to

$$\frac{d\mathcal{L}}{dE_{\gamma\gamma}} (1 + \langle \lambda\lambda' \rangle + \mathcal{CP} \langle \lambda_T \lambda'_T \rangle \cos 2\delta) \quad (8.2)$$

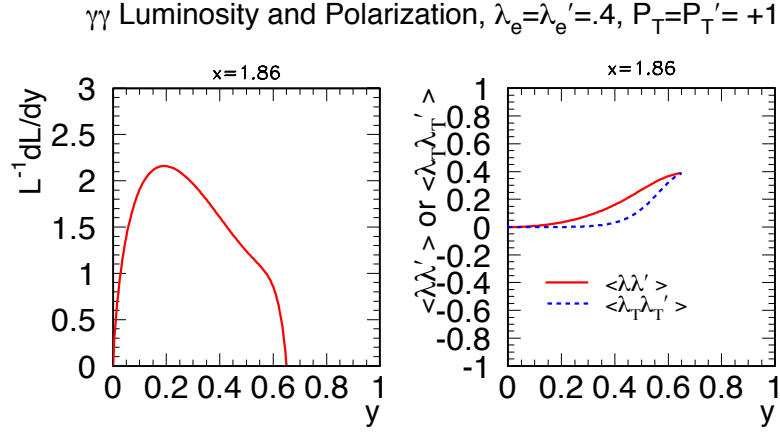
where $\mathcal{CP} = +1$ ($\mathcal{CP} = -1$) for a pure CP-even (CP-odd) Higgs boson and δ is the angle between the transverse polarizations of the laser photons. Thus, one measure of the CP nature of a Higgs is the asymmetry for parallel vs. perpendicular orientation of the transverse linear polarizations of the initial laser beams. In the absence of background, this would take the form

$$\mathcal{A} \equiv \frac{N_{\parallel} - N_{\perp}}{N_{\parallel} + N_{\perp}} = \frac{\mathcal{LCP} \langle \lambda_T \lambda'_T \rangle}{1 + \langle \lambda\lambda' \rangle}, \quad (8.3)$$

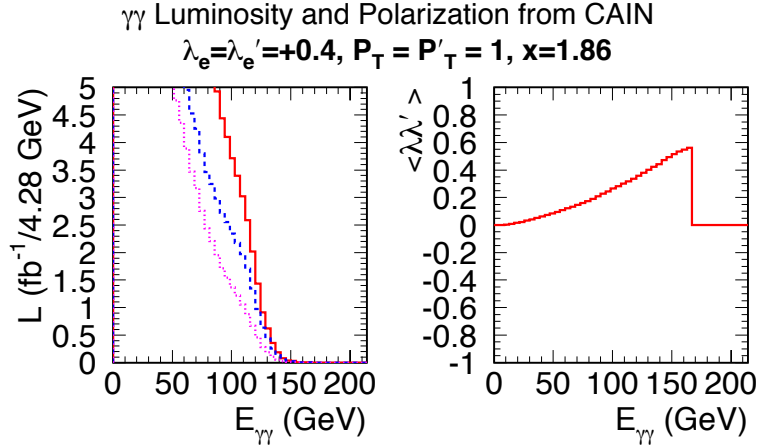
which is positive (negative) for a CP-even (odd) state. The $b\bar{b}(g)$ and $c\bar{c}(g)$ backgrounds result in

Figure 8.6

We plot the luminosities and corresponding $\langle\lambda\lambda'\rangle$ and $\langle\lambda_T\lambda'_T\rangle$ for operation at $\sqrt{s} = 206$ GeV and $x = 1.86$, assuming 100% transverse polarization for the laser photons and $\lambda_e = \lambda'_e = 0.4$. These plots are for the naive non-CAIN distributions.

**Figure 8.7**

We plot the luminosity, $L = d\mathcal{L}/dE_{\gamma\gamma}$, in units of $\text{fb}^{-1}/4.28 \text{ GeV}$ and corresponding $\langle\lambda\lambda'\rangle$ predicted by CAIN for operation at $\sqrt{s} = 206$ GeV and $x = 1.86$, assuming 100% transverse polarization for the laser photons and $\lambda_e = \lambda'_e = 0.4$. The dashed (dotted) curve gives the component of the total luminosity that derives from the $J_z = 0$ ($J_z = 2$) two-photon configuration. The solid luminosity curve is the sum of these two components and $\langle\lambda\lambda'\rangle = (L_{J_z=0} - L_{J_z=2}) / (L_{J_z=0} + L_{J_z=2})$.



additional contributions to the $N_{\parallel} + N_{\perp}$ denominator, which dilutes the asymmetry. The backgrounds do not contribute to the numerator for CP invariant cuts. Since, as described below, total linear polarization for the laser beams translates into only partial polarization for the back-scattered photons which collide to form the Higgs boson, both N_{\parallel} and N_{\perp} will be non-zero for the signal. The expected value of \mathcal{A} must be carefully computed for a given model and given cuts.

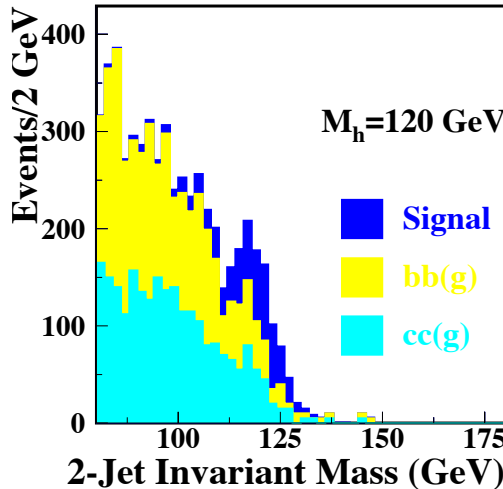
At the kinematic limit, $z = z_{\max} = x/(1+x)$, the ratio of λ to λ_T is given by

$$\frac{\lambda}{\lambda_T} = \lambda_e x \frac{2+x}{1+x} \sim 1 \quad (8.4)$$

for $\lambda_e = 0.4$ and $x = 1.86$. Substantial luminosity and values of λ_T close to the maximum are achieved for moderately smaller z . Operation at $x = 1.86$ (corresponding to $\sqrt{s} = 206$ GeV and laser wave length of $\lambda \sim 1 \mu$) would allow $\lambda_T^{\max} \sim \lambda^{\max} \sim 0.6$. Making these choices for both beams is very nearly optimal for the CP study for the following reasons. First, these choices will maximize $\frac{d\mathcal{L}}{dE_{\gamma\gamma}} \langle\lambda_T\lambda'_T\rangle$ at $E_{\gamma\gamma} = 120$ GeV. As seen from earlier equations, it is the square root of the former quantity that essentially determines the accuracy with which the CP determination can be made. Second, $\lambda_e = \lambda'_e = 0.4$ results in $\langle\lambda\lambda'\rangle > 0$. This is desirable for suppressing the background. (If there were no background, Eq. (8.3) implies that the optimal choice would be to employ λ_e and λ'_e such that $\langle\lambda\lambda'\rangle < 0$. However, in practice the background is very substantial and it is very

Figure 8.8

We plot the signal and $b\bar{b}$ and $c\bar{c}$ backgrounds for a SM Higgs boson with $m_{h_{SM}} = 120$ GeV assuming $\gamma\gamma$ operation at $\sqrt{s} = 206$ GeV and $x = 1.86$, based on the luminosity and polarization distributions of Fig. 8.7 for the case of linearly polarized laser photons. The cross sections presented are those for $\delta = \pi/4$, i.e. in the absence of any contribution from the transverse polarization term in Eq. (8.2).



important to have $\langle\lambda\lambda'\rangle > 0$ to suppress it as much as possible.) In Fig. 8.6, we plot the naive luminosity distribution and associated values of $\langle\lambda\lambda'\rangle$ and $\langle\lambda_T\lambda'_T\rangle$ obtained for $\lambda_e = \lambda'_e = 0.4$ and 100% transverse polarization for the laser beams.

As discussed in [293], the asymmetry studies discussed below are not very sensitive to the polarization of the colliding e beams. Thus, the studies could be performed in parasitic fashion during e^-e^+ operation if the e^+ polarization is small. (As emphasized earlier, substantial e^+ polarization would be needed for precision studies of other h_{SM} properties.)

The luminosity distribution predicted by the CAIN Monte Carlo for transversely polarized laser photons and the corresponding result for $\langle\lambda\lambda'\rangle$ are plotted in Fig. 8.7. We note that even though the luminosity spectrum is not peaked, it is very nearly the same at $E_{\gamma\gamma} = 120$ GeV as in the circular polarization case. As expected from our earlier discussion of the naive luminosity distribution, at $E_{\gamma\gamma} = 120$ GeV we find $\langle\lambda\lambda'\rangle \sim \langle\lambda_T\lambda'_T\rangle \sim 0.36$. Since CAIN includes multiple interactions and non-linear Compton processes, the luminosity is actually non-zero for $E_{\gamma\gamma}$ values above the naive kinematic limit of ~ 132 GeV. Both $\langle\lambda\lambda'\rangle$ and $\langle\lambda_T\lambda'_T\rangle$ continue to increase as one enters this region. However, the luminosity becomes so small that we cannot make effective use of this region for this study. We employ these luminosity and polarization results in the vicinity of $E_{\gamma\gamma} = 120$ GeV in a full Monte Carlo for Higgs production and decay as outlined earlier in the circular polarization case. All the same cuts and procedures are employed.

The resulting signal and background rates for $\delta = \pi/4$ are presented in Fig. 8.8. The width of the Higgs resonance peak is 5.0 ± 0.3 GeV (using a Gaussian fit), only slightly larger than in the circularly polarized case. However, because of the shape of the luminosity distribution, the backgrounds rise more rapidly for $m_{b\bar{b}}$ values below 120 GeV than in the case of circularly polarized laser beams. Thus, it is best to use a slightly higher cut on the $m_{b\bar{b}}$ values in order to obtain the best statistical significance for the signal. Ref. [284] finds ~ 360 reconstructed two-jet signal events with $m_{b\bar{b}} \geq 114$ GeV in one year of operation, with roughly 440 background events in this same region. Under luminosity assumptions similar to those used in Table 8.1, this corresponds to a precision of $\sqrt{S+B}/S \sim 0.032$ for the measurement of $\Gamma(h_{SM} \rightarrow \gamma\gamma)B(h_{SM} \rightarrow b\bar{b})$. Not surprisingly, this is not as good as for the circularly polarized setup, but it is still indicative of a very strong Higgs signal. Turning to the CP determination, let us assume that we run 50% in the parallel polarization configuration and 50% in the perpendicular polarization configuration. Then, because we have only 60% linear polarization for the colliding photons for $E_{\gamma\gamma} \sim 120$ GeV, $N_{\parallel} \sim 180[1 + (0.6)^2] + 273 \sim 518$ and $N_{\perp} \sim 180[1 - (0.6)^2] + 273 = 388$. For these numbers, $\mathcal{A} = 130/906 \sim 0.14$. The error in \mathcal{A} (again with luminosity assumptions similar to those used in Table 8.1) is $\delta\mathcal{A} = \sqrt{N_{\parallel}N_{\perp}/N^3} \sim 0.007$ ($N \equiv N_{\parallel} + N_{\perp}$), yielding $\frac{\delta\mathcal{A}}{\mathcal{A}} = \frac{\delta\mathcal{CP}}{\mathcal{CP}} \sim 0.05$. This measurement would thus provide a fairly strong

Figure 8.9
Summary of gamma-gamma collider golden modes

Reaction	Remarks
$\gamma\gamma \rightarrow h^0 \rightarrow bb$	SM/MSSM Higgs, $M_{h^0} < 160 \text{ GeV}/c^2$
$\gamma\gamma \rightarrow h^0 \rightarrow WW(*)$	SM Higgs, $140 < M_{h^0} < 190 \text{ GeV}/c^2$
$\gamma\gamma \rightarrow h^0 \rightarrow ZZ(*)$	SM Higgs, $180 < M_{h^0} < 350 \text{ GeV}/c^2$
$\gamma\gamma \rightarrow h^0 \rightarrow \gamma\gamma$	SM Higgs, $120 < M_{h^0} < 160 \text{ GeV}/c^2$
$\gamma\gamma \rightarrow h^0 \rightarrow tt$	SM Higgs, $M_{h^0} > 350 \text{ GeV}/c^2$
$\gamma\gamma \rightarrow H, A \rightarrow bb$	MSSM heavy Higgs, interm. $\tan \beta$
$\gamma\gamma \rightarrow \tilde{f}\tilde{f}^*, \tilde{\chi}_i^+ \tilde{\chi}_i^-$	large cross sections
$\gamma\gamma \rightarrow \tilde{g}\tilde{g}$	measurable cross sections
$\gamma\gamma \rightarrow H^+ H^-$	large cross sections
$\gamma\gamma \rightarrow S[\tilde{t}\tilde{t}]$	$\tilde{t}\tilde{t}$ stoponium
$e\gamma \rightarrow \tilde{e}^- \tilde{\chi}_1^0$	$M_{\tilde{e}^-} < 0.9 \times 2E_0 - M_{\tilde{\chi}_1^0}$
$\gamma\gamma \rightarrow \gamma\gamma$	non-commutative theories
$e\gamma \rightarrow eG$	Extra Dimensions
$\gamma\gamma \rightarrow \phi$	Radions
$e\gamma \rightarrow \tilde{e}\tilde{G}$	superlight gravitons
$\gamma\gamma \rightarrow W^+ W^-$	anom. W interactions, extra dimensions
$e\gamma^- \rightarrow W^- \nu_e$	anom. W couplings
$\gamma\gamma \rightarrow 4W/(Z)$	WW scatt., quartic anom. W, Z
$\gamma\gamma \rightarrow tt$	anomalous top quark interactions
$e\gamma^- \rightarrow \bar{t}b\nu_e$	anomalous Wtb coupling
$\gamma\gamma \rightarrow \text{hadrons}$	total $\gamma\gamma$ cross section
$e\gamma^- \rightarrow e^- X, \nu_e X$	NC and CC structure functions
$\gamma g \rightarrow q\bar{q}, c\bar{c}$	gluon in the photon
$\gamma\gamma \rightarrow J/\psi J/\psi$	QCD Pomeron

confirmation of the CP=+ nature of the h_{SM} after three 10^7 sec years devoted to this study.

8.3 Understanding gamma-gamma backgrounds at the ILC

QCD aspects of gamma-gamma physics have been studied at electron-positron colliders over the last several decades years. At LEP, gamma-gamma collisions with \sqrt{s} up to 140 GeV have been studied. Up to now, the photons have been produced via bremsstrahlung from the electron and positron beams, leading to soft energy spectra with only limited statistics at high \sqrt{s} , whereas the gamma-gamma option of the ILC will produce collisions in the high-energy part of the spectrum. A plethora of QCD physics topics in two-photon interactions can be addressed with a gamma-gamma collider, as discussed in [287]. These topics include total gamma-gamma to hadrons cross sections and studies of the (polarized) photon structure functions. Furthermore, good knowledge and understanding of two-photon processes will be essential for controlling physics background contributions to other processes and machine backgrounds at TeV and multi-TeV linear electron-positron colliders.

8.4 Summary

A gamma-gamma (and e-gamma) collider provide exciting physics opportunities that are complementary to and thus strengthen the physics case for the ILC. This section presented a summary of Higgs studies possible at a gamma-gamma collider. The broader physics program of a photon collider is summarized in Table 8.9.

Chapter 9

Summary

A summary of all model independent coupling precisions is given in Table 9.1.

Table 9.1. Summary of expected accuracies $\Delta g_i/g_i$ for model independent determinations of the Higgs boson couplings. The theory errors are $\Delta F_i/F_i = 0.1\%$. For the invisible branching ratio, the numbers quoted are 95% confidence upper limits.

\sqrt{s} (GeV)	ILC(250)	ILC(500)	ILC(1000)	ILC(LumUp)
L (fb^{-1})	250	250+500	250+500+1000	250+500+1000
	250	250+500	250+500+1000	1150+1600+2500
$\gamma\gamma$	18 %	8.4 %	4.0 %	2.4 %
gg	6.4 %	2.3 %	1.6 %	0.9 %
WW	4.8 %	1.1 %	1.1 %	0.6 %
ZZ	1.3 %	1.0 %	1.0 %	0.5 %
$t\bar{t}$	–	14 %	3.1 %	1.9 %
$b\bar{b}$	5.3 %	1.6 %	1.3 %	0.7 %
$\tau^+\tau^-$	5.7 %	2.3 %	1.6 %	0.9 %
$c\bar{c}$	6.8 %	2.8 %	1.8 %	1.0 %
$\mu^+\mu^-$	91%	91%	16 %	10 %
$\Gamma_T(h)$	12 %	4.9 %	4.5 %	2.3 %
hhh	–	83 %	21 %	13 %
BR(invis.)	< 0.9 %	< 0.9 %	< 0.9 %	< 0.4 %

For the purpose of comparing ILC coupling precisions with those of other facilities we present the coupling errors in Table 9.2.

Table 9.2. Summary of expected accuracies $\Delta g_i/g_i$ of Higgs boson couplings using, for each coupling, the fitting technique that most closely matches that used by LHC experiments. For $g_g, g_\gamma, g_W, g_Z, g_b, g_t, g_\tau, \Gamma_T(h)$ the seven parameter HXSWG benchmark parameterization described in Section 10.3.7 of Ref. [205] is used. For the couplings g_μ, g_{hhh} and the limit on invisible branching ratio independent analyses are used. The charm coupling g_c comes from our 10 parameter model independent fit. All theory errors are 0.1%. For the invisible branching ratio, the numbers quoted are 95% confidence upper limits.

\sqrt{s} (GeV)	ILC(250)	ILC(500)	ILC(1000)	ILC(LumUp)
L (fb^{-1})	250	250+500	250+500+1000	250+500+1000
	250	250+500	250+500+1000	1150+1600+2500
$\gamma\gamma$	17 %	8.3 %	3.8 %	2.3 %
gg	6.1 %	2.0 %	1.1 %	0.7 %
WW	4.7 %	0.4 %	0.3 %	0.2 %
ZZ	0.7 %	0.5 %	0.5 %	0.3 %
$t\bar{t}$	6.4 %	2.5 %	1.3 %	0.9 %
$b\bar{b}$	4.7 %	1.0 %	0.6 %	0.4 %
$\tau^+\tau^-$	5.2 %	1.9 %	1.3 %	0.7 %
$\Gamma_T(h)$	9.0 %	1.7 %	1.1 %	0.8 %
$\mu^+\mu^-$	91 %	91 %	16 %	10 %
hhh	–	83 %	21 %	13 %
BR(invis.)	< 0.9 %	< 0.9 %	< 0.9 %	< 0.4 %
$c\bar{c}$	6.8 %	2.8 %	1.8 %	1.0 %

In the energy and luminosity scenarios discussed in this paper it was assumed that the luminosity upgrades at 250 and 500 GeV center of mass energy occurred after the energy upgrade at 1000 GeV. It is of interest to consider a scenario where the 250 GeV and 500 GeV luminosity upgrade running

Table 9.3. Energy and luminosities assuming no running at 1 TeV center of mass energy.

Nickname	Ecm(1) (GeV)	Lumi(1) (fb ⁻¹)	+	Ecm(2) (GeV)	Lumi(2) (fb ⁻¹)	Runtime (yr)	Wallplug E (MW-yr)
ILC(250)	250	250				1.1	130
ILC(500)	250	250		500	500	2.0	270
ILC500(LumUp)	250	1150		500	1600	3.9	660

occurs before the energy upgrade to 1000 GeV. This would correspond to the energies and luminosities in Table 9.3.

A summary of all model independent coupling precisions for the case where the 250 GeV and 500 GeV luminosity upgrade running occurs before the energy upgrade to 1000 GeV is shown in Table 9.4.

Table 9.4. Summary of expected accuracies $\Delta g_i/g_i$ for model independent determinations of the Higgs boson couplings. The theory errors are $\Delta F_i/F_i = 0.1\%$. For the invisible branching ratio, the numbers quoted are 95% confidence upper limits.

	ILC(250)	ILC(500)	ILC500(LumUp)
\sqrt{s} (GeV)	250	250+500	250+500
L (fb ⁻¹)	250	250+500	1150+1600
$\gamma\gamma$	18 %	8.4 %	4.5 %
gg	6.4 %	2.3 %	1.2 %
WW	4.8 %	1.1 %	0.6 %
ZZ	1.3 %	1.0 %	0.5 %
$t\bar{t}$	—	14 %	7.8 %
$b\bar{b}$	5.3 %	1.6 %	0.8 %
$\tau^+\tau^-$	5.7 %	2.3 %	1.2 %
$c\bar{c}$	6.8 %	2.8 %	1.5 %
$\mu^+\mu^-$	91 %	91 %	42 %
$\Gamma_T(h)$	12 %	4.9 %	2.5 %
hhh	—	83 %	46 %
BR(invis.)	< 0.9 %	< 0.9 %	< 0.4 %

The facility comparison table in the case where the 250 GeV and 500 GeV luminosity upgrade running occurs before the energy upgrade to 1000 GeV is shown in Table 9.5.

Table 9.5. Summary of expected accuracies $\Delta g_i/g_i$ of Higgs boson couplings using, for each coupling, the fitting technique that most closely matches that used by LHC experiments. For $g_g, g_\gamma, g_W, g_Z, g_b, g_t, g_\tau, \Gamma_T(h)$ the seven parameter HXSWG benchmark parameterization described in Section 10.3.7 of Ref. [205] is used. For the couplings g_μ, g_{hhh} and the limit on invisible branching ratio independent analyses are used. The charm coupling g_c comes from our 10 parameter model independent fit. All theory errors are 0.1%. For the invisible branching ratio, the numbers quoted are 95% confidence upper limits.

	ILC(250)	ILC(500)	ILC500(LumUp)
\sqrt{s} (GeV)	250	250+500	250+500
L (fb ⁻¹)	250	250+500	1150+1600
$\gamma\gamma$	17 %	8.3 %	4.4 %
gg	6.1 %	2.0 %	1.1 %
WW	4.7 %	0.4 %	0.3 %
ZZ	0.7 %	0.5 %	0.3 %
$t\bar{t}$	6.4 %	2.5 %	1.4 %
$b\bar{b}$	4.7 %	1.0 %	0.6 %
$\tau^+\tau^-$	5.2 %	1.9 %	1.0 %
$\Gamma_T(h)$	9.0 %	1.7 %	1.0 %
$\mu^+\mu^-$	91 %	91 %	42 %
hhh	—	83 %	46 %
BR(invis.)	< 0.9 %	< 0.9 %	< 0.4 %
$c\bar{c}$	6.8 %	2.8 %	1.5 %

A comparison of model independent coupling precisions with and without 1 TeV running is shown in Table 9.6.

The facility comparison table with and without 1 TeV running is shown in Table 9.7.

Table 9.6. Summary of expected accuracies $\Delta g_i/g_i$ for model independent determinations of the Higgs boson couplings. The theory errors are $\Delta F_i/F_i = 0.1\%$. For the invisible branching ratio, the numbers quoted are 95% confidence upper limits.

\sqrt{s} (GeV) L (fb ⁻¹)	ILC500(LumUp)	ILC(LumUp)
	250+500 1150+1600	250+500+1000 1150+1600+2500
$\gamma\gamma$	4.5 %	2.4 %
gg	1.2 %	0.9 %
WW	0.6 %	0.6 %
ZZ	0.5 %	0.5 %
$t\bar{t}$	7.8 %	1.9 %
$b\bar{b}$	0.8 %	0.7 %
$\tau^+\tau^-$	1.2 %	0.9 %
$c\bar{c}$	1.5 %	1.0 %
$\mu^+\mu^-$	42 %	10 %
$\Gamma_T(h)$	2.5 %	2.3 %
hhh	46 %	13 %
BR(invis.)	< 0.4 %	< 0.4 %

Table 9.7. Summary of expected accuracies $\Delta g_i/g_i$ of Higgs boson couplings using, for each coupling, the fitting technique that most closely matches that used by LHC experiments. For $g_g, g_\gamma, g_W, g_Z, g_b, g_t, g_\tau, \Gamma_T(h)$ the seven parameter HXSWG benchmark parameterization described in Section 10.3.7 of Ref. [205] is used. For the couplings g_μ, g_{hhh} and the limit on invisible branching ratio independent analyses are used. The charm coupling g_c comes from our 10 parameter model independent fit. All theory errors are 0.1%. For the invisible branching ratio, the numbers quoted are 95% confidence upper limits.

\sqrt{s} (GeV) L (fb ⁻¹)	ILC500(LumUp)	ILC(LumUp)
	250+500 1150+1600	250+500+1000 1150+1600+2500
$\gamma\gamma$	4.4 %	2.3 %
gg	1.1 %	0.7 %
WW	0.3 %	0.2 %
ZZ	0.3 %	0.3 %
$t\bar{t}$	1.4 %	0.9 %
$b\bar{b}$	0.6 %	0.4 %
$\tau^+\tau^-$	1.0 %	0.7 %
$\Gamma_T(h)$	1.0 %	0.8 %
$\mu^+\mu^-$	42 %	10 %
hhh	46 %	13 %
BR(invis.)	< 0.4 %	< 0.4 %
$c\bar{c}$	1.5 %	1.0 %

Bibliography

- [1] Ties Behnke, James E. Brau, Brian Foster, Juan Fuster, Mike Harrison, et al. The International Linear Collider Technical Design Report - Volume 1: Executive Summary. 2013, 1306.6327.
- [2] Howard Baer, Tim Barklow, Keisuke Fujii, Yuanning Gao, Andre Hoang, et al. The International Linear Collider Technical Design Report - Volume 2: Physics. 2013, 1306.6352.
- [3] Chris Adolphsen, Maura Barone, Barry Barish, Karsten Buesser, Philip Burrows, et al. The International Linear Collider Technical Design Report - Volume 3.I: Accelerator R & D in the Technical Design Phase. 2013, 1306.6353.
- [4] Chris Adolphsen, Maura Barone, Barry Barish, Karsten Buesser, Philip Burrows, et al. The International Linear Collider Technical Design Report - Volume 3.II: Accelerator Baseline Design. 2013, 1306.6328.
- [5] Ties Behnke, James E. Brau, Philip N. Burrows, Juan Fuster, Michael Peskin, et al. The International Linear Collider Technical Design Report - Volume 4: Detectors. 2013, 1306.6329.
- [6] R. Heuer. Parameters for the Linear Collider. 2003.
- [7] Steven Weinberg. The Quantum Theory of Fields. Vol. 1: Foundations. 1995.
- [8] Steven Weinberg. The Quantum Theory of Fields. Vol. 2: Modern applications. 1996.
- [9] F. Englert and R. Brout. Broken Symmetry and the Mass of Gauge Vector Mesons. *Phys.Rev.Lett.*, 13:321–323, 1964.
- [10] Peter W. Higgs. Broken symmetries, massless particles and gauge fields. *Phys.Lett.*, 12:132–133, 1964.
- [11] Peter W. Higgs. Broken Symmetries and the Masses of Gauge Bosons. *Phys.Rev.Lett.*, 13:508–509, 1964.
- [12] G.S. Guralnik, C.R. Hagen, and T.W.B. Kibble. Global Conservation Laws and Massless Particles. *Phys.Rev.Lett.*, 13:585–587, 1964.
- [13] G. S. Guralnik and C. R. Hagen. Massless particles and the goldstone theorem. *Nuovo Cim.*, 43(1):1–32, 1965.
- [14] T.W.B. Kibble. Symmetry breaking in nonAbelian gauge theories. *Phys.Rev.*, 155:1554–1561, 1967.
- [15] Steven Weinberg. A Model of Leptons. *Phys.Rev.Lett.*, 19:1264–1266, 1967.
- [16] S.L. Glashow. Partial Symmetries of Weak Interactions. *Nucl.Phys.*, 22:579–588, 1961.
- [17] Abdus Salam. Weak and Electromagnetic Interactions. *Conf.Proc.*, C680519:367–377, 1968.
- [18] Stephen F. King. Dynamical electroweak symmetry breaking. *Rept.Prog.Phys.*, 58:263–310, 1995, hep-ph/9406401.
- [19] Georges Aad et al. Observation of a new particle in the search for the Standard Model Higgs boson with the ATLAS detector at the LHC. *Phys.Lett.*, B716:1–29, 2012, 1207.7214.
- [20] Serguei Chatrchyan et al. Observation of a new boson at a mass of 125 GeV with the CMS experiment at the LHC. *Phys.Lett.*, B716:30–61, 2012, 1207.7235.

- [21] Georges Aad et al. Measurements of Higgs boson production and couplings in diboson final states with the ATLAS detector at the LHC. *Phys.Lett., B*, 2013, 1307.1427.
- [22] Georges Aad et al. Evidence for the spin-0 nature of the Higgs boson using ATLAS data. *Phys.Lett., B*726:120–144, 2013, 1307.1432.
- [23] Serguei Chatrchyan et al. Observation of a new boson with mass near 125 GeV in pp collisions at $\sqrt{s} = 7$ and 8 TeV. *JHEP*, 1306:081, 2013, 1303.4571.
- [24] Serguei Chatrchyan et al. Study of the Mass and Spin-Parity of the Higgs Boson Candidate Via Its Decays to Z Boson Pairs. *Phys.Rev.Lett.*, 110:081803, 2013, 1212.6639.
- [25] C.H. Llewellyn Smith. High-Energy Behavior and Gauge Symmetry. *Phys.Lett.*, B46:233–236, 1973.
- [26] John M. Cornwall, David N. Levin, and George Tiktopoulos. Uniqueness of spontaneously broken gauge theories. *Phys.Rev.Lett.*, 30:1268–1270, 1973.
- [27] John M. Cornwall, David N. Levin, and George Tiktopoulos. Derivation of Gauge Invariance from High-Energy Unitarity Bounds on the S Matrix. *Phys.Rev.*, D10:1145, 1974.
- [28] J.F. Gunion, H.E. Haber, and J. Wudka. Sum rules for Higgs bosons. *Phys.Rev.*, D43:904–912, 1991.
- [29] J. Erler and P. Langacker. Electroweak model and constraints on new physics, in Ref. [85], pp. 136–156.
- [30] M. Baak, M. Goebel, J. Haller, A. Hoecker, D. Kennedy, R. Kogler, K. Moenig, M. Schott, and T. Stelzer. The Electroweak Fit of the Standard Model after the Discovery of a New Boson at the LHC. *Eur.Phys.J.*, C72:2205, 2012, 1209.2716.
- [31] John F. Gunion, Howard E. Haber, Gordon L. Kane, and Sally Dawson. The Higgs Hunter's Guide. *Front.Phys.*, 80:1–448, 2000.
- [32] E.S. Abers and B.W. Lee. Gauge Theories. *Phys.Rept.*, 9:1–141, 1973.
- [33] Peter Minkowski. $\mu \rightarrow e\gamma$ at a Rate of One Out of 1-Billion Muon Decays? *Phys.Lett.*, B67:421, 1977.
- [34] Murray Gell-Mann, Pierre Ramond, and Richard Slansky. Complex Spinors and Unified Theories. *Conf.Proc.*, C790927:315–321, 1979, 1306.4669.
- [35] Tsutomu Yanagida. Horizontal Symmetry and Masses of Neutrinos. *Prog.Theor.Phys.*, 64:1103, 1980.
- [36] Rabindra N. Mohapatra and Goran Senjanovic. Neutrino Mass and Spontaneous Parity Violation. *Phys.Rev.Lett.*, 44:912, 1980.
- [37] Rabindra N. Mohapatra and Goran Senjanovic. Neutrino Masses and Mixings in Gauge Models with Spontaneous Parity Violation. *Phys.Rev.*, D23:165, 1981.
- [38] John R. Ellis, Mary K. Gaillard, and Dimitri V. Nanopoulos. A Phenomenological Profile of the Higgs Boson. *Nucl.Phys.*, B106:292, 1976.
- [39] Mikhail A. Shifman, A.I. Vainshtein, M.B. Voloshin, and Valentin I. Zakharov. Low-Energy Theorems for Higgs Boson Couplings to Photons. *Sov.J.Nucl.Phys.*, 30:711–716, 1979.
- [40] Marcela Carena, Ian Low, and Carlos E.M. Wagner. Implications of a Modified Higgs to Diphoton Decay Width. *JHEP*, 1208:060, 2012, 1206.1082.
- [41] Thomas Appelquist and J. Carazzone. Infrared Singularities and Massive Fields. *Phys.Rev.*, D11:2856, 1975.
- [42] A. Sirlin and R. Zucchini. Dependence of the Quartic Coupling $\bar{h}_{\overline{\text{MS}}}$ on m_H and the Possible Onset of New Physics in the Higgs Sector of the Standard Model. *Nucl.Phys.*, B266:389, 1986.
- [43] Shinya Kanemura, Yasuhiro Okada, Eibun Senaha, and C.-P. Yuan. Higgs coupling constants

- as a probe of new physics. *Phys.Rev.*, D70:115002, 2004, hep-ph/0408364.
- [44] Andrew G. Cohen, D.B. Kaplan, and A.E. Nelson. Progress in electroweak baryogenesis. *Ann.Rev.Nucl.Part.Sci.*, 43:27–70, 1993, hep-ph/9302210.
 - [45] David E. Morrissey and Michael J. Ramsey-Musolf. Electroweak baryogenesis. *New J.Phys.*, 14:125003, 2012, 1206.2942.
 - [46] Shinya Kanemura, Yasuhiro Okada, and Eibun Senaha. Electroweak baryogenesis and quantum corrections to the triple Higgs boson coupling. *Phys.Lett.*, B606:361–366, 2005, hep-ph/0411354.
 - [47] S Heinemeyer et al. Handbook of LHC Higgs Cross Sections: 3. Higgs Properties. 2013, 1307.1347.
 - [48] N. Cabibbo, L. Maiani, G. Parisi, and R. Petronzio. Bounds on the Fermions and Higgs Boson Masses in Grand Unified Theories. *Nucl.Phys.*, B158:295–305, 1979.
 - [49] Giuseppe Degrandi, Stefano Di Vita, Joan Elias-Miro, Jose R. Espinosa, Gian F. Giudice, Gino Isidori, and Alessandro Strumia. Higgs mass and vacuum stability in the Standard Model at NNLO. *JHEP*, 1208:098, 2012, 1205.6497.
 - [50] Marc Sher. Electroweak Higgs Potentials and Vacuum Stability. *Phys.Rept.*, 179:273–418, 1989.
 - [51] Shinya Kanemura, Takashi Kasai, and Yasuhiro Okada. Mass bounds of the lightest CP even Higgs boson in the two Higgs doublet model. *Phys.Lett.*, B471:182–190, 1999, hep-ph/9903289.
 - [52] G.C. Branco, P.M. Ferreira, L. Lavoura, M.N. Rebelo, Marc Sher, and Joao P. Silva. Theory and phenomenology of two-Higgs-doublet models. *Phys.Rept.*, 516:1–102, 2012, 1106.0034.
 - [53] T.D. Lee. A Theory of Spontaneous T Violation. *Phys.Rev.*, D8:1226–1239, 1973.
 - [54] Sheldon L. Glashow and Steven Weinberg. Natural Conservation Laws for Neutral Currents. *Phys.Rev.*, D15:1958, 1977.
 - [55] E.A. Paschos. Diagonal Neutral Currents. *Phys.Rev.*, D15:1966, 1977.
 - [56] Sacha Davidson and Howard E. Haber. Basis-independent methods for the two-Higgs-doublet model. *Phys.Rev.*, D72:035004, 2005, hep-ph/0504050.
 - [57] Gustavo C. Branco, Luis Lavoura, and Joao P. Silva. CP Violation. *Int.Ser.Monogr.Phys.*, 103:1–536, 1999.
 - [58] Howard E. Haber and Deva O'Neil. Basis-independent methods for the two-Higgs-doublet model. II. The Significance of tan beta. *Phys.Rev.*, D74:015018, 2006, hep-ph/0602242.
 - [59] Howard E. Haber and Deva O'Neil. Basis-independent methods for the two-Higgs-doublet model III: The CP-conserving limit, custodial symmetry, and the oblique parameters S, T, U. *Phys.Rev.*, D83:055017, 2011, 1011.6188.
 - [60] Michael E. Peskin and Tatsu Takeuchi. Estimation of oblique electroweak corrections. *Phys.Rev.*, D46:381–409, 1992.
 - [61] M.J.G. Veltman. Limit on Mass Differences in the Weinberg Model. *Nucl.Phys.*, B123:89, 1977.
 - [62] C.D. Froggatt, R.G. Moorhouse, and I.G. Knowles. Leading radiative corrections in two scalar doublet models. *Phys.Rev.*, D45:2471–2481, 1992.
 - [63] C.D. Froggatt, R.G. Moorhouse, and I.G. Knowles. Two scalar doublet models with softly broken symmetries. *Nucl.Phys.*, B386:63–114, 1992.
 - [64] W. Grimus, L. Lavoura, O.M. Ogreid, and P. Osland. The Oblique parameters in multi-Higgs-doublet models. *Nucl.Phys.*, B801:81–96, 2008, 0802.4353.
 - [65] Benjamin W. Lee, C. Quigg, and H.B. Thacker. Weak Interactions at Very High-Energies: The

- Role of the Higgs Boson Mass. *Phys.Rev.*, D16:1519, 1977.
- [66] H. Arthur Weldon. The Effects of Multiple Higgs Bosons on Tree Unitarity. *Phys.Rev.*, D30:1547, 1984.
 - [67] Howard E. Haber and Yosef Nir. Multiscalar Models With a High-energy Scale. *Nucl.Phys.*, B335:363, 1990.
 - [68] John F. Gunion and Howard E. Haber. The CP conserving two Higgs doublet model: The Approach to the decoupling limit. *Phys.Rev.*, D67:075019, 2003, hep-ph/0207010.
 - [69] Nathaniel Craig, Jamison Galloway, and Scott Thomas. Searching for Signs of the Second Higgs Doublet. 2013, 1305.2424.
 - [70] Howard E. Haber. The decoupling and alignment limits of the Two-Higgs Doublet Model. *In preparation*, 2013.
 - [71] A. Djouadi, H.E. Haber, and P.M. Zerwas. Multiple production of MSSM neutral Higgs bosons at high-energy e^+e^- colliders. *Phys.Lett.*, B375:203–212, 1996, hep-ph/9602234.
 - [72] A. Djouadi, W. Kilian, M. Muhlleitner, and P.M. Zerwas. Testing Higgs selfcouplings at e^+e^- linear colliders. *Eur.Phys.J.*, C10:27–43, 1999, hep-ph/9903229.
 - [73] A. Djouadi, W. Kilian, M. Muhlleitner, and P.M. Zerwas. Production of neutral Higgs boson pairs at LHC. *Eur.Phys.J.*, C10:45–49, 1999, hep-ph/9904287.
 - [74] Giancarlo Ferrera, Jaume Guasch, David Lopez-Val, and Joan Sola. Triple Higgs boson production in the Linear Collider. *Phys.Lett.*, B659:297–307, 2008, 0707.3162.
 - [75] Robert N. Hodgkinson, David Lopez-Val, and Joan Sola. Higgs boson pair production through gauge boson fusion at linear colliders within the general 2HDM. *Phys.Lett.*, B673:47–56, 2009, 0901.2257.
 - [76] David Lopez-Val and Joan Sola. Neutral Higgs-pair production at Linear Colliders within the general 2HDM: Quantum effects and triple Higgs boson self-interactions. *Phys.Rev.*, D81:033003, 2010, 0908.2898.
 - [77] S.L. Glashow, J. Iliopoulos, and L. Maiani. Weak Interactions with Lepton-Hadron Symmetry. *Phys.Rev.*, D2:1285–1292, 1970.
 - [78] Lawrence J. Hall and Mark B. Wise. Flavor changing Higgs boson couplings. *Nucl.Phys.*, B187:397, 1981.
 - [79] Mayumi Aoki, Shinya Kanemura, Koji Tsumura, and Kei Yagyu. Models of Yukawa interaction in the two Higgs doublet model, and their collider phenomenology. *Phys.Rev.*, D80:015017, 2009, 0902.4665.
 - [80] Vernon D. Barger, J.L. Hewett, and R.J.N. Phillips. New Constraints on the Charged Higgs Sector in Two Higgs Doublet Models. *Phys.Rev.*, D41:3421–3441, 1990.
 - [81] Shufang Su and Brooks Thomas. The LHC Discovery Potential of a Leptophilic Higgs. *Phys.Rev.*, D79:095014, 2009, 0903.0667.
 - [82] Heather E. Logan and Deanna MacLennan. Charged Higgs phenomenology in the lepton-specific two Higgs doublet model. *Phys.Rev.*, D79:115022, 2009, 0903.2246.
 - [83] Thomas Hermann, Mikolaj Misiak, and Matthias Steinhauser. $\bar{B} \rightarrow X_s \gamma$ in the Two Higgs Doublet Model up to Next-to-Next-to-Leading Order in QCD. *JHEP*, 1211:036, 2012, 1208.2788.
 - [84] Marco Ciuchini, G. Degrossi, P. Gambino, and G.F. Giudice. Next-to-leading QCD corrections to $B \rightarrow X_s \gamma$: Standard model and two Higgs doublet model. *Nucl.Phys.*, B527:21–43, 1998, hep-ph/9710335.
 - [85] J. Beringer et al. Review of Particle Physics (RPP). *Phys.Rev.*, D86:010001, 2012.
 - [86] E. Barberio et al. Averages of b -hadron and c -hadron properties at the end of 2007. 2008,

0808.1297.

- [87] Toru Goto and Yasuhiro Okada. Charged Higgs mass bound from the $b \rightarrow s\gamma$ process in the minimal supergravity model. *Prog.Theor.Phys.*, 94:407–416, 1995, hep-ph/9412225.
- [88] Marco Ciuchini, G. Degrossi, P. Gambino, and G.F. Giudice. Next-to-leading QCD corrections to $B \rightarrow X_s\gamma$ in supersymmetry. *Nucl.Phys.*, B534:3–20, 1998, hep-ph/9806308.
- [89] Mikolaj Misiak and Matthias Steinhauser. NNLO QCD corrections to the $\overline{B} \rightarrow X_s\gamma$ matrix elements using interpolation in m_c . *Nucl.Phys.*, B764:62–82, 2007, hep-ph/0609241.
- [90] M. Misiak, H.M. Asatrian, K. Bieri, M. Czakon, A. Czarnecki, et al. Estimate of $B(\overline{B} \rightarrow X_s\gamma)$ at $\mathcal{O}(\alpha_s^2)$. *Phys.Rev.Lett.*, 98:022002, 2007, hep-ph/0609232.
- [91] Thomas Becher and Matthias Neubert. Analysis of $\text{Br}(\overline{B} \rightarrow X_s\gamma)$ at NNLO with a cut on photon energy. *Phys.Rev.Lett.*, 98:022003, 2007, hep-ph/0610067.
- [92] A.G. Akeroyd and S. Recksiegel. The Effect of H^\pm on $B^\pm \rightarrow \tau^\pm \nu_\tau$ and $B^\pm \rightarrow \mu^\pm \nu_\mu$. *J.Phys.*, G29:2311–2317, 2003, hep-ph/0306037.
- [93] Maria Krawczyk and Dorota Sokolowska. The Charged Higgs boson mass in the 2HDM: Decoupling and CP violation. *eConf*, C0705302:HIG09, 2007, 0711.4900.
- [94] Maria Krawczyk and David Temes. 2HDM(II) radiative corrections in leptonic tau decays. *Eur.Phys.J.*, C44:435–446, 2005, hep-ph/0410248.
- [95] R. Jackiw and Steven Weinberg. Weak interaction corrections to the muon magnetic moment and to muonic atom energy levels. *Phys.Rev.*, D5:2396–2398, 1972.
- [96] K. Fujikawa, B.W. Lee, and A.I. Sanda. Generalized Renormalizable Gauge Formulation of Spontaneously Broken Gauge Theories. *Phys.Rev.*, D6:2923–2943, 1972.
- [97] Jacques P. Leveille. The Second Order Weak Correction to $(g-2)_\mu$ in Arbitrary Gauge Models. *Nucl.Phys.*, B137:63, 1978.
- [98] H.E. Haber, Gordon L. Kane, and T. Sterling. The Fermion Mass Scale and Possible Effects of Higgs Bosons on Experimental Observables. *Nucl.Phys.*, B161:493, 1979.
- [99] Maria Krawczyk and Jan Zochowski. Constraining 2HDM by present and future muon $g-2$ data. *Phys.Rev.*, D55:6968–6974, 1997, hep-ph/9608321.
- [100] Stephen M. Barr and A. Zee. Electric Dipole Moment of the Electron and of the Neutron. *Phys.Rev.Lett.*, 65:21–24, 1990.
- [101] Farvah Mahmoudi and Oscar Stål. Flavor constraints on the two-Higgs-doublet model with general Yukawa couplings. *Phys.Rev.*, D81:035016, 2010, 0907.1791.
- [102] Alexander L. Kagan and Matthias Neubert. Isospin breaking in $B \rightarrow K^*\gamma$ decays. *Phys.Lett.*, B539:227–234, 2002, hep-ph/0110078.
- [103] Stefan W. Bosch and Gerhard Buchalla. The Radiative decays $B \rightarrow V\gamma$ at next-to-leading order in QCD. *Nucl.Phys.*, B621:459–478, 2002, hep-ph/0106081.
- [104] J.P. Lees et al. Evidence for an excess of $\overline{B} \rightarrow D^{(*)}\tau^-\bar{\nu}_\tau$ decays. *Phys.Rev.Lett.*, 109:101802, 2012, 1205.5442.
- [105] Minoru Tanaka and Ryoutaro Watanabe. New physics in the weak interaction of $\overline{B} \rightarrow D^{(*)}\tau\bar{\nu}$. *Phys.Rev.*, D87(3):034028, 2013, 1212.1878.
- [106] Riccardo Barbieri, Lawrence J. Hall, and Vyacheslav S. Rychkov. Improved naturalness with a heavy Higgs: An Alternative road to LHC physics. *Phys.Rev.*, D74:015007, 2006, hep-ph/0603188.
- [107] Nilendra G. Deshpande and Ernest Ma. Pattern of Symmetry Breaking with Two Higgs Doublets. *Phys.Rev.*, D18:2574, 1978.
- [108] Laura Lopez Honorez, Emmanuel Nezri, Josep F. Oliver, and Michel H.G. Tytgat. The Inert

- Doublet Model: An Archetype for Dark Matter. *JCAP*, 0702:028, 2007, hep-ph/0612275.
- [109] Michael Gustafsson, Sara Rydbeck, Laura Lopez-Honorez, and Erik Lundstrom. Status of the Inert Doublet Model and the Role of multileptons at the LHC. *Phys.Rev.*, D86:075019, 2012, 1206.6316.
 - [110] A. Goudelis, B. Herrmann, and O. Stål. Dark matter in the Inert Doublet Model after the discovery of a Higgs-like boson at the LHC. 2013, 1303.3010.
 - [111] Thomas Hambye and Michel H.G. Tytgat. Electroweak symmetry breaking induced by dark matter. *Phys.Lett.*, B659:651–655, 2008, 0707.0633.
 - [112] Talal Ahmed Chowdhury, Miha Nemevsek, Goran Senjanovic, and Yue Zhang. Dark Matter as the Trigger of Strong Electroweak Phase Transition. *JCAP*, 1202:029, 2012, 1110.5334.
 - [113] Ernest Ma. Verifiable radiative seesaw mechanism of neutrino mass and dark matter. *Phys.Rev.*, D73:077301, 2006, hep-ph/0601225.
 - [114] I.F. Ginzburg, K.A. Kanishev, M. Krawczyk, and D. Sokolowska. Evolution of Universe to the present inert phase. *Phys.Rev.*, D82:123533, 2010, 1009.4593.
 - [115] Qing-Hong Cao, Ernest Ma, and G. Rajasekaran. Observing the Dark Scalar Doublet and its Impact on the Standard-Model Higgs Boson at Colliders. *Phys.Rev.*, D76:095011, 2007, 0708.2939.
 - [116] Erik Lundstrom, Michael Gustafsson, and Joakim Edsjo. The Inert Doublet Model and LEP II Limits. *Phys.Rev.*, D79:035013, 2009, 0810.3924.
 - [117] M. Acciarri et al. Search for charginos and neutralinos in e^+e^- collisions at $\sqrt{s} = 189$ -GeV. *Phys.Lett.*, B472:420–433, 2000, hep-ex/9910007.
 - [118] G. Abbiendi et al. Search for chargino and neutralino production at $\sqrt{s} = 189$ GeV at LEP. *Eur.Phys.J.*, C14:187–198, 2000, hep-ex/9909051.
 - [119] J. Abdallah et al. Searches for supersymmetric particles in e^+e^- collisions up to 208-GeV and interpretation of the results within the MSSM. *Eur.Phys.J.*, C31:421–479, 2003, hep-ex/0311019.
 - [120] Ethan Dolle, Xinyu Miao, Shufang Su, and Brooks Thomas. Dilepton Signals in the Inert Doublet Model. *Phys.Rev.*, D81:035003, 2010, 0909.3094.
 - [121] Xinyu Miao, Shufang Su, and Brooks Thomas. Trilepton Signals in the Inert Doublet Model. *Phys.Rev.*, D82:035009, 2010, 1005.0090.
 - [122] Mayumi Aoki, Shinya Kanemura, and Hiroshi Yokoya. Reconstruction of Inert Doublet Scalars at the International Linear Collider. *Phys.Lett.*, B725:302–309, 2013, 1303.6191.
 - [123] Howard E. Haber. Supersymmetry, Part I (Theory), in Ref. [85], pp. 1420–1437.
 - [124] Howard E. Haber and John D. Mason. Hard supersymmetry-breaking 'wrong-Higgs' couplings of the MSSM. *Phys.Rev.*, D77:115011, 2008, 0711.2890.
 - [125] Marcela S. Carena, Howard E. Haber, Heather E. Logan, and Stephen Mrenna. Distinguishing a MSSM Higgs boson from the SM Higgs boson at a linear collider. *Phys.Rev.*, D65:055005, 2002, hep-ph/0106116.
 - [126] Howard E. Haber and Ralf Hempfling. Can the mass of the lightest Higgs boson of the minimal supersymmetric model be larger than m_Z ? *Phys.Rev.Lett.*, 66:1815–1818, 1991.
 - [127] Yasuhiro Okada, Masahiro Yamaguchi, and Tsutomu Yanagida. Upper bound of the lightest Higgs boson mass in the minimal supersymmetric standard model. *Prog.Theor.Phys.*, 85:1–6, 1991.
 - [128] John R. Ellis, Giovanni Ridolfi, and Fabio Zwirner. Radiative corrections to the masses of supersymmetric Higgs bosons. *Phys.Lett.*, B257:83–91, 1991.

- [129] Kenzo Inoue, Akira Kakuto, Hiromasa Komatsu, and Seiichiro Takeshita. Low-Energy Parameters and Particle Masses in a Supersymmetric Grand Unified Model. *Prog.Theor.Phys.*, 67:1889, 1982.
- [130] Ricardo A. Flores and Marc Sher. Higgs Masses in the Standard, Multi-Higgs and Supersymmetric Models. *Annals Phys.*, 148:95, 1983.
- [131] J.F. Gunion and Howard E. Haber. Higgs Bosons in Supersymmetric Models. 1. *Nucl.Phys.*, B272:1, 1986.
- [132] G. Degrandi, S. Heinemeyer, W. Hollik, P. Slavich, and G. Weiglein. Towards high precision predictions for the MSSM Higgs sector. *Eur.Phys.J.*, C28:133–143, 2003, hep-ph/0212020.
- [133] Stephen P. Martin. Three-loop corrections to the lightest Higgs scalar boson mass in supersymmetry. *Phys.Rev.*, D75:055005, 2007, hep-ph/0701051.
- [134] P. Kant, R.V. Harlander, L. Mihaila, and M. Steinhauser. Light MSSM Higgs boson mass to three-loop accuracy. *JHEP*, 1008:104, 2010, 1005.5709.
- [135] Marcela S. Carena, John R. Ellis, A. Pilaftsis, and C.E.M. Wagner. CP violating MSSM Higgs bosons in the light of LEP-2. *Phys.Lett.*, B495:155–163, 2000, hep-ph/0009212.
- [136] Marcela S. Carena, John R. Ellis, A. Pilaftsis, and C.E.M. Wagner. Higgs boson pole masses in the MSSM with explicit CP violation. *Nucl.Phys.*, B625:345–371, 2002, hep-ph/0111245.
- [137] Marcela S. Carena and Howard E. Haber. Higgs boson theory and phenomenology. *Prog.Part.Nucl.Phys.*, 50:63–152, 2003, hep-ph/0208209.
- [138] E. Accomando, A.G. Akeroyd, E. Akhmetzyanova, J. Albert, A. Alves, et al. Workshop on CP Studies and Non-Standard Higgs Physics. 2006, hep-ph/0608079.
- [139] Hung-Sheng Tsao. Higgs Boson Quantum Numbers and the Pell Equation. in *Proceedings of the 1980 Guangzhou Conference on Theoretical Particle Physics*, edited by H. Ning and T. Hung-yuan, (Science Press, Beijing, 1980):1240, 1980.
- [140] Howard Georgi and Marie Machacek. Doubly charged Higgs bosons. *Nucl.Phys.*, B262:463, 1985.
- [141] J.F. Gunion, R. Vega, and J. Wudka. Naturalness problems for $\rho = 1$ and other large one loop effects for a standard model Higgs sector containing triplet fields. *Phys.Rev.*, D43:2322–2336, 1991.
- [142] Junji Hisano and Koji Tsumura. The Higgs boson mixes with an SU(2) septet representation. 2013, 1301.6455.
- [143] Shinya Kanemura, Mariko Kikuchi, and Kei Yagyu. Probing exotic Higgs sectors from the precise measurement of Higgs boson couplings. 2013, 1301.7303.
- [144] Michael S. Chanowitz and Mitchell Golden. Higgs boson triplets with $m_W = m_Z \cos \theta_W$. *Phys.Lett.*, B165:105, 1985.
- [145] J.F. Gunion, R. Vega, and J. Wudka. Higgs triplets in the standard model. *Phys.Rev.*, D42:1673–1691, 1990.
- [146] Shaaban Khalil. Low scale B–L extension of the Standard Model at the LHC. *J.Phys.*, G35:055001, 2008, hep-ph/0611205.
- [147] Ulrich Ellwanger, Cyril Hugonie, and Ana M. Teixeira. The Next-to-Minimal Supersymmetric Standard Model. *Phys.Rept.*, 496:1–77, 2010, 0910.1785.
- [148] Lorenzo Basso, Stefano Moretti, and Giovanni Marco Pruna. The Higgs sector of the minimal B–L model at future Linear Colliders. *Eur.Phys.J.*, C71:1724, 2011, 1012.0167.
- [149] Pavel Fileviez Perez, Tao Han, Gui-yu Huang, Tong Li, and Kai Wang. Neutrino Masses and the CERN LHC: Testing Type II Seesaw. *Phys.Rev.*, D78:015018, 2008, 0805.3536.

- [150] Mayumi Aoki, Shinya Kanemura, and Kei Yagyu. Testing the Higgs triplet model with the mass difference at the LHC. *Phys.Rev.*, D85:055007, 2012, 1110.4625.
- [151] Georges Aad et al. Search for doubly-charged Higgs bosons in like-sign dilepton final states at $\sqrt{s} = 7$ TeV with the ATLAS detector. *Eur.Phys.J.*, C72:2244, 2012, 1210.5070.
- [152] Serguei Chatrchyan et al. A search for a doubly-charged Higgs boson in pp collisions at $\sqrt{s} = 7$ TeV. *Eur.Phys.J.*, C72:2189, 2012, 1207.2666.
- [153] Shinya Kanemura, Kei Yagyu, and Hiroshi Yokoya. First constraint on the mass of doubly-charged Higgs bosons in the same-sign diboson decay scenario at the LHC. 2013, 1305.2383.
- [154] M. Maniatis. The Next-to-Minimal Supersymmetric extension of the Standard Model reviewed. *Int.J.Mod.Phys.*, A25:3505–3602, 2010, 0906.0777.
- [155] Graham G. Ross and Kai Schmidt-Hoberg. The Fine-Tuning of the Generalised NMSSM. *Nucl.Phys.*, B862:710–719, 2012, 1108.1284.
- [156] Ulrich Ellwanger and Cyril Hugonie. The Upper bound on the lightest Higgs mass in the NMSSM revisited. *Mod.Phys.Lett.*, A22:1581–1590, 2007, hep-ph/0612133.
- [157] Lawrence J. Hall, David Pinner, and Joshua T. Ruderman. A Natural SUSY Higgs Near 126 GeV. *JHEP*, 1204:131, 2012, 1112.2703.
- [158] W. Buchmuller and D. Wyler. Effective Lagrangian Analysis of New Interactions and Flavor Conservation. *Nucl.Phys.*, B268:621, 1986.
- [159] B. Grzadkowski, M. Iskrzynski, M. Misiak, and J. Rosiek. Dimension-Six Terms in the Standard Model Lagrangian. *JHEP*, 1010:085, 2010, 1008.4884.
- [160] A. David et al. LHC HXSWG interim recommendations to explore the coupling structure of a Higgs-like particle. 2012, 1209.0040.
- [161] M. Duhrssen, S. Heinemeyer, H. Logan, D. Rainwater, G. Weiglein, et al. Extracting Higgs boson couplings from CERN LHC data. *Phys.Rev.*, D70:113009, 2004, hep-ph/0406323.
- [162] V.F. Weisskopf. On the Self-Energy and the Electromagnetic Field of the Electron. *Phys.Rev.*, 56:72–85, 1939.
- [163] Leonard Susskind. The Gauge Hierarchy Problem, Technicolor, Supersymmetry, and all that. *Phys.Rept.*, 104:181–193, 1984.
- [164] L. Maiani. All You Need to Know about the Higgs Boson. *Conf.Proc.*, C7909031:1–52, 1979.
- [165] Edward Witten. Dynamical Breaking of Supersymmetry. *Nucl.Phys.*, B188:513, 1981.
- [166] Savas Dimopoulos and Howard Georgi. Softly Broken Supersymmetry and SU(5). *Nucl.Phys.*, B193:150, 1981.
- [167] N. Sakai. Naturalness in Supersymmetric Guts. *Z.Phys.*, C11:153, 1981.
- [168] Romesh K. Kaul. Gauge Hierarchy in a Supersymmetric Model. *Phys.Lett.*, B109:19, 1982.
- [169] Romesh K. Kaul and Parthasarathi Majumdar. Cancellation of Quadratically Divergent Mass Corrections in Globally Supersymmetric Spontaneously Broken Gauge Theories. *Nucl.Phys.*, B199:36, 1982.
- [170] Gautam Bhattacharyya. A Pedagogical Review of Electroweak Symmetry Breaking Scenarios. *Rept.Prog.Phys.*, 74:026201, 2011, 0910.5095.
- [171] Edward Farhi and Leonard Susskind. Technicolor. *Phys.Rept.*, 74:277, 1981.
- [172] Romesh K. Kaul. Technicolor. *Rev.Mod.Phys.*, 55:449, 1983.
- [173] Christopher T. Hill and Elizabeth H. Simmons. Strong dynamics and electroweak symmetry breaking. *Phys.Rept.*, 381:235–402, 2003, hep-ph/0203079.
- [174] Estia Eichten, Kenneth Lane, and Adam Martin. A Higgs Impostor in Low-Scale Technicolor. 2012, 1210.5462.

- [175] Roshan Foadi, Mads T. Frandsen, and Francesco Sannino. 125 GeV Higgs from a not so light Technicolor Scalar. *Phys.Rev.*, D87:095001, 2013, 1211.1083.
- [176] Howard Georgi and A. Pais. Vacuum Symmetry and the PseudoGoldstone Phenomenon. *Phys.Rev.*, D12:508, 1975.
- [177] Howard Georgi and David B. Kaplan. Composite Higgs and Custodial SU(2). *Phys.Lett.*, B145:216, 1984.
- [178] Michael J. Dugan, Howard Georgi, and David B. Kaplan. Anatomy of a Composite Higgs Model. *Nucl.Phys.*, B254:299, 1985.
- [179] Nima Arkani-Hamed, Andrew G. Cohen, Thomas Gregoire, and Jay G. Wacker. Phenomenology of electroweak symmetry breaking from theory space. *JHEP*, 0208:020, 2002, hep-ph/0202089.
- [180] Martin Schmaltz and David Tucker-Smith. Little Higgs review. *Ann.Rev.Nucl.Part.Sci.*, 55:229–270, 2005, hep-ph/0502182.
- [181] Mu-Chun Chen. Models of little Higgs and electroweak precision tests. *Mod.Phys.Lett.*, A21:621–638, 2006, hep-ph/0601126.
- [182] Maxim Perelstein. Little Higgs models and their phenomenology. *Prog.Part.Nucl.Phys.*, 58:247–291, 2007, hep-ph/0512128.
- [183] Hsin-Chia Cheng and Ian Low. TeV symmetry and the little hierarchy problem. *JHEP*, 0309:051, 2003, hep-ph/0308199.
- [184] Hsin-Chia Cheng and Ian Low. Little hierarchy, little Higgses, and a little symmetry. *JHEP*, 0408:061, 2004, hep-ph/0405243.
- [185] Roberto Contino. The Higgs as a Composite Nambu-Goldstone Boson. 2010, 1005.4269.
- [186] Marco Serone. Holographic Methods and Gauge-Higgs Unification in Flat Extra Dimensions. *New J.Phys.*, 12:075013, 2010, 0909.5619.
- [187] Alex Pomarol and Francesco Riva. The Composite Higgs and Light Resonance Connection. *JHEP*, 1208:135, 2012, 1205.6434.
- [188] Csaba Csáki, Christophe Grojean, and John Terning. Alternatives to an Elementary Higgs. *In preparation*, 2013.
- [189] Brando Bellazzini, Csaba Csaki, Jay Hubisz, Javi Serra, and John Terning. A Higgslike Dilaton. *Eur.Phys.J.*, C73:2333, 2013, 1209.3299.
- [190] Zackaria Chacko, Roberto Franceschini, and Rashmish K. Mishra. Resonance at 125 GeV: Higgs or Dilaton/Radion? *JHEP*, 1304:015, 2013, 1209.3259.
- [191] L.D. Landau. On the angular momentum of a two-photon system. *Dokl.Akad.Nauk Ser.Fiz.*, 60:207–209, 1948.
- [192] Chen-Ning Yang. Selection Rules for the Dematerialization of a Particle Into Two Photons. *Phys.Rev.*, 77:242–245, 1950.
- [193] John P. Ralston. The Need to Fairly Confront Spin-1 for the New Higgs-like Particle. 2012, 1211.2288.
- [194] Projections of Higgs Boson measurements with 30 fb^{-1} at 8 TeV and 300 fb^{-1} at 14 TeV, .
- [195] Lance J. Dixon and M. Stewart Siu. Resonance continuum interference in the diphoton Higgs signal at the LHC. *Phys.Rev.Lett.*, 90:252001, 2003, hep-ph/0302233.
- [196] Stephen P. Martin. Shift in the LHC Higgs diphoton mass peak from interference with background. *Phys.Rev.*, D86:073016, 2012, 1208.1533.
- [197] Stephen P. Martin. Interference of Higgs diphoton signal and background in production with a jet at the LHC. *Phys.Rev.*, D88:013004, 2013, 1303.3342.
- [198] Lance J. Dixon and Ye Li. Bounding the Higgs Boson Width Through Interferometry. 2013,

- 1305.3854.
- [199] Fabrizio Caola and Kirill Melnikov. Constraining the Higgs boson width with ZZ production at the LHC. *Phys.Rev.*, D88:054024, 2013, 1307.4935.
 - [200] M. Carena, S. Heinemeyer, O. Stål, C.E.M. Wagner, and G. Weiglein. MSSM Higgs Boson Searches at the LHC: Benchmark Scenarios after the Discovery of a Higgs-like Particle. 2013, 1302.7033.
 - [201] Rick S. Gupta, Heidi Rzehak, and James D. Wells. How well do we need to measure Higgs boson couplings? *Phys.Rev.*, D86:095001, 2012, 1206.3560.
 - [202] Pier Paolo Giardino, Kristjan Kannike, Isabella Masina, Martti Raidal, and Alessandro Strumia. The universal Higgs fit. 2013, 1303.3570.
 - [203] The CMS Collaboration. Jet Energy Scale performance in 2011. 2012.
 - [204] Shinya Kanemura, Takahiro Kubota, and Eiichi Takasugi. Lee-Quigg-Thacker bounds for Higgs boson masses in a two doublet model. *Phys.Lett.*, B313:155–160, 1993, hep-ph/9303263.
 - [205] S. Dittmaier, C. Mariotti, G. Passarino, R. Tanaka, et al. Handbook of LHC Higgs Cross Sections: 1. Inclusive Observables. 2011, 1101.0593.
 - [206] G. Aad et al. Expected Performance of the ATLAS Experiment—Detector, Trigger and Physics. 2009, 0901.0512.
 - [207] B.D. Fields and S. Sarkar. Big-Bang Nucleosynthesis, in Ref. [85], pp. 275–279.
 - [208] A.D. Sakharov. Violation of CP Invariance, C Asymmetry, and Baryon Asymmetry of the Universe. *Pisma Zh.Eksp.Teor.Fiz.*, 5:32–35, 1967.
 - [209] V.A. Kuzmin, V.A. Rubakov, and M.E. Shaposhnikov. On the Anomalous Electroweak Baryon Number Nonconservation in the Early Universe. *Phys.Lett.*, B155:36, 1985.
 - [210] Lars Fromme, Stephan J. Huber, and Michael Seniuch. Baryogenesis in the two-Higgs doublet model. *JHEP*, 0611:038, 2006, hep-ph/0605242.
 - [211] Christophe Grojean, Geraldine Servant, and James D. Wells. First-order electroweak phase transition in the standard model with a low cutoff. *Phys.Rev.*, D71:036001, 2005, hep-ph/0407019.
 - [212] M. Ross and N. Walker. Private communication. 2013.
 - [213] Barry Barish et al. International Linear Collider Submission to European Strategy Discussion. 2012.
 - [214] I. Will, T. Quast, H. Redlin, and W. Sandner. A laser system for the TESLA photon collider based on an external ring resonator. *Nucl.Instrum.Meth.*, A472:79–85, 2001.
 - [215] A. Variola. The ThomX Project. *Conf.Proc.*, C110904:1903–1905, 2011.
 - [216] Masafumi Fukuda, Sakae Araki, Alexander Aryshev, Yosuke Honda, Nobuhiro Terunuma, et al. Status and Future Plan of the Accelerator for Laser Undulator Compact X-ray Source LUCX. *Conf.Proc.*, C100523:TUPD089, 2010.
 - [217] Fred Hartemann, Felicie Albert, Scott Anderson, Christopher Barty, Andy Bayramian, et al. Overview of Mono-energetic Gamma-ray Sources and Applications. *Conf.Proc.*, C100523:TUPD098, 2010.
 - [218] Nicolas Delerue, J. Bonis, Iryna Chaikovska, R. Chiche, R. Cizeron, et al. High flux polarized gamma rays production: first measurements with a four-mirror cavity at the ATF. *Conf.Proc.*, C110904:1446–1448, 2011, 1110.3243.
 - [219] F. Gaede. Marlin and LCCD: Software tools for the ILC. *Nucl.Instrum.Meth.*, A559:177–180, 2006.
 - [220] J.S. Marshall and M.A. Thomson. The Pandora Particle Flow Algorithm. 2013, 1308.4537.

- [221] LCFIPlus, <https://confluence.slac.stanford.edu/display/ilc/LCFIPlus>.
- [222] (Ed.) Aihara, H., (Ed.) Burrows, P., (Ed.) Oreglia, M., et al. SiD Letter of Intent. 2009, 0911.0006. arXiv:0911.0006, SLAC-R-944.
- [223] Higgs Hadronic Branching Ratios in the $ZH \rightarrow llqq$ channel, http://ilcild.org/documents/ild-letter-of-intent/ild-loi-material/higgs_branching_ratios.pdf/at_download/file.
- [224] Toshinori Abe et al. The International Large Detector: Letter of Intent. 2010, 1006.3396.
- [225] H. Li et al. HZ Recoil Mass and Cross Section Analysis in ILD. 2012, 1202.1439.
- [226] M.T. Dova, Pablo Garcia-Abia, and W. Lohmann. Determination of the Higgs boson spin with a linear e^+e^- collider. pages 182–186, 2003, hep-ph/0302113.
- [227] 2 Miller, D.J., S.Y. Choi, B. Eberle, M.M. Muhlleitner, and P.M. Zerwas. Measuring the spin of the Higgs boson. *Phys.Lett.*, B505:149–154, 2001, hep-ph/0102023.
- [228] M. Schumacher. Determination of the CP quantum numbers of the Higgs boson and test of CP invariance in the Higgsstrahlung process at a future e^+e^- linear collider. 2001.
- [229] I. Anderson, Bolognesi S., F. Caola, Y. Gao, V.A. Gritsan, C.B. Martin, K. Melnikov, M. Schulze, N.V. Tran, A. Whitbeck, and Y. Zhou. Constraining anomalous HVV interactions at proton and lepton colliders. 2013, hep-ph/1309.4819.
- [230] M. Kramer, Johann H. Kuhn, M.L. Stong, and P.M. Zerwas. Prospects of measuring the parity of Higgs particles. *Z.Phys.*, C64:21–30, 1994, hep-ph/9404280.
- [231] K. Desch, A. Imhof, Z. Was, and M. Worek. Probing the CP nature of the Higgs boson at linear colliders with tau spin correlations: The case of mixed scalar–pseudoscalar couplings. *Phys.Lett.*, B579:157–164, 2004, hep-ph/0307331.
- [232] Marcel Reinhard. *CP violation in the Higgs sector with a next-generation detector at the ILC*. PhD thesis, 2009.
- [233] P.S. Bhupal Dev, A. Djouadi, R.M. Godbole, M.M. Muhlleitner, and S.D. Rindani. Determining the CP properties of the Higgs boson. *Phys.Rev.Lett.*, 100:051801, 2008, 0707.2878.
- [234] R.M. Godbole, C. Hangst, M. Muhlleitner, S.D. Rindani, and P. Sharma. Model-independent analysis of Higgs spin and CP properties in the process $e^+e^- \rightarrow t\bar{t}\Phi$. *Eur.Phys.J.*, C71:1681, 2011, 1103.5404.
- [235] T. Tanabe. Private communication. 2013.
- [236] Ono, Hiroaki and Akiya Miyamoto. A study of measurement precision of the Higgs boson branching ratios at the International Linear Collider. *Euro.Phys.J.*, C73:2343, 2013.
- [237] Junping Tian and Keisuke Fujii. Summary of Higgs coupling measurement with staged running of ILC and 250 GeV, 500 GeV and 1 TeV. *LC-REP-2013-021*, 2013.
- [238] Junping Tian, Claude Duerig, Keisuke Fujii, and Jenny List. Determination of the Higgs total width with WW -fusion production at ILC up to 500 GeV. *LC-REP-2013-022*, 2013.
- [239] Hiroaki Ono. Higgs branching ratio study for DBD detector benchmarking in ILD. *LC-REP-2013-005*, 2013.
- [240] S. Catani, Yuri L. Dokshitzer, M. Olsson, G. Turnock, and B.R. Webber. New clustering algorithm for multi-jet cross-sections in e^+e^- annihilation. *Phys.Lett.*, B269:432–438, 1991.
- [241] Shin-ichi Kawada, Keisuke Fujii, Taikan Suehara, Tohru Takahashi, Tomohiko Tanabe. $H \rightarrow \tau^+\tau^-$ branching ratio study at $\sqrt{s} = 250$ GeV at the ILC with the ILD detector. *LC-REP-2013-001*, 2013.
- [242] Shin-ichi Kawada, Keisuke Fujii, Taikan Suehara, Tohru Takahashi, and Tomohiko Tanabe. Evaluation of measurement accuracy of $h \rightarrow \tau^+\tau^-$ branching ratio at the ILC with the $\sqrt{s} = 250$ GeV and 500 GeV. 2013, 1308.5489.

- [243] E. Boos, J.C. Brient, D.W. Reid, H.J. Schreiber, and R. Shanidze. Measuring the Higgs branching fraction into two photons at future linear e^+e^- colliders. *Eur.Phys.J.*, C19:455–461, 2001, hep-ph/0011366.
- [244] Timothy L. Barklow. Higgs coupling measurements at a 1 TeV linear collider. 2003, hep-ph/0312268.
- [245] C. Calancha. Presentation at the 32nd General Meeting of the ILC Physics Subgroup, June 2013. http://ilcphys.kek.jp/meeting/physics/archives/2013-06-22/calancha_2013_06_22_generalMeeting.pdf.
- [246] Christoph Englert, Tilman Plehn, Dirk Zerwas, and Peter M. Zerwas. Exploring the Higgs portal. *Phys.Lett.*, B703:298–305, 2011, 1106.3097.
- [247] H. Ono. presentation at the Asian Physics and Software Meeting, June, 2012.
- [248] A. Yamamoto. presentation at the Asian Physics and Software Meeting, June, 2012.
- [249] S. Dittmaier, M. Kramer, Y. Liao, M. Spira, and P.M. Zerwas. Higgs radiation off top quarks in e^+e^- collisions. *Phys.Lett.*, B441:383–388, 1998, hep-ph/9808433.
- [250] S. Dawson and L. Reina. QCD corrections to associated Higgs boson heavy quark production. *Phys.Rev.*, D59:054012, 1999, hep-ph/9808443.
- [251] G. Belanger, F. Boudjema, J. Fujimoto, T. Ishikawa, T. Kaneko, et al. Full $\mathcal{O}(\alpha)$ electroweak and $\mathcal{O}(\alpha_s)$ corrections to $e^+e^- \rightarrow t\bar{t}H$. *Phys.Lett.*, B571:163–172, 2003, hep-ph/0307029.
- [252] Ansgar Denner, S. Dittmaier, M. Roth, and M.M. Weber. Radiative corrections to Higgs boson production in association with top quark pairs at e^+e^- colliders. *Nucl.Phys.*, B680:85–116, 2004, hep-ph/0309274.
- [253] Yu You, Wen-Gan Ma, Hui Chen, Ren-You Zhang, Sun Yan-Bin, et al. Electroweak radiative corrections to $e^+e^- \rightarrow t\bar{t}h$ at linear colliders. *Phys.Lett.*, B571:85–91, 2003, hep-ph/0306036.
- [254] Cailin Farrell and Andre H. Hoang. The Large Higgs energy region in Higgs associated top pair production at the linear collider. *Phys.Rev.*, D72:014007, 2005, hep-ph/0504220.
- [255] Cailin Farrell and Andre H. Hoang. Next-to-leading-logarithmic QCD corrections to the cross-section $\sigma(e^+e^- \rightarrow t\bar{t}H)$ at 500 GeV. *Phys.Rev.*, D74:014008, 2006, hep-ph/0604166.
- [256] A. Juste, Y. Kiyo, F. Petriello, T. Teubner, K. Agashe, et al. Report of the 2005 Snowmass top/QCD working group. 2006, hep-ph/0601112.
- [257] Ryo Yonamine, Katsumasa Ikematsu, Tomohiko Tanabe, Keisuke Fujii, Yuichiro Kiyo, et al. Measuring the top Yukawa coupling at the ILC at $\sqrt{s} = 500$ GeV. *Phys.Rev.*, D84:014033, 2011, 1104.5132.
- [258] Hajrah Tabassam and Victoria Martin. Top Higgs Yukawa Coupling Analysis from $e^+e^- \rightarrow t\bar{t}H \rightarrow bW^+ \bar{b}W^- b\bar{b}$. 2012, 1202.6013.
- [259] Aurelio Juste and Gonzalo Merino. Top Higgs-Yukawa coupling measurement at a linear e^+e^- collider. 1999, hep-ph/9910301.
- [260] Arnaud Gay. Measurement of the top-Higgs Yukawa coupling at a Linear e^+e^- Collider. *Eur.Phys.J.*, C49:489–497, 2007, hep-ph/0604034.
- [261] Junping Tian and Keisuke Fujii. Study of Higgs self-coupling at the ILC based on the full detector simulation at $\sqrt{s} = 500$ GeV and $\sqrt{s} = 1$ TeV. *LC-REP-2013-003*, 2013.
- [262] Y. Yasui, S. Kanemura, S. Kiyoura, K. Odagiri, Y. Okada, et al. Measurement of the Higgs self-coupling at JLC. pages 112–114, 2002, hep-ph/0211047.
- [263] Masakazu Kurata, Tomohiko Tanabe, Junping Tian, Keisuke Fujii, and Taikan Suehara. Study of Higgs self-coupling at the ILC Using $HH \rightarrow b\bar{b}WW^*$. *LC-REP-2013-025*, 2013.
- [264] Michael E. Peskin. Comparison of LHC and ILC Capabilities for Higgs Boson Coupling

- Measurements. 2012, 1207.2516.
- [265] Ian Low and Joseph Lykken. Revealing the electroweak properties of a new scalar resonance. *JHEP*, 1010:053, 2010, 1005.0872.
 - [266] Yosuke Takubo, Robert N. Hodgkinson, Katsumasa Ikematsu, Keisuke Fujii, Nobuchika Okada, et al. Measuring anomalous couplings in $H \rightarrow WW^*$ decays at the International Linear Collider. *Phys.Rev.*, D88:013010, 2013, 1011.5805.
 - [267] J. A. Aguilar-Saavedra et al. TESLA Technical Design Report Part III: Physics at an e^+e^- Linear Collider. 2001, hep-ph/0106315.
 - [268] K. Desch, T. Klimovich, T. Kuhl, and A. Raspereza. Study of Higgs boson pair production at linear collider. 2004, hep-ph/0406229.
 - [269] S. Schael et al. Search for neutral MSSM Higgs bosons at LEP. *Eur.Phys.J.*, C47:547–587, 2006, hep-ex/0602042.
 - [270] J. Abdallah et al. Search for doubly charged Higgs bosons at LEP-2. *Phys.Lett.*, B552:127–137, 2003, hep-ex/0303026.
 - [271] K. Tsumura. presentation at the KILC12 workshop (2012).
 - [272] Tao Liu and C.T. Potter. Exotic Higgs Decay $h \rightarrow aa$ at the International Linear Collider: a Snowmass White Paper. 2013, 1309.0021.
 - [273] A. Djouadi, J. Kalinowski, and P.M. Zerwas. Measuring the $Ht\bar{t}$ coupling in e^+e^- collisions. *Mod.Phys.Lett.*, A7:1765–1769, 1992.
 - [274] A. Djouadi, J. Kalinowski, and P.M. Zerwas. Higgs radiation off top quarks in high-energy e^+e^- colliders. *Z.Phys.*, C54:255–262, 1992.
 - [275] Sachio Komamiya. Searching for charged Higgs bosons at $\sim 1/2$ –1 TeV e^+e^- colliders. *Phys.Rev.*, D38:2158, 1988.
 - [276] Marco Battaglia, Arnaud Ferrari, Ari Kiiskinen, and Tuula Maki. Pair production of charged Higgs bosons at future linear e^+e^- colliders. *eConf*, C010630:E3017, 2001, hep-ex/0112015.
 - [277] S. Moretti. Detection of heavy charged Higgs bosons in $e^+e^- \rightarrow t\bar{b}H^-$ production at future linear colliders. *Eur.Phys.J.*, C34:157–163, 2004, hep-ph/0306297.
 - [278] John F. Gunion, T. Han, J. Jiang, and A. Sopczak. Determining tan beta with neutral and charged Higgs bosons at a future e^+e^- linear collider. *Phys.Lett.*, B565:42–60, 2003, hep-ph/0212151.
 - [279] Shinya Kanemura, Koji Tsumura, and Hiroshi Yokoya. Determination of $\tan\beta$ from the Higgs boson decay at linear colliders. 2013, 1305.5424.
 - [280] Vernon D. Barger, Tao Han, and J. Jiang. $\tan\beta$ determination from heavy Higgs boson production at linear colliders. *Phys.Rev.*, D63:075002, 2001, hep-ph/0006223.
 - [281] T. Barklow. Particle physics research at a 500 GeV e^+e^- linear collider. *Conf.Proc.*, C9006252:440–450, 1990.
 - [282] John F. Gunion and Howard E. Haber. Higgs boson production in the photon-photon collider mode of a high-energy e^+e^- linear collider. *Phys.Rev.*, D48:5109–5120, 1993.
 - [283] Douglas L. Borden, Daniel A. Bauer, and David O. Caldwell. Higgs boson production at a photon linear collider. *Phys.Rev.*, D48:4018–4028, 1993.
 - [284] David M. Asner, Jeffrey B. Gronberg, and John F. Gunion. Detecting and studying Higgs bosons at a photon-photon collider. *Phys.Rev.*, D67:035009, 2003, hep-ph/0110320.
 - [285] I.F. Ginzburg, G.L. Kotkin, V.G. Serbo, and Valery I. Telnov. Colliding γe and $\gamma\gamma$ Beams Based on the Single Pass Accelerators (of VLEPP Type). *Nucl.Instrum.Meth.*, 205:47–68, 1983.
 - [286] I.F. Ginzburg, G.L. Kotkin, S.L. Panfil, V.G. Serbo, and Valery I. Telnov. Colliding γe and $\gamma\gamma$

- Beams Based on the Single Pass e^+e^- Accelerators. 2. Polarization Effects. Monochromatization Improvement. *Nucl.Instrum.Meth.*, A219:5–24, 1984.
- [287] D. Asner, H. Burkhardt, A. De Roeck, J. Ellis, J. Gronberg, et al. Higgs physics with a $\gamma\gamma$ collider based on CLIC I. *Eur.Phys.J.*, C28:27–44, 2003, hep-ex/0111056.
- [288] Tomomi Ohgaki. Precision mass determination of the Higgs boson at photon-photon colliders. *Int.J.Mod.Phys.*, A15:2605–2612, 2000, hep-ph/0002083.
- [289] T. Ohgaki, T. Takahashi, and I. Watanabe. Measuring the two photon decay width of intermediate mass Higgs at a photon-photon collider. *Phys.Rev.*, D56:1723–1729, 1997, hep-ph/9703301.
- [290] M. Dittmar and Herbert K. Dreiner. How to find a Higgs boson with a mass between 155 GeV—180 GeV at the LHC. *Phys.Rev.*, D55:167–172, 1997, hep-ph/9608317.
- [291] G. Jikia and A. Tkabladze. Neutral gauge boson pair production at the photon linear collider: $\gamma\gamma \rightarrow ZZ, \gamma Z, \gamma\gamma$. *Proceedings of the 2nd International Workshop on Physics and Experiments with Linear e^+e^- Colliders, 26-30 Apr 1993. Waikoloa, Hawaii, edited by F.A. Harris, S.L. Olsen, S. Pakvasa, X. Tata. (World Scientific, River Edge, NJ), pages 558–562, 1993.*
- [292] B. Grzadkowski and J.F. Gunion. Using back scattered laser beams to detect CP violation in the neutral Higgs sector. *Phys.Lett.*, B294:361–368, 1992, hep-ph/9206262.
- [293] J.F. Gunion and J.G. Kelly. Determining the CP eigenvalues of the neutral Higgs bosons of the minimal supersymmetric model in $\gamma\gamma$ collisions. *Phys.Lett.*, B333:110–117, 1994, hep-ph/9404343.